THÈSE PRÉSENTÉE

POUR OBTENIR LE GRADE DE

DOCTEUR
DE L'UNIVERSITÉ DE BORDEAUX

ÉCOLE DOCTORALE SCIENCES PHYSIQUES ET DE L'INGÉNIEUR

ASTROPHYSIQUE, PLASMAS, NUCLÉAIRE

Par **Matthieu LECOCQ**

Simulation tool optimisation and analysis of early calibration and reactor neutrino data for the JUNO experiment

---

Sous la direction de : **Cécile JOLLET**

Soutenue le 8 Octobre 2026

Membres du jury :

Mme. Margherita BUIZZA AVANZINI	Chargée de Recherche	LLR	Examinatrice
M. Davide FRANCO	Directeur de Recherche	APC	Rapporteur
Mme. Cécile JOLLET	Maître de Conférence	LP2I	Directrice
M. David LHUILLIER	Directeur de Recherche	CEA	Rapporteur
Mme. Claudia NONES	Directrice de Recherche	CEA	Examinatrice
Mme. Nadia SMIRNOVA	Professeure des Universités	LP2I	Présidente du jury

Optimisation des outils de simulation et analyse des premières données d'étalonnage et de neutrinos de réacteur de l'expérience JUNO

Résumé : Près d'un siècle après sa première théorisation, le neutrino occupe aujourd'hui une place de premier plan en physique des particules. La découverte des oscillations a démontré qu'un neutrino produit dans une saveur donnée pouvait être détecté dans une saveur différente, établissant surtout que les neutrinos sont massifs, en contradiction directe avec le Modèle Standard. Cette découverte a ouvert un riche programme expérimental visant à mesurer précisément les paramètres d'oscillation et à répondre aux questions encore ouvertes sur les neutrinos. Parmi celles-ci, l'ordre de masse des neutrinos — savoir quel neutrino est le plus lourd ou le plus léger — reste l'un des paramètres nécessaires pour compléter notre compréhension des oscillations. Le Jiangmen Underground Neutrino Observatory (JUNO) est un détecteur à scintillateur liquide de nouvelle génération, d'une masse de 20 kilotonnes et doté d'une résolution en énergie sans précédent de 3%. Conçu pour sonder l'ordre de masse des neutrinos à l'aide d'antineutrinos de réacteur, l'expérience vise également une précision inférieure au pourcent sur les paramètres d'oscillation, tout en offrant un vaste programme de physique incluant l'étude des neutrinos solaires, atmosphériques et de supernova. Cette thèse s'inscrit dans une période cruciale de l'expérience, marquée par l'achèvement de la construction du détecteur et le début de la prise de données. Ce travail présente plusieurs études de mise en service du détecteur et d'analyse menées à partir des premières données de JUNO, centrées sur le canal de détection par désintégration bêta inverse (IBD).

Avant la mise en service, la thèse s'est concentrée sur l'optimisation des outils de simulation de JUNO, puis sur leur validation par comparaison aux données d'étalonnage collectées lors du remplissage en double phase jusqu'au détecteur entièrement rempli. À l'aide de sources radioactives et de neutrons déployées à différentes positions, le rendement lumineux, la non-uniformité et non-linéarité de la réponse en énergie du détecteur sont caractérisés et comparés à la simulation pour les deux systèmes de photomultiplicateurs, permettant d'améliorer la fidélité du modèle de réponse du détecteur. En s'appuyant sur cette compréhension validée, l'analyse centrale de cette thèse présente la sélection des événements IBD sur les 60 premiers jours de données, ainsi que la caractérisation du bruit de fond cosmogénique ^{9}Li/^{8}He, produit par spallation des muons dans le scintillateur et constituant l'un des bruits de fond corrélés les plus significatifs pour le signal IBD. Enfin, cette thèse explore la formation de l'ortho-positronium (o-Ps), dont la signature dans la distribution temporelle des événements permet de distinguer positrons et électrons, ouvrant la voie à une nouvelle méthode d'estimation de la pureté de l'échantillon IBD. La fraction de formation et la durée de vie de l'o-Ps dans le scintillateur de JUNO sont estimées, et les perspectives ainsi que les limites de cette technique sont discutées.

Mots-clés : Neutrinos, Oscillations, Detecteur à Scintillation, Ordre de Masse

Simulation tool optimisation and analysis of early calibration and reactor neutrino data for the JUNO experiment

Abstract: Nearly a century after it was first theorised, the neutrino is at the forefront of research in particle physics. The discovery of neutrino oscillations demonstrated that a neutrino produced in a given flavour could be detected in a different one, and established that neutrinos are massive, in direct contradiction with the Standard Model. This discovery opened a rich experimental program aimed at precisely measuring the oscillation parameters and addressing the questions that remain open about neutrinos. Among these, the neutrino mass ordering — determining which neutrino is the heaviest or the lightest — remains one of the parameters required to complete our understanding of oscillations.

The Jiangmen Underground Neutrino Observatory (JUNO) is a next-generation, 20-kiloton liquid scintillator detector, with an unprecedented 3% energy resolution. The experience is designed to probe the neutrino mass ordering using reactor antineutrinos, while reaching a sub-percent precision on the oscillation parameters and offering a broad physics program including the study of solar, atmospheric, and supernova neutrinos. This thesis comes at a crucial period of the experiment, marked by the completion of the detector's construction and the beginning of data-taking. This work presents several detector commissioning and analysis studies conducted using the early data collected by JUNO, centered on the Inverse Beta Decay (IBD) detection channel.

Prior to commissioning, the thesis focused on the optimisation of JUNO's simulation tools, followed by their validation against calibration data collected during the dual-phase filling period, up to the fully filled detector. Using radioactive and neutron sources deployed at various positions, the detector's light yield, energy non-uniformity and non-linearity are characterised and compared to simulation for both photomultiplier systems, improving the fidelity of the detector's response model. Building on this validated understanding, the central analysis of this thesis presents the IBD event selection applied to the first 60 days of data, along with the characterisation of the ^{9}Li/^{8}He cosmogenic background, produced by muon spallation in the scintillator and constituting one of the most significant correlated backgrounds to the IBD signal. Finally, this thesis explores the formation of ortho-positronium (o-Ps), whose signature in the event time distribution allows positrons to be distinguished from electrons, opening the way to a new method for estimating the purity of the IBD sample. The formation fraction and lifetime of o-Ps in JUNO's scintillator are estimated, and the prospects and limitations of this technique are discussed.

Keywords: Neutrinos, Oscillations, Scintillator Detector, Mass Ordering

---

Unité de recherche

UMR 5797 Université, 33000 Bordeaux, France.

Remerciements

Cette thèse n'aurait pas été possible sans l'implication et le soutien de nombreuses personnes, que je tiens à remercier ici.

Je tiens d'abord à remercier les membres du jury d'avoir pris le temps de lire ma thèse et d'être venus assister à ma soutenance pour juger mon travail. Je remercie en particulier mes deux rapporteurs, M. Davide Franco et M. David Lhuillier, qui ont lu mon manuscrit avec soin et dont j'ai apprécié lire les rapports.

Cette thèse est aussi le fruit de rencontres avec des personnes qui m'ont fait découvrir et aimer la recherche : M. Pascal Pralavorio et Mme Corinne Augier, mes maîtres de stage, que je remercie de m'avoir guidé, motivé et soutenu dans mon objectif.

Bien sûr, ce travail n'aurait pas vu le jour sans Cécile Jollet, ma directrice de thèse, que je remercie sincèrement pour son accompagnement, sa pédagogie, sa patience et sa disponibilité tout au long de la thèse, surtout durant l'écriture du manuscrit. J'ai énormément appris grâce à ta supervision et à tes conseils. J'espère qu'on aura l'occasion de travailler à nouveau ensemble, et je croise les doigts pour le poste de prof !

Je remercie aussi tous les membres du groupe neutrino, et surtout ceux du groupe JUNO, pour ces trois années. En particulier Loïc, que je considère comme mon mentor et mon ami, qui a été très présent pendant ma thèse, qui m'a formé, et sur qui j'ai toujours pu m'appuyer quand j'en ai eu besoin. Merci pour toutes les discussions qu'on a eues, et je te souhaite le meilleur pour la suite à Strasbourg.

Ces trois ans au LP2I n'auraient pas été les mêmes sans tous les bons moments passés avec le groupe des non-permanents : nos soirées et tous les pranks qu'on a pu se faire les uns aux autres. Merci pour tout, bon courage à ceux qui n'ont pas encore terminé, j'ai hâte d'assister à vos soutenances.

Parmi les doctorants, j'aimerais surtout remercier Mathis, qui a vraiment été un soutien tout au long de cette thèse, et que je remercie aussi pour tous les moments passés ensemble dans ce bureau, où on a bien rigolé pendant ces trois ans. On l'a fait, on l'a eue, cette thèse !

J'ai maintenant une pensée pour mes amis, qui m'ont beaucoup soutenu : Driss, Axel, Sameo, Greg, Mehdi et Romain, que j'étais très heureux de voir tous réunis pour ma soutenance. J'ai une pensée toute particulière pour JB, mon meilleur ami, qui a toujours été présent, qui a toujours cru en moi et m'a soutenu dans les périodes difficiles. Cette thèse c'est aussi un peu

la tienne.

Je ne peux pas oublier ma famille, et surtout ma mère, pour qui j'ai un grand respect et sans qui je n'aurais jamais pu espérer obtenir un doctorat. Merci pour tout ce que tu as fait pour nous !

Enfin, j'ai une pensée pour ma copine, Emma, qui a été un grand soutien moral à la fin de cette thèse, et que je remercie d'avoir été présente durant cette période.

Résumé étendu en français

Introduction

Près d'un siècle après sa première proposition théorique, le neutrino demeure l'une des particules les plus activement étudiées en physique. La découverte des oscillations de neutrinos a établi que ces derniers sont massifs, en contradiction directe avec le Modèle Standard, et a ouvert un riche programme expérimental visant à mesurer précisément les paramètres d'oscillation et à résoudre les questions ouvertes sur l'origine et la nature de la masse des neutrinos. Parmi ces questions, l'ordre de masse des neutrinos — savoir si les neutrinos sont ordonnés en masse de la même manière que leurs leptons chargés correspondants, ou non — occupe une place centrale dans la génération actuelle d'expériences. Sa détermination permet de répondre à plusieurs autres questions ouvertes du domaine, notamment la mesure de la phase CP et la sensibilité aux recherches de la double désintégration bêta sans émission de neutrinos.

Le Jiangmen Underground Neutrino Observatory (JUNO) est une expérience de nouvelle génération dédiée conçue pour déterminer l'ordre de masse des neutrinos à l'aide d'antineutrinos produits dans des centrales nucléaires et grâce à une résolution en énergie sans précédent de $3\%/\sqrt{E\ [\mathrm{MeV}]}$. Atteindre cet objectif impose de fortes contraintes sur la réponse en énergie du détecteur ainsi que sur sa stratégie de contrôle des bruits de fond, qui doivent tous deux être bien maîtrisés pour l'analyse spectral final de JUNO. Cette thèse est rédigée à une periode charnière de l'expérience : la construction et le remplissage de JUNO sont terminés, et le détecteur a débuté sa première campagne de prise de données de physique. Le travail présenté ici suit directement cette transition, depuis la mise en service et la validation du détecteur, jusqu'à l'optimisation de sa simulation et aux premières analyses de physique réalisées sur les données de JUNO.

Cette thèse est organisée en six chapitres, suivant cette progression. Le chapitre 1 introduit le cadre théorique des oscillations de neutrinos et de la génération de leur masse, et présente le contexte expérimental actuel de la physique des neutrinos, avant de détailler les méthodes actuellement employées pour déterminer l'ordre de masse, en comparant l'approche de JUNO, utilisant une source de neutrino à moyenne distance, aux expériences de neutrinos d'accélérateur et atmosphériques à longues distances. Le chapitre 2 présente l'expérience JUNO elle-même, de son principe de détection et de la conception du détecteur jusqu'aux résultats sur

ses performances initiales, issus de sa mise en service et de sa première campagne d'étalonnage. L'expérience satellite de JUNO, TAO, fait l'objet d'une section dédiée, qui détaille son intérêt physique et son rôle dans la mesure de l'ordre de masse par JUNO.

Au cours de cette thèse, un travail important a été mené sur l'optimisation du logiciel de simulation de JUNO et sur sa validation par comparaison aux données de mise en service et d'étalonnage. Le chapitre 3 présente la structure du logiciel de simulation de JUNO, construit pour soutenir le vaste programme de physique de l'expérience, avant de décrire la validation et la mise à niveau de l'outil de simulation Geant4, de la version 10.4.2 à la version 11.2. Plusieurs écarts identifiés dans la modélisation de la physique électromagnétique et hadronique ont été signalés aux développeurs de Geant4, certains corrigés par les développeurs dans la dernière version 11.4, et d'autres corrigés en interne, puis validée et intégrée au logiciel de simulation de JUNO. Une analyse supplémentaire est menée sur cette dernière version afin d'évaluer sa capacité à reproduire les rendements d'isotopes cosmogéniques utiles aux chapitres suivants. Le chapitre 4 présente une validation complémentaire de la réponse en énergie simulée de JUNO par rapport aux données collectées lors de sa première campagne d'étalonnage, en caractérisant le rendement lumineux, l'uniformité spatiale et la non-linéarité en énergie du détecteur. Ces analyses ont servi de procédure de validation et ont permis d'établir le niveau de compréhension de la réponse en énergie du détecteur avant la première campagne de prise de données.

Les deux derniers chapitres présentent des analyses de physique réalisées sur les premières données collectées par JUNO. Le chapitre 5 présente la sélection des candidats de désintégration bêta inverse (IBD) et sa révision pour les 60 premiers jours de données de JUNO. Cette sélection révisée a conduit à une évaluation approfondie du bruit de fond résiduel, et une méthode est présentée pour estimer le taux résiduel du bruit de fond cosmogénique de ^{9}Li/^{8}He subsistant dans l'échantillon final. Le chapitre 6 explore une méthode complémentaire de rejet du bruit de fond, fondée sur l'identification de la formation de l'ortho-positronium dans le scintillateur liquide de JUNO. Les performances de la méthode d'identification développée sont d'abord évaluées sur des échantillons simulés, puis la méthode est appliquée à un jeu de données de JUNO plus important, de 193,2 jours, fournissant la première mesure de la probabilité de formation et de la durée de vie moyenne de l'ortho-positronium dans le scintillateur liquide de JUNO.

L'ensemble de ces chapitres suit ainsi l'expérience depuis sa motivation théorique jusqu'à son détecteur, sa simulation et ses premiers résultats de physique.

Résumé des chapitres

Le neutrino et l'ordre de masse

Le premier chapitre pose le cadre théorique. Postulé par Pauli en 1930 pour sauver la conservation de l'énergie dans la désintégration bêta, puis détecté par Reines et Cowan auprès d'un réacteur en 1956, le neutrino est une particule neutre, uniquement sensible à l'interaction faible, et produite en abondance dans le Soleil, l'atmosphère, les réacteurs nucléaires, les supernovæ ou encore la croûte terrestre. Le chapitre rappelle les grandes étapes historiques qui ont fait du neutrino un sujet majeur de la physique des particules : la mise en évidence de plusieurs saveurs (électron, muon et tau), ainsi que le déficit de neutrinos observé en provenance du Soleil et de l'atmosphère par rapport aux prédictions théoriques. Ce déficit a été expliqué par l'observation de l'oscillation des neutrinos — la possibilité pour un neutrino émis dans une saveur donnée d'être détecté dans une saveur différente.

Dans le Modèle Standard, le neutrino est dépourvu de masse. Les oscillations, qui ne peuvent se produire que si les neutrinos sont massifs, constituent donc la première indication solide de physique au-delà de ce modèle. Elles s'expliquent par le fait que les états de saveur, produits et détectés dans les interactions faibles, sont des superpositions d'états de masse qui se propagent avec des phases différentes. Ce mélange est décrit par la matrice PMNS, paramétrée par trois angles de mélange (θ_{12}, θ_{13}, θ_{23}) et une phase de violation de CP, tandis que la propagation fait intervenir deux différences de carrés de masse (Δm^2_{21} et Δm^2_{31}). Le chapitre développe le formalisme des oscillations dans le vide, puis dans la matière : les neutrinos y acquièrent un potentiel effectif lié à la diffusion cohérente sur les électrons, qui modifie les probabilités d'oscillation (effet MSW).

Plusieurs questions restent aujourd'hui ouvertes, que le chapitre passe en revue. La première concerne la nature du neutrino, de Dirac ou de Majorana. Dans le second cas, le mécanisme de bascule (*seesaw*) explique la petitesse de sa masse, et la double désintégration bêta sans émission de neutrinos, dont l'observation constituerait une preuve expérimentale de la nature de Majorana du neutrino, fait l'objet d'une intense recherche. La deuxième est l'échelle absolue de la masse, contrainte par les mesures directes de KATRIN, par la cosmologie et par les mesures de neutrinos de supernovæ. Vient ensuite la valeur de la phase de violation de CP. Ces questions dépendent toutes en partie de l'ordre de masse, c'est-à-dire du signe de Δm^2_{31}, qui détermine si l'état de masse le plus léger est celui qui contient le plus de ν_e (ordre normal) ou, au contraire, le plus de ν_μ et ν_τ (ordre inversé). Les trois grandes familles d'approches disponibles pour déterminer l'ordre de masse reposent sur des effets distincts et souffrent de dégénérescences différentes : les expériences à longue distance auprès d'accélérateurs, sensibles à l'effet de la matière terrestre mais dégénérées avec la phase de violation de CP ; les neutrinos atmosphériques, qui profitent d'une large gamme d'énergies et de distances ; et les réacteurs à moyenne distance, qui ne dépendent ni de la matière ni de la phase de violation de CP, mais

qui exigent une résolution en énergie exceptionnelle. Leur complémentarité est un argument central du programme expérimental actuel.

JUNO appartient à cette dernière catégorie. En mesurant le spectre en énergie des antineutrinos électroniques à environ 52,5 km des réacteurs, il est possible de résoudre simultanément les oscillations lentes, pilotées par Δm^2_{21} et par θ_{12}, et les oscillations rapides, pilotées par Δm^2_{31} et par θ_{13}, qui se superposent aux premières. Le signe de Δm^2_{31} se lit alors dans de fines déformations du spectre, indépendamment de l'effet de la matière et de la phase de violation de CP. Cette même mesure donne aussi accès, avec une précision inférieure au pourcent, à $\sin^2\theta_{12}$, Δm^2_{21} et Δm^2_{31}. Le prix à payer est une exigence inhabituelle sur le détecteur : la déformation recherchée est faible, elle varie rapidement avec l'énergie et ne peut être extraite que si celle-ci est mesurée avec une résolution et une exactitude exceptionnelles. C'est cette contrainte qui détermine la conception de l'expérience.

Mesurer l'ordre de masse avec JUNO

Le deuxième chapitre montre comment cette exigence s'est traduite en choix de conception. L'expérience est installée à environ 700 m sous terre, afin d'atténuer le flux de muons cosmiques. Son détecteur central est une sphère acrylique contenant 20 kt de scintillateur liquide (LS), un LAB dopé avec 2,5 g/L de PPO et 3 mg/L de bis-MSB, dans lequel les antineutrinos de réacteur interagissent par désintégration bêta inverse (IBD). Cette réaction produit un signal prompt, dû au positron, suivi d'un signal retardé, dû à la capture du neutron, avec un temps caractéristique de $\sim 200\,\mu$s. Le détecteur central ne peut pas être exploité sans un environnement qui en maîtrise les bruits de fond. Il est plongé dans une piscine d'eau instrumentée, qui sert à la fois de blindage contre la radioactivité de la roche et de veto Cherenkov pour les muons, et il est surmonté d'un trajectographe à muons. Un certain nombre de bruits de fond imitant la signature de l'IBD sont néanmoins attendus (radioactivité naturelle, isotopes cosmogéniques, antineutrinos ne provenant pas des réacteurs étudiés, neutrinos atmosphériques) et doivent être estimés correctement.

La lumière de scintillation est collectée par deux systèmes de photomultiplicateurs (PMT) : 17 596 photomultiplicateurs de grande taille (LPMT), de deux modèles, Hamamatsu et NNVT, qui offrent un bon compromis entre reconstruction en énergie et reconstruction en position, complétés par 25 587 photomultiplicateurs de petite taille (SPMT). Ces derniers fonctionnent dans un régime de comptage de photons et fournissent une mesure indépendante de l'énergie, utile pour contrôler certaines incertitudes systématiques du système principal. La résolution visée, $3\%/\sqrt{E\,[\mathrm{MeV}]}$, impose des contraintes strictes sur les performances du scintillateur liquide et des photomultiplicateurs, et exige une production et une collection élevées de photons de scintillation. Les performances initiales du détecteur montrent un rendement lumineux du scintillateur supérieur à 1600 photoélectrons (PE) par MeV, ainsi que des performances des LPMT et des SPMT au-delà des exigences de l'expérience.

La validation des performances du détecteur repose sur la stratégie d'étalonnage de l'expérience. Une résolution de 3% n'a de sens que si l'échelle d'énergie est elle-même connue à mieux que le pourcent, y compris en fonction de la position dans le volume. JUNO dispose pour cela de plusieurs systèmes complémentaires : une unité d'étalonnage automatique (ACU) le long de l'axe central, un treuil à câble (CLS) pour les positions hors axe, un système de guide-tubes (GT) sur la surface de la sphère et un véhicule télécommandé (ROV). Ils permettent de déployer des sources variées, émettrices de γ ou de neutrons, dont ^{68}Ge, ^{137}Cs, ^{54}Mn, ^{60}Co, ^{40}K, AmBe et AmC, couvrant la gamme d'énergie correspondant aux antineutrinos de réacteur.

En parallèle de JUNO, une expérience satellite, TAO, est construite à proximité de l'un des réacteurs nucléaires sources de JUNO. Son détecteur a un design similaire à celui de JUNO, mais à une échelle bien plus petite, et avec une résolution en énergie de $2\%/\sqrt{E\,[\mathrm{MeV}]}$. L'objectif principal de l'expérience est de réaliser une mesure très précise du spectre en énergie des antineutrinos de réacteur, afin non seulement d'en extraire les structures fines, qui pourront être comparées aux modèles théoriques, mais surtout de fournir à JUNO un spectre en énergie de référence non oscillé.

Mise à jour de Geant4 dans JUNOSW

La simulation est un ingrédient clé de toute expérience moderne. Elle permet de modéliser chaque élément du détecteur, de prédire sa réponse, d'estimer les efficacités de sélection et de construire les modèles utilisés pour extraire les paramètres d'oscillation. L'expérience JUNO dispose d'un logiciel de simulation complet (JUNOSW), qui permet d'évaluer la sensibilité de l'expérience à différentes sources physiques de neutrinos. Ce logiciel est fondé sur Geant4, un outil de simulation très répandu en physique, en médecine et en ingénierie, qui permet non seulement de décrire la géométrie, mais aussi de générer, propager et faire interagir des particules dans les différents volumes, au moyen d'un large choix de *physics lists*. Nombre de ces dernières ont dû être modifiées dans JUNOSW pour obtenir une réponse correcte des interactions dans JUNO. La version utilisée jusqu'ici, la 10.4.2, ne pouvait cependant plus être maintenue à long terme, et la migration vers une version plus récente est devenue nécessaire. Ce travail ne se limite pas à recompiler le code : chaque modification des *physics lists* dans JUNOSW peut nécessiter des adaptations supplémentaires sur une nouvelle version de Geant4. Il faut donc comparer les versions, comprendre chaque écart, puis décider s'il faut le corriger, l'accepter ou le documenter.

La diffusion coulombienne multiple des particules chargées dans le scintillateur a été examinée en premier. Le modèle Goudsmit-Saunderson, utilisé dans les versions récentes de Geant4, s'est avéré problématique lorsque la production de photons optiques secondaires est activée : celle-ci conduit à une augmentation du nombre d'étapes de suivi des particules, ce qui modifie la forme et la valeur moyenne du spectre en énergie quenchée. La distribution des photons de scintillation produits en est directement affectée, et cet effet se propage ensuite à l'énergie

reconstruite par les algorithmes de l'expérience. Les causes de ces problèmes ont été identifiées, communiquées aux développeurs de Geant4 et corrigées dans la version 11.4.

Cette nouvelle version a donc été utilisée pour la mise à jour de JUNOSW, et les performances de la physique hadronique ont ensuite été examinées. La portée des particules α dans le scintillateur, essentielle pour la modélisation de certains bruits de fond radioactifs et de la réponse non linéaire du liquide, a notamment été comparée aux références : 42,3 μm avec SRIM contre 42,6 μm avec Geant4, soit un excellent accord avec cette nouvelle version.

Le point le plus délicat concerne la capture neutronique. Pour un détecteur dédié à l'observation des antineutrinos par désintégration bêta inverse, la capture du neutron fournit le signal retardé qui sert de signature à l'événement. Son temps caractéristique, la répartition des captures entre l'hydrogène et le carbone et les cascades de γ qui les accompagnent déterminent directement l'efficacité de sélection. Les simulations présentaient pourtant des écarts marqués avec les données de référence : un temps de capture d'environ 380 μs au lieu d'environ 200 μs, des intensités incorrectes pour les γ de désexcitation du ^{13}C, et un spectre γ continu dans le cas de la capture sur l'hydrogène. Ces défauts, attribués au constructeur de la capture et aux sections efficaces utilisées, n'ont pas pu être corrigés rapidement par les développeurs de Geant4 ; il a donc fallu modifier directement les constructeurs de la capture neutronique dans JUNOSW. À la suite de ces modifications, la version 11.4 de Geant4 a finalement pu être intégrée dans JUNOSW. Enfin, les rendements de production des isotopes cosmogéniques simulés par Geant4 ont été comparés aux valeurs tabulées par les expériences KamLAND et Daya Bay, renormalisées aux conditions expérimentales de JUNO, et montrent un bon accord pour certains isotopes, notamment le ^{9}Li. Cette validation de la physique ne dit toutefois rien de la description du détecteur lui-même, c'est-à-dire de son optique, de sa géométrie et de son électronique, qui ne peut être testée que sur des données réelles.

Validation de la réponse en énergie

Le quatrième chapitre aborde cette question en comparant systématiquement données et simulation à partir des sources d'étalonnage, tout au long de la mise en service du détecteur. Ces comparaisons ont été effectuées dès le début du remplissage en scintillateur liquide, dans un détecteur en double phase LS/eau. Dans cette phase, les études sont menées à l'aide d'une source de neutrons AmBe, qui produit un signal prompt de 4,4 MeV et un signal retardé de 2,2 MeV. On s'intéresse à la charge produite par ce dernier, mesurée en photoélectrons (PE), pour différentes positions le long de l'axe vertical (z). Ces études ont permis non seulement de montrer une homogénéisation des performances optiques du scintillateur liquide après l'introduction de lots non conformes au début du remplissage, mais aussi d'identifier plusieurs points d'optimisation de la simulation du détecteur.

Il a notamment été observé que, pour différentes positions de la source, la quantité de PE produite dans la simulation était systématiquement plus élevée que dans les données, en

particulier au pôle nord du détecteur. Ces écarts ont d'abord été réduits par l'introduction, dans la simulation, de nouvelles mesures des longueurs d'absorption de l'eau et du LS. Celle du LS présentait une diminution par rapport à la valeur nominale, en corrélation directe avec l'introduction de lots non conformes de LS dans le détecteur. Les écarts observés au pôle nord ont ensuite pu être attribués à des éléments de la géométrie simulée manquants au niveau de la cheminée du détecteur, notamment des tuyaux créant de l'ombrage dans les données. Ces études ont alors motivé une optimisation complète de la réponse simulée du détecteur : meilleure description des géométries, mesure des efficacités relatives de collection de photons des PMT, mesure des gains de chaque PMT et nouvelle mesure des longueurs d'absorption à la fin du remplissage, qui a montrée une augmentation de la longueur d'absorption du LS au-delà de la valeur nominale.

Ces optimisations se sont étendues sur toute la durée du remplissage en LS. Leurs effets ont ensuite été comparés à la réponse du détecteur entièrement rempli, au moyen d'une source de ^{68}Ge, émettrice de deux photons de 511 keV, déployée à différentes positions en z. Le système LPMT y est reproduit à $\pm 5\,\%$ par la première simulation, puis à $\pm 2\,\%$ pour $|z| < 15$ m par la version mise à jour. Le comportement du système SPMT est très différent : la simulation y sous-estime la lumière de manière importante et pratiquement uniforme sur toutes les régions du détecteur, sans signature géométrique évidente. Le fait que les LPMT soient bien décrits écarte un défaut général de la simulation optique et désigne plutôt une description incomplète des SPMT eux-mêmes. Plusieurs hypothèses ont été testées. La suppression du seuil de déclenchement simulé, qui constitue un moyen rapide d'évaluer l'effet d'un gain plus élevé, n'a eu aucun effet significatif, et le changement de version de Geant4 n'a rien résolu non plus. L'ajustement d'un facteur d'échelle global sur le rendement de photodétection (PDE) des SPMT conduit à un minimum pour une augmentation de 30 % et ramène l'écart sous 10 % pour toutes les positions de la source. Une telle correction ne se justifie cependant pas par les seules caractéristiques des photomultiplicateurs. L'extension aux SPMT du modèle optique mis à jour pour les LPMT, ou l'étude d'un éventuel ombrage des SPMT par les LPMT, constituent les pistes d'investigations possibles pour expliquer ces différences.

Le chapitre se conclut par la mesure de la non-linéarité de la réponse en énergie, c'est-à-dire de l'écart entre l'énergie visible et l'énergie déposée en fonction de l'énergie du γ émis. Cette grandeur est directement liée à la mesure de l'ordre de masse, puisqu'une non-linéarité mal connue déforme le spectre précisément là où le signal est recherché. Elle a été mesurée entre 0,511 et 6,13 MeV à l'aide de six sources, la capture neutronique sur l'hydrogène (2,223 MeV), observée avec la source AmC, servant de point d'ancrage. Ce choix correspond à un signal propre et abondant, et il fixe le facteur de conversion entre la charge collectée et l'énergie, de 1786,5 PE/MeV. Plusieurs fonctions d'ajustement des spectres de charge ont été comparées (gaussienne simple, gaussienne avec polynôme, gaussienne avec fonction erfc modélisant le front Compton) : leur effet sur la non-linéarité reste inférieur à 0,5 %, ce qui montre la robustesse

du résultat, tandis que la largeur des pics est réduite d'environ 10 % avec les fonctions les plus élaborées, ce qui conduit à une meilleure estimation de la résolution en énergie. Enfin, la simulation de la chaîne complète reproduit la non-linéarité mesurée à ±1 % près, et à ±0,5 % avec Geant4 11.4. L'amélioration obtenue avec cette dernière version prend toutefois la forme d'un décalage global de la courbe vers le bas sous 2,223 MeV, ce qui suggère une réduction globale de la production de lumière plutôt qu'une meilleure description de chaque source. Des études supplémentaires seront nécessaires, notamment l'ajustement des constantes de quenching de Birks, actuellement en cours. L'ensemble de ces résultats établit que, pour les LPMT, la simulation décrit la réponse en énergie avec une précision compatible avec le démarrage des analyses de physique, le système SPMT restant le principal chantier ouvert.

Estimation du bruit de fond cosmogénique ^{9}Li/^{8}He

Le cinquième chapitre présente la première analyse de neutrinos de réacteur, menée sur les 60 premiers jours de prise de données et dédiée à une première mesure des paramètres solaires θ_{12} et Δm^2_{21}. Cette mesure repose sur un échantillon d'événements IBD aussi pur que possible, dans lequel un antineutrino interagit avec un proton pour produire un positron (signal prompt) et un neutron, dont la capture retardée permet de réduire la contamination en bruits de fond. Cette signature peut tout de même être reproduite par différentes sources de bruit de fond, listées précédemment. Parmi elles, les isotopes ^{9}Li et ^{8}He, produits par spallation des noyaux de carbone du scintillateur sous l'effet des muons cosmiques, sont les plus importants. Ils se désintègrent en émettant un électron suivi d'un neutron, c'est-à-dire exactement la signature d'un IBD — JUNO étant incapable de distinguer un électron d'un positron — et leur durée de vie, de l'ordre de la centaine de millisecondes, empêche de les éliminer simplement par un veto sur les muons sans perdre une fraction inacceptable du temps de prise de données. Leur taux résiduel doit donc être estimé avec précision.

La première étape de cette étude est dédiée à la sélection IBD elle-même, adaptée aux performances du détecteur au moment des premières données. Elle combine une coupure fiducielle ($R < 16{,}5$ m, avec exclusion de la région de la cheminée), un intervalle de temps entre les signaux prompt et retardé compris entre 5 μs et 1 ms, et une condition de multiplicité. Le veto cylindrique autour des traces reconstruites des muons, utilisé pour réduire la contamination en événements cosmogéniques, a été remplacé par un veto temporel sur les muons et un veto sphérique (4 m, 1,2 s) autour des neutrons de spallation qui accompagnent la formation d'isotopes cosmogéniques. L'efficacité de cette sélection est de 70,3 %, inférieure à l'efficacité nominale de 82,2 %, ce qui reflète le caractère préliminaire de l'analyse. Après validation des différents critères de sélection, un algorithme dédié a été développé à Bordeaux et utilisé pour identifier les événements IBD dans le premier échantillon de l'expérience, ce qui conduit à 46,1 candidats par jour.

La deuxième étape concerne l'estimation de la contamination résiduelle en bruit de fond

dans le spectre en énergie final du signal prompt. L'étude du bruit de fond cosmogénique est en particulier cruciale, du fait du changement de méthode de veto. Elle est réalisée en étudiant d'abord le taux de ^{9}Li/^{8}He avant application du veto neutron, par corrélation temporelle entre les événements IBD et les événements muons qui les précèdent. L'ajustement de la distribution des différences de temps IBD–muon ($dt_{p-\mu}$) permet d'en extraire la contribution de chaque isotope cosmogénique. Dans un second temps, le taux de ^{9}Li/^{8}He retiré par le veto neutron est évalué par corrélation temporelle entre les événements IBD et les muons parents des neutrons ayant conduit au rejet de l'IBD. Un ajustement de la distribution de $dt_{p-\mu}$ permet d'extraire ce taux et de le soustraire au taux de ^{9}Li/^{8}He de l'échantillon total avant application du veto neutron. Le taux résiduel de ^{9}Li/^{8}He obtenu est de $6{,}6 \pm 2{,}7$ événements par jour, soit beaucoup plus que les 0,8 événement par jour attendus avec un veto cylindrique autour de la trace des muons. Cette valeur constitue la contribution principale au bruit de fond de ce premier échantillon. Elle illustre bien le caractère jeune de l'expérience et la nécessité d'améliorer autant que possible les critères de sélection.

Formation de l'ortho-positronium dans JUNO

Le sixième chapitre utilise les premiers échantillons IBD de l'expérience pour étudier la formation de l'ortho-positronium (o-Ps), l'état lié d'un positron et d'un électron, qui offre la possibilité d'identifier sans ambiguïté la présence d'un positron et, ainsi, de construire un échantillon IBD pur. Cette étude porte principalement sur la possibilité d'observer cet état lié dans le détecteur, où sa probabilité de formation et sa durée de vie moyenne dans le scintillateur liquide de JUNO sont respectivement de 50 % et de 3 ns. Il se désintègre en émettant deux ou trois γ, pour une énergie totale de 1,022 MeV. L'identification de l'o-Ps repose sur la mise en évidence, dans la distribution temporelle d'arrivée des photons, d'un signal prompt d'ionisation du positron suivi d'un signal retardé d'annihilation. Sa principale limitation est la résolution temporelle des LPMT utilisés dans le détecteur, en particulier celle des NNVT, d'environ 7,5 ns.

La première partie de cette étude est consacrée au développement d'une méthode d'identification de l'o-Ps, qui s'appuie sur la source ^{68}Ge, émettrice de deux γ de 511 keV. La densité de probabilité des temps d'arrivée des photons est construite à partir de cette source, puis ajustée aux données IBD au moyen d'un χ^2 de Poisson à cinq paramètres : les amplitudes de l'ionisation et de l'annihilation, A_1 et A_2, le temps de référence t_0, le temps de vie de l'o-Ps dt, et un paramètre c modélisant la contribution du bruit d'obscurité dans la distribution temporelle. Un balayage préalable en (t_0, dt) fournit les valeurs initiales, et est suivi d'une minimisation par MINUIT utilisant successivement SIMPLEX, MIGRAD et HESSE. Le domaine de validité de la méthode est ensuite évalué, ce qui montre la nécessité de restreindre son application aux événements situés à une distance du centre $R \leq 15{,}0$ m et d'énergie reconstruite $E \leq 5$ MeV. Enfin, l'évaluation des performances de la méthode sur un échantillon de ^{60}Co, qui ne produit pas d'o-Ps, montre qu'elle ne parvient pas à identifier correctement les événements sans o-Ps.

Cela conduit à introduire une limite à $dt = 7$ ns, en dessous de laquelle la méthode n'est pas assez fiable pour distinguer un événement avec o-Ps d'un événement sans o-Ps. Appliquée à un échantillon simulé d'événements avec o-Ps, la méthode montre un accord satisfaisant pour une statistique correspondant aux ~ 200 premiers jours de données de l'expérience.

La deuxième partie est consacrée à l'extraction de la probabilité de formation et de la durée de vie moyenne de l'o-Ps à partir de la distribution de dt obtenue sur les événements IBD. Cette extraction nécessite notamment de prendre en compte l'erreur associée à la valeur de dt extraite par la méthode d'identification. La distribution de dt est ajustée par une exponentielle décroissante convoluée à une gaussienne dont l'écart-type est égal à l'erreur sur dt. L'application de cette méthode aux données fournit une durée de vie de l'o-Ps $\tau = 3{,}26 \pm 0{,}21$ ns et une fraction de formation $f = 54{,}2 \pm 8{,}1\,\%$, en très bon accord avec des mesures par spectroscopie effectuées sur un échantillon de scintillateur liquide proche de la formulation de JUNO. Une étude supplémentaire restreinte aux LPMT Hamamatsu, de meilleure résolution temporelle mais bien moins nombreux que les NNVT dans le détecteur, montre que le compromis entre résolution temporelle et statistique de photons est déterminant pour la sensibilité de la méthode. Ces résultats démontrent la faisabilité de la mesure de l'o-Ps dans JUNO, première étape indispensable à son utilisation comme discriminant dans les analyses futures, notamment pour la réjection de bruits de fond tels que les isotopes cosmogéniques étudiés plus haut.

Conclusion

La physique des neutrinos est entrée dans une ère de mesures de précision, où plusieurs décennies de percées ont façonné le paysage expérimental actuel et réduit le nombre de ses questions ouvertes. Parmi elles, l'ordre de masse des neutrinos est crucial pour dévoiler le cadre complet des oscillations de neutrinos. L'expérience JUNO a été conçue avec pour objectif principal la détermination de l'ordre de masse des neutrinos, tout en visant une précision inférieure $< 1\%$ sur les paramètres solaires. Cette thèse a suivi l'expérience JUNO durant une période charnière, de la validation de son logiciel de simulation à l'analyse de ses premières données de physique.

La première partie de cette thèse a été consacrée à l'optimisation du logiciel de simulation de JUNO et à sa validation par rapport aux données de mise en service et d'étalonnage du détecteur. Elle a débuté par la validation et la mise à niveau de la boîte à outils de simulation Geant4 de JUNO, testée d'abord de la version 10.4 à la version 11.2. Un écart identifié entre les deux versions a été relié à un suivi excessif (*over-tracking*) dans le modèle de diffusion multiple de Goudsmit–Saunderson mis à jour, désormais utilisé par défaut dans la liste de physique EmLivermore des versions récentes de Geant4. Ce défaut a été signalé aux développeurs de Geant4 et corrigé dans la version 11.4 suivante. Par ailleurs, les versions récentes de Geant4 présentent une meilleure description des particules alpha, mais une description imprécise de la

capture des neutrons. La capture neutronique de la dernière version, la 11.4, a été corrigée en interne avant son intégration au logiciel de simulation de JUNO. Il a en outre été montré que cette nouvelle version de Geant4 reproduit avec précision le rendement cosmogénique du ^{9}Li, bien que des écarts plus importants subsistent pour la plupart des autres isotopes, dont le ^{8}He. La simulation a ensuite été validée par une série d'études données/Monte-Carlo réalisées à partir des données de mise en service et d'étalonnage, afin de caractériser le rendement lumineux, la non-uniformité spatiale et la non-linéarité en énergie du détecteur pour les deux sous-systèmes de PMT, ce qui a conduit à une optimisation supplémentaire de la simulation. La réponse en énergie fondée sur les LPMT a montré un bon accord avec les données après ces améliorations de la simulation, la non-linéarité simulée se trouvant à moins de 1% de la valeur mesurée ; la réponse des SPMT, en revanche, nécessite une investigation plus poussée pour identifier l'origine de l'énergie collectée manquante. L'ensemble de ces études a permis d'établir le niveau de compréhension de la réponse en énergie de JUNO précédant la première campagne de prise de données de physique.

La dernière partie de cette thèse a été consacrée aux analyses menées sur les premiers jeux de données de JUNO. Elle a débuté par des contributions à la première analyse d'oscillation de l'expérience, au cours de laquelle un travail important a été consacré au développement d'un cadre de sélection des événements IBD pour le groupe de Bordeaux, fournissant des vérifications croisées qui ont contribué à établir la stratégie de sélection IBD de l'un des trois groupes d'analyse de JUNO. Une fois stabilisée, cette sélection a été appliquée aux 60 premiers jours de données de JUNO, donnant un taux d'IBD de 46,1 cpd, compatible avec les attentes. Une méthode a ensuite été développée pour estimer la contamination résiduelle en bruit de fond de ^{9}Li/^{8}He dans l'échantillon IBD final, donnant un taux résiduel de $R^{\text{final}}_{\text{Li/He}} = 6{,}6 \pm 2{,}7$ cpd, supérieur à l'attente nominale et attribué à l'absence temporaire d'un veto sur les traces de muons dans cette analyse de début de vie du détecteur. Une méthode complémentaire de rejet du bruit de fond, fondée sur l'identification de la formation d'ortho-positronium dans le scintillateur liquide de JUNO, a ensuite été explorée : un cadre d'ajustement dédié a été développé et appliqué événement par événement, fournissant la première mesure de la fraction de formation et de la durée de vie de l'ortho-positronium dans le scintillateur liquide de JUNO, $\tau_{oPs} = 3{,}26 \pm 0{,}21$ ns et $f_{oPs} = 54{,}2\% \pm 8{,}2\%$, compatibles avec les mesures PALS précédentes dans la limite de l'incertitude statistique de ce jeu de données initial.

Plusieurs résultats présentés tout au long de cette thèse restent préliminaires, reflétant le stade précoce des performances du détecteur de JUNO et de sa simulation sous-jacente, et indiquent des directions concrètes pour les travaux futurs. Les écarts restants dans la description par Geant4 des rendements d'isotopes cosmogéniques pourront être mieux contraints par les futures mesures de JUNO. L'origine de l'écart de réponse en énergie des SPMT a été reliée à un déficit inexpliqué d'environ 30% de l'efficacité quantique des PMT, sans origine physique claire identifiée à ce jour, ce qui nécessite une investigation plus poussée de son modèle de

réponse optique et d'éventuels effets d'ombrage dus aux LPMT. Les deux analyses menées sur les premières données de JUNO sont directement limitées par les performances du détecteur à ce stade précoce : la contamination résiduelle extraite en ^{9}Li/^{8}He est limitée par l'absence actuelle de veto sur les traces de muons, tandis que l'analyse de l'o-Ps est actuellement limitée principalement par la statistique, et devrait devenir de plus en plus compétitive à mesure que les algorithmes de reconstruction seront affinés et que des corrections de temps de vol intégrant des processus optiques détaillés seront incorporées à JUNOSW.

Dans l'ensemble, le travail présenté dans cette thèse a contribué à établir les performances du détecteur et de la simulation de JUNO à ses débuts, ainsi qu'à mener des analyses sur le premier échantillon d'IBD de l'expérience. Au-delà de ces résultats spécifiques, cette thèse a produit un ensemble de procédures, de méthodes et d'outils — du cadre de validation de Geant4 et de la chaîne de sélection des IBD développée pour le groupe de Bordeaux, à la méthode d'estimation du taux de ^{9}Li/^{8}He et au cadre d'ajustement de l'o-Ps — qui dépassent leurs résultats immédiats et sont directement disponibles pour soutenir les futures itérations de ce travail. Alors que JUNO continue d'accumuler des données dans les années à venir, ces outils devraient servir de références pour évaluer les futures améliorations du détecteur et de la simulation, soutenant directement la progression de la collaboration vers son objectif central : la détermination de l'ordre de masse des neutrinos.

Table des matières

Introduction **23**

1 Introduction to Neutrino Physics **25**

1.1 A Brief History of the Neutrino . . . 26
1.1.1 Birth of the Neutrino . . . 26
1.1.2 Discovery of the Three Neutrino Flavours . . . 27
1.1.3 More Active Neutrinos ? . . . 28
1.2 The Neutrino in the Standard Model . . . 29
1.2.1 The Standard Model of Particle Physics . . . 29
1.2.2 Neutrino Interactions . . . 31
1.3 Neutrino Oscillations . . . 34
1.3.1 Experimental Evidence . . . 34
1.3.2 Neutrino Oscillations in Vacuum . . . 37
1.3.3 Neutrino Oscillations in Matter : The MSW Effect . . . 42
1.4 Neutrino Mass . . . 44
1.4.1 Fermion Mass Generation . . . 44
1.4.2 Dirac Neutrinos . . . 46
1.4.3 Majorana Neutrinos and the Seesaw Mechanism . . . 47
1.5 Current Neutrino Experimental Landscape . . . 49
1.5.1 $0\nu\beta\beta$ Decay Experiments . . . 49
1.5.2 Absolute Mass Scale Measurement . . . 50
1.5.3 CP violation in the Lepton Sector . . . 52
1.5.4 Light Sterile Neutrinos . . . 54
1.6 Neutrino Mass Ordering Determination . . . 56
1.6.1 Long Baseline Accelerator Experiments . . . 56
1.6.2 Atmospheric Neutrino Experiments . . . 58
1.6.3 Medium-Baseline Experiments . . . 59
1.6.4 Atmospheric Δm^2 Comparison . . . 62
1.7 Conclusion . . . 64

2 The JUNO Experiment **66**
2.1 Introduction . . . 67
2.2 Neutrino Mass Ordering Measurement . . . 68
2.2.1 Neutrino Survival Probability . . . 68
2.2.2 Reactor Neutrino Flux . . . 68
2.2.3 Detection Channel . . . 69
2.2.4 Neutrino Signal at JUNO . . . 70
2.2.5 Backgrounds . . . 72
2.3 The JUNO Detector . . . 74
2.3.1 Overview . . . 74
2.3.2 The Central Detector . . . 75
2.3.3 Liquid Scintillator . . . 77
2.3.4 Veto System . . . 79
2.3.5 Large PMT system . . . 82
2.3.6 Small PMT System . . . 85
2.4 Calibration . . . 87
2.4.1 Detector Response . . . 87
2.4.2 Calibration System Design . . . 88
2.4.3 Radioactive Sources . . . 89
2.5 JUNO-TAO . . . 92
2.6 Conclusion . . . 94

3 Geant4 Upgrade in JUNO Simulation Software **96**
3.1 Introduction . . . 97
3.2 JUNO Simulation Software . . . 97
3.2.1 Overview of JUNO offline software . . . 97
3.2.2 Geant4 in JUNOSW . . . 99
3.2.3 Upgrade motivation . . . 101
3.3 Electromagnetic physics update in Geant4 . . . 101
3.3.1 Electron simulation . . . 101
3.3.2 First attempt to correct electron simulation . . . 103
3.3.3 Multiple Coulomb Scattering models in Geant4 . . . 105
3.3.4 Goudsmit Saunderson boundary crossing management . . . 106
3.3.5 Electron simulation correction in new Geant4 release . . . 107
3.4 Hadronic physics update in Geant4 . . . 109
3.4.1 Alpha Simulation . . . 110
3.4.2 Neutron Simulation . . . 111
3.4.3 Neutron Capture on Hydrogen . . . 112
3.4.4 Neutron Capture on Carbon . . . 113

3.4.5 Correction to Neutron Simulation . . . 115
3.5 Cosmogenic Yield Simulation . . . 116
3.5.1 Geant4 v11.4 Simulation . . . 116
3.5.2 Expected Yield at JUNO site . . . 117
3.5.3 Results . . . 117
3.6 Conclusion . . . 119

4 Simulation Validation of JUNO's Energy Response 121
4.1 Introduction . . . 122
4.2 Early liquid scintillator performance . . . 122
4.2.1 AmBe Source . . . 123
4.2.2 Selection Method . . . 125
4.2.3 Light Yield . . . 128
4.3 Performance of the JUNO simulation . . . 130
4.3.1 Optical parameters . . . 130
4.3.2 Data/MC comparison of the Light Yield . . . 133
4.3.3 Additional implementation to JUNOSW . . . 135
4.4 SPMT energy response . . . 136
4.4.1 Ge68 source . . . 136
4.4.2 First look at SPMT response . . . 139
4.4.3 Layer Response . . . 141
4.4.4 SPMT Photo Detection Efficiency . . . 144
4.5 Energy non-linearity . . . 146
4.5.1 Energy Computation Method . . . 147
4.5.2 Fitting methods . . . 150
4.5.3 Simulation validation . . . 151
4.6 Conclusion . . . 154

5 Cosmogenic Background Rate Estimation in JUNO 156
5.1 Introduction . . . 157
5.2 Inverse Beta Decay Selection . . . 157
5.2.1 Nominal Selection Strategy . . . 158
5.2.2 Early Data-Taking Period Adjustments . . . 159
5.2.3 Results . . . 161
5.3 Cosmogenic ^{9}Li/^{8}He . . . 164
5.3.1 Production . . . 164
5.3.2 Impact on IBD Measurement . . . 165
5.4 Li/He Rate Estimation . . . 166
5.4.1 General Strategy . . . 166

5.4.2 Rate Before the Neutron Veto . . . 166
5.4.3 Accompanying Neutron Efficiency . . . 168
5.4.4 Rate Inside the Neutron Veto . . . 170
5.4.5 Residual Rate After the Neutron Veto . . . 172
5.5 Conclusion . . . 173

6 Ortho-Positronium formation in JUNO **174**
6.1 Introduction . . . 175
6.2 Ortho-Positronium . . . 175
6.2.1 Formation and Signature . . . 175
6.2.2 Experimental Measurements . . . 176
6.2.3 Limitations . . . 177
6.3 Fitting Framework . . . 178
6.3.1 Building the Model . . . 178
6.3.2 Fit Architecture . . . 179
6.3.3 Parameter Initialisation and Constraints . . . 181
6.3.4 Minimisation Strategy . . . 182
6.4 Characterisation on Simulated Data . . . 183
6.4.1 Single-Point Analysis at 3 MeV . . . 183
6.4.2 Constraining non o-Ps Population . . . 185
6.4.3 Formation Fraction and Lifetime Estimation . . . 186
6.4.4 Spatial Dependence . . . 189
6.4.5 Energy Dependence . . . 192
6.5 Results on JUNO Data . . . 195
6.5.1 IBD Candidate Sample . . . 195
6.5.2 Fitted o-Ps Parameters . . . 196
6.5.3 Outlook . . . 200
6.6 Prospects with Improved PMT Timing (Hamamatsu Subset) . . . 200
6.6.1 Fit Performance on Simulated Data . . . 201
6.6.2 Investigating the Origin of Bias . . . 202
6.6.3 Prospects . . . 203
6.7 Conclusion . . . 204

Conclusion **206**

Introduction

Nearly a century after its first theoretical proposal, the neutrino remains one of the most actively studied particles in physics. The discovery of neutrino oscillations established that neutrinos are massive, in direct contradiction with the Standard Model, and opened a rich experimental program aimed at precisely measuring the oscillation parameters and resolving the open questions surrounding the origin and nature of the neutrino mass. Among these questions, the neutrino mass ordering — knowing if neutrinos are arranged in mass similarly to their corresponding charged leptons, or not — occupies a central place in the current generation of experiments. Its determination unlocks several other open questions in the field, including the extraction of the CP-violating phase at long-baseline accelerator experiments and the sensitivity to neutrinoless double beta decay.

The Jiangmen Underground Neutrino Observatory (JUNO) is a next-generation reactor antineutrino experiment designed to determine the neutrino mass ordering with an unprecedented $3\%/\sqrt{E\ [\mathrm{MeV}]}$ energy resolution, while providing a sub-percent measurement of the remaining oscillation parameters. Achieving this goal places strong constraints on both the detector's energy response and its background control strategy, both of which must be well understood for JUNO's final spectral fit. This thesis is written at a crucial moment for the experiment : JUNO's construction and filling have been completed, and the detector has begun its first physics data-taking campaign. The work presented here follows this transition directly, from the commissioning and validation of the detector, to its simulation optimisation, and the first physics analyses performed on JUNO data.

This thesis is organised into six chapters, following this progression. Chapter 1 introduces the theoretical framework of neutrino oscillations and neutrino mass generation, and presents the current neutrino experimental landscape before detailing the methods currently used to determine the neutrino mass ordering, comparing JUNO's medium-baseline reactor approach to long-baseline accelerator and atmospheric methods. Chapter 2 presents the JUNO experiment itself, from its detection principle and detector design to the results of its low-level performance extracted from detector commissioning and its first calibration campaign. JUNO's satellite experiment, TAO, is presented in a dedicated section, further detailing its physics reach and its role in JUNO's mass ordering measurement.

During this thesis, extensive work has been performed on the optimisation of the JUNO

simulation software and its validation against commissioning and calibration data. Chapter 3 presents the design of JUNO's simulation software, built to support the experiment's broad physics program, before presenting the validation and upgrade of its Geant4 physics engine from version 10.4.2 to the 11.2 release. Several discrepancies identified in both its electromagnetic and hadronic physics modelling were reported to the Geant4 developers, subsequently corrected in the latest version 11.4 release, which was then validated and integrated into JUNO's simulation software. An additional analysis is performed on this latest version to assess its ability to reproduce the cosmogenic isotope yields relevant to later chapters. Chapter 4 presents further validation of JUNO's simulated energy response against calibration data collected during JUNO's first calibration campaign, characterising the detector's light yield, spatial uniformity, and energy non-linearity. These analysis acted as validation procedure and helped establishing the level of understanding of the detector's energy response prior to the first data taking campaign.

The final two chapters present physics analyses performed on the first data collected by JUNO. Chapter 5 presents the selection of Inverse Beta Decay (IBD) candidate events, and its revision for the first 60 days of JUNO data. This revised selection led to a thorough evaluation of the residual background, and a method developed to estimate the residual rate of the ^{9}Li/^{8}He cosmogenic background remaining in the final sample is presented. Chapter 6 explores a complementary background rejection method, based on the identification of ortho-positronium formation in the liquid scintillator as a pulse-shape discrimination technique. The method's identification performance is first evaluated on simulated samples, before being applied to a larger, 193.2-day, JUNO dataset, providing the first measurement of the ortho-positronium formation fraction and lifetime in JUNO's liquid scintillator.

Together, these chapters follow the experiment from its theoretical motivation to its detector, its simulation, and its first physics results.

Chapitre 1

Introduction to Neutrino Physics

Summary

1.1 A Brief History of the Neutrino . . . 26
1.1.1 Birth of the Neutrino . . . 26
1.1.2 Discovery of the Three Neutrino Flavours . . . 27
1.1.3 More Active Neutrinos ? . . . 28
1.2 The Neutrino in the Standard Model . . . 29
1.2.1 The Standard Model of Particle Physics . . . 29
1.2.2 Neutrino Interactions . . . 31
1.3 Neutrino Oscillations . . . 34
1.3.1 Experimental Evidence . . . 34
1.3.2 Neutrino Oscillations in Vacuum . . . 37
1.3.3 Neutrino Oscillations in Matter : The MSW Effect . . . 42
1.4 Neutrino Mass . . . 44
1.4.1 Fermion Mass Generation . . . 44
1.4.2 Dirac Neutrinos . . . 46
1.4.3 Majorana Neutrinos and the Seesaw Mechanism . . . 47
1.5 Current Neutrino Experimental Landscape . . . 49
1.5.1 $0\nu\beta\beta$ Decay Experiments . . . 49
1.5.2 Absolute Mass Scale Measurement . . . 50
1.5.3 CP violation in the Lepton Sector . . . 52
1.5.4 Light Sterile Neutrinos . . . 54
1.6 Neutrino Mass Ordering Determination . . . 56
1.6.1 Long Baseline Accelerator Experiments . . . 56
1.6.2 Atmospheric Neutrino Experiments . . . 58
1.6.3 Medium-Baseline Experiments . . . 59
1.6.4 Atmospheric Δm^2 Comparison . . . 62
1.7 Conclusion . . . 64

1.1 A Brief History of the Neutrino

1.1.1 Birth of the Neutrino

The story of the neutrino dates back to 1896, when Henri Becquerel discovered radiation coming from uranium salts [1, 2], which was later given the name of radioactivity [3]. A few years later, in 1899, Rutherford identified two types of radiations, alpha and beta ; gamma radiation was later discovered by Villard in 1900. The beta decay was identified to be nothing more than the decay of a nucleus ${}^{A}_{Z}X$ into a nucleus ${}^{A}_{Z+1}Y$ with the emission of an electron :

$$ {}^{A}_{Z}X \rightarrow {}^{A}_{Z+1}Y + e^{-} \tag{1.1} $$

Thanks to conservation of energy, the beta radiation, which is a single electron, should have a fixed energy. In 1914, James Chadwick showed that the beta spectrum was continuous [4], in contrast to alpha and gamma rays, which were unique in energy, and was later confirmed by Ellis and Wooster in 1927 [5]. If only the parent nucleus and the emitted electron were involved, the conservation of energy appeared to be violated in a two-body decay. This lead to believe that a missing particle must be involved in the beta decay mechanism and should take part of the total reaction energy, or as Niels Bohr suggested, that perhaps the energy was not conserved.

In 1930, in an attempt to save the energy and momentum conservation principle, and explain the continuous β spectrum, Wolfgang Pauli suggested the existence of a new particle he named *neutron*. The particle has to be very light ($< 0.01 \times \mathrm{m}_{\mathrm{proton}}$), neutral, with spin $\frac{1}{2}$, with at least 10 times the ability to go through material than a γ-ray, and should carry part of the β decay energy such that the sum of the electron and neutron energy is constant [6].

In 1932, J. Chadwick discovered, through the bombardment of α particles on ^{9}Be, the existence of a neutral particle with mass close to that of the proton, corresponding to the neutron as we know it today [7]. To distinguish Pauli's particle from the newly discovered heavy neutron, E. Fermi proposed the name *neutrino* (little neutron in Italian), and suggested that neutrinos might be massless. At the end of 1933, Fermi formulated the theory of beta decay [8, 9], incorporating the neutrino hypothesis, in which a neutron decays into a proton and emits an electron alongside a neutrino — later identified as an antineutrino — re-writing Eq. 1.1 as :

$$ {}^{A}_{Z}X \rightarrow {}^{A}_{Z+1}Y + e^{-} + \overline{\nu} \tag{1.2} $$

1.1.2 Discovery of the Three Neutrino Flavours

Discovery of the $\overline{\nu}_e$

Fermi's theory of beta decay met remarkable success, leaving few physicists in doubt of the neutrino's existence. Nevertheless, no direct experimental observation of neutrino interaction had been achieved, primarily because the cross-section of a neutrino interacting with a proton, was estimated by H. Bethe and R. Peierls to be vanishingly small ($\sim 10^{-44}$ cm^2), leading them to conclude that neutrino observation might be impossible [10].

In 1956, Frederick Reines and Clyde Cowan set out to observe the antineutrino through the inverse beta decay process, first proposed by Bruno Pontecorvo in 1946, in which an antineutrino interacts with a proton to produce a positron and a neutron. They employed a target made of 400 liters of a water loaded with cadmium chloride, placed in close proximity to a nuclear power plant. Antineutrinos produced in the reactor interact with protons of the target, producing a positron and a neutron. The positron promptly annihilates in the medium producing two photons while the neutron thermalises until it's captured by a cadmium nucleus, emitting additional photons tens of microseconds after the positron annihilation. This distinctive prompt–delayed coincidence signature allowed Reines and Cowan to successfully detect the antineutrino in 1956 [11], in what stands as the first reactor neutrino experiment using a liquid scintillator target.

Discovery of the $\overline{\nu}_\mu$

The year 1937 was marked by the discovery of the muon, μ, a charge particle with a mass between that of the electron and the proton, by J.C. Street and E.C. Stevenson [12]. In the late 1940s, the muon was found to be produced in the decay of charged pions, alongside a neutrino :

$$\begin{aligned} \pi^- &\rightarrow \mu^- + \overline{\nu} \\ \pi^+ &\rightarrow \mu^+ + \nu \end{aligned} \tag{1.3}$$

The neutrino discovered by Reines and Cowan is an electron-neutrino, ν_e, since the charged particle produced in the β decay is an electron. This naturally raised the question of whether the neutrino produced in pion decay was the same particle. The answer was provided in 1962 by a team led by Melvin Schwartz, Leon Lederman, and Jack Steinberger at Brookhaven National Laboratory, in what is regarded as the first accelerator-based neutrino experiment. The accelerator used 15 GeV protons colliding on a beryllium target to produce pions, which decayed in flight into muons and neutrinos. The muons where stopped by heavy materials (steel, lead, concrete) while the neutrinos were directed towards a detector in which they could interact via the following reaction :

$$\nu + n \rightarrow p + e^{-}(\text{or } \mu^{-}) \tag{1.4}$$

$$\overline{\nu} + n \rightarrow p + e^{+}(\text{or } \mu^{+}) \tag{1.5}$$

The experiment successfully observed an excess of muon emissions above background, with no corresponding excess of electron events [13]. This demonstrated, not only lepton number conservation, but also the existence of a muon flavored neutrino, ν_μ.

Discovery of the $\overline{\nu}_\tau$

The question of a third flavor of neutrino subsequently arose. A first answer was provided in 1975, when Martin Perl and his collaborators, working at the SLAC electron–positron storage ring, discovered the third-generation charged lepton, the tau, τ [14], thereby suggesting the existence of a corresponding neutrino. Finally, in 2000, the DONUT experiment achieved the first direct observation of the tau neutrino, ν_τ [15].

1.1.3 More Active Neutrinos ?

The existence of additional neutrino species beyond the discovered three flavours is a question that remains open to this day. However, the number of neutrino flavours participating in the weak interaction has been precisely constrained by the LEP experiments at CERN — ALEPH, DELPHI, L3 and OPAL [16]. These experiments studied the Z^0 boson, which decays into quark-antiquark, charged lepton pairs, or neutrino-antineutrino pairs. The total decay width of the Z^0 provides direct access to the number of neutrino species coupling to the weak interaction :

$$\Gamma_Z = \Gamma_l + \Gamma_q + N_\nu \Gamma_\nu \tag{1.6}$$

where Γ_l, Γ_q, and Γ_ν are the partial widths into charged leptons, quarks, and a single neutrino flavour respectively, and N_ν is the number of light neutrinos coupling to the weak interaction. The last term of Eq. 1.6 is commonly referred to as the *invisible width*, as neutrinos escape the detector undetected. Its contribution can be extracted by comparing the measured Z^0 cross-section to theoretical predictions computed assuming two, three, or four active neutrino species, as shown in Figure 1.1. The combined LEP result yields :

$$N_\nu = 2.9840 \pm 0.0082 \tag{1.7}$$

which is in excellent agreement with three active neutrino flavours. The three active neutrino species are therefore established to be ν_e, ν_μ, and ν_τ. Should additional neutrino flavours exist, they would necessarily be decoupled from the weak interaction.

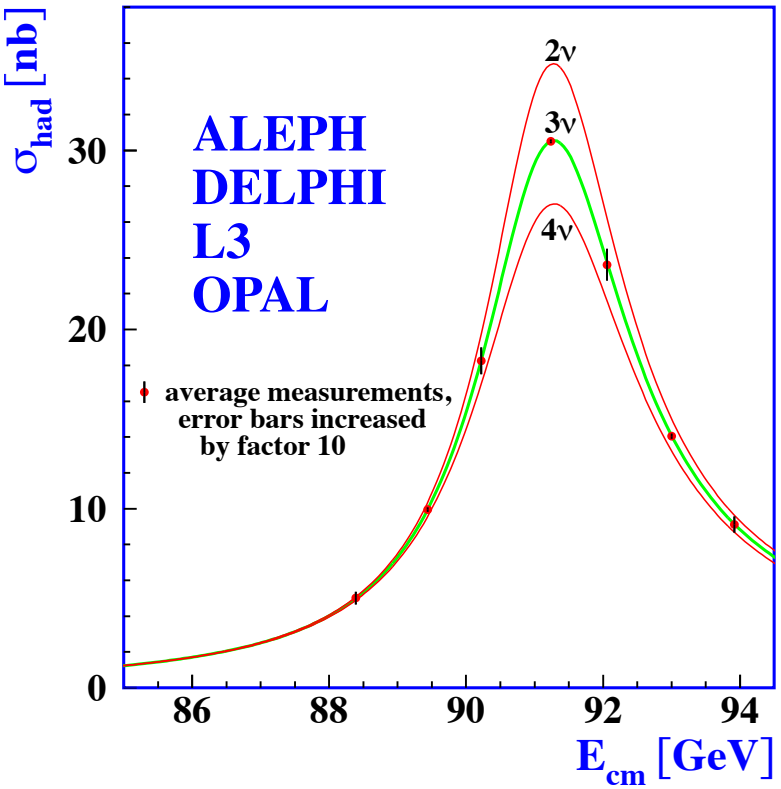

FIGURE 1.1 – Cross-section measurement around the Z resonance. The solid curves indicate the predicted cross-section for two, three and four neutrino species with Standard Model couplings and negligible mass [16].

1.2 The Neutrino in the Standard Model

1.2.1 The Standard Model of Particle Physics

Structure

The Standard Model (SM) of particle physics is a Quantum Field theory that describes the electromagnetic, weak and strong interactions of elementary particles in order to match experimental observations in the most economical way. It is formulated as a gauge theory under the local symmetry group $SU(3)_C \times SU(2)_L \times U(1)_Y$, where C, L and Y denote color charge, left-handed chirality and weak hypercharge respectively. The particle content of the SM is summarised in Figure 1.2 and consist of two categories : fermions, which are $\frac{1}{2}$ spin particles that constitute matter, and bosons, which are integer-spin particles that mediate the fundamental interactions.

The fermionic sector is organised into three generations [1] of quarks and leptons, where each generation is a heavier copy of the previous one with identical quantum numbers. Each genera-

1. The words *families* or *flavors* are also commonly used.

tion contains two quarks and two leptons : a charged lepton and its associated neutrino. Quarks participate in all three interactions, whereas leptons do not carry color charge and are therefore insensitive to the strong interaction. Furthermore, quarks are never observed as free particles : due to the property of color confinement, they are bound into hadrons, either as assembly of three quarks (baryons) or as quark-antiquark pair (mesons).

The number of generators associated with each gauge group determines the number of gauge bosons. From Lie algebra, $SU(n)$ has $n^2 - 1$ generators, and $U(n)$ has n^2 generators. Consequently, $SU(3)_C$ gives rise to eight massless gluons mediating the strong interaction, $SU(2)_L$ gives rise to three massive bosons, $W^{\pm}$ and Z^0, associated with the weak interaction, and $U(1)_Y$ gives rise to one massless boson, the photon γ, which mediate the electromagnetic interaction. The model is completed by the Higgs boson — the only spin-0 particle of the SM — whose discovery at the LHC in 2012 [17, 18] brought the last missing piece of the SM.

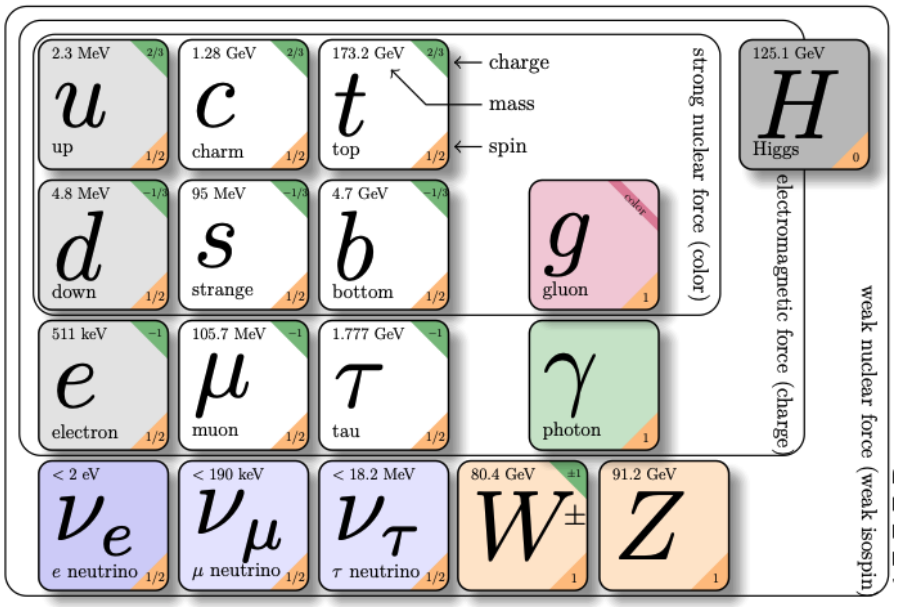

FIGURE 1.2 – Elementary particles and interactions of the Standard Model. The first three columns represent the three generations of fermions ; the remaining columns show the gauge bosons and the Higgs boson. The fermions are further divided into quarks (first two rows) and leptons (last two rows). The interactions are represented by black-lined boxes that contains the fermions and gauge bosons involved in the corresponding interactions. From [19].

Electroweak interaction

Since neutrinos are electrically neutral and carry no colour charge, they interact exclusively through the weak interaction, making this sector of the SM the only one directly relevant to the physics of neutrinos discussed throughout this thesis. In the SM, the electromagnetic and weak interactions are unified into a single electroweak interaction described by the gauge group $SU(2)_L \times U(1)_Y$. One key property of a gauge theory is invariance of the Lagrangian under local

gauge transformations (gauge invariance). A fundamental consequence of gauge invariance is that the group gauge bosons must be massless, since an explicit mass term in the Lagrangian would not be invariant under any gauge transformations. However, the $W^{\pm}$ and Z^0 bosons — the mediators of the weak interaction — are observed to be massive, with $m_W \sim 80$ GeV/c^2 and $m_Z \sim 91$ GeV/c^2, which requires a mechanism to generate their masses without explicitly breaking gauge invariance.

This is achieved through the Higgs Mechanism [20, 21, 22, 23] via the spontaneous breaking of the $SU(2)_L \times U(1)_Y$ symmetry down to $U(1)_{EM}$. As a consequence, the $W^{\pm}$ and Z^0 bosons acquire mass by absorbing the Goldstone bosons produced by the symmetry breaking, while the charged fermions acquire mass through their Yukawa couplings to the Higgs field (see Section 1.4.1). The remainder of this section will be focused on the electroweak part of the SM, which govern neutrino interactions. Moreover, electroweak interactions can be studied separately from strong interaction, as the symmetry under the group $SU(3)_C$ is unbroken due to the Higgs field being a color singlet, resulting in no mixing between the $SU(3)_C$ and $SU(2)_L \times U(1)_Y$ sectors.

1.2.2 Neutrino Interactions

Neutrinos are electrically neutral and do not carry colour charge, making them singlet under $SU(3)_C$ and $U(1)_{EM}$. They interact with matter solely through the weak interaction via two distinct channels : the charged-current (CC) interaction and neutral-current (NC) interaction.

Chirality

In relativistic quantum field theory, fermion fields can be decomposed into two chirality eigenstates : left-handed (L) and right-handed (R) components. Chirality is a Lorentz-invariant property defined through the γ^5 operator, and it is chirality that determines how fermions couple to the gauge boson of the SM. A key feature of the $SU(2)_L$ symmetry group — reflected in the subscript L — is that the charged current weak interaction couples exclusively to left-handed fermion fields, making it maximally parity-violating, while the neutral-current weak interaction couples to both left and right-handed components of fermion fields. Left-handed leptons and quarks therefore pair-up to transform as doublets under $SU(2)$:

$$L_L = \begin{pmatrix} \nu_{eL} \\ e_L \end{pmatrix}, \begin{pmatrix} \nu_{\mu L} \\ \mu_L \end{pmatrix}, \begin{pmatrix} \nu_{\tau L} \\ \tau_L \end{pmatrix}, \qquad Q_L = \begin{pmatrix} u_L \\ d_L \end{pmatrix}, \begin{pmatrix} c_L \\ s_L \end{pmatrix}, \begin{pmatrix} t_L \\ b_L \end{pmatrix}. \tag{1.8}$$

The right-handed components of charged fermions transform as singlets under $SU(2)_L$, $e_R = \{e_R,\ \mu_R,\ \tau_R\}$, $u_R = \{u_R,\ c_R,\ t_R\}$, and $d_R = \{d_R,\ s_R,\ b_R\}$, and do not participate in the charged-current interaction.

The neutral-current weak interaction, on the other hand, couples to both left and right-handed components of charged fermion fields, though with different strengths. This asymmetry arises from the mixed origin of the Z^0 boson, which is a combination of the $SU(2)_L$ and $U(1)_Y$ gauge fields after electroweak symmetry breaking. The $SU(2)_L$ contribution couples exclusively to left-handed fermions, while the $U(1)_Y$ hypercharge contribution couples to both chiralities. As a result, the NC coupling of the Z^0 to a fermion f depends on both its weak isospin I_3^f and its electric charge $Q_f = I_3^f + \frac{Y}{2}$, leading to different effective coupling strengths for left and right-handed components.

Notably, no right-handed neutrino field $\nu_{\alpha R}$ ($\alpha = e,\ \mu,\ \tau$) has been observed : the Goldhaber experiment [24] mesured the helicity of the neutrino to be purely left-handed, and since neutrinos are relativistic, their helicity and chirality eigenstates are identical. The absence of right-handed neutrino makes the weak interaction purely left-handed for neutrinos, and prevents the neutrino from acquiring mass through the Higgs mechanism, which led to the predictions that the neutrino was massless. This prediction was later contradicted by the observation of neutrino oscillations, discussed in Section 1.3, representing the first evidence of physics beyond the minimal SM.

Charged-Current Interaction

The charged-current (CC) interaction operates through the exchange of a W^- or W^+ boson. At the leptonic vertex, it connects a neutrino ν_α to its associated lepton l_α ($\alpha = e, \mu, \tau$) within the same $SU(2)_L$ doublet, with the charge of the exchanged W boson determined by charge conservation at the vertex. Since the charged lepton produced in the final state identifies the flavour of the initial neutrino, CC interactions are the primary tool for neutrino flavour identification in experimental setups. An example is given in Figure 1.3a for neutrino-electron scattering via W^+ exchange.

Of particular importance for this thesis is the CC process describing the Inverse Beta Decay (IBD) reaction :

$$\overline{\nu}_e + p \rightarrow e^+ + n \tag{1.9}$$

in which an electron antineutrino interacts with a proton to produce a positron and a neutron via the exchange of a W^- boson as shown in Figure 1.3b. The positron in the final state uniquely identifies the interaction as that of a $\overline{\nu}_e$, since only an electron antineutrino can produce a positron in the CC interaction. This reaction constitutes the primary detection channel of reactor neutrino experiments, from the pioneering experiment of Reines and Cowan's to the next generation JUNO experiment, as discussed in Chapter 2.

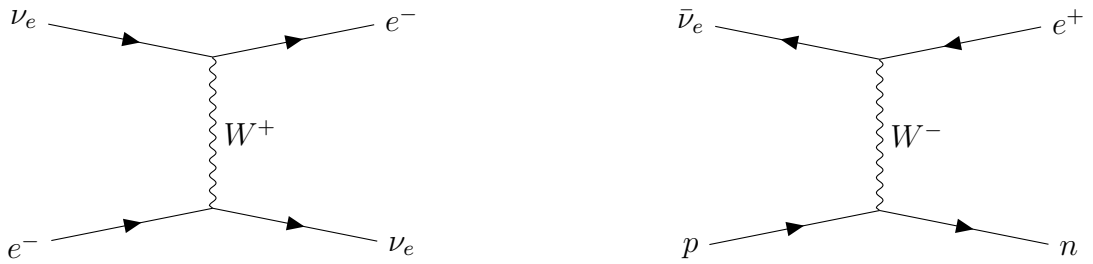

FIGURE 1.3 – Charged-current weak interaction processes. **(a)** : Neutrino–electron scattering ($\nu_e + e^- \rightarrow e^- + \nu_e$) via W^+ exchange. **(b)** : Inverse beta decay ($\bar{\nu}_e + p \rightarrow e^+ + n$) via W^- exchange.

Neutral-Current Interaction

The neutral-current (NC) interaction is mediated by the $Z^{(0)}$ boson, which is electrically neutral. Unlike the CC interaction, the NC interaction does not connect the two members of an $SU(2)_L$ doublet — a neutrino ν_α scatters off a target and continues as the same ν_α. The NC interaction is therefore *flavour-blind* : the Z^0 couples to all three neutrino flavours with equal strength, and the final state carries no information about which neutrino flavour was involved. This is illustrated by the two diagrams in Figure 1.4, which are physically indistinguishable in the final state, as both produce a neutrino and an electron, with no observable difference between ν_e and $\nu_{\mu,\tau}$ induced scattering.

The flavour-blindness and universality of the NC interaction make it a useful normalisation tool in neutrino oscillation experiments, where it provides a flavour-independent event rate that can be compared to the flavour-sensitive CC rate to extract oscillation probabilities.

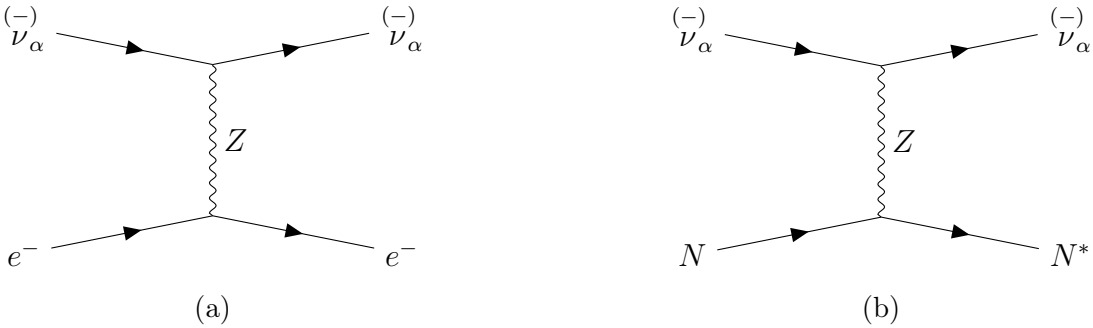

FIGURE 1.4 – Neutral-current interaction process. **(a)** : Neutrino–electron scattering ($\nu_\alpha + e^- \rightarrow \nu_\alpha + e^-$) via Z exchange. **(b)** : Neutrino–nucleus scattering ($\nu_\alpha + N \rightarrow \nu_\alpha + N^*$) via Z exchange.

1.3 Neutrino Oscillations

The first idea of neutrino mass and mixing was proposed by Bruno Pontecorvo in 1957 [25], in analogy with $K^0 \leftrightarrow \overline{K}^0$ oscillations, which he translated into the concept of neutrino–antineutrino oscillations. The discovery of the muon neutrino lead to a generalisation of this idea to a two-neutrino mixing framework, first proposed by Z.Maki, N.Nakagawa and S.Sakata in 1962 [26], and further developed by Pontecorvo in 1967 [27]. The later discovery of the tau neutrino lead to the full three-flavor phenomenological theory of neutrino mixing as it is understood today, which also opened the possibility of non-zero neutrino mass — in direct contradiction with the SM prediction of massless neutrinos.

This section briefly presents the first experimental evidence of neutrino oscillations before introducing the theoretical formalism.

1.3.1 Experimental Evidence

Neutrino research history is a history of anomalies. After the continous β spectrum anomaly, which led to discovery of the neutrino, the massless property of neutrinos was challenged by a succession of anomalies.

The Solar Neutrino Anomaly

In 1968, Raymond Davis designed an experiment with the primary goal of testing the Standard Solar Model (SSM) by detecting the electron neutrinos produced in the Sun's thermonuclear reactions. The solar neutrino energy spectrum given in Figure 1.5, is dominated by neutrinos from proton-proton (pp) fusion reactions, with subdominant contributions from ^{7}Be, ^{8}B, and CNO cycle reactions at higher energies.

Davis' experiment, located 1500 m underground at the Homestake Mine, detected solar neutrinos from the sun via the inverse beta decay process on Chlorine [29] :

$$\nu_e + {}^{37}\mathrm{Cl} \rightarrow {}^{37}\mathrm{Ar} + e^- \tag{1.10}$$

The energy threshold of 0.814 MeV, made the experiment completely blind to the pp channel, and mainly sensitive to ^{7}Be, pep, ^{8}B and the remainder of CNO cycle neutrinos. The measured rate of $\phi = 2.56 \pm 0.16\ (stat.) \pm 0.16\ (syst.)$ Solar Neutrino Unit [2] (SNU) [30] corresponded to only 30% of the SSM prediction of 8.5 ± 1.8 SNU [31], establishing the solar neutrino anomaly. The deficit was later confirmed by the GALLEX [32] and SAGE [33] experiments using Gallium instead of Chlorine, effectively reducing the energy threshold to 0.233 MeV, and gaining sensitivity to the pp channel. Gallium experiments measured rates compatible with 60% of the SSM

2. 1 SNU $= 10^{-36}$ ν captures/atoms/s

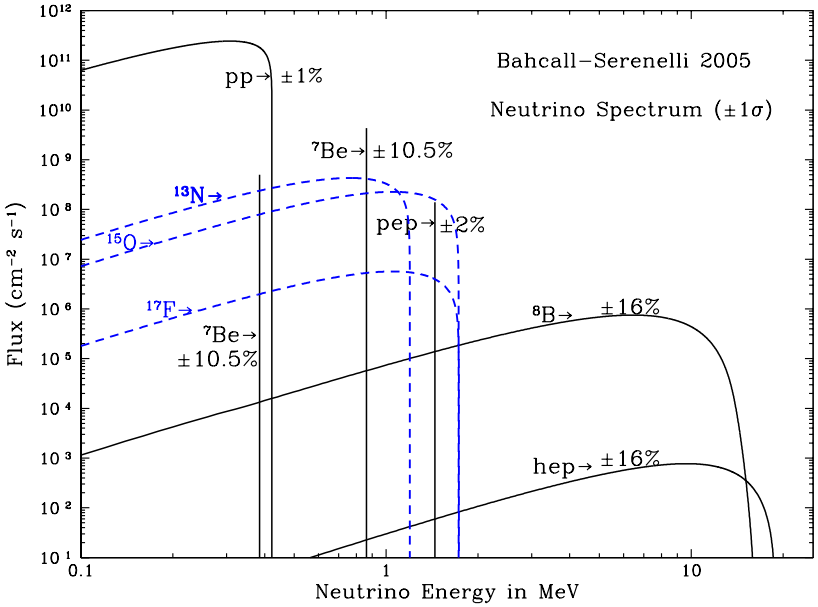

FIGURE 1.5 – Solar neutrino energy spectrum for the solar model BS05(OP) [28].

prediction, which was later confirmed by other experiments. Similar conclusions were drawn by the water Cherenkov Kamiokande [34], and Super-Kamiokande [35] experiments, which observed a deficit of about 50% compared to the SSM prediction.

A consistent deficit was observed across multiple experiments using different detection techniques and energy thresholds. The observed deficit could be interpreted as a neutrino flavour transformation. However, experiments were sensitive only to ν_e through CC interactions, or to a flux-weighted combination of flavors through elastic scattering with cross-section few times higher for ν_e than for $\nu_{\mu,\tau}$. Neither channel could measure the total neutrino flux independent of flavour.

The definitive resolution came from the Sudbury Neutrino Observatory (SNO) [36], a 1 kton heavy-water Cherenkov detector that could simultaneously measure three interaction channels for ^{8}B solar neutrinos : the CC reaction ($\nu_e + d \rightarrow p + p + e^-$), the ES reaction ($\nu_\alpha + e^- \rightarrow \nu_\alpha + e^-$), and crucially the flavour-blind NC reaction :

$$\nu_\alpha + d \rightarrow p + n + \nu_\alpha, \qquad (\alpha = e,\ \mu,\ \tau) \tag{1.11}$$

in which all neutrino flavors break up the deuteron via Z exchange, with the released neutron

serving as the event tag. The measured flux were [36] :

$$\phi_{CC}^{SNO} = 1.76^{+0.06}_{-0.05}(stat.)^{+0.09}_{-0.09}(syst.) \tag{1.12}$$

$$\phi_{ES}^{SNO} = 2.39^{+0.24}_{-0.23}(stat.)^{+0.12}_{-0.12}(syst.) \tag{1.13}$$

$$\phi_{NC}^{SNO} = 5.09^{+0.44}_{-0.43}(stat.)^{+0.46}_{-0.43}(syst.) \tag{1.14}$$

all in units of 10^6 cm^{-2}s^{-1}. The NC flux, sensitive to all flavours equally, was in excellent agreement with the SSM predictions. This demonstrated that a large fraction of the ν_e produced in the Sun had transformed into ν_μ or ν_τ during propagation, providing unambiguous evidence of neutrino flavor oscillations.

The Atmospheric Neutrino Anomaly

The discovery of muon neutrino introduced a new natural source of neutrinos : the neutrinos produced by the interaction of cosmic rays with the upper atmosphere of the Earth, referred to as atmospheric neutrinos. When cosmic ray protons interact with the atmospheric nuclei, they produce pions that decay into muon and muon neutrinos according to Eq. 1.3. The muons subsequently decay, producing an electron, an electron anti neutrino and a muon neutrino :

$$\mu^{\pm} \rightarrow e^{\pm} + \nu_e(\overline{\nu}_e) + \overline{\nu}_\mu(\nu_\mu) \tag{1.15}$$

Considering the full decay chain, one expects approximately two times more ν_μ than ν_e in the atmospheric neutrino flux. However, experiments including IMB [37], MACRO [38], Soudan [39], Kamiokande [40] and Super Kamiokande [41] reported about equal proportion of ν_e and ν_μ, establishing the atmospheric neutrino anomaly.

The Super-Kamiokande experiment provided the key evidence to resolve this anomaly by studying the atmospheric neutrinos flux as a function of the incoming direction, reconstructed form the directionality of the Cherenkov cone. Neutrinos arriving from above the detector have traveled a baseline $L \sim 10$ km through the atmosphere, while neutrinos arriving from below the detector have propagated through the entire diameter of the Earth, corresponding to $L \sim 10^4$ km.

The zenith angle distibution of e-like (ν_e) and μ-like (ν_μ) events for sub-GeV ($E < 1.33$ GeV) and multi-GeV ($E > 1.33$ GeV) samples are shown in Figure 1.6 and compared to predictions for the non-oscillating scenario (hashed region) and for the $\nu_\mu \leftrightarrow \nu_\tau$ oscillation hypothesis (solid lines). While the e-like distributions show good agreement with both hypotheses, the μ-like distributions in the upward-going direction ($\cos\Theta < 0$) show a clear depletion with respect to the non-oscillating expectation, but excellent agreement with the $\nu_\mu \leftrightarrow \nu_\tau$ oscillation scenario.

The observed depletion is interpreted as ν_μ produced in the upper atmosphere oscillating into ν_τ during propagation through the Earth, with the latter being effectively invisible to the detector at the time, resulting in the observed deficit. This provided a second clear and unambiguous evidence of neutrino flavour oscillations.

The leaders of the SNO and Super-Kamiokande experiments were jointly awarded the Nobel Prize in Physics in 2015 *for the discovery of neutrino oscillations, which shows that neutrinos have mass.*

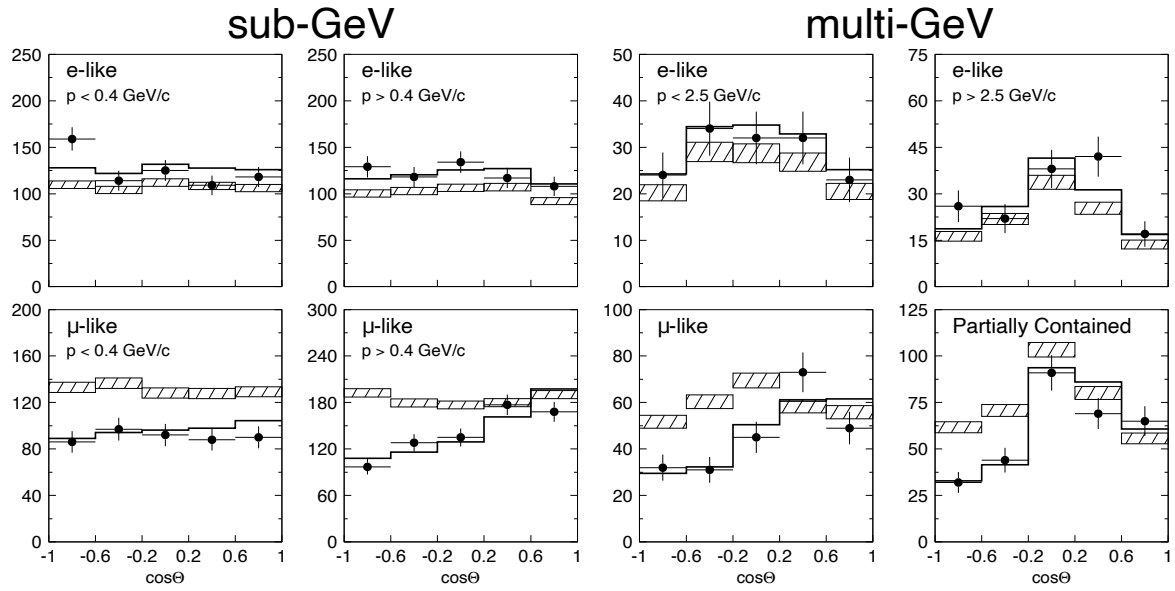

FIGURE 1.6 – Zenith angle distributions of μ-like and e-like events for sub-GeV and multi-GeV data sets. Upward-going particles have $\cos\Theta < 0$ and downward-going particles have $\cos\Theta > 0$. Sub-GeV data are shown separately for $p < 400$ MeV/c and $p > 400$ MeV/c, while Multi-GeV distributions are shown for $p < 2.5$ GeV/c and $p > 2.5$ GeV/c. The hatched region shows the Monte Carlo expectation for no oscillations normalized to the data live-time with statistical errors. The bold line is the best-fit expectation for $\nu_\mu \leftrightarrow \nu_\tau$ oscillations with the overall flux normalization fitted as a free parameter [41].

1.3.2 Neutrino Oscillations in Vacuum

Neutrino oscillations are now a well-established concept, with experimental evidence backing up the theory. In this part we will develop the theoretical framework of the neutrino oscillation theory in the standard plane wave approximation.

Neutrino Mixing : The PMNS Matrix

The experimental evidence presented in the previous sections demonstrates that neutrinos change flavour during propagation. This naturally raises a question familiar to the quark sec-

tor : are the flavour states, $\nu_e,\ \nu_\mu,\ \nu_\tau$, that are produced and detected via the weak interaction the same as the mass states, $\nu_1,\ \nu_2,\ \nu_3$, that propagate through space and time. In the quark sector, the answer is no : the flavor and mass eigenstates are related by the CKM matrix [42, 43], giving rise to the quark flavour mixing.

By analogy, one can postulate that in the lepton sector, the flavor eigenstate produced and detected via weak interaction are linear combination of mass eigenstates that propagate through space, therefore requiring neutrinos to be massive. This mismatch between the interaction basis and the propagation basis gives rise to neutrino oscillation, and the unitary matrix connecting the two bases is known as the Pontecorvo-Maki-Nakagawa-Sakata (PMNS) matrix [25, 26, 27], U_{PMNS} :

$$\begin{pmatrix} \nu_e \\ \nu_\mu \\ \nu_\tau \end{pmatrix} = \underbrace{\begin{pmatrix} U_{e1} & U_{e2} & U_{e3} \\ U_{\mu 1} & U_{\mu 2} & U_{\mu 3} \\ U_{\tau 1} & U_{\tau 2} & U_{\tau 3} \end{pmatrix}}_{U_{PMNS}} \begin{pmatrix} \nu_1 \\ \nu_2 \\ \nu_3 \end{pmatrix} \tag{1.16}$$

The PMNS matrix is a 3×3 unitary matrix parametrised by three mixing angles θ_{12}, θ_{13}, θ_{23}, and one CP-violating phase δ_{CP} (see Section 1.5.3) :

$$U_{PMNS} = \begin{pmatrix} 1 & 0 & 0 \\ 0 & c_{23} & s_{23} \\ 0 & -s_{23} & c_{23} \end{pmatrix} \begin{pmatrix} c_{13} & 0 & s_{13}e^{-i\delta_{CP}} \\ 0 & 1 & 0 \\ -s_{13}e^{i\delta_{CP}} & 0 & c_{13} \end{pmatrix} \begin{pmatrix} c_{12} & s_{12} & 0 \\ -s_{12} & c_{12} & 0 \\ 0 & 0 & 1 \end{pmatrix} \tag{1.17}$$

where $c_{ij} = \cos\theta_{ij}$ and $s_{ij} = \sin\theta_{ij}$. The three rotation matrices correspond to mixing in the 23-sector (atmospheric), the 13-sector (reactor) and the 12-sector (solar), respectively, representing the experimental context in which each angle was measured. The parameters of the PMNS matrix are determined through a global fit of neutrino oscillation data published by various experiments. The values of the mixing parameters, dating from 2024, are summarised in Table 1.1 for both normal and inverted ordering (see Section 1.6).

	Normal Ordering (best fit)		Inverted Ordering ($\Delta\chi^2 = 6.1$)	
	bfp $\pm 1\sigma$	3σ range	bfp $\pm 1\sigma$	3σ range
$\sin^2\theta_{12}$	$0.308^{+0.012}_{-0.011}$	$0.275 \to 0.345$	$0.308^{+0.012}_{-0.011}$	$0.275 \to 0.345$
$\theta_{12}/^\circ$	$33.68^{+0.73}_{-0.70}$	$31.63 \to 35.95$	$33.68^{+0.73}_{-0.70}$	$31.63 \to 35.95$
$\sin^2\theta_{23}$	$0.470^{+0.017}_{-0.013}$	$0.435 \to 0.585$	$0.550^{+0.012}_{-0.015}$	$0.440 \to 0.584$
$\theta_{23}/^\circ$	$43.3^{+1.0}_{-0.8}$	$41.3 \to 49.9$	$47.9^{+0.7}_{-0.9}$	$41.5 \to 49.8$
$\sin^2\theta_{13}$	$0.02215^{+0.00056}_{-0.00058}$	$0.02030 \to 0.02388$	$0.02231^{+0.00056}_{-0.00056}$	$0.02060 \to 0.02409$
$\theta_{13}/^\circ$	$8.56^{+0.11}_{-0.11}$	$8.19 \to 8.89$	$8.59^{+0.11}_{-0.11}$	$8.25 \to 8.93$
$\delta_{CP}/^\circ$	212^{+26}_{-41}	$124 \to 364$	274^{+22}_{-25}	$201 \to 335$
$\frac{\Delta m^2_{21}}{10^{-5}\ \mathrm{eV}^2}$	$7.49^{+0.19}_{-0.19}$	$6.92 \to 8.05$	$7.49^{+0.19}_{-0.19}$	$6.92 \to 8.05$
$\frac{\Delta m^2_{3\ell}}{10^{-3}\ \mathrm{eV}^2}$	$+2.513^{+0.021}_{-0.019}$	$+2.451 \to +2.578$	$-2.484^{+0.020}_{-0.020}$	$-2.547 \to -2.421$

TABLE 1.1 – Best-fit values and 3σ ranges of the neutrino oscillation parameters for normal and inverted mass ordering, from the NuFIT global analysis [44]. The quantity $\Delta m^2_{3\ell}$ is defined as $\Delta m^2_{31} > 0$ for normal ordering and $\Delta m^2_{32} < 0$ for inverted ordering.

Neutrino Oscillation Probability

In the standard theory of neutrino oscillation, a neutrino (antineutrino) of flavour α is produced in a charged-current interaction alongside the corresponding charged anti-lepton ℓ^+_α (charged lepton ℓ^-_α). Assuming neutrino mixing as introduced in Eq. 1.16, a flavor eigenstate $|\nu_\alpha\rangle$ can be written as a linear combination of mass eigenstates :

$$|\nu_\alpha\rangle = \sum_k U^*_{\alpha k} |\nu_k\rangle \tag{1.18}$$

where $U^*_{\alpha,k}$ are the complex conjugate elements of the PMNS matrix. Mass eigenstates are eigenstates of the Hamiltonian $\mathcal{H}$:

$$\mathcal{H} |\nu_k\rangle = E_k |\nu_k\rangle \tag{1.19}$$

with energy eigenvalues given by the relativistic energy-momentum relation :

$$E_k = \sqrt{\vec{p}^2_k + m^2_k} \tag{1.20}$$

The time evolution of the mass eigenstates is governed by the Schrödinger equation :

$$i\frac{\partial}{\partial t} |\nu_k\rangle = \mathcal{H} |\nu_k\rangle \tag{1.21}$$

In the plane-wave approximation, the solution takes the form :

$$|\nu_k(x,t)\rangle = e^{-i(E_k \cdot t - p_k \cdot x)} |\nu_k\rangle \tag{1.22}$$

Substituting Eq. 1.22 into Eq 1.18, the time evolution of the flavour eigenstate $|\nu_\alpha\rangle$ is :

$$|\nu_\alpha(x,t)\rangle = \sum_k U^*_{\alpha k} e^{-i(E_k \cdot t - p_k \cdot x)} |\nu_k\rangle \tag{1.23}$$

Using the unitarity of U, the mass eigenstates can be expressed as linear combinations of flavor eigenstates :

$$|\nu_k\rangle = \sum_\alpha U_{\alpha k} |\nu_\alpha\rangle \tag{1.24}$$

Substituting this into Eq. 1.23, the flavor state $|\nu_\alpha\rangle$ at time t can be expressed as a combination of other flavour eigenstates :

$$|\nu_\alpha(x,t)\rangle = \sum_{\beta=e,\mu,\tau} \left[\sum_k U^*_{\alpha k} e^{-i(E_k \cdot t - p_k \cdot x)} U_{\beta k} \right] |\nu_\beta\rangle \tag{1.25}$$

The probability of observing the neutrino in flavour state β at time t, having been produced in flavour state α, is obtained by projecting onto $|\nu_\beta\rangle$:

$$\mathcal{P}_{\nu_\alpha \to \nu_\beta}(x,t) = |\langle \nu_\beta | \nu_\alpha(x,t) \rangle|^2 = \sum_k \sum_j U^*_{\alpha k} U_{\beta k} U_{\alpha j} U^*_{\beta j} e^{-i[(E_k - E_j)t - (p_k - p_j)x]} \tag{1.26}$$

For ultra-relativistic neutrinos, $E \simeq p_k \gg m_k$, the energy in Eq 1.20 can be approximated as :

$$E_k \simeq E + \frac{m_k^2}{2E} \tag{1.27}$$

so that $E_k - E_j \simeq \frac{\Delta m^2_{kj}}{2E}$, where $\Delta m^2_{kj} \equiv m^2_k - m^2_j$. Furthermore, the propagation time t is not directly accessible experimentally, and can be approximated by the source-to-detector distance $x = L$ (in natural units c = 1) for ultra-relativistic neutrinos. The phase in Eq. 1.26 can therefore be written as :

$$\begin{aligned} E_k t - p_k x &= (E_k - p_k) L \\ &= \frac{E_k^2 - p_k^2}{E_k + p_k} L \\ &= \frac{m_k^2}{2E} L \end{aligned} \tag{1.28}$$

The oscillation probability as a function of L and E is given by :

$$\mathcal{P}_{\nu_\alpha \to \nu_\beta}(L,E) = \sum_{k,j} U^*_{\alpha k} U_{\beta k} U_{\alpha j} U^*_{\beta j} e^{-i\frac{\Delta m^2_{kj}}{2E}L} \tag{1.29}$$

The oscillation probability therefore depends on three physical quantities : the mass-squared difference Δm^2, the source-detector distance L and the neutrino energy E, as well as the elements of the mixing matrix U through the quartic products $U^*_{\alpha k} U_{\beta k} U_{\alpha j} U^*_{\beta j}$. It is often useful to write Eq 1.29 by separating its real and imaginary parts :

$$\begin{aligned}\mathcal{P}_{\nu_\alpha \to \nu_\beta}(L,E) = \delta_{\alpha\beta} &- 4\sum_{k>j} \mathrm{Re}\left[U^*_{\alpha k} U_{\beta k} U_{\alpha j} U^*_{\beta j}\right] \sin^2\left(\frac{\Delta m^2_{kj} L}{4E}\right) \\ &\pm 2\sum_{k>j} \mathrm{Im}\left[U^*_{\alpha k} U_{\beta k} U_{\alpha j} U^*_{\beta j}\right] \sin\left(\frac{\Delta m^2_{kj} L}{2E}\right)\end{aligned} \tag{1.30}$$

where the + (−), sign applies to neutrinos (antineutrinos). Oscillation probabilities with $\alpha \neq \beta$ are referred to as *transition probabilities*, while those with $\alpha = \beta$ are called *survival probabilities*. In the latter case, the quartic product in Eq.1.30 reduces to the real quantity $|U_{\alpha k}|^2 |U_{\alpha j}|^2$, and the imaginary terms vanishes, giving :

$$\mathcal{P}_{\nu_\alpha \to \nu_\alpha}(L,E) = 1 - 4\sum_{k>j} |U_{\alpha k}|^2 |U_{\alpha j}|^2 \sin^2\left(\frac{\Delta m^2_{kj} L}{4E}\right) \tag{1.31}$$

Two-flavour oscillations

The two-flavour approximation considers mixing between neutrino mass eigenstates and is applicable in experiment contexts where one mass-squared difference dominates over the others. For instance, atmospheric neutrino experiments have $|\Delta m^2_{31}| \gg |\Delta m^2_{12}|$.

In this approximation, two flavors eigenstates $|\nu_\alpha\rangle$ and $|\nu_\beta\rangle$ are related to two mass eigenstates $|\nu_1\rangle$, $|\nu_2\rangle$ by a single mixing angle θ :

$$\begin{pmatrix}\nu_\alpha \\ \nu_\beta\end{pmatrix} = \underbrace{\begin{pmatrix}\cos\theta & \sin\theta \\ -\sin\theta & \cos\theta\end{pmatrix}}_{U} \begin{pmatrix}\nu_1 \\ \nu_2\end{pmatrix} \tag{1.32}$$

The transition probability in the two flavor approximation can be easily derived from Eq 1.29 :

$$\mathcal{P}_{\nu_\alpha \to \nu_\beta}(L,E) = \sin^2 2\theta \sin^2\left(\frac{\Delta m^2 L}{4E}\right) \tag{1.33}$$

By conservation of probability in the two-flavour case :

$$\mathcal{P}_{\nu_\alpha \to \nu_\beta} + \mathcal{P}_{\nu_\alpha \to \nu_\alpha} = 1 \tag{1.34}$$

The survival probability is therefore :

$$\mathcal{P}_{\nu_\alpha \to \nu_\alpha}(L, E) = 1 - \sin^2 2\theta \sin^2 \left(\frac{\Delta m^2 L}{4E} \right) \tag{1.35}$$

For reactor neutrinos with energy E $\sim$ 1 MeV, the survival probability can be written, using physical units, by :

$$\mathcal{P}_{\nu_\alpha \to \nu_\alpha}(L, E) = 1 - \sin^2 2\theta \sin^2 \left(1.27 \frac{\Delta m^2[\text{eV}^2] L[\text{m}]}{E[\text{MeV}]} \right) \tag{1.36}$$

where the numerical factor 1.27 arises from expressing $\Delta m^2 L/4E$ in the convenient units of eV^2, m, and MeV respectively.

This result clearly illustrates the key features of neutrino oscillations : the amplitude of the oscillation is governed by the mixing angle θ, while the oscillation length is determined by the ratio L/E and the mass-squared difference Δm^2. Notably, oscillation vanish when $\Delta m^2 = 0$, confirming that non-zero neutrino masses are a necessary condition for flavour oscillation to occur.

1.3.3 Neutrino Oscillations in Matter : The MSW Effect

The oscillation formalism derived in Section 1.3 assumes neutrino propagation in vacuum. When neutrinos propagate through matter, they are subject to coherent forward scattering [3] with particles of the medium (electrons and nucleons), resulting in an additional potential term in the Hamiltonian that acts much like a refractive index, modifying the neutrino mixing pattern. This effect is known as the Mikheyev-Smirnov-Wolfenstein (MSW) effect [45, 46].

Effective Potential in Matter

Neutrinos interact with matter through both the weak charged-current (CC) and neutral-current (NC) interaction, each introducing a potential term to the Hamiltonian. The CC interaction, mediated by the $W^\pm$ boson, is available only to ν_e (or $\overline{\nu}_e$) since matter only contains electrons but not muons or taus. This generates an effective potential :

$$V = \sqrt{2}\, G_F\, N_e \tag{1.37}$$

where G_F is the Fermi constant and N_e is the electron density in the medium. This potential takes an opposite sign for $\overline{\nu}_e$. The NC interactions, however, couples equally to all three neutrino flavours, and the resulting NC effective potential has no effect on oscillation probabilities.

3. Neutrinos can undergo incoherent scattering off individual particles in the medium, but the associated cross-section is negligible over astrophysical or terrestrial path lengths and can safely be ignored in most cases.

The total Hamiltonian in matter is then given by :

$$\mathcal{H} = \mathcal{H}_0 + \mathcal{H}_1 \tag{1.38}$$

where $\mathcal{H}_0$ is the vacuum Hamiltonian defined in Eq. 1.19 and $\mathcal{H}_1$ is the Hamiltonian describing the matter effects of the CC interaction, defined in the flavour basis by :

$$\mathcal{H}_1 = \text{diag}(V, 0, 0) \tag{1.39}$$

acting exclusively on the electron flavour component ν_e.

Two-Flavour Oscillations in Matter

As in the vacuum case, the essential physics of matter effects can be captured in the two flavour approximation. Considering the simplified case of $\nu_e \leftrightarrow \nu_\mu$, related to the mass eigentstates ν_1, ν_2 by the vacuum mixing angle θ, it can be shown that the Hamiltonian in the flavour basis becomes :

$$\mathcal{H} = \frac{1}{4E}\begin{pmatrix} -\Delta m^2 \cos 2\theta + A & \Delta m^2 \sin 2\theta \\ \Delta m^2 \sin 2\theta & \Delta m^2 \cos 2\theta - A \end{pmatrix} \tag{1.40}$$

where $A \equiv 2\,E\,V \equiv 2\sqrt{2}\,G_F N_e E$ parameterises the matter potential. Diagonalising Eq. 1.40 yields an effective mixing angle θ_M and effective mass-squared splitting Δm^2_M in matter :

$$\tan 2\theta_M = \frac{\Delta m^2 \sin 2\theta}{\Delta m^2 \cos 2\theta - A}, \qquad \Delta m^2_M = \sqrt{(\Delta m^2 \cos 2\theta - A)^2 + (\Delta m^2 \sin 2\theta)^2} \tag{1.41}$$

The transition probability has the same form as in vacuum, with the vacuum parameters replaced by their matter-modified counterparts :

$$P(\nu_e \to \nu_\mu) = \sin^2 2\theta_M \, \sin^2\left(\frac{\Delta m^2_M L}{4E}\right) \tag{1.42}$$

An interesting feature of oscillation in matter is the existence of a *resonance* when the matter potential satisfies $A = \Delta m^2 \cos 2\theta$. At the resonance the effective mixing angle is maximal $\theta_M = \pi/4$, leading to the possibility of total transition.

Physical Implications

The MSW effect plays a central role in the two experimental contexts introduced earlier in this section. Within the Sun, electron neutrinos propagate outward through a continuously decreasing electron density profile, and satisfy the resonance condition, leading to conversion

from ν_e to a state that is predominantly ν_2 before exiting the Sun.

A second context where MSW effect becomes relevant, is in the propagation of atmospheric neutrinos through the Earth, where the matter density for upward-going events — $\sim 10^4$ km baseline — is high enough for the matter potential to modify the vacuum oscillation pattern significantly.

1.4 Neutrino Mass

The observation of neutrino oscillations implies that neutrinos are massive, raising a fundamental question about the mechanism responsible for their mass. In the SM, the masses of fermions arise through Yukawa couplings to the Higgs field, but as will be shown, this mechanism is not directly applicable to neutrinos. Two possible extensions of the SM provide solutions : neutrinos could be either *Dirac* particle, like all other known fermions, or *Majorana* particles, which is only possible because neutrinos are neutral fermions.

1.4.1 Fermion Mass Generation

Higgs Mechanism

As briefly introduced in Section 1.2.1, the masses of charged fermions and electroweak gauge bosons are generated through the Higgs mechanism. The mechanism introduces a complex scalar field in the fundamental representation of $SU(2)_L$, the Higgs doublet :

$$\Phi(x) = \begin{pmatrix} \phi^+(x) \\ \phi^0(x) \end{pmatrix} \tag{1.43}$$

where $\phi^+(x)$ and $\phi^0(x)$ are, respectively, a charged and a neutral complex scalar field. The Lagrangian of the doublet is given by

$$\mathcal{L}_{Higgs} = (D_\mu \Phi)^\dagger (D^\mu \Phi) - V(\Phi), \tag{1.44}$$

with the Higgs potential $V(\Phi)$ defined as

$$V(\Phi) = -\mu^2 \Phi^\dagger \Phi + \lambda (\Phi^\dagger \Phi)^2, \tag{1.45}$$

where λ is the Higgs self-coupling coefficient, which must be positive to have a potential bounded from below, and the mass-like term μ^2 is assumed to be negative to realise the spontaneous breaking of symmetry. It can be shown that the minimum of the potential is given by :

$$\Phi^\dagger\Phi = \frac{v^2}{2}, \qquad v = \sqrt{\frac{-\mu^2}{\lambda}}. \tag{1.46}$$

which corresponds to a continuum of degenerate minima related to one another by $SU(2)_L \times U(1)_Y$ gauge transformations. The $U(1)_{EM}$ symmetry group is associated with the conservation of electric charge, which is well known to be unbroken. This implies that the minimum of the potential must be electrically neutral, forbidding charged scalar fields to have a non-zero vacuum value, which will otherwise lead to breaking of the $U(1)_{EM}$ symmetry and generation of a massive photon. Consequently, the vacuum expectation value (vev) $\langle\Phi\rangle$ of the Higgs field must be due to ϕ^0 :

$$\langle\Phi\rangle = \frac{1}{\sqrt{2}}\begin{pmatrix}0\\ v\end{pmatrix}. \tag{1.47}$$

Finally, expending around the vacuum expectation value and taking an appropriate choice of gauge gives :

$$\Phi(x) = \frac{1}{\sqrt{2}}\begin{pmatrix}0\\ v + H(x)\end{pmatrix} \tag{1.48}$$

where $H(x)$ describes the physical Higgs boson.

Fermion masses

Fermion masses are generated by the Higgs mechanism through Yukawa couplings between the fermion fields and the Higgs doublet. Considering leptons only, and denoting ℓ_L the $SU(2)_L$ doublet of left-handed charged leptons and ℓ_R the right-handed singlet, the Lagrangian describing the Yukawa couplings of charged leptons with the Higgs field is given by :

$$\mathcal{L}_{\mathrm{H,L}} = -\sum_{\alpha=e,\mu,\tau} y_\alpha^\ell \overline{\ell_{\alpha L}} \Phi\, \ell_{\alpha R} + \mathrm{h.c.}\,[4] \tag{1.49}$$

where y_α^ℓ is the Yukawa coupling constant for the charged lepton of flavour α. After electroweak symmetry breaking, the Higgs acquires its vev, and the Lagrangian becomes :

$$\mathcal{L}_{\mathrm{H,L}} = -\left(\frac{v+H}{\sqrt{2}}\right)\sum_{\alpha=e,\mu,\tau} y_\alpha^\ell \overline{\ell_{\alpha L}} \ell_{\alpha R} + \mathrm{h.c.} \tag{1.50}$$

The term proportional to the Higgs vev v is a mass term for the charged lepton :

$$m_\alpha = \frac{y_\alpha^\ell v}{\sqrt{2}}, \qquad \alpha = e, \mu, \tau \tag{1.51}$$

4. h.c stands for Hermitian conjugate

while the term proportional to the physical Higgs field H gives the trilinear coupling between the charged leptons and the Higgs boson.

The Yukawa term in Eq 1.49 is gauge invariant for charged leptons, but the same configuration fails for neutrinos. The left handed doublet $\ell_{\alpha L}$ has hypercharge Y = -1, the Higgs doublet has hypercharge $Y = 1$, and the right-handed neutrino singlet would necessarily have $Y = 0$. The term $\overline{\ell}_{\alpha L}\Phi\,\nu_{\alpha R}$ therefore carries a net hypercharge $Y = 2 \neq 0$, and is not gauge invariant. Gauge invariance can be restored by using instead the charge-conjugate Higgs doublet $\tilde{\Phi} = i\sigma_2\Phi^*$, which carries hypercharge $Y = -1$, and, after symmetry breaking, takes the form :

$$\tilde{\Phi}(x) = \frac{1}{\sqrt{2}}\begin{pmatrix} v + H(x) \\ 0 \end{pmatrix}, \tag{1.52}$$

allowing for the following gauge-invariant Lagrangian to be written :

$$\mathcal{L}_{\mathrm{H},\nu} = -\sum_{\alpha=e,\mu,\tau} y^{\nu}_{\alpha}\overline{\ell_{\alpha L}}\tilde{\Phi}\,\nu_{\alpha R} + \mathrm{h.c.} \tag{1.53}$$

An analogous term, using the same $\tilde{\Phi}$ field, is responsible for the mass generation of up-type quarks. However, the term in Eq. 1.53 does not exist in the minimal SM for neutrinos, since no right-handed neutrino field $\nu_{\alpha R}$ has ever been observed. The observation of neutrino oscillations nevertheless requires a mechanism to explain the non-zero neutrino mass, motivating extensions of the SM.

1.4.2 Dirac Neutrinos

Dirac Mass term

The simplest extension of the SM consists in introducing a right-handed neutrino $\nu_{\alpha R}$ for each generation. This allows the term in Eq. 1.53 to be written, and after electroweak symmetry breaking generates a Dirac mass term :

$$\mathcal{L}^{D}_{\mathrm{mass}} = -m^{\nu}_{\alpha}\left(\overline{\nu_{\alpha L}}\nu_{\alpha R} + \overline{\nu_{\alpha R}}\nu_{\alpha L}\right), \qquad m^{\nu}_{\alpha} = \frac{y^{\nu}_{\alpha}v}{\sqrt{2}} \tag{1.54}$$

with y^{ν}_{α} the Yukawa coupling constant for the neutrino of flavour α . The introduced right-handed neutrino is a singlet under the full SM gauge group, and is therefore often referred to as *sterile*, as opposed to the *active* left-handed neutrino involved in the weak interaction. In this scenario, the neutrino is described like any other SM fermion, but to agree with the experimental bounds on neutrino masses, a Yukawa coupling $y^{\nu} \lesssim 10^{-12}$ is required, a value that is commonly considered to be unnatural, and suggests that the Dirac mechanism alone may not be the complete picture.

Lepton Number

The Dirac nature of neutrinos is intimately tied to the conservation of total lepton number $L = L_e + L_\mu + L_\tau$, defined such that leptons carry $L = 1$ and antileptons carry $L = -1$. It can be noted that this is distinct from conservation of flavour lepton number L_e, L_μ, L_τ, which is violated by neutrino oscillations since a neutrino produced with flavour α can later be detected with flavour $\beta \neq \alpha$. A direct consequence of total lepton number conservation is that neutrinos and antineutrinos are two distinct particles in the Dirac formalism.

1.4.3 Majorana Neutrinos and the Seesaw Mechanism

Majorana Mass

An alternative possibility, is that the neutrino is a Majorana particle [47]. As opposed to Dirac neutrinos, for which the mass term couples both chiral components of a single field, the Majorana mass term couples a single chiral component to its own charge conjugate :

$$\mathcal{L}^M_{mass} = -\frac{1}{2} m \left(\overline{\nu_L} \nu_L^{\mathbf{C}} + \overline{\nu_L}^{\mathbf{C}} \nu_L \right) \tag{1.55}$$

where it can be shown that $\nu_L^{\mathbf{C}} = \mathcal{C} \bar{\nu_L}^T$ has right-handed chirality, with $\mathcal{C}$ the charge conjugation operator, so that $\overline{\nu_L^{\mathbf{C}}} \nu_L$ does not vanish. The Majorana field is defined as :

$$\nu = \nu_L + \nu_L^{\mathcal{C}} \tag{1.56}$$

which by construction satisfies $\nu^C = \nu$, so that the particle is identical to its charge conjugate. This condition is equivalent to stating that the Majorana neutrino is its own antiparticle — a possibility satisfied only by electrically neutral fermions. Equivalently, this can be understood through lepton number : the Majorana mass term in Eq. 1.55 violates total lepton number conservation by two units. With no conserved charge left to distinguish "particle" from "antiparticle", as is the case for the Dirac neutrino, the two labels become equivalent for a Majorana neutrino.

Mixing

The Majorana mass term in Eq 1.55 is not invariant under the global $U(1)$ gauge transformation, unlike the Dirac mass term. Consequently, two additional physical phases are introduced into the PMNS matrix :

$$U_{\text{PMNS}} = U^D \times \text{diag}\left(1, e^{i\lambda_1}, e^{i\lambda_2}\right) \tag{1.57}$$

where U^D is the Dirac mixing matrix defined in Eq.1.16. However, these additional Majorana phases have no observable effect on neutrino oscillations. This is a direct consequence of the

oscillation probability being built from $|\langle\nu_\beta|\nu_\alpha(t)\rangle|^2$, in which every mixing matrix element is paired with its own complex conjugate, leading the Majorana phase factors to cancel as $\left|e^{i\lambda_i}\right|^2 = 1$. Therefore, no oscillation experiment can ever provide any information on the Majorana phases, and no realistic prospect of a precision measurement currently exists.

Seesaw Mechanism

For any neutrino flavor, left-handed chiral field ν_L is known to exist since it participates in the charge-current weak interaction. In contrast, no evidence of ν_R exists, although its existence is allowed by the SM. If only ν_L exists, the neutrino mass term reduces to the Majorana term of Eq. 1.55 and the neutrino is a Majorana particle. If ν_R also exists, a Dirac mass term, generated by the Higgs mechanism and introducing a mass m^D, becomes possible. Interestingly, in the possible existence of ν_R, the neutrino mass Lagrangian may simultaneously contain a Majorana mass term for ν_L, with mass m_L^M, and a Majorana mass term for ν_R, with mass m_R^M, alongside the Dirac mass term. For a single neutrino flavor, the most general mass Lagrangian can be written in matrix form as [48] :

$$\mathcal{L}_{mass}^{D+M} = \frac{1}{2}\left(\overline{\nu_L}^{\mathcal{C}}, \overline{\nu_R}\right)\begin{pmatrix} m_L^M & m^D \\ m^D & m_R^M \end{pmatrix}\begin{pmatrix} \nu_L \\ \nu_R^{\mathcal{C}} \end{pmatrix} + h.c \tag{1.58}$$

However, a Majorana mass term built solely from the left-handed component of the neutrino field, as in Eq. 1.55, is forbidden in the SM, since the corresponding Majorana Lagrangian is not invariant under $SU(2)_L \times U(1)_Y$ gauge transformations, and forces $m_L^M = 0$. The right-handed field ν_R, however, is a singlet under the SM gauge group and may acquire its own Majorana mass term m_R^M. Setting $m_L^M = 0$ and diagonalising the mass matrix in Eq. 1.58 yields two mass eigenvalues :

$$m_{1,2} = \frac{m_L^M + m_R^M}{2} \pm \sqrt{\left(\frac{m_L^M - m_R^M}{2}\right)^2 + (m^D)^2} \tag{1.59}$$

In the natural limit $m_R^M \gg m^D$, the two values simplify to :

$$m_1 \approx m_R^M \qquad m_2 \approx \frac{(m^D)^2}{m_R^M} \tag{1.60}$$

This is known as the Type-I Seesaw mechanism [49, 50]. The light mass eigenstate is identified with the observed neutrino, with mass eigenvalues m_2 suppressed by the ratio $(m^D)^2/m_R^M$, while the heavy mass eigenstate, with mass eigenvalue m_1, corresponds to a hypothetical heavy Majorana neutrino that has not yet been observed. The Seesaw mechanism offers an elegant explanation to the lightness of the observed neutrinos mass by introducing a heavy right-handed Majorana neutrino, and without requiring the unnaturally small Yukawa couplings of the pure Dirac scenario.

1.5 Current Neutrino Experimental Landscape

Nearly 70 years after the discovery of the neutrino, several fundamental questions remain unanswered, and continue to shape the current experimental landscape in neutrino physics. Since the discovery of neutrino oscillations, the question of neutrino mass has been at the forefront of the field, connecting several open questions :

— What is the fundamental nature of the neutrino, and through which mechanism does it acquire its mass ?

— What is the absolute mass scale of the neutrino mass eigenstates ?

— What is the ordering of the neutrino masses ? Are neutrinos ordered in mass similarly to their corresponding charged leptons, or not ?

Beyond the question of mass, a number of open questions remain within the oscillation framework itself, most notably the determination of the CP-violating phase δ_{CP}, and the possible existence of additional, sterile neutrino states, participating in the oscillation mechanism.

1.5.1 $0\nu\beta\beta$ Decay Experiments

The nature of the neutrino remains an open question to this day, with the central goal of determining whether the neutrino is a Dirac or Majorana particle. As discussed in the previous section, neutrino oscillations are structurally insensitive to this question : the oscillation probability depends only on the mixing angles, the Dirac CP-violating phase, and the mass-squared differences, all of which are common to both Dirac and Majorana cases. Resolving the Dirac or Majorana nature requires the direct observation of neutrino mass-related effects, which oscillations — a purely propagative phenomenon – cannot access.

For certain radioactive nuclei, where ordinary single β decay is energetically forbidden, a decay proceeding via two simultaneous β decays becomes possible :

$$(A, Z) \rightarrow (A, Z+2) + 2e^- + 2\overline{\nu}_e \tag{1.61}$$

$$(A, Z) \rightarrow (A, Z-2) + 2e^+ + 2\nu_e \tag{1.62}$$

Although rare, this process known as two-neutrino double beta decay ($2\nu\beta\beta$), has been observed in several nuclei [51], with measured half-life in the range $T^{2\nu}_{1/2} \in [10^{19}, 10^{25}]$ years. A variant of this process was proposed in 1939 by W.H. Furry [52], in which the virtual neutrino exchanged via the two simultaneous beta decay is reabsorbed as its own antiparticle. This process is referred to as the neutrinoless double beta decay ($0\nu\beta\beta$) :

$$(A, Z) \rightarrow (A, Z+2) + 2e^- \tag{1.63}$$

$$(A, Z) \rightarrow (A, Z-2) + 2e^+ \tag{1.64}$$

In contrast to $2\nu\beta\beta$, where the available energy is shared between the electrons and the antineutrinos resulting in a continuous energy spectrum, the $0\nu\beta\beta$ process produces no neutrino : the full decay energy is shared by the two electrons alone, giving a monoenergetic peak at the reaction's Q-value. This process violates total lepton number conservation by two units, and is possible only if neutrinos are Majorana particle. As such, it constitutes the most promising experimental approach of determining the nature of the neutrino.

The predicted $0\nu\beta\beta$ half-life is related to the nuclear matrix element $M^{0\nu}$ of the transition and the effective Majorana neutrino mass $m_{\beta\beta}$ by :

$$\left(T^{0\nu}_{1/2}\right)^{-1} \propto |M^{0\nu}|^2 \times |m_{\beta\beta}|^2 \tag{1.65}$$

where the effecive mass depends on the first-row elements of the PMNS matrix and the eigenvalues of the neutrino mass eigenstates :

$$m_{\beta\beta} = \left| \sum_{i=1}^{3} U_{ei}^2 m_i \right| \tag{1.66}$$

Note that $0\nu\beta\beta$ depends on whether the mass eigenstates add constructively or destructively, which depends on the neutrino mass ordering, further developed in Section 1.6.

The current best limit on the $0\nu\beta\beta$ is set by the KamLAND-Zen experiment, using ^{136}Xe, with a measured half life limit of $T^{0\nu}_{1/2} < 3.8 \times 10^{26}$ yr [53]. The corresponding limit on the effective Majorana mass as a function of the lightest neutrino mass is given in Figure 1.7.

1.5.2 Absolute Mass Scale Measurement

Among the fundamental questions about neutrinos, the absolute mass scale remains a particularly active topic of research. As mentioned previously, the $0\nu\beta\beta$ experiments provide an upper limit on the effective Majorana mass, with the current best limit set by KamLAND-Zen at $\langle m_{\beta\beta} \rangle < (28 - 122)$ meV, with the range reflecting the uncertainty on the nuclear matrix elements. Beyond $0\nu\beta\beta$, other methods are available to constraint the absolute neutrino mass scale.

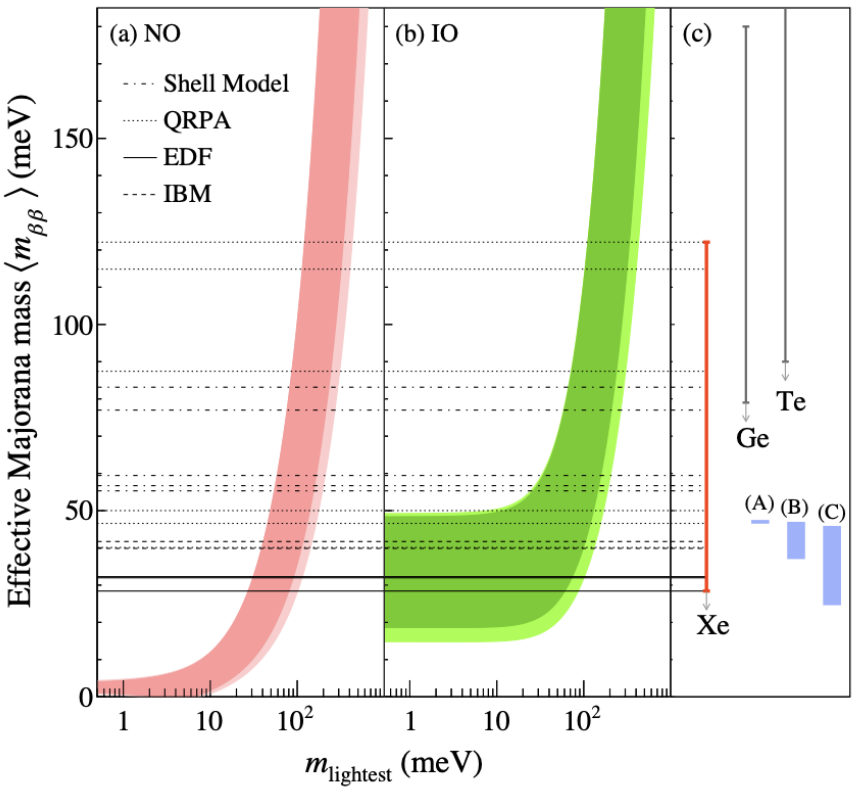

FIGURE 1.7 – Effective Majorana neutrino mass $m_{\beta\beta}$ as a function of the lightest neutrino mass. The horizontal lines indicated to the best upper limit obtained with ^{136}Xe by KamLAND-Zen, compared with limits obtained using ^{76}Ge and ^{130}Te [53].

Cosmological Constraints

Constraints can be obtained by fitting cosmological models to large-scale structure and Cosmic Microwave Background (CMB) data, which are sensitive to the sum of the neutrinos mass eigenvalues $M_\nu = \sum_{i=1}^{3} m_i$. Within the minimal ΛCDM model, current CMB datasets place an upper limit $M_\nu < 0.129$ (0.155) eV (95% C.L) for the normal (inverted) ordering [54].

More recently, the DESI collaboration published the results from the first year of their Baryon Acoustic Oscillation observation [55]. Combined with CMD data and assuming the minimal ΛCDM model, the results yield a substantially tighter limit of $M_\nu < 0.072$ (0.113) eV (95% C.L) for the normal (inverted) ordering.

Supernovae Constraints

A complementary method exploits the dispersion in the time of arrival of supernova neutrinos. The most successfully studied supernova is SN1987A, located in the Large Magellanic Cloud and optically discovered on 24 February 1987. A few hours before its optical discovery, the Kamiokande II, IMB and Baksan detectors recorded a burst of about 25 events with energies

of the order of 10 MeV within a time window of the order of 10 s [56].

The method relies on the group velocity of massive, ultra-relativistic neutrinos :

$$v \simeq 1 - \frac{m^2}{2E^2}. \tag{1.67}$$

Neutrinos of different energies E, emitted simultaneously from a source at distance L, arrive at slightly different times. The neutrinos observed from SN1987A had energies ranging from about 6 to 40 MeV, with a mean of $E \sim 15$ MeV, and travelled from the Large Magellanic Cloud, located at a distance $L \simeq 50$ kpc from Earth. The arrival-time difference between two neutrinos of energies $E_1 < E_2$ is given by :

$$\Delta t = \frac{L}{2c} m^2 \left(\frac{1}{E_1^2} - \frac{1}{E_2^2} \right). \tag{1.68}$$

Assuming the detected events are electron antineutrinos and neglecting mixing, an upper bound on the m_{ν_e} can be obtained by requiring that Δt must not exceed the duration of the neutrino burst. A combined analysis of the SN1987A data yields [57]

$$m_{\nu_e} < 5.7 \text{ eV} \quad (95\% \text{ C.L}) \tag{1.69}$$

Direct Measurement

The most model-independent approach of measuring the absolute neutrino mass scale relies on the kinematics of β decay. In the decay, a non-zero neutrino mass slightly reduces the maximum kinetic energy available to the emitted electron

$$E^e_{max} = Q - m_{\overline{\nu}_e} \tag{1.70}$$

where Q is the Q-value of the reaction and $m_{\overline{\nu}_e}$ is the mass of the electron antineutrino given by $m^2_{\overline{\nu}_e} = \sum_i |U^2_{ei}| m^2_i$. The resulting electron energy spectrum appears distorted toward the endpoint E_0 for non-zero neutrino mass, as illustrated in Figure 1.8.

The current best limit is obtained using tritium (^{3}H), which has an endpoint energy $E_0 =$ 18.6 keV and a half-life 12.3 years. The KATRIN experiment has set the current best laboratory limit on the electron antineutrino mass with $m_{\overline{\nu}e} < 0.45$ eV at 90% confidence level [58].

1.5.3 CP violation in the Lepton Sector

δ_{CP} Phase Measurement

As introduced in Section 1.3.2, the PMNS matrix contains a Dirac CP-violating phase δ_{CP}, analogous to the CP violating phase already established in the quark sector through the CKM

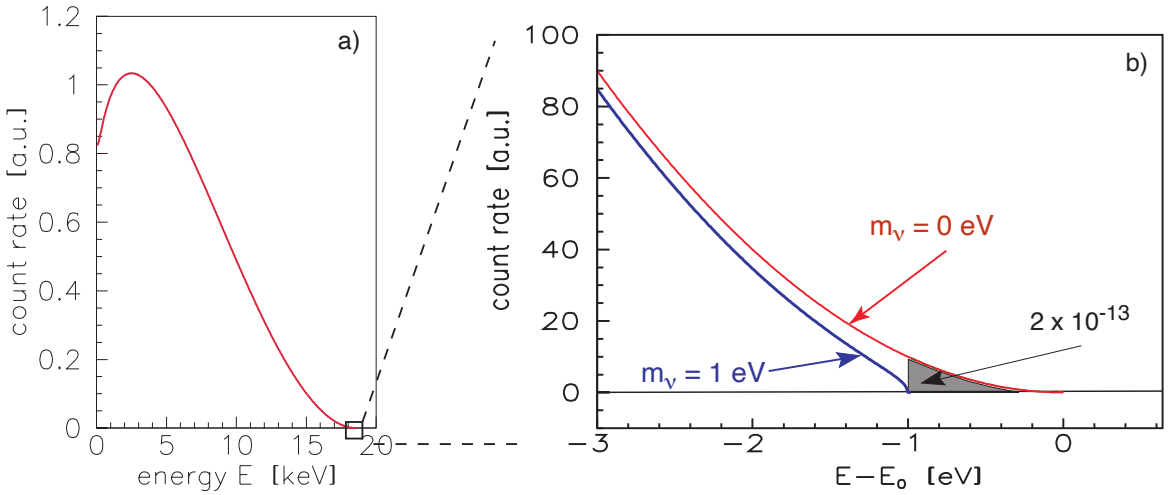

FIGURE 1.8 – The electron energy spectrum of tritium β decay : **(Left)** Complete spectrum. **(Right)** Zoom on the endpoint region. The β spectrum is shown for neutrino masses of 0 and 1 eV [59].

matrix. A non-conservative value of δ_{CP} ($\delta_{CP} \neq 0, \pi$) implies that neutrino and antineutrino probabilities differ :

$$P(\nu_\alpha \to \nu_\beta) \neq P(\bar{\nu}_\alpha \to \bar{\nu}_\beta) \tag{1.71}$$

This asymmetry, however, is not accessible to all oscillation channels, and can only be probed in transition probabilities, since the CP-violating phase enters the oscillation formula through the imaginary term of Eq. 1.30, that cancels for survival probabilities.

A significant complication in extracting δ_{CP} arises from a degeneracy with the neutrino mass ordering present already at the level of vacuum oscillations : a change in the sign of Δm^2_{31} can be compensated by a corresponding change in δ_{CP}, leaving the oscillation probability unchanged [60]. Resolving this degeneracy requires a separate handle capable of distinguishing the two effects. The MSW effect, presented in Section 1.3.3, can provide such a handle at sufficiently long baselines, where matter effects modify the appearance probability in a different way from δ_{CP} depending on the ordering : for normal ordering, the matter potential enhances the neutrino channel and suppresses the antineutrino channel, while for inverted ordering the pattern is reversed. Since this asymmetry is distinct from the δ_{CP}–ordering asymmetry, strong enough matter effects allows to disentangle the δ_{CP}–ordering degeneracy.

Experimental Status and Prospect

Experimentally, δ_{CP} is probed through long-baseline accelerator neutrino experiments, which measure the transition probability $P(\nu_\mu \to \nu_e)$ and its antineutrino counterpart $P(\overline{\nu}_\mu \to \overline{\nu}_e)$. As of today, a mild but persistent $\sim 2\sigma$ tension exists between the values measured by T2K

and NOνA [61] experiments, where T2K favours maximal CP violation ($\delta_{CP} \approx -\pi/2$), while NO$\nu$A leans toward CP conservation.

The next generation long-baseline experiments DUNE [62] and Hyper Kamiokande [63] are expected to provide a definite measurement of δ_{CP} withing the coming decade. These experiments employ different strategies to address the ordering–δ_{CP} degeneracy discussed above. Owing to its long, $\sim$ 1300 km baseline, DUNE benefits from matter effect strong enough to resolve the mass ordering and δ_{CP} degeneracy independently of external constraints. The Hyper Kamiokande configuration instead employs a shorter, $\sim$ 295 km baseline, chosen to maximize the statistical precision on δ_{CP} at the cost of much weaker matter effects, which leaves the experiment dependent on external determination of the mass ordering. The projected sensitivity of DUNE and Hyper Kamiokande to δ_{CP} are shown in Figure 1.9, assuming normal mass ordering.

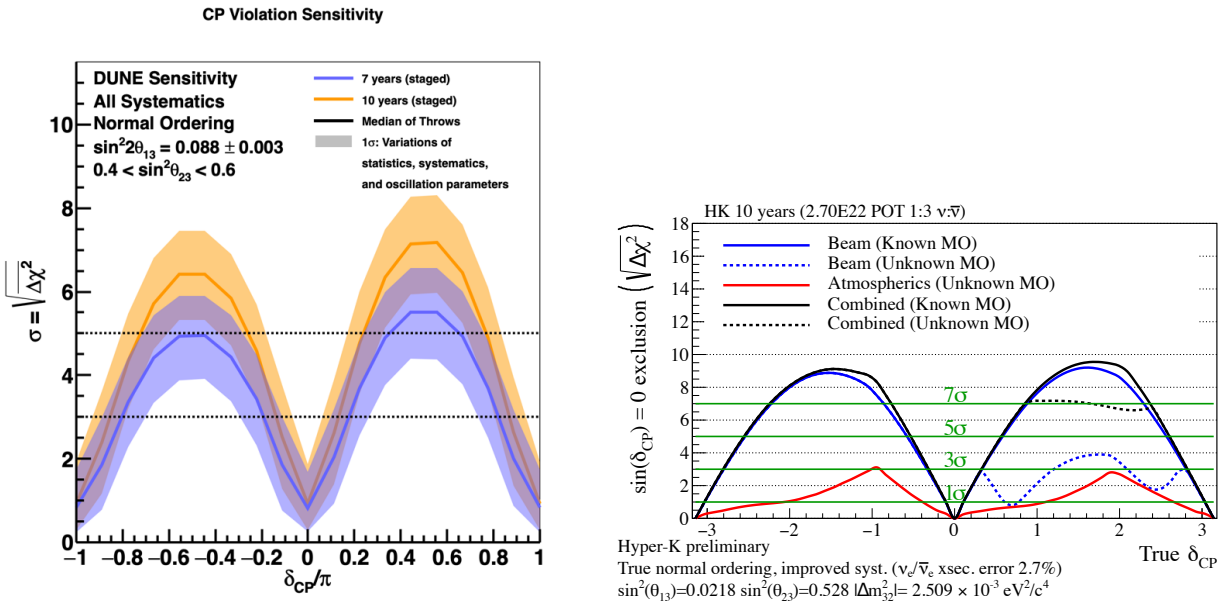

(a) (b)

FIGURE 1.9 – **(Left)**Significance of the DUNE determination of CP-violation as a function of the true value of δ_{CP}, for seven (blue) and ten (orange) years of exposure, and assuming normal mass ordering [62]. **(Right)** Hyper-Kamiokande sensitivity to exclude $\sin \delta_{CP} = 0$ as a function of the true value of δ_{CP} after 10 years of accumulated statistics in case of normal ordering [64].

1.5.4 Light Sterile Neutrinos

The number of neutrinos participating in the weak interaction has been successfully constrained by cosmology [54], which yields results consistent with LEP experiments. These measurements, however, do not exclude the existence of additional neutrino states that do not couple with the weak interaction — called *sterile*.

A motivation for sterile neutrinos arose from the succession of anomalies between the observed and predicted neutrino rates in short-baseline reactor and accelerator neutrino experiments. The first anomaly originates from a deficit in the number of ν_e observed in the calibration source runs by the GALLEX [65] and SAGE [66] experiments leading to the *gallium anomaly*, recently reinforced by the BEST experiment [67]. A similar deficit was found between the predicted and measured flux of $\overline{\nu}_e$ at short baselines from nuclear reactors, leading to the *reactor anomaly* [68]. Finally, the LSND experiment reported an excess of $\overline{\nu_e}$ appearance in a $\overline{\nu_\mu}$ beam [69], reffered to as the *LSND anomaly*.

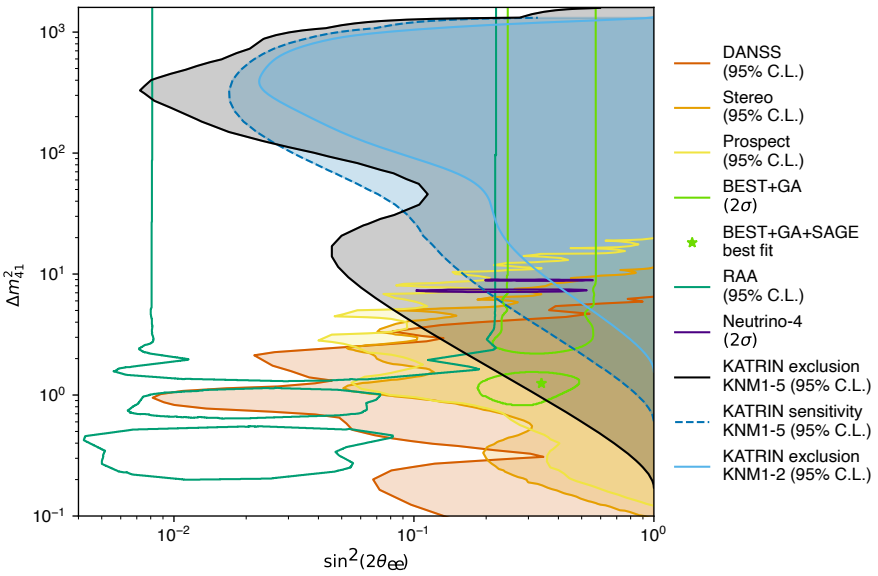

FIGURE 1.10 – 95% CL exclusion contours in the $(\Delta m^2_{41}, \sin^2(2\theta_{ee}))$ plane from the analysis of the first five KATRIN measurement campaigns, assuming a fixed active neutrino mass $m_\nu = 0$ eV (black). The light and dark green contours show the regions allowed at 95% CL by the reactor antineutrino anomaly and the gallium anomaly respectively, with the green star indicating the combined best-fit point from BEST, GALLEX, and SAGE. From [70].

These anomalies motivated the extension of the oscillation framework, incorporating one or more additional sterile neutrino mass eigenstates, leading to the 3+N scenarios. Unlike the heavy, GeV scale, right handed neutrino introduced in the context of the seesaw mechanism, the sterile neutrino(s) discussed here are hypothesised to have mass in the eV range. However, the existence of sterile neutrinos remain controversial, as several experiments, including PROSPECT [71], STEREO [72], MINOS [73], and more recently KATRIN [70], have reported null results in their searches of sterile neutrinos, partially contradicting the anomalies listed above. The exclusion curves in the $(\Delta m^2_{41},\ \sin^2(2\theta_{ee}))$ plane are presented in Figure 1.10, where the recent KATRIN result now excludes nearly the entire parameter space of the $3+1$ sterile hypothesis when combined with the Reactor Antineutrino Anomaly (RAA).

1.6 Neutrino Mass Ordering Determination

As established in the previous section, the Neutrino Mass Ordering (NMO) is the one piece of the oscillation framework that remains undetermined by data despite being essential to constraint other parameters. The NMO refers to the question of whether the neutrino mass eigenstates are arranged similarly to those of their corresponding charged leptons, referred to as the *normal ordering*, $m_1 < m_2 < m_3$, or in the opposite sense, the *inverted ordering*, $m_3 < m_1 < m_2$.

1.6.1 Long Baseline Accelerator Experiments

Long baseline accelerator neutrino experiments can probe the mass ordering by exploiting the same MSW effect introduced in Section 1.3.3, whose impact on CP violation measurements was discussed in Section 1.5.3.

Matter-Induced Ordering Sensitivity

As discussed in Section 1.5.3, the sign of Δm^2_{31} enters the ν_e appearance probability in two distinct ways, visible at leading order in the expansion [74] :

$$\begin{aligned}\mathcal{P}(\nu_\mu \to \nu_e) \simeq \sin^2\theta_{23}\sin^2 2\theta_{13}\frac{\sin^2(\Delta_{31}-aL)}{(\Delta_{31}-aL)^2}\Delta^2_{31} \\ + \sin 2\theta_{23}\sin 2\theta_{13}\sin 2\theta_{12}\frac{\sin(\Delta_{31}-aL)}{(\Delta_{31}-aL)}\Delta_{31}\frac{\sin(aL)}{(aL)}\Delta_{21}\cos(\Delta_{31}+\delta_{CP}) \\ + \cos^2\theta_{23}\sin^2 2\theta_{12}\frac{\sin^2(aL)}{(aL)^2}\Delta^2_{21}\end{aligned} \tag{1.72}$$

where $\Delta_{ij} = \Delta m^2_{ij} L/4E_\nu$, and $a = G_F N_e/\sqrt{2}$. First, the ordering enters the CP violating term as $\cos(\Delta_{31}+\delta_{CP})$, which gives rise to the degeneracy with δ_{CP} already discussed in Section 1.5.3. Second, and crucial for breaking the degeneracy, Δ_{31} also appears together with the matter term a as $\sin(\Delta_{31}-aL)/(\Delta_{31}-aL)$. Since a has a sign fixed by the presence of electrons and absence of positrons in ordinary matter, this combination gives a different response to a flip of the mass ordering when compared to the CP-violating term. For normal ordering ($\Delta m^2_{31} > 0$), the matter potential enhances the $\nu_\mu \to \nu_e$ appearance probability and suppress the corresponding antineutrino channel $\overline{\nu}_\mu \to \overline{\nu}_e$, while for inverted ordering the pattern is reversed. This effect grows in significance as aL becomes comparable to Δm^2_{31}, which happens for baseline in the order of $\sim$ 1000 km [75], providing enough leverage to break the ordering–CP-violation degeneracy.

This is illustrated in Figure 1.11, which shows the ν_e and $\bar{\nu}_e$ appearance probabilities as a function of E_ν for a baseline $L = 1300$ km, for four values of δ_{CP} and both mass ordering hypotheses. The ordering-induced enhancement and suppression discussed above are clearly visible, especially near the first oscillation maximum (~ 2.5 GeV). Resolving the degeneracy in practice relies on a combination of factors : a broadband experiment, capable of mapping the appearance probability over a sufficiently wide energy range, where the matter and CP-violating terms evolve differently ; the experiment's ability of functioning in both neutrino and antineutrino mode ; and precise measurements of the disappearance channels $\nu_\mu \to \nu_\mu$ and $\bar{\nu}_\mu \to \bar{\nu}_\mu$, which constrain θ_{23} and $|\Delta m^2_{31}|$ independently of δ_{CP} and thereby reduce the freedom available to compensate for an incorrect ordering hypothesis.

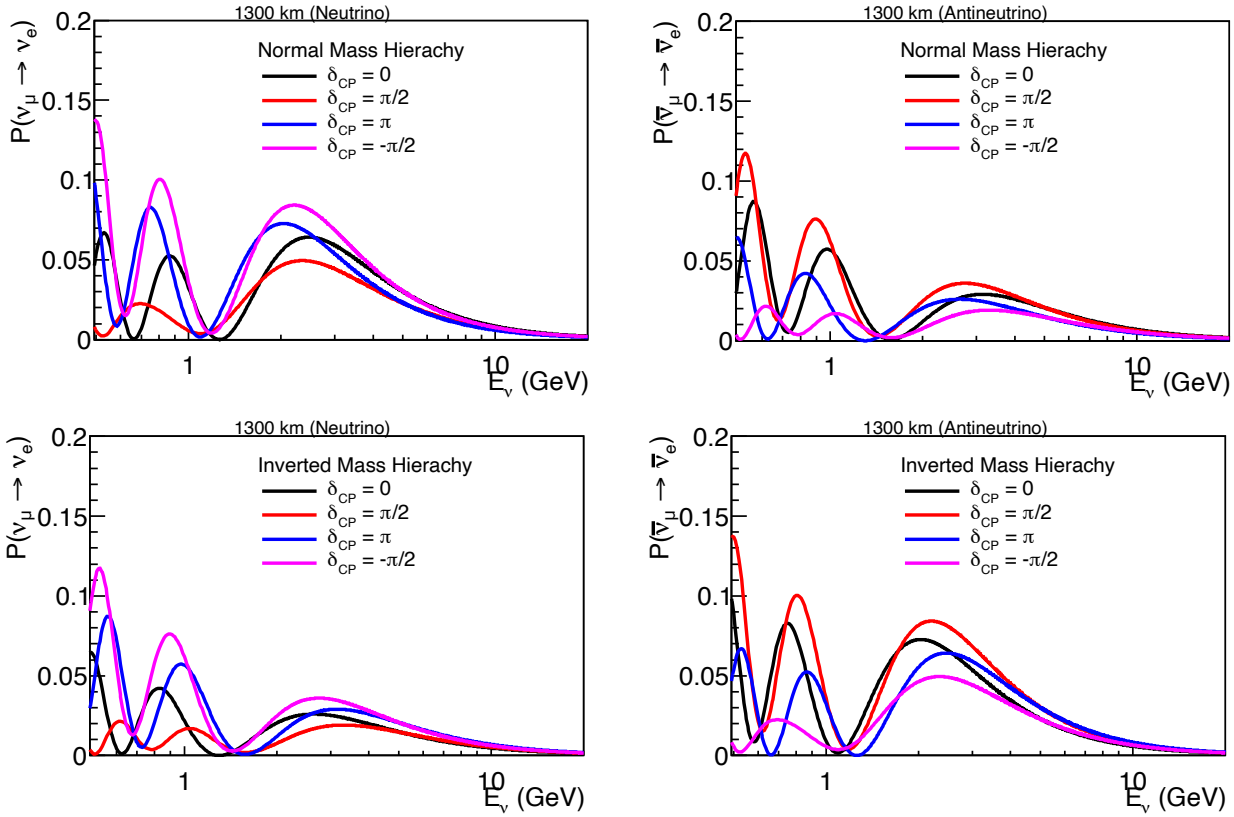

FIGURE 1.11 – Electron neutrino and antineutrino appearance oscillation probabilities as a function of the neutrino energy E_ν at $L = 1300$ km for the indicated four values of the CP phase δ_{CP} [76].

Current Status and Prospect

Current generation of experiments, T2K and NOνA, have combined their data in a joint analysis [61], finding only a mild, inconclusive preference for normal ordering, but no strong determination for either mass ordering to date. The next-generation DUNE experiment [77] is expected to be able to resolve the mass ordering at a significance of at least 5σ in a few years of operation for any δ_{CP} value, as shown in Figure 1.12.

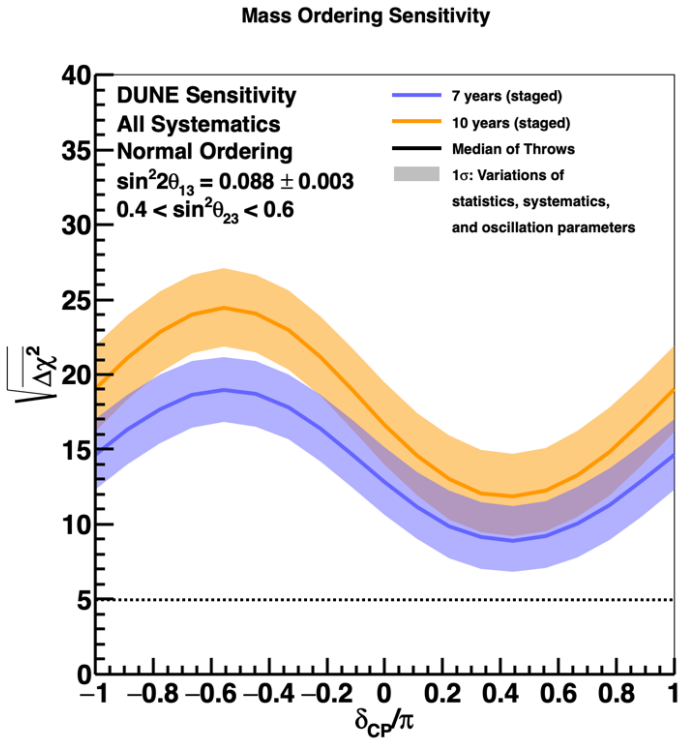

FIGURE 1.12 – Significance of the DUNE determination of the neutrino mass ordering, as a function of the true value of δ_{CP}, for seven (blue) and ten (orange) years of exposure. True normal ordering is assumed [62].

1.6.2 Atmospheric Neutrino Experiments

A similar approach in determining the neutrino mass ordering exploits the MSW resonance mechanism but applied on naturally produced atmospheric neutrinos rather than neutrinos produced in man-made accelerator beams. Atmospheric neutrinos, produced by cosmic-ray interactions in the Earth's atmosphere, arrive at a detector from all directions, with baselines ranging from $\sim$ 10 km (directly from above) to $\sim 10^4$ km (traversing the full diameter of the Earth), over an energy range of approximately 0.1–100 GeV.

Differences to Accelerator Neutrino Measurements

Experimentally, detection of atmospheric neutrinos is performed using water- or ice-based Cherenkov detectors, where the Cherenkov light cone provides a direct handle on the direction of the incoming particle. A key limitation is that such detectors are unable to distinguish neutrino-induced from antineutrino-induced events on an event-by-event basis, since Cherenkov light alone carries no information on the charge of the produced lepton.

A mass ordering determination remains possible by exploiting a pre-existing, ordering-independent physical asymmetry in the atmospheric event rate : a roughly two-times larger

interaction cross-section for neutrinos relative to antineutrinos at GeV-scale energies, combined with a small ($\sim 1.1\times$) excess of neutrinos over antineutrinos in the atmospheric flux itself [78]. Consequently, the detected atmospheric event sample already contains an excess of neutrino-induced events relative to the antineutrino-induced ones independently of any oscillation effects. The matter-effect-induced enhancement or suppression, which acts oppositely on neutrinos and antineutrinos depending on the ordering, introduces an additional asymmetry whose signature can be exploited by atmospheric neutrino experiments. This signature is nonetheless considerably diluted to what a event-by-event separation would provide, and has to be compensated by a longer exposure [79].

Prospects

Next generation water- and ice-based Cherenkov detector such as KM3NeT-ORCA [78], and the IceCube upgrade PINGU [80], are designed to exploit this effect by measuring high-statistics energy-angle spectra of atmospheric neutrino events to probe the mass ordering. The projected sensitivity of both experiments are presented in Figure 1.13.

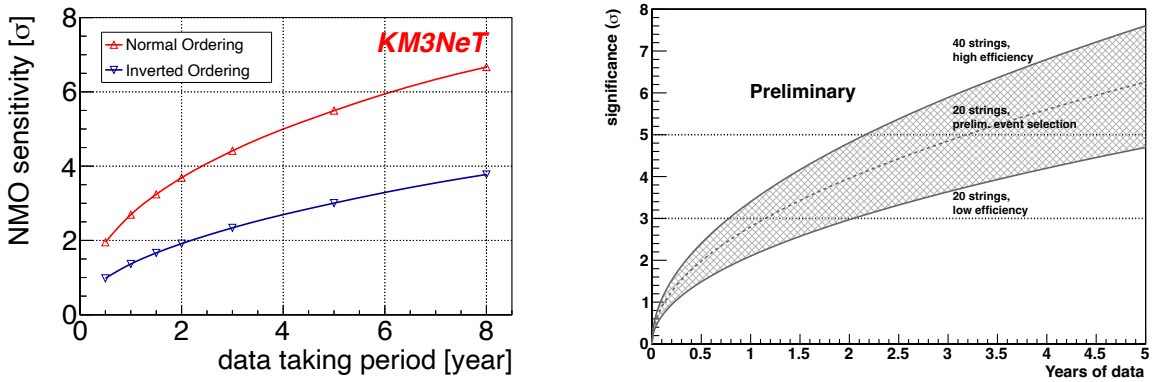

(a) (b)

FIGURE 1.13 – **(a)** KM3NeT/ORCA sensitivity to the mass ordering as a function of data taking time for both normal (red) and inverted (blue) ordering [78]. **(b)** IceCube/PINGU sensitivity to the normal mass ordering for different detector configuration and signal efficiency [80].

1.6.3 Medium-Baseline Experiments

Measurement Principle

An entirely different and complementary approach to determining the neutrino mass ordering relies on medium-baseline reactor antineutrino experiments [81, 82], which exploits the interference between the solar (Δm^2_{21}) and atmospheric (Δm^2_{31}, Δm^2_{32}) oscillation frequencies in the electron antineutrino survival probability P_{ee}, given in the vacuum approximation by :

$$
\begin{aligned}
P_{\overline{\nu}_e \to \overline{\nu}_e}(L/E) = 1 &- \cos^4(\theta_{13})\sin^2(2\theta_{12})\sin^2(\Delta_{21}) \\
&- \sin^2(2\theta_{13})\sin^2(|\Delta_{31}|) \\
&- \sin^2(\theta_{12})\sin^2(2\theta_{13})\sin^2(\Delta_{21})\cos(2|\Delta_{31}|) \\
&\pm \frac{\sin^2(\theta_{12})}{2}\sin^2(2\theta_{13})\sin(2\Delta_{21})\sin(2|\Delta_{31}|)
\end{aligned}
\tag{1.73}
$$

where the sign of the last term is fixed by the sign of the mass ordering Δm^2_{31}. A key feature of this method is that $P_{\overline{\nu}_e \to \overline{\nu}_e}$ is entirely free of the ordering–δ_{CP} degeneracy that complicates the long-baseline accelerator approach discussed in the previous section. However, the method presents a separate and significant experimental challenge : the mass ordering-sensitive term in Eq. 1.73 manifest as a fast oscillating spectral distortion driven by the small ratio $\Delta m^2_{21}/|\Delta m^2_{31}| \sim 3\%$, requiring an exceptionally fine energy resolution to resolve the relevant features of the spectrum.

Figure 1.14 shows the significance for mass ordering determination as a function of the baseline L, for energy resolutions ranging from 2 to $6\%/\sqrt{E_\nu}$. The results assume an experiment with 20 GW_{th} thermal power, a 5 kton target and 5 years of exposure. While an unambiguous result can be achieved with a 2% energy resolution, reaching such a value is extremely challenging on a technical standpoint. A satisfactory result can be achieve with a 3% energy resolution, corresponding to a determination of the mass ordering at $> 3\sigma$ significance, with an optimal baseline found at $L \sim 50$ km [83].

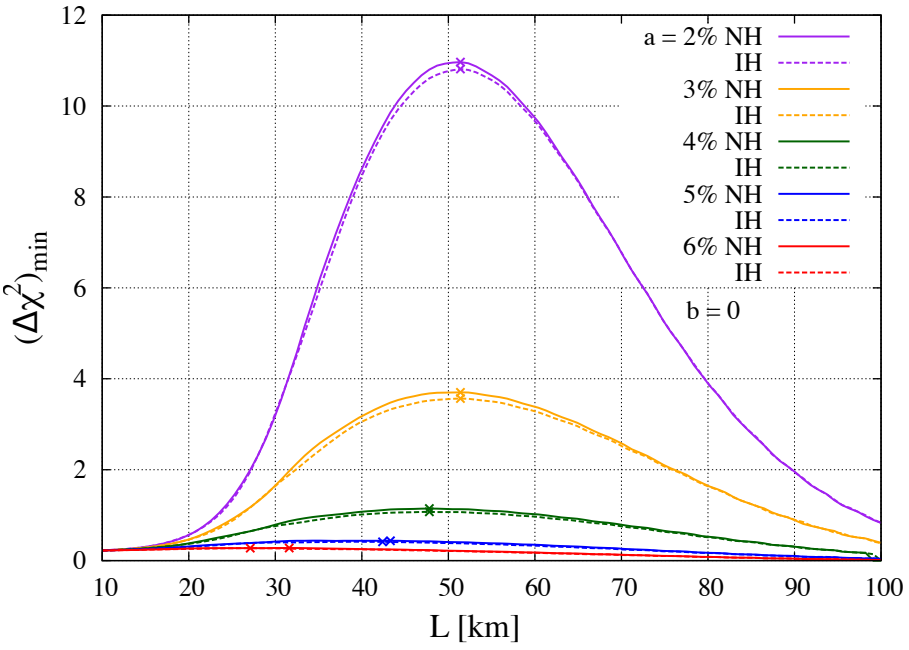

FIGURE 1.14 – Significance of the neutrino mass ordering determination as a function of the baseline L, for energy resolutions ranging from 2% to $6\%/\sqrt{E_\nu}$, assuming a 20 GW_{th} reactor thermal power, a 5 kton detector target mass, and 5 years of exposure [83].

This result is obtained by considering no systematic uncertainty on the energy resolution, which needs to be contained below the percent level in order to preserve a 3σ determination of the mass ordering for the experimental configuration considered. Notably, such an experiment has negligible sensitivity to MSW matter effects, since baselines in the order of $L \sim 50$ km are too short for any important matter potential to develop, allowing the measurement to rely mainly on vacuum oscillations.

Prospects

No past experiments has been built in order to probe the mass ordering through this method, due to the exceptionally demanding energy-resolution requirement, requiring an optimisation of every components of the detector. The JUNO experiment is the first experiment designed specifically to probe the mass ordering through this method. A similar medium-baseline approach was also proposed by the RENO-50 experiment [84], though this project has not been realised to date, leaving JUNO as the sole experiment currently pursuing this method. Located at a baseline of ∼53 km from a complex of nuclear reactors, JUNO aims to resolve the mass ordering by precisely measuring the fine spectral structure produced by the simultaneous solar and atmospheric oscillation frequencies in the survival probability. An independent measurement by JUNO could determine the mass ordering at 3σ significance after 6 years of data-taking, as illustrated in Figure 1.15

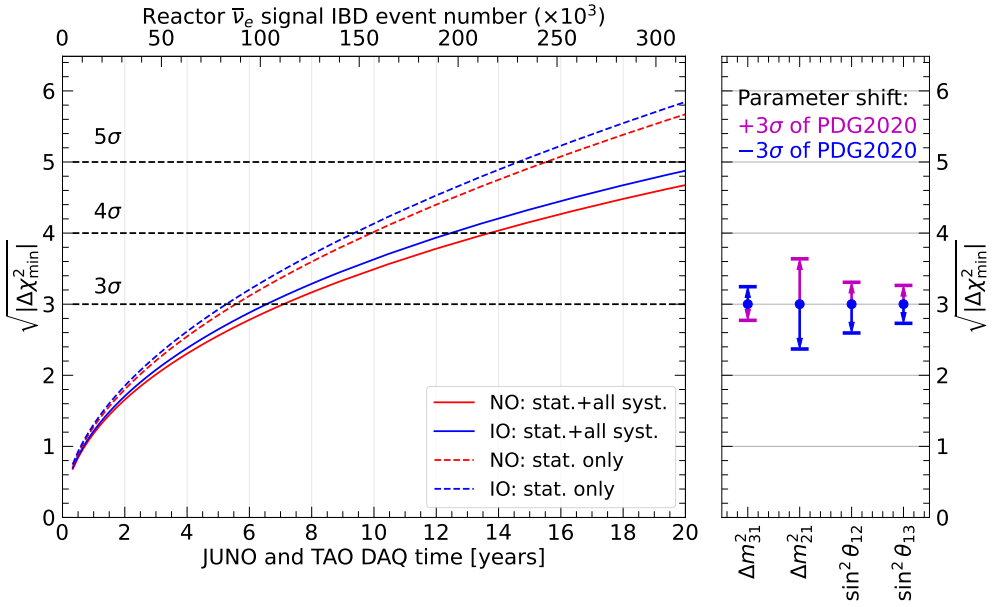

FIGURE 1.15 – (**Left**) NMO determination significance as a function of JUNO, and its satellite experiment TAO, data-taking time for both Normal Ordering (red) and Inverted Ordering (blue). (**Right**) Sensitivity dependence on the true value of the oscillation parameters evaluated by shifting the values by 3σ from the PDG2020 nominal values [85].

As shown in the right panel of Figure 1.15, JUNO's sensitivity to the mass ordering also

depends on the accurate knowledge of the other oscillation parameters. Improving their precision could therefore further constrain the significance of the mass ordering determination, and constitute one of JUNO's physics goals.

Finally, as discussed in Section 1.5.3, an independent determination of the mass ordering by JUNO would also have direct benefits for long-baseline accelerator experiments, by removing the ordering–δ_{CP} degeneracy from their analyses and thereby sharpening their sensitivity to δ_{CP}, particularly for relatively shorter-baseline configurations such as Hyper-Kamiokande.

1.6.4 Atmospheric Δm^2 Comparison

Measurement Principle

A distinct method, independent of matter effects, exploits the fact that the effective atmospheric mass-squared splitting, Δm^2, extracted from the ν_e ($\overline{\nu}_e$) and ν_μ ($\overline{\nu}_\mu$) disappearance channels is not exactly the same quantity, but a distinct mixing angle weighted combination of the two mass splittings Δm^2_{31} and Δm^2_{32}, due to the different roles played by θ_{12} and θ_{13} in each channel.

Specifically, it can be shown that medium-baseline reactor, such as Daya Bay and JUNO, which are sensitive to $\overline{\nu}_e$ disappearance, measure an effective mass-squared splitting Δm^2_{ee} [86] :

$$\Delta m^2_{ee} = \cos^2\theta_{12}\,\Delta m^2_{31} + \sin^2\theta_{12}\,\Delta m^2_{32} \tag{1.74}$$

while long-baseline ν_μ disappearance experiments such as T2K and NOνA measure an effective splitting $\Delta m^2_{\mu\mu}$ given by :

$$\Delta m^2_{\mu\mu} = \sin^2\theta_{12}\,\Delta m^2_{31} + \cos^2\theta_{12}\,\Delta m^2_{32} + \cos\delta\sin\theta_{13}\sin 2\theta_{12}\tan\theta_{23}\,\Delta m^2_{21} \tag{1.75}$$

with δ the CP-violating phase, and where the weighting roles of Δm^2_{31} and Δm^2_{32} are effectively exchanged relative to the ee channel. Since $\Delta m^2_{31} \neq \Delta m^2_{32}$ by exactly Δm^2_{21}, these two effective quantities differ by a small amount whose sign is fixed by the mass ordering :

$$|\Delta m^2_{ee}| - |\Delta m^2_{\mu\mu}| = \pm\Delta m^2_{21}\,(\cos 2\theta_{12} - \cos\delta\sin\theta_{13}\sin 2\theta_{12}\tan\theta_{23}) \tag{1.76}$$

where the + (-) sign, corresponding to $\Delta m^2_{ee} > \Delta m^2_{\mu\mu}$ ($\Delta m^2_{ee} < \Delta m^2_{\mu\mu}$), is for the normal (inverted) ordering.

The sensitivity of this method depends entirely on the achievable precision on $\Delta m^2_{\mu\mu}$ and Δm^2_{ee}, since the difference between the two is small ($\Delta m^2_{21}/\Delta m^2_{31} \sim 3\%$). This method therefore

requires both a precision long-baseline measurement of $\Delta m^2_{\mu\mu}$ and an independent, comparably precise measurement of Δm^2_{ee} from a medium-baseline reactor experiment.

Unlike the long-baseline appearance method described above, δ enters $\Delta m^2_{\mu\mu}$ as a fixed coefficient, without an accompanying mass ordering term to compensate for any shift in δ. The method is therefore free of CP-ordering degeneracy that affects the long-baseline appearance method. The CP-violation phase does, however, play a decisive role in the discriminating power of the method itself : the sensitivity is highest (lowest) for $\delta = \pi$ (0 or 2π) (see Eq. 1.77). Separately, matter effects are negligible for disappearance-based measurements : the shift they introduce remains below 0.3% for medium-baseline $\overline{\nu}_e$ disappearance experiments such as JUNO [87], and, for accelerator ν_μ disappearance experiment, it remains below 0.04% at baselines comparable to Hyper-Kamiokande's, rising to 0.3% for baselines comparable to DUNE's [88].

Prospects

The current best precision on the effective mass-splitting Δm^2_{ee} from medium-baseline reactor experiment is provided by the Daya Bay experiment, at 2.4%. Once JUNO begins data-taking, this precision is expected to reach 0.8% after a few months. For long-baseline experiments, the current precision on the effective mass-splitting $\Delta m^2_{\mu\mu}$ from T2K and NOνA is $\sim$ 2% individually, improving to $\sim$ 1.2% when combined. The observations from both types of experiments can be converted into a *mass ordering sum rule for the neutrino disappearance channels* [89] :

$$\left(\Delta m^2_{31}|^{\rm NO}_{\mu\, disp} - \Delta m^2_{31}|^{\rm NO}_{e\, disp}\right) + \left(|\Delta m^2_{32}|^{\rm IO}_{\mu\, disp} - |\Delta m^2_{32}|^{\rm IO}_{e\, disp}\right) = (3.1 - 0.9\,\widehat{\cos\delta})\%\,|\Delta m^2| \quad (1.77)$$

where $\widehat{\cos\delta}$ is the average $\cos\delta$ across the NO and IO fits. This expression provides a direct way of probing the mass ordering once JUNO releases its measurements : if the true ordering is normal (NO), the first term vanishes, while it is the second term that will be zero if the true ordering is inverted (IO). Consequently, if Nature has chosen NO, the χ^2 profiles of Δm^2_{32} measured by the two types of experiments, assuming IO, will be misaligned with a degree given by $(3.1 - 0.9\,\widehat{\cos\delta})\%\,|\Delta m^2|$.

The combination is performed by adding the χ^2 profile of (Δm^2_{31}, Δm^2_{32}) obtained from the existing long-baseline T2K/NOνA measurements to the χ^2 profiles obtained from JUNO, for each assumed mass ordering hypothesis. The resulting $\Delta\chi^2_{\rm min} \equiv \chi^2_{\rm IO}|_{\rm min} - \chi^2_{\rm NO}|_{\rm min}$ then quantifies the significance with which the two orderings can be distinguished. This is illustrated in Figure 1.16, which shows $\Delta\chi^2_{\rm min}$ as a function of JUNO's measured central value of Δm^2_{31}

under NO assumption, and of the precision achieved on that measurement. The current best-fit values from Daya Bay alone (DB) and from the combination Daya Bay and RENO are marked, corresponding to a precision of $\sim$ 2.4% and $\sim$ 2.0% respectively, falling in the blue (normal-ordering-preferred) region with $\Delta\chi^2_{\text{min}} \sim$ 1–4. As JUNO's precision improves from this level towards 0.8%, after approximately 100 days of data-taking, the combined significance grows rapidly, potentially reaching the 3σ level ($\Delta\chi^2_{\text{min}} \sim 9$) depending on the best fit value of $\Delta m^2_{31}|^{NO}$.

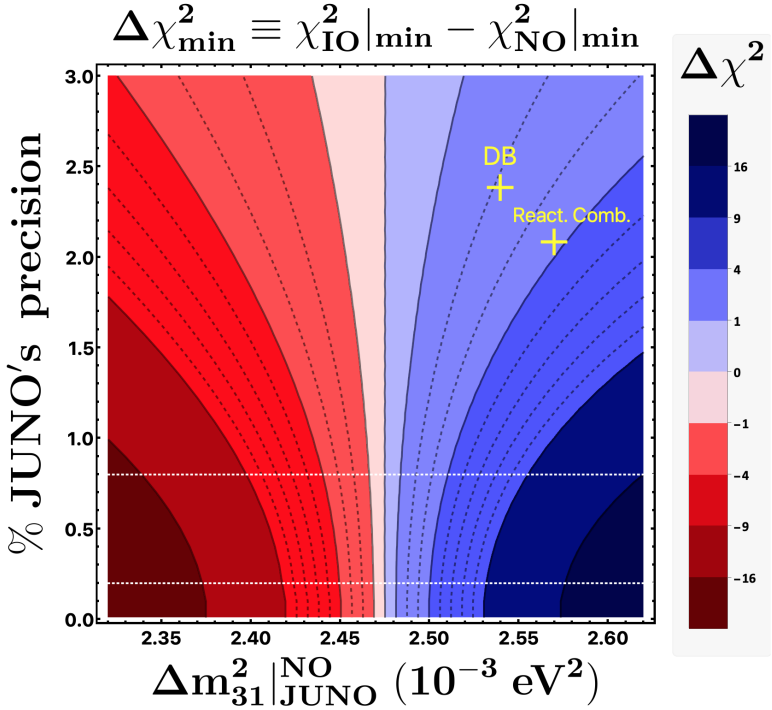

FIGURE 1.16 – Combined mass-ordering significance $\Delta\chi^2_{\text{min}} \equiv \chi^2_{\text{IO}}|_{\text{min}} - \chi^2_{\text{NO}}|_{\text{min}}$ as a function of JUNO's measured central value of $\Delta m^2_{31}|_{\text{NO}}$ (in units of 10^{-3} eV^2, horizontal axis) and the achieved precision on this measurement (vertical axis, in %), combining JUNO's reactor Δm^2_{ee} measurement with the current long-baseline $\Delta m^2_{\mu\mu}$ measurements from T2K and NOνA. Blue (red) regions indicate a preference for normal (inverted) ordering, with the colour scale showing the value of $\Delta\chi^2_{\text{min}}$. The horizontal dashed lines indicate the JUNO target precision after ~100 days (0.8%) and 6 years (0.2%) of operation. The yellow crosses mark the current best-fit values from Daya Bay (DB) and the combination of Daya Bay and RENO (React. Comb.) [89].

1.7 Conclusion

This chapter has established the theoretical framework of neutrino oscillations and reviewed the main areas of current research in neutrino physics, most of which are currently limited by the lack of knowledge on the neutrino mass ordering. The available strategies to determine the neutrino mass ordering were then presented : long-baseline accelerator experiments exploiting the MSW matter effect, atmospheric neutrino experiments using the same resonance mecha-

nism over a wide range of baselines, and medium-baseline reactor experiments exploiting a purely vacuum-oscillation interference effect, free of the matter-induced degeneracy with the CP-violating phase that affects the other two approaches. Among reactor experiments, JUNO is the leading experiment currently pursuing this method, and the remainder of this thesis is dedicated to its detector, simulation, and early physics performance. The following chapter introduces the JUNO experiment, detailing how the experiment was designed to probe the neutrino mass ordering.

Chapitre 2

The JUNO Experiment

Summary

2.1 Introduction . . . 67
2.2 Neutrino Mass Ordering Measurement . . . 68
2.2.1 Neutrino Survival Probability . . . 68
2.2.2 Reactor Neutrino Flux . . . 68
2.2.3 Detection Channel . . . 69
2.2.4 Neutrino Signal at JUNO . . . 70
2.2.5 Backgrounds . . . 72
2.3 The JUNO Detector . . . 74
2.3.1 Overview . . . 74
2.3.2 The Central Detector . . . 75
2.3.3 Liquid Scintillator . . . 77
2.3.4 Veto System . . . 79
2.3.5 Large PMT system . . . 82
2.3.6 Small PMT System . . . 85
2.4 Calibration . . . 87
2.4.1 Detector Response . . . 87
2.4.2 Calibration System Design . . . 88
2.4.3 Radioactive Sources . . . 89
2.5 JUNO-TAO . . . 92
2.6 Conclusion . . . 94

2.1 Introduction

Having reviewed the theoretical motivation for determining the neutrino mass ordering and the experimental strategies available to do so, this chapter turns to the specific experiment designed to pursue the medium-baseline reactor approach introduced in Section 1.6. The Jiangmen Underground Neutrino Observatory (JUNO) is a large-scale reactor neutrino experiment designed in 2014 with the primary goal of determining the Neutrino Mass Ordering (NMO) [90, 91, 92, 83]. The detector is composed of 20 kilotons of liquid scintillator and a massive array of photo multiplier tubes that is expected to reach an ambitious 3% energy resolution at 1 MeV. JUNO is expected to determine the NMO with a 3σ significance after 6 years of data taking while also reaching sub-percent precision on $\sin^2(\theta_{12})$, Δm^2_{12} and Δm^2_{31} [93].

Additionally, JUNO's energy resolution and large target mass makes it sensitive to many neutrino sources such as geoneutrinos [94], solar neutrinos [95, 96, 97], atmospheric neutrinos [98] and neutrinos from core-collapse supernovae [99]. In addition, the experiment provides opportunities to search for physics beyond the Standard Model [100, 101]. This broad physics program positions JUNO as one of the most highly anticipated neutrino experiment of the coming years.

The civil construction of the JUNO detector began on 19 December 2021 and was completed three years later, on 17 December 2024. The collaboration then promptly proceeded with the filling of ultra-pure water into the detector, which took place from 18 December 2024 to 2 February 2025. The water was then replaced with liquid scintillator, with the filling completed on 25 August 2025, with extensive calibration campaigns conducted to properly assess the detector performance. The commissioning phase was carried out during both the water and liquid scintillator stages. Finally, 26 August 2025 marked the beginning of JUNO's physics data taking, with the collaboration's first physics paper published on 18 November 2025.

This chapter aims to provide a global and concise overview of the JUNO experiment while presenting some of the latest low level performance of the detector. Section 2.2 introduces how JUNO uses reactor electron antineutrinos to probe the neutrino mass ordering, while the detector description is presented in Section 2.3. Particular emphasis is placed on the liquid scintillator and photomultiplier tube system, as they have been extensively optimized and tested to reach the target energy resolution and achieve the best possible energy reconstruction. Then, the overall calibration strategy is detailed in Section 2.4, including a brief discussion of the main systematic effects affecting the detector response, which motivates the design of the calibration system and the choice of calibration sources. Finally, a brief description of JUNO's satellite experiment, TAO, is carried out in Section 2.5, whose main purpose is to provide a reference reactor antineutrino spectrum to JUNO with an unprecedented energy resolution.

2.2 Neutrino Mass Ordering Measurement

2.2.1 Neutrino Survival Probability

The heart of mass ordering determination lies in the three neutrinos survival probability. As opposed to long baseline neutrino experiment, reactor neutrino experiment can probe neutrino mass ordering in the vacuum oscillation approximation, considering relatively low baseline (up to hundreds of kilometers) where the matter effects are small. In this approximation, the electron anti-neutrino survival probability is given by :

$$\begin{aligned} P_{ee}(L/E) = 1 &- \cos^4(\theta_{13})\sin^2(2\theta_{12})\sin^2(\Delta_{21}) \\ &- \sin^2(2\theta_{13})\sin^2(|\Delta_{31}|) \\ &- \sin^2(\theta_{12})\sin^2(2\theta_{13})\sin^2(\Delta_{21})\cos(2|\Delta_{31}|) \\ &\pm \frac{\sin^2(\theta_{12})}{2}\sin^2(2\theta_{13})\sin(2\Delta_{21})\sin(2|\Delta_{31}|) \end{aligned} \tag{2.1}$$

where $\Delta_{ij} = \Delta m^2_{ij} L/4E$, Δm^2_{ij} is the neutrino mass-squared difference $(m_i^2 - m_j^2)$ in eV^2, θ_{ij} is the neutrino mixing angle, L is the baseline in meters and E is the $\overline{\nu}_e$ energy in MeV. The sensitivity on the mass ordering is given by the last term of Eq. 2.1, which takes plus or minus sign if the ordering is respectively normal or inverted. Interestingly, this probability is independent of our knowledge of the CP violating phase δ_{CP} as well as the atmospheric mixing angle θ_{23}. As a result, the measurement of medium baseline reactor neutrino experiment doesn't suffer from parameter degeneracies that affect long baseline experiment such as Hyper-Kamiokande, which measure NMO via the disappearance channel and must simultaneously determine δ_{CP}, θ_{23} and the mass ordering.

2.2.2 Reactor Neutrino Flux

Nuclear reactors produce electricity using the thermal power released by the sustained nuclear chain reaction, and are also electron anti-neutrino sources : every nuclear fission release ~200 MeV, with on average 6 $\overline{\nu}_e$ emitted from β decays of the fission fragments, and for 1 gigawatt (GW) of reactor thermal power, 2×10^{20} $\overline{\nu}_e$ are emitted isotropically. ^{235}U and ^{238}U, together with ^{239}Pu and ^{241}Pu are the four main isotopes used in reactors, and generate more than 99.7% of the reactor $\overline{\nu}_e$. The flux of electron anti-neutrinos coming from a reactor can be estimated using :

$$\phi(E) = \frac{W_{th}}{\sum_i f_i e_i} \cdot \sum f_i \cdot S_i(E) \tag{2.2}$$

where W_{th} is the reactor thermal power, f_i, e_i and $S_i(E)$ are respectively the fission fraction, the thermal energy released per fission, and the neutrino flux per fission of the i_{th} isotope. The

flux parameters values for each isotopes are listed in table 2.1. The accurate knowledge of the reactor neutrino flux is important for oscillation measurements. While Eq. 2.2 gives a good approximation of reactor neutrino flux, recent reactor experiment showed discrepancies between predicted and measured reactor flux in the 4-6 MeV region [102, 103]. Model independent prediction could avoid this bias and help improve the precision to 1%.

Isotopes	$\mathbf{e}_i$ **[MeV]**	$\mathbf{f}_i$	$\mathbf{S}_i$
^{235}U	201.7	0.58	$\exp(0.870 - 0.160E_\nu - 0.091E_\nu^2)$
^{238}U	205.0	0.07	$\exp(0.976 - 0.162E_\nu - 0.0790E_\nu^2)$
^{214}Pu	214.2	0.05	$\exp(0.793 - 0.080E_\nu - 0.1085E_\nu^2)$
^{239}Pu	210	0.30	$\exp(0.896 - 0.239E_\nu - 0.0981E_\nu^2)$

TABLE 2.1 – Reactor flux parameters values [83].

2.2.3 Detection Channel

Inverse Beta Decay

Similarly to past reactor neutrino experiment, such as KamLAND [104], Daya Bay [105] and Double Chooz [106], JUNO is detecting reactor electron anti-neutrino through the Inverse Beta Decay (IBD) process, first exploited in the Reines and Cowan experiment in 1956, which describes the interaction of an electron anti-neutrino with a proton to produce a positron and a neutron :

$$\overline{\nu}_e + p \rightarrow n + e^+ \tag{2.3}$$

The identification of an IBD interaction is based on the space and time correlation of a prompt and delay signal. The prompt signal is induced by the positron ionisation in the detector, such as liquid scintillator, followed by its annihilation with an electron, giving rise to two back-to-back 511 keV γ. The delay signal is given by the neutron capture : following its production, the neutron will thermalise quickly in the detector until it is captured on a nucleus. In the absence of neutron-absorbing elements, the neutron is captured on hydrogen, where the hydrogen de-excitation emits a single γ ray of 2.223 MeV. The IBD interaction steps are illustrated in Figure 2.1.

Energy Threshold

In order for the IBD interaction to occur in the detector, the neutrino must have an energy than exceeds the energy threshold required to produce a positron and compensate for the neutron and proton mass difference. The latter condition can be translated to :

$$\mathrm{s} \geq (\mathrm{m}_n + \mathrm{m}_e)^2 \tag{2.4}$$

where s is the energy squared in the center of mass frame defined as :

$$\begin{aligned} \mathrm{s} &= (E_{\overline{\nu}_e} + E_p)^2 + (p_{\overline{\nu}_e} + p_p)^2 \\ &= m_p^2 + 2m_p E_{\overline{\nu}_e} \end{aligned} \tag{2.5}$$

if we consider the proton at rest in the center of mass and the neutrino mass negligible compared to the masses of the other particles. Moreover, this is true for hydrocarbon or water targets where hydrogen can be consider as a free proton. For heavier nuclei the threshold energy must be higher and include molecular binding energy and momentum. Finally, applying condition 2.4 to Eq. 2.5 gives :

$$E_{\overline{\nu}_e} \geq \frac{(m_e + m_n)^2 - m_p^2}{2m_p} \approx 1.806 \text{ MeV} \tag{2.6}$$

Thus, the incoming neutrino must have an energy greater than 1.806 MeV for the IBD process to occur on hydrogen nuclei.

Cross Section

The IBD process attractiveness comes from the convenient correlation between the prompt positron signal followed by a delayed and spatially correlated neutron capture, but also due to its relatively large cross section given by [107] :

$$\sigma_{tot}^{(0)} = 0.0952 \left(\frac{E_e^{(0)} p_e^{(0)}}{1\text{MeV}^2} \right) \times 10^{-42} \text{cm}^2. \tag{2.7}$$

The energy dependence of the reactor $\overline{\nu}_e$ flux, IBD cross section, and the resulting measured spectrum is shown in Figure 2.1. The different components of the reactor flux is detailed, where the major contribution comes from ^{235}U. The IBD measured spectrum is obtained by convoluting the reactor $\overline{\nu}_e$ flux with the IBD cross section given by Eq. 2.7.

2.2.4 Neutrino Signal at JUNO

Experimental Site

JUNO was built in an underground cavern with about 650 m overburden (corresponding to 1800 m.w.e) close to Jinji town, 43 km south-west from Kaiping city, in the prefecture city of Jiangmen, Guangdong province, China. The detector location was meticulously optimized to have the best sensitivity for the NMO determination [92, 83]. As shown in Figure 2.2, JUNO is placed at roughly 53 km and equidistant from the Yangjiang and Taishan nuclear power plants (NPP).

The Yangjiang NPP has 6 cores of 2.9 GW_{th} where the Taishan NPP has 2 cores of 4.6 GW_{th} for a total thermal power of 26.6 GW_{th}. Aside from those two sites, JUNO is also sensitive from

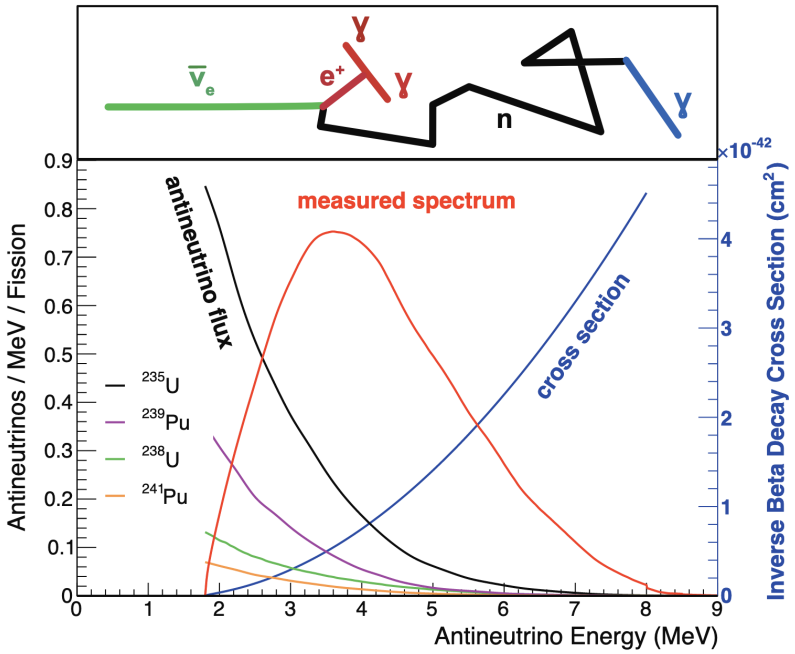

FIGURE 2.1 – (Top Pad) Steps involved in the IBD interaction. (Bottom Pad) Measured neutrino spectrum obtained from the product of the reactor $\overline{\nu}_e$ flux and the IBD cross section [108]. The contribution of each radioactive isotopes to the reactor antineutrino spectrum is shown.



FIGURE 2.2 – JUNO Location.

neutrinos coming from the Daya Bay nuclear complex, located 215 km away from JUNO site, including the Daya Bay NPP, the Ling Ao NPP and the Ling Ao-II NPP for a total thermal power of 17.4 GW_{th}. They will contribute to 6.4% of the reactor neutrinos events in JUNO considering oscillations. Additionnaly, the Huizhou NPP located 265 km from JUNO site, is supposed to finish construction in 2025 and should add 6 more cores of 2.9 GW_{th} thermal power each. The total thermal power and baseline of each nuclear power plants and cores are listed in Tab. 2.2.

Cores	YJ-1	YJ-2	YJ-3	YJ-4	YJ-5	YJ-6	TS-1	TS-2	DYB	HZ
Power (GW)	2.9	2.9	2.9	2.9	2.9	2.9	4.6	4.6	17.4	17.4
Baseline (km)	52.74	52.82	52.41	52.49	52.11	52.19	52.77	52.64	215	265

TABLE 2.2 – Summary table of reactor cores thermal power and baseline to JUNO experimental site.

IBD Signal

Given JUNO's baseline to the NPPs, the IBD spectrum shown in Figure 2.1 must also account for the $\overline{\nu}_e$ survival probability given by Eq. 2.1. The expected IBD spectrum at the JUNO site is illustrated in Figure 2.3, where the unoscillated spectrum is shown alongside the oscillated spectra under the normal (blue curve) and inverted (red curve) neutrino mass ordering hypotheses. The contributions from the different neutrino oscillation parameters are also indicated. This spectrum is obtained assuming 2000 days of data taking and an energy resolution of 3% at 1 MeV.

At JUNO's baseline, the feasibility of determining the neutrino mass ordering relies critically on the detector's energy resolution. Any degradation from the target 3% results in a smearing of the oscillation patterns driven by Δm^2_{32}, as shown in Figure 2.3, thereby reducing the experiment's ability to distinguish between the normal and inverted hierarchies.

2.2.5 Backgrounds

While the space and time correlations of the prompt and delay IBD signals reduce backgrounds significantly, the measured IBD signal is not background free. The IBD signature can be mimic by a given set of physics events in the detector and their contribution to the IBD spectrum must be well understood.

Accidentals

Accidental backgrounds are defined as random coincidences inside the detector and exist mainly in three types : (radioactivity, radioactivity), (radioactivity, cosmogenic isotope), (ra-

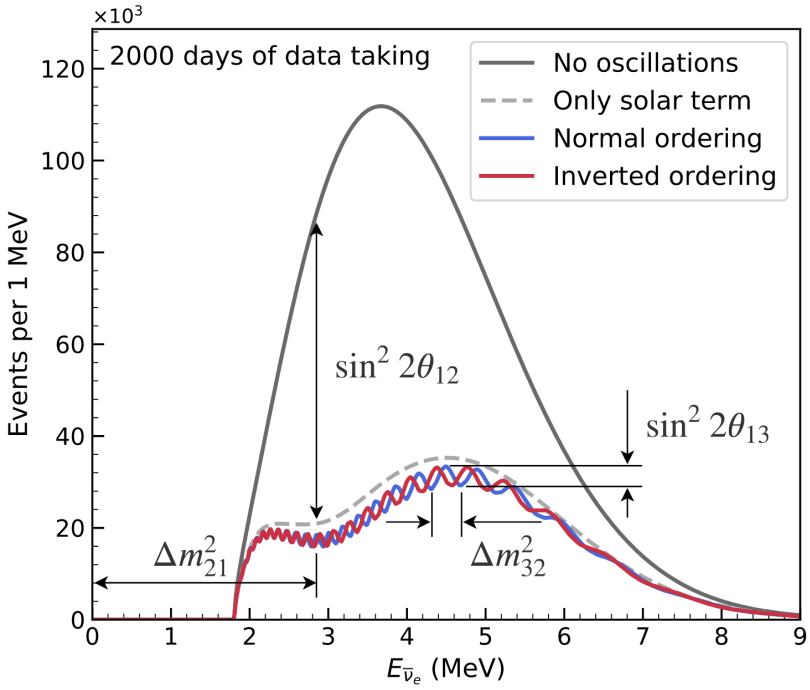

FIGURE 2.3 – The reactor anti-neutrino energy spectrum with and without oscillation for normal (blue curve) and inverted (red curve) ordering assuming 2000 days of data taking. The contribution of the four oscillation parameters involved in Eq. 2.1 is shown [109].

dioactivity, spallation neutrons). Radioactivity events are mostly located at the boundary of the detector, and produced by the photomultipliers glass, and the detector materials. This background can effectively be suppressed by applying a fiducial volume cut.

Cosmogenic ^{9}Li and ^{8}He

^{9}Li and ^{8}He are cosmogenic isotopes produced by muon spallation on ^{12}C. These isotopes decay by (β-n) process which perfectly mimics the IBD signal and are one of the most important source of background for JUNO. The ^{9}Li/^{8}He background reduction strategy uses space and time correlation to the parent muon to effectively reduce the ^{9}Li/^{8}He contamination in the IBD sample.

Fast Neutrons

Fast neutron backgrounds are neutrons produced by muon spallation in the rock surrounding the detector. The neutrons will scatter on protons before being captured in the LS. The parent muons are almost impossible to tag, however, a fraction of muons clipping the top of the detector could be identified by JUNO muon tracker, allowing tagging of fast neutrons.

Radiogenic $^{13}C(\alpha, n)^{16}O$ Backgrounds

$^{13}C(\alpha, n)^{16}O$ backgrounds are produced by α particles from the U, Th radioactivities. The alpha is captured by ^{13}C to produce ^{16}O and a neutron, which could lead to correlated background if the neutron is fast enough or from the de-excitation gamma of $^{16}O^{*}$.

Geo-neutrinos

Geo-neutrinos are low energy (< 3 MeV) electron anti-neutrinos that are produced in the radioactive decays of Uranium and Thorium inside the Earth. They interact in the detector through IBD and are indistinguishable from reactor $\overline{\nu}_e$ on an event-by-event basis. However, JUNO can effectively measure the rate of geo-neutrinos, which are of key importance to evaluate the Earth radiogenic heating from Uranium and Thorium. Such measurement from JUNO will provide world leading results, where the main source of backgrounds are reactor neutrinos.

2.3 The JUNO Detector

2.3.1 Overview

The JUNO detector is the assembly of a Central Detector (CD), a water Cerenkov detector, in which the CD is submerged, and covered by an array of plastic scintillator. A schematic view of JUNO is shown in Figure 2.4. The CD is a 20 kton liquid scintillator (LS) detector designed to reach an energy resolution $\sigma/E = 3\%/\sqrt{E(MeV)}$. The LS is contained in a spherical acrylic vessel of 35.4 inner diameter, supported by a stainless steel (SS) structure via 590 connecting bars. The light emitted by interactions in the LS are collected by two photomultiplier tube (PMT) systems : 17,596 20-inch PMTs (referred to as *large PMT* or *LPMT*) and 25,587 3-inch PMTs (referred to as *small-PMT* or *SPMT*) installed on the inner surface of the SS structure giving a total photocathode coverage of ~78% (75.2% for the LPMT and 2.7% for the SPMT). The entire CD is submerged in a cylindrical Water Pool (WP) of 43.5 m diameter and 44 m height, providing sufficient shielding in all direction to protect the LS from radioactivity coming from the surrounding rock. The WP is instrumented with a separated PMT system placed on the outer surface of the SS structure that act as a water Cerenkov detector for cosmic muons. Additionally, four rings of PMT have been added to the top of the WP to increase Cerenkov light collection. The entire SS structure is surrounded by compensation coils, mounted to minimize the impact of Earth's magnetic field on the PMT photo-electron collection efficiency. On top of the WP, an array of plastic scintillator strips from the Target Tracker of the OPERA experiment [110] is used as the JUNO Top Tracker (TT) [111] to accurately tag muons crossing the detector. The TT covers about 60% of the WP top surface area.

The unprecedented scale of the experiment gives rise to very challenging mechanical requirements. Moreover, the target energy resolution requires good control of the LS radiopurity and optical properties as well as enhanced PMT characteristics.

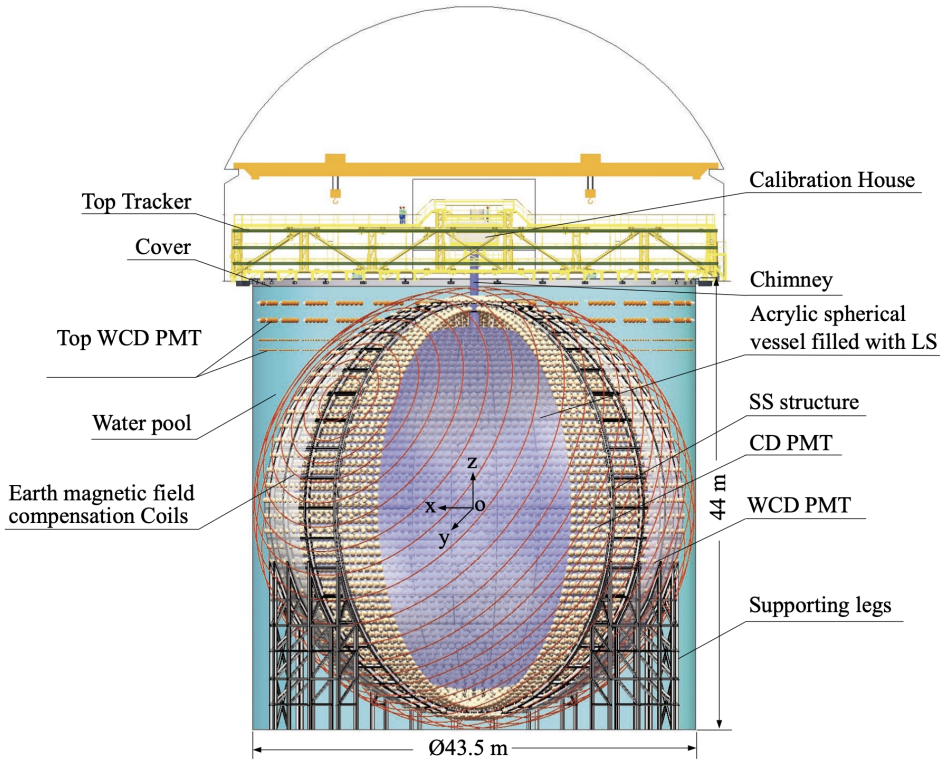

FIGURE 2.4 – Schematic view of the JUNO detector.

2.3.2 The Central Detector

The CD is the most mechanically challenging part of JUNO because of its huge size and heavy instrumentation, which have to be operational for the whole 30 years lifetime of the experiment.

Acrylic Vessel

The heart of the CD is the Acrylic Vessel, a sphere of 35.4 m inner diameter, 120 mm thickness, weighting 600 ton and designed to host JUNO's liquid scintillator. A schematic representation of the acrylic sphere is shown in Figure 2.5a. The Vessel is made of 265 pieces of acrylic panels, which are coming out of a dedicated production line established for JUNO. Because the acrylic is in direct contact with the LS, it is of upmost importance that it is radiopure and has enhanced optical properties to allow the scintillation light to reach the PMTs. The acrylic recipe was tuned to increase the transparency, with each acrylic panel having a transparency $> 96\%$ in water. Moreover, each panel has been treated carefully to

reduce radioactivity background contamination, reaching a radiopurity < 0.5 ppt in uranium and thorium. To optimize the construction time, acrylic panels were bonded and assembled in layers, and the entire acrylic sphere is attached to the main structure using connecting bars that are plugged on each panel. Figure 2.5b shows how the first layer of the acrylic sphere was installed and connected to the main structure.

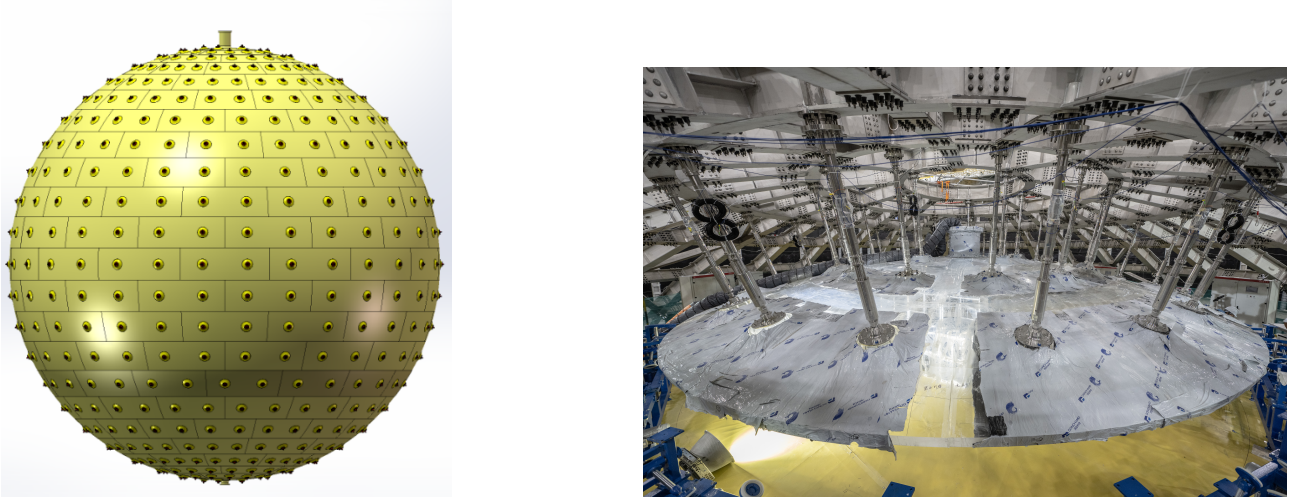

(a) (b)

FIGURE 2.5 – **(a)** 3D Schematic view of JUNO acrylic vessel. **(b)** Installation of the first layer of acrylic panels. Each panel is connected to the SS structure by the means of connecting bars.

Moreover, to facilitate the filling of the CD as well as the deployment of calibration sources, the acrylic sphere has two openings at each pole, commonly referred to as the CD chimneys.

Main Structure

The main structure refers to the stainless steel (SS) shell structure that supports the acrylic sphere and the supporting legs as shown in Figure 2.4. In total, 590 connecting bars have been used to connect the Acrylic Vessel to the SS structure, each connecting bars have been carefully places to reduce stress and maintain the overall structure stability. The SS structure itself is supported by 30 supporting legs made out of SS truss structures. In addition to the acrylic sphere, the SS structure also host the CD PMT systems and their electronics on its inner surface as well as the WP PMT system on its outer surface. Finally, the gap between the acrylic sphere and the SS structure is filled with ultra pure water, providing shielding against radioactivity coming from the PMT glass.

2.3.3 Liquid Scintillator

Recipe

The 20 kton of LS filled in the CD act as the active target of JUNO. Its recipe is similar to the one used in the Daya Bay experiment [112], and is made of three components in different concentration : Linear alkylbenzene (LAB) as the solvent, due to it excellent transparency and good light yield, doped with 2.5 g/L of 2,5-diphenyloaxazole (PPO) as primary fluor, and 3 mg/L of 1,4-bis(2-methylstyryl)benzene (bis-MSB) as wavelength shifter. To prevent optical degradation and ensure excellent transparency throughout the experiment lifetime, it was decided to also mix 42.7 mg/L of butylated hydroxytoluene (BHT) as anti-oxidant in the original recipe.
To meet JUNO's requirements for the NMO determination, the LS photoelectron (PE) yield is expected to reach 1665 PE/MeV [85]. Moreover, the target LS radio-purity for reactor neutrino studies is set to be $< 1 \times 10^{-15}$ g/g in uranium (U) and thorium (Th) [85] and is expected to reach 1×10^{-17} g/g after a dedicated purification route illustrated in Figure 2.6.

Purification System

The LAB supplied by specialized companies have relatively low contamination levels of U and Th. However, a complete purification system has been designed to further enhance the LS optical and radio-purity properties :

— The raw LAB is first purified in alumina (Al_2O_3) columns to improve its transparency and attenuation length. The design of the alumina columns is based on pilot plant experiment and showed that the LAB optical properties enhancement can be done without apparent increase in radioactivity background contamination [113].

— The purified LAB is then transferred to a distillation tower that operates in partial vacuum and high temperature [114] to remove the heaviest radio-impurities (^{238}U, ^{232}Th and ^{40}K) from the LAB and further improve its absorbance and attenuation length.

— Following these two first stages of the purification, the LAB is mixed with PPO, bis-MSB and BHT in the concentration specified earlier to produce the LS master solution batch by batch. Additionally, the master solution undergoes water washing to purify PPO and bis-MSB from U and Th contamination. Using distilled LAB, the master solution is diluted to give JUNO's LS recipe and is sent to the underground laboratory.

— In the underground laboratory, the LS first go through the water extraction system [115] to remove U/Th backgrounds contaminants introduced by PPO and bis-MSB.

— Finally, a gas stripping plant [114] using high purity nitrogen [116], effectively removes radioactive gases (^{222}Rn, ^{85}Kr, and ^{39}Ar) from the LS.

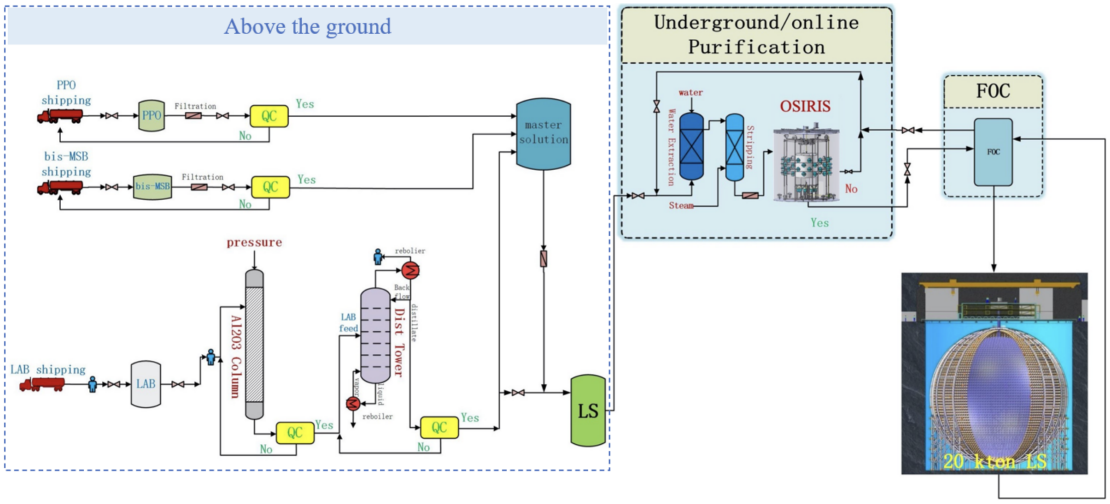

FIGURE 2.6 – Flowchart of the liquid scintillator processing steps, from shipping to filling in the central detector.

OSIRIS

At the end of the LS purity control route stands the Online Scintillator Internal Radioactivity Investigation System (OSIRIS). OSIRIS is a stand-alone detector that consists of a cylindrical Acrylic Vessel with a height and diameter of 3 m that can host 20 ton of LS, and is surrounded by 80 LPMTs. The whole system is submerged in a 9-by-9-meter cylindrical water tank. Figure 2.7 shows an inner view of OSIRIS. The detector was designed to confirm the proper operation of the purification plants and monitor the levels of radon, ^{238}U, ^{232}Th, ^{210}Po and ^{14}C so it does not exceed the given limits for reactor or solar neutrino studies [117]. The monitoring strategy relies on the fast BiPo coincidences signatures from the uranium and thorium decay chains : ^{214}Bi-^{214}Po ($\tau \sim 164$ μs) and ^{212}Bi-^{212}Po ($\tau \sim 300$ ns). Assuming secular equilibrium, the Bi-Po β–α coincidences provide a powerful and direct tool to estimate the ^{238}U and ^{232}Th concentrations inside the LS. OSIRIS effectively measured sensitivities better than 10^{-15} g/g for ^{238}U and 10^{-16} g/g for ^{232}Th.

The Filling, Overflow and Circulation System

Before being introduced into the CD, the LS passes through the Filling, Overflow, and Circulation (FOC) system. The FOC consists of a storage tank, two overflow tanks of 50 m^3 each, an ultrapure nitrogen flushing system, as well as multiple auxiliary tanks, pipelines, circulation pumps, and monitoring sensors used to manage both purified water and LS within the detector. The system is primarily designed to fill the CD with LS during JUNO's second filling phase, or with high-purity water during the first filling phase. In addition, the FOC enables the circulation of LS from the detector through the underground purification system when re-purification is required, and it ensures precise control and stabilization of the LS level

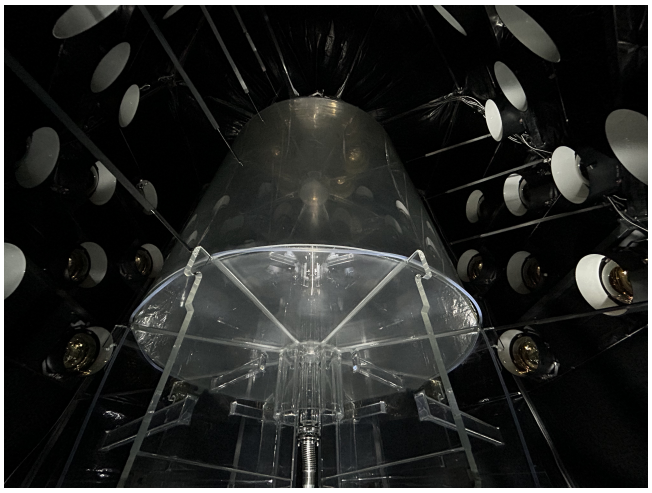

FIGURE 2.7 – Inner view of the OSIRIS detector.

within the CD.

Liquid Scintillator Performance

As discussed throughout this section, the optical properties and radiopurity of the liquid scintillator are critical to achieving JUNO's target energy resolution of 3% at 1 MeV. Among the key optical requirements, particular attention is paid to the LS transparency, which must meet an attenuation length of at least 20 m at 430 nm, corresponding to an average absorption length of 77 m at the same wavelength [118]. Although approximately 500 m^3 of low-quality LS were introduced during the early stages of filling, the optical quality of the scintillator has since recovered, with the average attenuation length reaching 20.6 m at 430 nm [119] as illustrated by Figure 2.8.

The radiopurity of the LS inside the CD was assessed using the same BiPo fast coincidence technique employed by OSIRIS, exploiting ^{214}Bi–^{214}Po and ^{212}Bi–^{212}Po coincidences from the ^{238}U and ^{232}Th decay chains respectively. The current performance of the energy and vertex reconstruction [119] motivates the adoption of a reduced fiducial volume of $R < 16.5$ m, slightly smaller than the nominal value of $R < 17.2$ m assumed in Ref. [109]. Within this volume, the uranium and thorium concentrations were measured at $(7.5 \pm 0.9) \times 10^{-17}$ g/g for ^{238}U and $(8.2 \pm 0.7) \times 10^{-17}$ g/g for ^{232}Th. These values are approximately one order of magnitude below the requirements for the neutrino mass ordering determination, and are also within the range required for solar neutrino measurements [95], representing a strong validation of the purification campaign.

2.3.4 Veto System

The CD is complemented by two veto systems that help effectively reduce and estimate the rate of environmental radioactivity and cosmic muon-related backgrounds.

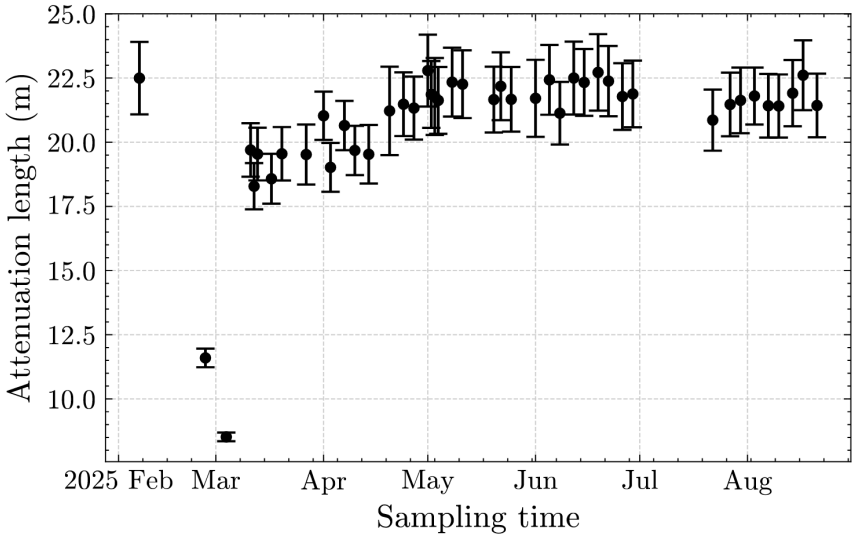

FIGURE 2.8 – Evolution of the liquid scintillator attenuation length, measured at a wavelength of 430 nm throughout the 6 months of filling. The average attenuation length over all LS batches reaches 20.6 m [119].

Water Cerenkov Detector

As illustrated in Figure 2.4, the CD is entirely immersed in a cylindrical Water Pool (WP) with a height of 44 m and a diameter of 43.5 m, filled with 35 kton of ultra-pure water. The water provides effective shielding against neutrons and gamma radiation, and a minimum shield thickness of 2.5 m has been found to optimally reduce radioactive backgrounds originating from the surrounding rock [120]. However, the water itself can introduce radioactive backgrounds into the detector through the decay of radon daughter nuclei in the ^{238}U and ^{232}Th chain. The radon concentration in tap water is estimated to be $\sim$10 Bq/m^3 and must be reduced to below 0.2 Bq/m^3 to meet JUNO's reactor neutrino study requirements. To achieve this, a dedicated degassing plant was designed, and tests have demonstrated the possibility of reaching sub-mBq/m^3 levels after multiple cycles [121]. Additionally, a 5 mm thick HDPE film covers the pool walls to prevent radon ingress from the surrounding rock into the water. To ensure the detector's mechanical stability, the water surrounding the Acrylic Vessel is maintained at 21°C by a circulation system that effectively mitigates heat generated by the electronic underwater boxes.

The water pool design is inspired by the Daya Bay experiment, which demonstrated the successful use of a water Cherenkov detector as a muon veto system [122]. In JUNO, the WP functions as a Cherenkov detector by equipping the outer surface of the Main Structure with an array of 2400 PMTs to collect Cherenkov light, with a higher density of PMTs in the lower hemisphere. In this way, the effective detection efficiency of the upper hemisphere, when coupled with the Top Tracker, becomes comparable to that of the lower hemisphere. In addition, four

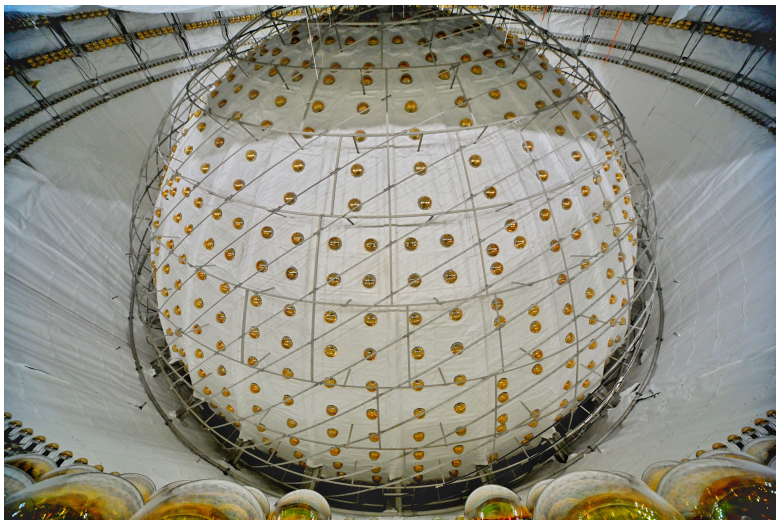

FIGURE 2.9 – Inner view of JUNO water pool.

rings of PMTs are installed at the top of the WP : two rings at $z = 20.66$ m and $z = 18.98$ m, comprising a total of 348 20-inch MCP-PMTs, and two rings at $z = 17.05$ m and $z = 16.05$ m, consisting of 600 8-inch PMTs from the Daya Bay experiment [123]. To further enhance Cherenkov light collection efficiency, the WP walls and base, as well as the outer surface of the Main Structure, are covered with Tyvek reflective foils, as illustrated in Figure 2.9.

Top Tracker

JUNO's veto system is complemented by the Top Tracker (TT) [111], whose primary purpose is to accurately reconstruct atmospheric muon tracks originating from above and to provide an additional veto for the detector.

The TT is constructed using scintillator strips from the Target Tracker of the OPERA experiment [110]. All modules were transported to China under careful quality control, and no significant degradation of the plastic scintillator properties has been observed. The TT is segmented into 6.7×6.7 m^2 "walls", corresponding to the black outlined squares shown in Figure 2.10a, and arranged in three horizontal layers. Each wall consists of 512 plastic scintillator strips, grouped into 64 strips per TT module. Each strip is coupled to wavelength-shifting fibers and read out at both ends of the module by 64-channel multi-anode photomultiplier tubes. A schematic representation of a TT wall and its segmentation into modules is shown in Figure 2.10b, where four vertical modules are illustrated.

The rate of radioactive background in the JUNO cavern is approximately two orders of magnitude higher than that observed at the Laboratori Nazionali del Gran Sasso, where OPERA was placed. This has led to a redesign of the readout electronics and trigger logic. The TT is expected to achieve a reconstruction efficiency of about 93%, with a median angular resolution of 0.2°. When requiring coincidence with signals in both the CD and the WP, the TT can provide a reconstructed muon sample with a purity exceeding 99%.

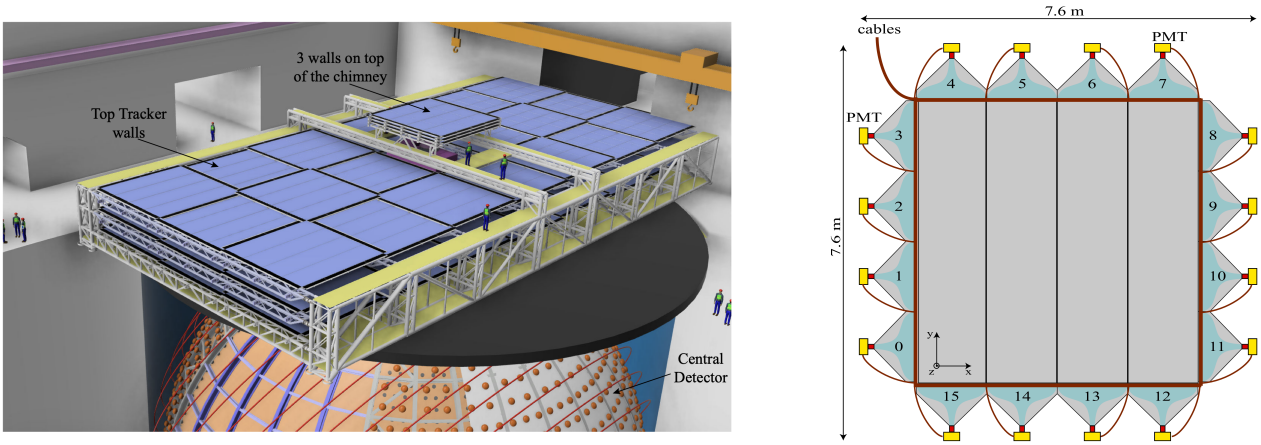

(a) (b)

FIGURE 2.10 – **(a)** 3D Schematic view of JUNO Top Tracker. **(b)** Schematic view of a plastic scintillator strip wall. Below the 4 vertical modules (y) clearly visible, 4 additional horizontal modules (x) are placed, going for example between PMT number 0 to 11.

In contrast to the OPERA Target Tracker, the JUNO TT is installed horizontally on a dedicated bridge and covers approximately 60% of the top surface of the WP. An opening is maintained to accommodate the CD chimney, with three TT walls positioned above it. With this configuration, approximately 1/3 of atmospheric muons traversing the CD will also pass through all three TT layers and can therefore be reconstructed. For these events, the TT provides an effective veto, while for the remaining muons the veto relies solely on the WP.

JUNO's cosmogenic background reduction strategy heavily relies on the good reconstruction of muon tracks. The TT provides additional information on the entry point of down-going muons, allowing to effectively enhance and fine tune the combined WP and CD muon event reconstruction. In addition, the TT can be used to estimate the fast neutron rate by selecting muons that traverse both the TT and the surrounding rock, thus reducing uncertainties associated with the simulation of neutron production, propagation, and interaction within the detector.

2.3.5 Large PMT system

Motivation

Photomultiplier tubes (PMTs) are widely used in neutrino detectors for the detection of low-intensity light signals. Their operation is based on three main stages : the conversion of incident photons into photoelectrons at the photocathode via the photoelectric effect, the amplification of these electrons, and the collection of the resulting charge at the anode. The ambitious goal of the JUNO detector to reach 3% energy resolution at 1 MeV requires optimization of all the parts involved in the light collection and detection. From the perspective of PMTs, photo

coverage, photon detection efficiency, dark noise, pre/after pulses, transit time spread, etc, are key ingredients to reach JUNO's target energy resolution.

Considering JUNO's physics goal, a 20-inch PMTs selection strategy [124] led JUNO to equip the CD with 2 systems of LPMT : 4939 high quantum efficiency Hamamatsu dynode-PMTs and 12657 Micro-Channel Plate PMTs (MCP-PMTs) manufactured by North Night Vision Technology (NNVT).

PMT Types

In dynode PMTs, electron multiplication is achieved through a cascade of discrete electrodes (dynodes). A photoelectron emitted from the photocathode is accelerated towards the first dynode, where it produces multiple secondary electrons. This process is repeated across a series of dynodes, resulting in an exponential amplification of the signal. An illustration of dynode PMTs light conversion is given in Figure 2.11a.

Microchannel plate PMTs replace the discrete dynode chain with one or more microchannel plates consisting of a dense array of microscopic channels, as illustrated in Figure 2.11b. Each channel acts as an independent electron multiplier : a photoelectron entering a channel undergoes repeated secondary emissions upon collisions with the channel walls, leading to signal amplification.

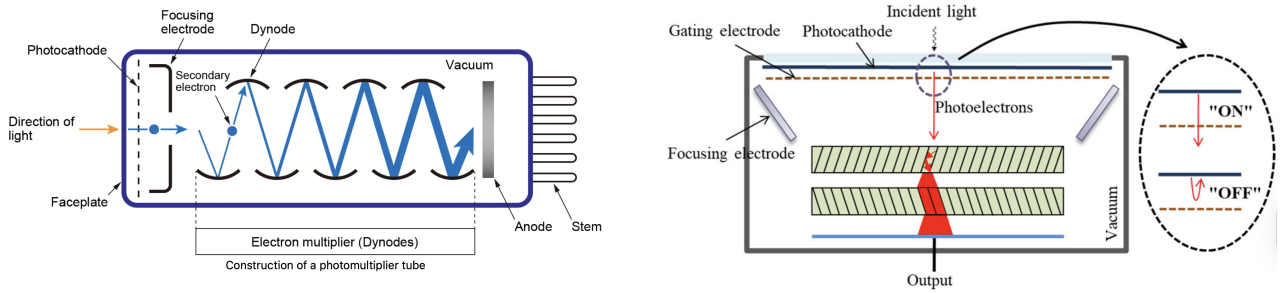

(a) (b)

FIGURE 2.11 – Light collection mechanism in the different PMT types used in JUNO : **(a)** Photon conversion to PE and collection mechanism in Dynode PMTs [125]. **(b)** Photon collection and conversion in large area MCP PMTs [126].

Performances

A challenging aspect of JUNO's PMT system optimization was achieving the target 27% Photo Detection Efficiency (PDE), which led to extensive R&D on MCP-PMTs to further improve their already high PDE [127]. Dynode PMTs are a well-understood technology with

excellent timing performance and a stable charge response, but a lower PDE compared to MCP-PMTs. However, PMTs manufactured by Hamamatsu were expected to show improved PDE, reaching at least 25% [128].

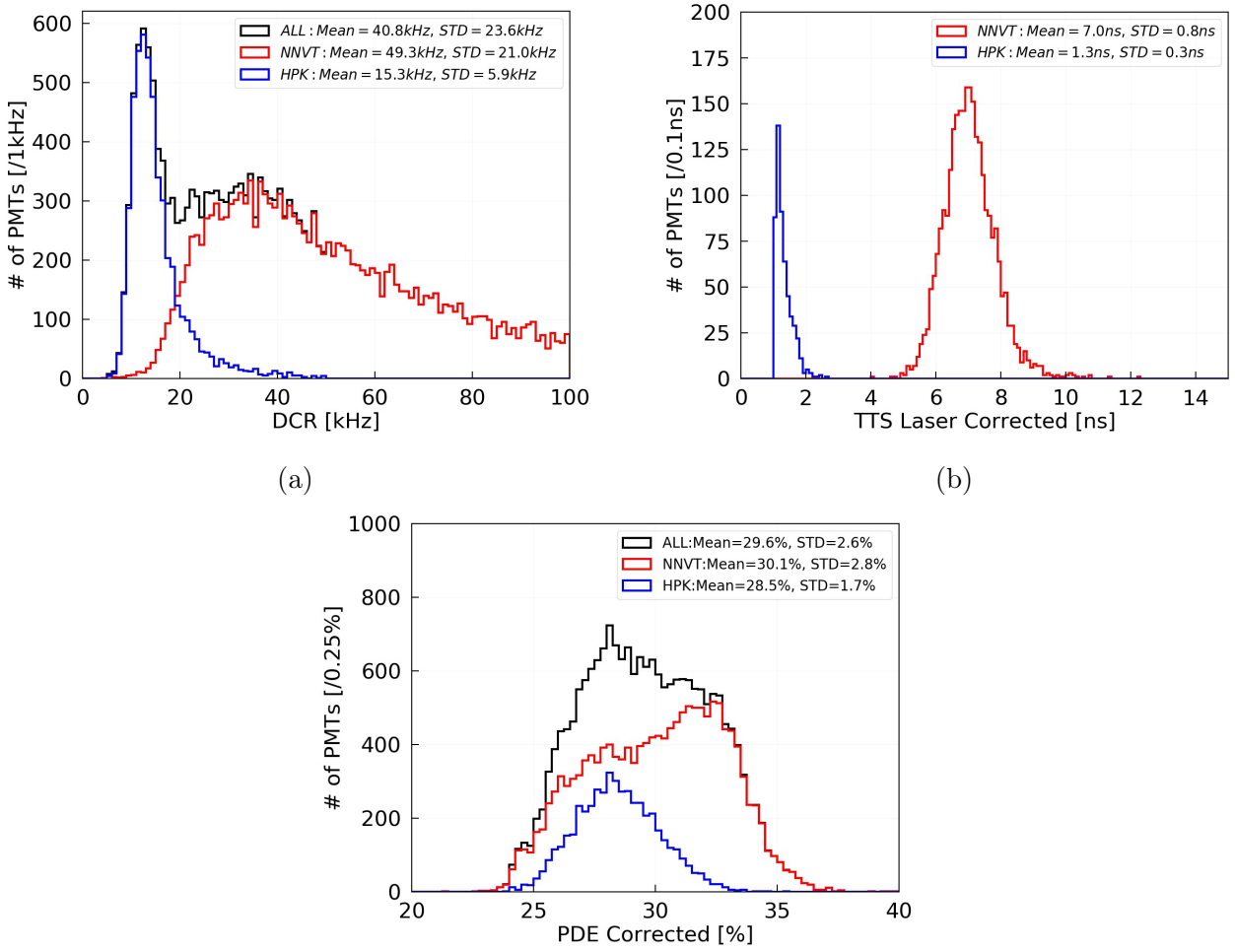

FIGURE 2.12 – Performance of the MCP (NNVT) and dynode (HPK) PMTs measured during the PMTs mass testing [129]. **(a)** PMTs dark count rate. **(b)** Extracted PMT timing resolution using a laser run. The value is dominated by the transit time spread. **(c)** Measured photo detection efficiency.

The performance of each LPMT sub-system was carefully evaluated through extensive testing [129] prior to installation in the JUNO detector. A sample of the PMT performance is given in Figure 2.12. The MCP-PMTs exhibit a very high PDE, with a mean value measured at 30.1%, at the expense of a larger Transit Time Spread (TTS) and Dark Count Rate (DCR). Meanwhile, the dynode PMTs show relatively small TTS, with a mean value of 1.7 ns, and low DCR, while still maintaining a relatively high PDE on average. This allows the overall LPMT system to achieve an average PDE of 29%, exceeding the 27% target.

The use of both MCP and dynode PMTs reflects a deliberate design strategy to combine

their complementary advantages. MCP-PMTs, with their high PDE, enhance the number of detected photoelectrons, improving energy reconstruction. In contrast, dynode PMTs provide superior timing resolution due to their small TTS, which is essential for accurate event vertex reconstruction and time-based analyses. This hybrid configuration allows JUNO to simultaneously optimize photon statistics and timing precision.

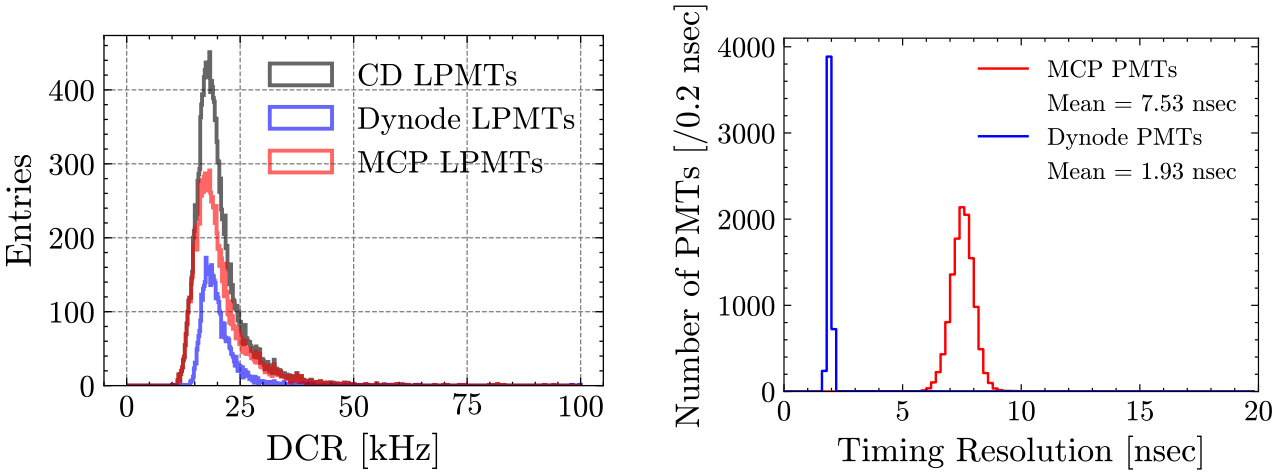

(a) (b)

FIGURE 2.13 – Initial performance of the LPMT system [119]. **(a)** PMTs dark count rate. Recent DCR performance were measured through online hit counting in the electronics and offline analysis of periodic triggers. **(b)** : PMT timing resolution.

Since the beginning of civil construction, PMT performance has been regularly monitored through light-off and light-on tests. Upon reaching the end of construction, the PMTs were also tested during the different filling phases. The current performance of the LPMT system [119] is presented in Figure 2.13. Although a direct comparison with the mass testing measurements is not straightforward due to differing operational conditions, the LPMT system exhibits a lower dark count rate, in particular in the MCP-PMT sub-system, which reaches 22.7 kHz. However, the LPMTs show a slight degradation in timing resolution, which rise from 1.3 ns and 7.0 ns to 1.93 ns and 7.53 ns for the dynodes and MCP PMTs respectively.

2.3.6 Small PMT System

Motivation

In addition to the LPMTs, JUNO is instrumented with a complementary system of 25,587 3-inch PMTs, commonly referred to as the small PMT (SPMT) system, which are positioned in the gaps between the LPMTs, as shown in Figure 2.14. This subsystem plays a crucial role in enhancing the overall detector performance by increasing the total photocathode coverage to ∼78%, while also providing an independent and complementary measurement of the scintillation light.

The primary motivation for the SPMT system lies in its capability to operate in a photon-counting regime, due to its significantly smaller photocathode area. This characteristic makes the SPMT system particularly valuable for constraining systematic uncertainties associated with non-linearity effects in the LPMT readout. Moreover, SPMTs have a much lower probability of detecting multiple photoelectrons from the same event within a single PMT. As a result, their response is intrinsically more linear and significantly less sensitive to saturation effects compared to LPMTs, especially in high-energy events.

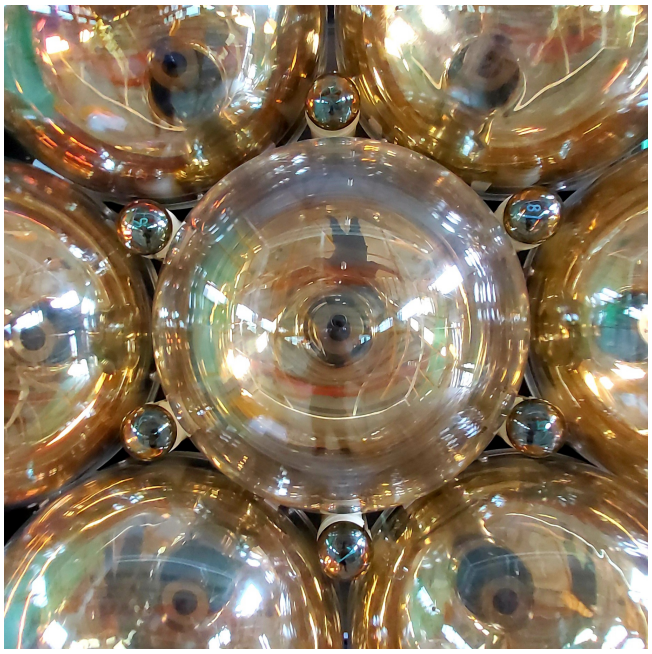

FIGURE 2.14 – Photograph showing the positioning of 3-inch photo multipliers relative to the 20-inch ones.

At the time this thesis was written, the SPMT system was not fully operational, with only $\sim 50\%$ of the system functioning, and with most of the operational SPMTs located in the upper hemisphere of the detector (see Section 4.4.3). The number of operational SPMTs is expected to increase throughout the first year of detector operation.

Performance

The characterization of the SPMT system was carried out through a joint effort between the manufacturer and the JUNO collaboration [130]. Thanks to their operating regime, the SPMTs do not require the same level of optimization of PMT characteristics as the LPMTs, whose performance is more sensitive to charge integration effects and non-linearities.
The average quantum efficiency of the SPMTs was measured to be $\sim$25%, which is sufficient for detecting the relatively small number of photons per event expected in each channel. Furthermore, the system can tolerate a slightly worse Single Photoelectron (SPE) charge resolution, since the probability of pileup within a single PMT is very low. Nevertheless, an average SPE

resolution of 33.2% was achieved, which is comparable to that of the LPMT system.
The average dark count rate (DCR) was measured to be ∼500 Hz at a 0.25 PE threshold and ∼7 Hz at a 3 PE threshold, thereby minimizing the probability of fake photon counts. In addition, the low afterpulsing probability further limits spurious contributions to the photon-counting measurement.
Although timing is not the primary role of the SPMT system, the timing performance of the SPMTs is also noteworthy. Their TTS is comparable to that of the dynode LPMTs (∼1.3 ns), allowing the use of SPMTs to improve the reconstruction of high-energy events such as cosmic-ray muons and atmospheric neutrinos.

Even though the SPMTs detect significantly less light, the accumulation of sufficient statistics allows the system to perform physics measurements in a semi-independent way from the LPMTs. In particular, this enables an independent determination of solar oscillation parameters such as $\sin^2(\theta_{12})$ and Δm^2_{21}.

2.4 Calibration

The neutrino mass ordering determination requires the JUNO detector to have 3% energy resolution and less than 1% uncertainty on the energy linearity [131]. Reaching the energy resolution target is done with the liquid scintillator and PMT systems while energy non-linearity requires a dedicated energy and spatial-response calibration of the detector. This section aims at describing the different mechanisms inducing energy non linearity or spatial non-uniformity inside the detector, and present JUNO calibration system design.

2.4.1 Detector Response

Energy non-linearity

The particles interactions in the LS will produce scintillating and Cerenkov photons, which will then be converted in photoelectrons (PE) by the PMTs. However both mechanism have intrinsic non-linearity. The scintillation photons, emitted by de-excitation of the fluor molecules, are not proportional to the deposited energy due to the quenching phenomenon [132], while the number of emitted Cerenkov photons [133] is sensitive to the path length of the particle in the LS, that can vary due to the generation of secondary particles. Moreover, photons generated by both mechanism can undergo absorption, re-emission, scattering and transmission at volume boundaries, where only a fraction of the re-emitted photons will be detected by the PMTs and converted to PE.

Detector Non-Uniformity

The number of generated PE also depends on the position of the event in the detector. As events occur closer to the edge of the detector, the probability of total internal reflection at the volume boundary increases, owing to the difference in refractive index between the acrylic and the surrounding water. This increases the average photon path and the probability of absorption before reaching a PMT. Other effects, such as the PMT's angular response and shadowing by opaque detector materials, can further reduce the number of photons collected, leading to a smaller number of detected PE.

Instrumental Non-Linearity

Additional non-linearity is introduced by the PMT characteristics and the associated electronics. The single photoelectron resolution, dark rate and after pulses have direct impact on the number of PE produced, while the PMT TTS can affect the accuracy of vertex reconstruction, leading to a degraded energy resolution due to non-uniformity effects. Instrumental non-linearity can be corrected with the dual calorimetry method [134], which uses both large and small PMT systems that work under different photon occupancy regimes to calibrate this non-linearity.

2.4.2 Calibration System Design

JUNO calibration system was designed in agreement with the strategy established to tackle all non-linearity effects in the detector [135]. The system is made of 4 sub-systems that allows to deploy radioactive sources in every part of the detector. The sources and calibration systems are installed in an air-tight calibration house to avoid radon contamination and diffusion in the LS. The calibration house is located on top of the detector and connected to the CD top chimney as illustrated in Figure 2.4.

Automatic Calibration Unit

The Automatic Calibration Unit (ACU) was developed to do calibration along the z axis of the CD with a similar design to the ACU used in the Daya Bay experiment [136]. Due to the system's simplicity and robustness, the ACU is regularly deployed during data taking to monitor the stability of the energy scale and do a partial calibration of the position non-uniformity. Radioactive sources are often deployed at different z positions in the detector, with a 1 cm positioning precision. Timing calibrations are also performed using the ACU by placing a UV laser coupled to a diffuser ball [137] at the center of the detector.

Guide Tube System

The Guide Tube system (GT) surrounds the acrylic sphere and runs in a longitudinal circle. Radioactive sources, attached by both ends, are deployed within the tube with a positioning precision of 3 cm. The GT is used to calibrate non-uniformity response, but also evaluate the energy response at the CD boundary, since part of the gammas energy will be deposited in the acrylic. This subsytem was deemed sufficient to properly calibrate the CD non-uniformity at the boundary [138].

Cable Loop System

Two Cable Loop Systems (CLS) are installed in the two opposite vertical half-planes to deploy sources to off-axis positions, as shown in Figure 2.15. The two sets of CLS allows for a 79% effective coverage on an entire vertical plane. Radioactive sources are attached by two cables to a CLS which allows to deploy and retract the source with a 3 cm positioning precision.

Remotely Operated Vehicule

For regions of the detector not covered by the CLS, a Remotely Operated under-LS Vehicle (ROV) can deploy radioactive sources to any location within the liquid scintillator with a positioning precision of 3 cm. The ROV is additionally equipped with a camera, enabling visual inspection of the CD. This subsystem was designed to complement the ACU, GT, and CLS calibration systems, and is expected to be deployed only occasionally.

2.4.3 Radioactive Sources

For the calibration of the JUNO detector, gamma sources were selected over electron or positron sources for both safety and practical reasons. Any contamination of JUNO's active volume would be catastrophic for the experiment since it will permanently damage to the detector's sensitivity. Electron and positron sources require extremely thin-walled enclosures so that the particles are not absorbed before reaching the scintillator. However, this mechanical fragility poses a risk of radionuclide leakage into the liquid scintillator volume. In contrast, gamma sources are far more penetrating and do not require such delicate enclosures, they can be housed in thicker containers ($\sim$ mm) that are far less likely to fail, while still delivering well-defined energy depositions within the detector for calibration purposes.
The list of sources used to calibrate the detector is given in Table 2.3. For the ^{68}Ge source, the emitted positron from the β^+ decay to ^{68}Zn is annihilated inside the source enclosure, only the two 511 keV gammas are released.

Gamma sources are complemented by neutron sources that provide high energy gammas after neutron capture on different nuclei, effectively covering the entire IBD energy range. The

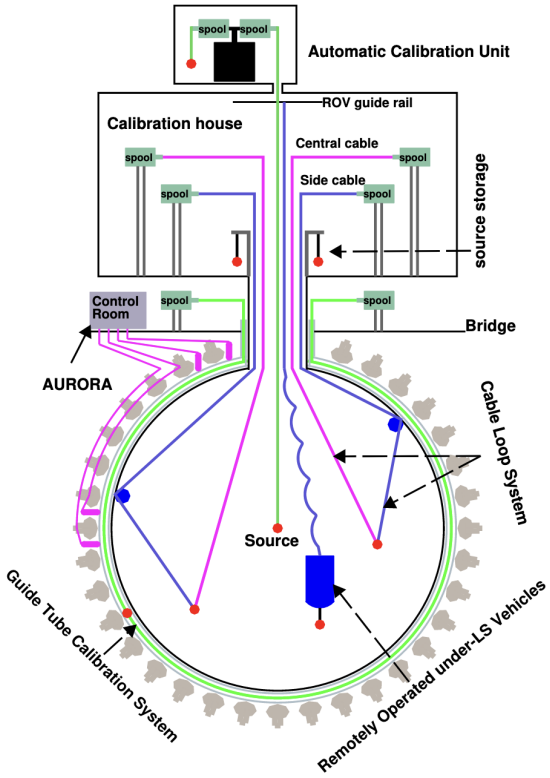

FIGURE 2.15 – Schematic of the calibration system (not to scale), including the Automatic Calibration Unit (ACU), two Cable Loop Systems (CLSs), the Guide Tube (GT), and the Remotely Operated Vehicle (ROV) [135].

Source	Energy	System	Activity
	Gamma Sources		
^{68}Ge	0.511×2 MeV	ACU	595 Bq[a]
^{137}Cs	0.662 MeV	ACU	140 Bq[b]
^{54}Mn	0.835 MeV	ACU	521 Bq[a]
^{40}K	1.460 MeV	ACU	13 Bq
^{60}Co	$1.173 + 1.333$ MeV	ACU	165 Bq[b]
	Neutron Sources		
^{241}Am–^{13}C	neutron + 6.13 MeV (^{16}O*) (n,γ)p 2.223 MeV $(n,\gamma)^{12}$C 4.94 MeV $(n,\gamma)^{56}$Fe 7.63 MeV, etc.	ACU CLS	130 Bq 100 Bq
^{241}Am–^{9}Be	neutron + 4.43 MeV (^{12}C*) (n,γ)p 2.223 MeV	GT	30 Bq
	Optical Calibration		
Laser	Optical pulses (420 nm and 266 nm)	ACU	50 Hz

[a] Reference activity measured on 6/21/2023.
[b] Reference activity measured on 4/6/2021.

TABLE 2.3 – List of γ, neutron and laser calibration source deployed in JUNO [119].

charge spectrum in NPE for the different calibration sources is shown in Figure 2.16.

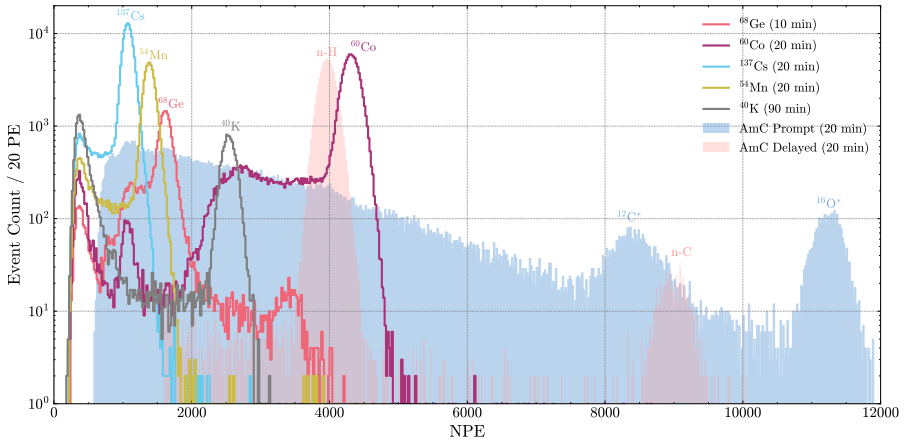

FIGURE 2.16 – Charge spectrum (NPE) of the different neutron and gamma calibration sources in JUNO after dark noise subtraction [119].

The AmC source is regularly deployed via the ACU to monitor the energy scale. The 2.223 MeV gamma ray from neutron capture on ^{1}H serves as the anchor point from which the gamma energy non-linearity curve is constructed, using the other gamma sources as additional calibration nodes. Cosmogenic isotopes are also exploited for non-linearity measurements : ^{12}B and ^{12}N, which decay via β^- emission, are used to characterise the electron energy non-linearity, while ^{11}C, which decays via β^+ emission, provides the equivalent measurement for positrons [119, 139].

2.5 JUNO-TAO

The Taishan Antineutrino Observatory (TAO), also referred to as JUNO-TAO, is a satellite experiment of JUNO, designed to operate in close proximity to one of the reactor cores of the Taishan Nuclear Power Plant in Guangdong, China [140]. Positioned at a baseline of approximately 30 m from the reactor core, TAO serves a dual purpose : providing a high-statistics, high-resolution reference spectrum for JUNO, and pursuing an independent physics program in its own right. The construction and installation of the TAO detector have recently been completed, and the detector has started its begin data-taking in February 2026.

Physics Goals

The primary motivation for TAO is to supply JUNO with a model-independent reference reactor antineutrino spectrum, thereby eliminating uncertainties arising from the fine structure of the reactor antineutrino spectrum in the neutrino mass ordering determination. Current theoretical predictions of the reactor antineutrino spectrum, based on both the summation and beta-conversion methods, disagree with measurements from very short baseline reactor neutrino experiment such, referred to as the reactor antineutrino anomaly [68], and later confirmed by the RENO [141], Daya Bay [142], and Double Chooz [143] experiments. Past reactor neutrino experiments exhibited an excess around 5 MeV in the energy spectrum when compared to Huber-Muller predictions [144, 145]. Moreover, the energy resolution of past experiment is insufficient to constrain spectral fine structure at the percent level. TAO, with its sub-percent energy resolution, will measure the antineutrino energy spectrum with sufficient precision to provide this constraint, reducing the bin-to-bin spectral shape uncertainty for JUNO to below 1% [131].

Beyond its role as a near detector for JUNO, TAO pursues several additional physics goals. The high-resolution spectral measurement will serve as a benchmark to test nuclear databases via comparison with summation method predictions, and will provide an opportunity to improve the knowledge of neutron-rich isotopes produced in commercial reactors. TAO is also sensitive to the existence of light sterile neutrinos with a mass splitting of $\Delta m^2_{41} \sim 1$ eV^2, complementing existing constraints from Daya Bay [146], STEREO [147], and NEOS [148] at its intermediate $\sim$30 m baseline. Finally, the precise measurement of individual isotopic antineutrino yields and spectra contributes to the ongoing international effort on reactor monitoring and nuclear safeguard applications.

Detector Design

The TAO has a similar design as the JUNO detector, were some parts have been altered to improve photodetection efficiency and light yield. The TAO detector is represented in Figure 2.17. It consists of a central detector (CD) made of a spherical acrylic vessel of 1.8 m inner

diameter containing 2.8 tonnes of gadolinium-doped liquid scintillator (GdLS), with a 0.1% Gd loading by mass. The GdLS is based on Linear Alkylbenzene (LAB) with 2 g/L PPO as the primary fluor and 1 mg/L bis-MSB as the wavelength shifter. The scintillator is viewed by approximately 4100 Silicon Photomultiplier (SiPM) tiles covering a total area of ∼10 m^2, achieving a photon coverage exceeding 95%. The use of SiPMs with a photon detection efficiency greater than 50% results in an unprecedented photoelectron yield of approximately 4500 PE/MeV, an order of magnitude higher than existing large-scale liquid scintillator detectors.

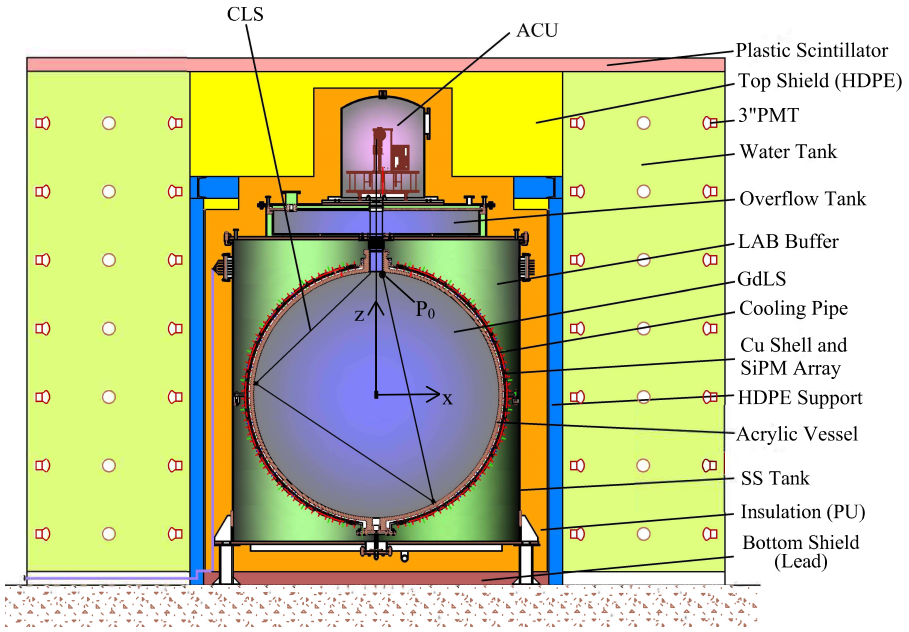

FIGURE 2.17 – Schematic representation of the TAO detector, which consists of a central detector, an outer shielding and a veto system [149].

A critical design requirement is the operation of the entire central detector at −50°C. This low temperature is necessary to reduce the dark noise of the SiPMs to an acceptable level of ∼100 Hz/mm^2. The acrylic vessel is submerged in a non-scintillating LAB buffer contained within a cylindrical cryostat, which also provides thermal stabilisation. The central detector is surrounded by 1.2 m thick water tanks on the sides, instrumented with PMTs to form a water Cherenkov muon veto, and by 1 m of High Density Polyethylene (HDPE) on top as passive shielding against cosmogenic neutrons. A plastic scintillator layer above the HDPE provides additional muon tagging.

Signal and Background

Reactor antineutrinos are detected via the IBD reaction, with the neutron captured predominantly on gadolinium, producing a delayed signal of ∼8 MeV, well above the natural radioactivity background, with a mean capture time of ∼30 μs. The expected IBD event rate in the fiducial volume is approximately 2000 events per day. The dominant backgrounds are fast neutrons produced by cosmic muon spallation in the surrounding materials, with a rate of

$\sim$1880 events/day before vetoing, reduced to below 200 events/day after application of a 20 μs muon veto window ; accidental coincidences at a rate below 190 events/day ; and the correlated ^{9}Li/^{8}He cosmogenic background at $\sim$54 events/day. Together, these are designed to maintain a total background-to-signal ratio below 10%.

Energy Resolution

The expected energy resolution of TAO is sub-percent across most of the antineutrino energy range of interest (2–8 MeV), a significant improvement over existing reactor neutrino experiments. This performance results from the combination of high photon coverage, high SiPM detection efficiency, the compact detector geometry reducing photon absorption losses, and the enhanced scintillation yield at low temperature. The dominant non-statistical contributions to the energy resolution are scintillator quenching, SiPM charge resolution, optical cross-talk, and SiPM dark noise. With this resolution, TAO will be able to resolve the fine structure of the reactor antineutrino spectrum at the percent level, providing the high-fidelity reference spectrum required by the JUNO mass ordering analysis.

2.6 Conclusion

This chapter has given a detailed description of the JUNO experiment, starting from its physical motivation and detection principle, leading to the detector design and calibration strategy.

The detector construction ended in December 2024, and the filling started soon after, followed by extensive validation of the detector performance throughout the water and liquid scintillator filling phases. The results presented in this chapter indicate that the initial low-level performance of the detector is, in most aspects, already at or beyond the design requirements. The liquid scintillator recovered from the early low-quality batches to reach an average attenuation length of 20.6 m at 430 nm, above the 20 m requirement, while the measured ^{238}U and ^{232}Th concentrations of a few 10^{-17} g/g are roughly an order of magnitude below the radiopurity requirement for the mass ordering measurement. Similarly, the combined LPMT system reaches an average photon detection efficiency of 29%, exceeding the 27% target, and the SPMT system, although only partially operational at the time of writing, already provides SPE and timing performance comparable to the LPMTs. The main point of vigilance identified so far is the modest degradation of the LPMT timing resolution relative to mass-testing values, which will need to be monitored as it can propagate into the vertex reconstruction and, in turn, into the energy non-uniformity correction. The four calibration sub-systems (ACU, GT, CLS and ROV) are operational and, together with the source set summarised in Table 2.3, cover the full detector volume and IBD energy range needed to constrain the non-linearity and non-uniformity effects discussed in Section 2.4. JUNO-TAO, whose construction has now been completed, will

complement this program by supplying a model-independent reference spectrum that removes the reactor flux fine-structure uncertainty from the mass ordering fit.

Taken together, these results are encouraging for the physics reach of the experiment, but they remain low-level. The next step is to assess the achieved energy response once all of these effects are combined, which is performed through extensive calibration measurements compared against simulation. This step therefore requires an accurate Monte Carlo simulation of the detector, able to reproduce with great fidelity the detector response throughout its volume and the resulting calibration measurements. The next chapter presents the JUNO simulation software, and the work carried out to upgrade and validate its Geant4 physics toolkit.

Chapitre 3

Geant4 Upgrade in JUNO Simulation Software

Summary

3.1 Introduction . . . 97
3.2 JUNO Simulation Software . . . 97
3.2.1 Overview of JUNO offline software . . . 97
3.2.2 Geant4 in JUNOSW . . . 99
3.2.3 Upgrade motivation . . . 101
3.3 Electromagnetic physics update in Geant4 . . . 101
3.3.1 Electron simulation . . . 101
3.3.2 First attempt to correct electron simulation . . . 103
3.3.3 Multiple Coulomb Scattering models in Geant4 . . . 105
3.3.4 Goudsmit Saunderson boundary crossing management . . . 106
3.3.5 Electron simulation correction in new Geant4 release . . . 107
3.4 Hadronic physics update in Geant4 . . . 109
3.4.1 Alpha Simulation . . . 110
3.4.2 Neutron Simulation . . . 111
3.4.3 Neutron Capture on Hydrogen . . . 112
3.4.4 Neutron Capture on Carbon . . . 113
3.4.5 Correction to Neutron Simulation . . . 115
3.5 Cosmogenic Yield Simulation . . . 116
3.5.1 Geant4 v11.4 Simulation . . . 116
3.5.2 Expected Yield at JUNO site . . . 117
3.5.3 Results . . . 117
3.6 Conclusion . . . 119

3.1 Introduction

The previous chapter introduced the JUNO detector and the demanding energy resolution requirements imposed by the mass ordering measurement. Meeting these requirements relies heavily on accurate Monte Carlo simulation of the detector response, motivating the simulation software development effort presented in this chapter. Modern physics experiments require larger, more precise and more sensitive detectors in order to probe new physics. This leads to higher demand for large-scale and comprehensive simulations of detectors to better estimate their efficiency and ability to meet a given physics goal. In this context, Monte Carlo simulations have become an indispensable tool, allowing researchers to model complex physical systems where analytical solutions are hard or impossible to implement.
JUNO is a multi-purpose experiment with a physics program that spans from low energy solar and reactor anti-neutrinos to high energy atmospheric neutrinos, demanding a very accurate detector modeling and extensive Monte Carlo simulation capabilities.

This chapter introduces the simulation software of the JUNO experiment and its main components, and also describe the effort undertaken during this thesis to upgrade the Geant4 version used in the software. Section 3.2 gives an overview of JUNO simulation software and how it was designed to answer JUNO's physics requirements. The integration of Geant4 within the JUNO software framework is detailed, together with the modifications made to Geant4 to ensure full compatibility. Then, a study is performed to assess the reliability of newer Geant4 versions for JUNO, and is presented in the next two sections. First, Section 3.3 focuses on electromagnetic physics, in particular electron simulation, and discusses issues found in the description of multiple Coulomb scattering. Then, Section 3.4 presents the studies performed on hadronic physics, with a focus on α particles and neutron. Several modifications and improvements were introduced in newer Geant4 versions, and this section evaluates the impact and correctness of those improvements for JUNO simulations. Upon integrating the latest Geant4 version, a short analysis assessing the reliability of Geant4 in the generation of comsogenic isotopes is presented in Section 3.5.

3.2 JUNO Simulation Software

3.2.1 Overview of JUNO offline software

At the core of JUNO's software ecosystem lies the JUNO Offline Software (JUNOSW) [150], built on the SNiPER (Software for Non-collider Physics Experiment) framework [151], developed in order to answer JUNO's simulation requirements and support all computing needs from detector simulation to event reconstruction and physics analysis.

Physics simulation

JUNO's broad physics program requires a large number of event generators as well as various generation tools to produce events in different volumes, positions and materials inside the detector. The simulation is also required to dynamically deploy the various calibration sources and their corresponding support structures. JUNOSW includes generators for cosmic muons, reactor neutrinos, atmospheric neutrinos, solar neutrinos, geoneutrinos, supernova burst neutrinos, diffuse supernova background neutrinos, natural radioactivity and calibration sources. Physics generators are built as SNiPER tools and managed by a SNiPER algorithm that unifies the generated particles from the various tools. This architecture makes JUNOSW physics simulation very flexible and allows simple integration of any generators of interest.

Detector simulation

The detector's exceptionally large size and heavy instrumentation requires a large number of input parameters for the geometries, materials optical properties, and PMT response parameters that need to be implemented in the simulation. A very detailed simulation of JUNO detector geometry was constructed based on the final design [128], and includes CD, WP, TT, corresponding support structures as well as extensive description of PMT's inner and outer components. The additional 8-inch WP PMTs were also recently included in the detector simulation as well as CD chimney components and water distributor pipes to account for shadowing observed in the data. The liquid scintillator and water optical properties (Birks constants, liquid scintillator light yield, absorption lengths...) and PMTs measured characteristics (quantum efficiency, dark rate, resolution...) are stored in data files and accessed using dedicated SNiPER services. Moreover, accurate description of the PMTs optical model is included in the detector simulation, and accounts for light interaction with the PMT glass as well as optical processes that occurs inside the PMT vessel.

Electronics simulation

The accurate handling of JUNO's electronic readout chain is performed by the electronic simulation workflow. It consists of three SNiPER algorithms that simulate the readout of each sub-system : the LPMT and SPMT systems in the CD, the WP PMT system, and the TT system. Simulated hits arriving at the PMTs are first converted into time-ordered pulses by the PMT algorithm, incorporating PMT effects such as gain resolution and variation, dark noise, pre- and after-pulses, transit time, and transit-time spread. The trigger algorithm retrieves these pulses to generate hardware trigger signals, while the electronics algorithm applies waveform modeling and digitization to produce the final electronic output signal.

3.2.2 Geant4 in JUNOSW

Within the SNiPER framework, the simulation software integrates the Geant4 simulation toolkit [152] with JUNO-specific detector geometry, physics processes, and event handling. This integration required careful coordination between the distinct event-loop control mechanisms of Geant4 and SNiPER, while maintaining flexible and transparent user control over the simulation configuration. The modular structure provided by the SNiPER framework allows users to easily enable, disable, or modify individual components of the detector geometry.

Geant4 is a well-established simulation toolkit, thanks to its extensive catalog of physics processes that enables the accurate modeling of a wide range of particle interactions. Consequently, it has been widely adopted across multiple research domains, including high-energy physics, medical physics, and mechanical engineering. To facilitate the implementation of accurate and consistent simulations, Geant4 provides predefined physics constructors, which are collections of physics processes that have been extensively validated and optimized for different experimental contexts. These physics lists define which processes are applied to specific particles, ensuring that simulations reflect the underlying physics as faithfully as possible. They are commonly used as defaults due to their demonstrated precision, robustness, and compatibility with experimental results. For JUNOSW, the physics constructors employed are summarized in Table 3.1. Some of these constructors were slightly modified to better suit JUNO's specific experimental conditions, while others were retained unchanged to preserve their validated behavior.

Physics Lists	**Status**
G4EmLivermorePhysics	Customized
G4EmExtraPhysics	Unchanged
G4DecayPhysics	Unchanged
G4RadioactiveDecayPhysics	Customized
G4HadronPhysicsQGSP_BERT_HP	Customized
G4StoppingPhysics G4IonPhysics	Unchanged
G4IonPhysics or G4IonPhysicsPHP	Unchanged
G4OpticalPhysics	Customized

TABLE 3.1 – List of Geant4 Physics constructors used in JUNOSW.

Electromagnetic physics

The EmLivermorePhysics list records electromagnetic processes for photons, electrons, muons, hadrons and ions and include e^-/e^+ pair production, Compton scattering, photo electric effect, multiple coulomb scattering, ionization and more. In addition, the process that describes Positronium formation in liquid scintillator has been registered in G4EmLivermorePhysics for

JUNOSW [1] based on experimental results from [153].

Hadronic physics

The G4HadronPhysicsQGSP_BERT_HP list provides extensive description of purely hadronic inelastic and capture processes. However, at the time of Geant4 integration in JUNOSW, the description of neutron capture, and especially the energy spectrum of the capture gammas, were not in agreement with experimental results on neutron capture in liquid scintillator. To correct the gamma energy values, data files, based on the National Nuclear Data Center (NNDC) data base, were created and added to JUNOSW for many isotopes. Moreover, for a given number of isotopes, those files are used to build the nucleus final state after the capture.

Radioactive decays

Background control and estimation is of key importance for JUNO's physics goals and Geant4 Radioactive Decay Module (GRDM) is used to get accurate description of our background. The most important background for JUNO comes from muon-induced ^{9}Li and ^{8}He (β, n) decays that effectively mimic the IBD signal. In Geant4, the final state of ^{9}Li and ^{8}He beta decay was correctly defined, but the decay chains for ^{9}Be and ^{8}Li were not accounted for. The GRDM and related data files have been modified following [154] to correctly handle ^{9}Li and ^{8}He decays.

Optical physics

Optical photons are produced through the G4Scintillation and G4Cerenkov processes, and were modified to meet the specific requirements of the JUNO experiment. In its standard implementation, G4Cerenkov process assumes a refractive index that increases monotonically with photon energy. Since this assumption does not hold for the refractive index of the JUNO liquid scintillator, the process was customized to support more general refractive index dependencies. The G4Scintillation process was further customized in several aspects to accurately reproduce the scintillation response of the detector. First, Birks constants were introduced to account for the quenching behaviors of gammas, electrons, positrons, alphas, neutrons and protons. Second, particle-specific emission time constants and multiple exponential decay components were implemented. Finally, photon reemission in the liquid scintillator was included, allowing optical photons originating from both scintillation and Cerenkov processes to be absorbed and subsequently re-emitted at different wavelengths. SNiPER tools were developed to easily adjust the properties of Scintillation and Cerenkov processes for specific simulation studies.

1. Since version 11.3 of Geant4, a description of Positronium formation has officially been implemented.

3.2.3 Upgrade motivation

As the completion of civil construction and the commissioning of the detector approached, several working groups were established within the JUNO collaboration to prepare for the first phase of commissioning data analysis. One of these working groups was dedicated to the fine tuning of the JUNO simulation software, with the objective of achieving the highest possible accuracy in Monte Carlo simulations. In particular, ensuring the precision of the Geant4-based detector simulation was of critical importance, as it directly impacts the reliability of later physics analyses.

At that time, JUNOSW was based on Geant4 version 10.4.2, released in 2018. While stable and well validated, this version lacked several significant improvements introduced in later Geant4 releases that are essential for JUNO simulations. These include, among others, updated treatments of ^{9}Li and ^{8}He decays implemented from Geant4 version 10.6 onward, an overall improved precision in radioactive decay processes, a more accurate description of electron and positron multiple Coulomb scattering, and corrections to the modeling of ion interactions such as those involving alpha particles.

In this context, a detailed comparison between the Geant4 version implemented in JUNOSW (v10.4.2) and the most recent release available at the time, Geant4 v11.2.0 was performed. The objective of this study was to identify, understand, and, where necessary, correct discrepancies between the two versions within the JUNOSW framework, in preparation for the integration of Geant4 v11.2.0 into the official simulation software.

3.3 Electromagnetic physics update in Geant4

An essential component of JUNO's event simulation is the accurate modeling of electromagnetic physics processes. In JUNO, these electromagnetic interactions are modeled in Geant4 using the EmLivermore physics list, which performs better than Geant4's standard electromagnetic physics list in the keV-MeV energy range. Consequently, a detailed validation of the EmLivermore physics list and its associated electromagnetic processes is required when comparing the Geant4 version currently used in JUNOSW with the version targeted for the software upgrade.

3.3.1 Electron simulation

To investigate possible discrepancies in the electromagnetic treatment between Geant4 versions, simulations of monoenergetic electrons were first performed.

Figure 3.1 presents the initial results of the comparison between Geant4 versions using 1

MeV electrons simulated at the center of JUNO's detector. As shown in Figure 3.1a, a striking difference is observed in the shape of the quenched energy obtained with Geant4 v10 and v11. Here, the quenched energy is computed by applying Birks' formula to the energy deposited along the electron track in Geant4 :

$$Q_{edep} = \sum_i \frac{dE_i}{1 + k_B \cdot \frac{dE_i}{dx_i}\frac{1}{\rho_{LS}} + k_C \cdot (\frac{dE_i}{dx_i}\frac{1}{\rho_{LS}})^2} \tag{3.1}$$

where dE_i is the deposited energy at the ith step, dE_i/dx_i corresponding to the stopping power, k_B and k_C are Birks' constants and $\rho_{LS} = 0.859$ g/cm^3 is the liquid scintillator density. This quenched energy is used to determine the number of photoelectrons generated, which serves as input for the electronic simulation. As illustrated in Figure 3.1b, the average number of photoelectrons produced is systematically lower using Geant4 v11.2. Such a reduction can directly impact on our energy resolution estimation and would require additional tuning of the liquid scintillator optical parameters within JUNOSW.

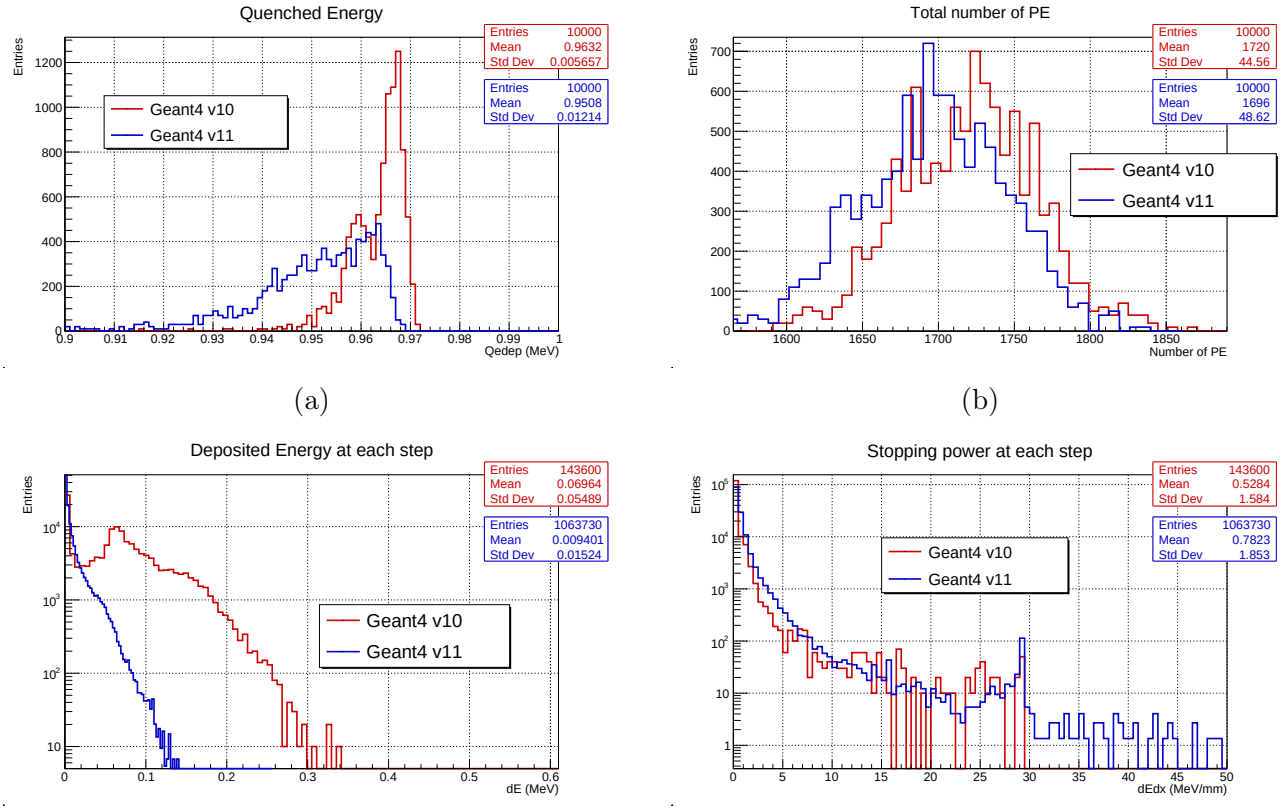

FIGURE 3.1 – Simulation of 10 000 1 MeV electrons at the detector center : **(a)** Total quenched energy computed using Birks formula at each step then summed over the number of steps. **(b)** Total number of photoelectrons produced by the electron. **(c)** Deposited energy (dE) at each step of the electron track. **(d)** Stopping power of the electron computed at each step of the track by dividing the deposited energy (dE) by the step length (dx).

The observed discrepancies can be attributed to a significant increase in the number of

tracking steps used by Geant4 to propagate the electron, which rises by almost an order of magnitude from Geant4 v10.4 to Geant4 v11.2. As a consequence, the deposited energy per step is much smaller in v11.2, while the stopping power evaluated at each step is higher on average. This behaviour is illustrated in Figure 3.1c and 3.1d. The resulting quenched energy, computed using Eq. 3.1, is therefore reduced on average in Geant4 v11.2.

3.3.2 First attempt to correct electron simulation

To better understand the origin of this behavior, optical processes were initially removed from the simulation in order to restrict the set of physics processes potentially responsible for the observed differences.

Simulations without optical processes revealed that the electron transport was governed primarily by ionization and multiple Coulomb scattering, with ionisation as the dominant step limiting process. In Geant4, processes may establish additional step limitation by using a smooth StepFunction characterized by two parameters controlling the step size. The first parameter, α_R (parameter dRoverRange), limits the maximum allowed step size such that the particle stopping power does not decrease by more than approximately 20% within the step. By default $\alpha_R = 0.2$. This condition mainly affects particles with kinetic energies above 1 MeV and relatively long ranges. The second parameter, ρ_R (parameter FinalRange), defines the threshold below which the step size is no longer scaled with the remaining range but instead set to a small constant value to accurately describe the final stages of energy loss. The default value is $\rho_R = 1$ mm.

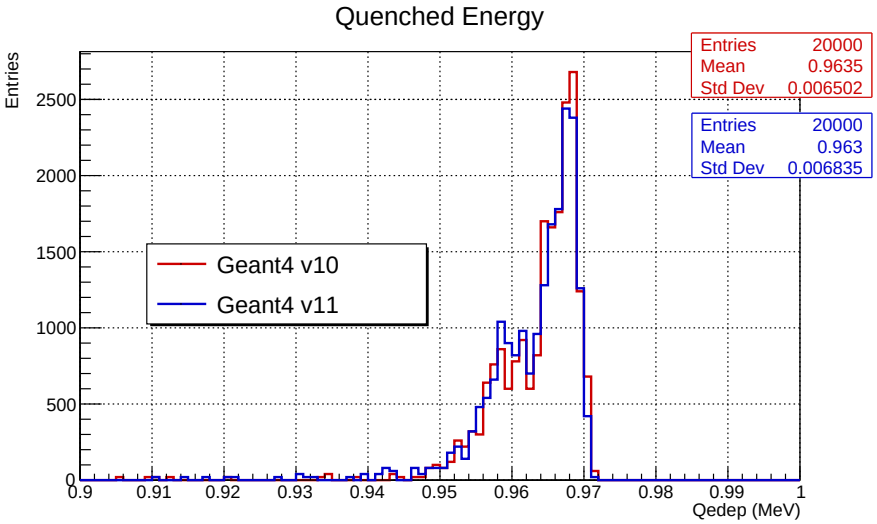

FIGURE 3.2 – Electron quenched energy distribution after removing optical processes and setting StepFunction FinalRange parameter to 100μm in both versions of Geant4.

The default value of the FinalRange for electrons differs between Geant4 versions : $\rho_R = 100$ μm in Geant4 v10.4 and $\rho_R = 10$ μm in Geant4 v11.2. By setting $\rho_R = 100$ μm and disabling optical processes, the resulting quenched energy distribution in Figure 3.2 exhibits good agreement between Geant4 v10.4 and Geant4 v11.2. However, this adjustment alone does not fully resolve the discrepancies observed when optical processes are enabled. Reintroducing optical processes while using the same FinalRange value in both Geant4 versions reproduces the differences seen in Figure 3.1.

Fortunately, the origin of the behaviour can be narrowed down to the optical processes used for the electron simulation, namely Cerenkov and Scintillation. Figure 3.3 illustrates the attempt to identify the exact process responsible for this effect by removing optical processes one by one. Removing only Cerenkov process has little to no impact on the number of tracking steps generated by Geant4 v11, as shown by the blue dotted curve. In contrast, the blue dashed curve, corresponding to disabled Scintillation process, presents a significant reduction of the number of steps. However, it still remains higher compared to Geant4 v10, and comparison on the structure of the G4Scintillation model between both versions did not provide a decisive solution to the behaviour we see.

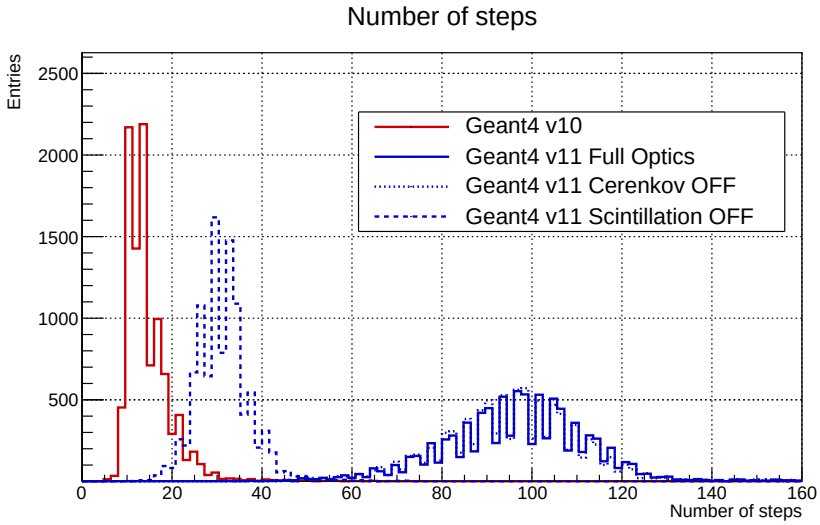

FIGURE 3.3 – Impact of Geant4 optical processes on the number of tracking steps generated for the simulation of an electron. The dotted blue line represents the optical physics list without Cerenkov process while the blue dashed line corresponds to disabled Scintillation process.

While the activation of optical processes appears to be correlated with the increased number of tracking steps, it is not the only cause. Instead, it was observed that when optical processes are enabled in Geant4 v11.2, the process responsible for limiting the electron step changes : ionization no longer dominates, but multiple Coulomb scattering becomes the primary step-limiting process.

3.3.3 Multiple Coulomb Scattering models in Geant4

Multiple Coulomb scattering (MSC) is a fundamental component of charged-particle transport, describing the cumulative effect of numerous small-angle elastic scatterings with atomic nuclei. This effect becomes increasingly significant at lower energies, where the elastic scattering cross section increases and progressively dominates the particle transport behavior. An accurate description of MSC is therefore essential for realistic simulations of angular distributions and energy deposition patterns, particularly for electrons and positrons due to their low mass and the large number of elastic scatterings they undergo during propagation. The default MSC model used in the EmLivermore physics constructor changed from G4UrbanMscModel to G4GoudsmitSaundersonMscModel between Geant4 versions v10.4 and v11.2.

G4UrbanMscModel

The G4UrbanMscModel [155] was for many years the default MSC model for electrons and positrons below 100 MeV, and is applicable to a broad range of particles and energies. It is a semi-empirical condensed model designed with computational efficiency in mind, relying on approximations that perform well in typical detector simulations while offering good CPU performance. However, since the model is based on tuned empirical behavior rather than a fully theoretical formulation, it can exhibit limitations in accurately reproducing detailed angular distributions [156]. In addition, achieving improved accuracy often requires smaller step sizes, which can lead to an increased number of simulation steps and, consequently, higher CPU consumption.

G4GoudsmitSaundersonMscModel

While the Urban model satisfies the requirements of LHC experiments, users seeking higher accuracy in the simulation of electrons, positrons, and photons have traditionally favored algorithms developed in codes such as Penelope and EGSnrc. This was a primary motivation for the development of the Goudsmit–Saunderson (GS) multiple scattering model in Geant4. Grounded in the Goudsmit–Saunderson theoretical formalism [157], the GS model aims to provide a more accurate description of electron and positron scattering, particularly in low-energy regimes and near geometry boundaries where the empirical approximations of the Urban model can be less robust.
The G4GoudsmitSaundersonMscModel was introduced in Geant4 starting from version 10.4. However, due to its higher computational cost compared to the Urban model, it was not initially adopted as the default MSC model in the EmLivermore physics constructor. More recent improvements to the GS implementation [158] have significantly enhanced its performance and robustness, promoting it to the preferred choice in contexts requiring higher physical fidelity in electron and positron transport. As a result, the GS model has become the default MSC model

in the G4EmLivermorePhysics constructor.

For JUNOSW, retaining the more accurate GS model was a relatively straightforward choice. Additional investigation was made by replacing G4GoudsmitSaundersonMscModel with the G4UrbanMscModel within the EmLivermore physics constructor for Geant4 v11.2, while keeping optical processes enabled. The simulation produced a quenched energy distribution similar to the blue distribution we obtained in Figure 3.2. Consequently, it became mandatory to investigate which specific modifications within the G4GoudsmitSaundersonMscModel were responsible for the increased number of tracking steps in the electron simulation.

3.3.4 Goudsmit Saunderson boundary crossing management

In Geant4, MSC models treat particle crossings at geometry boundaries using a dedicated algorithm. This algorithm prevents excessively large last steps in a given volume and large first steps in the next volume. In practice, the step length around a boundary crossing is constrained to be no larger than the elastic scattering mean free path of the particle in the material. Following these small boundary steps, the particle is scattered according to a single-scattering law in order to accurately describe the boundary crossing.

In the Goudsmit Saunderson MSC model, the boundary crossing algorithm is controlled by a dedicated Presafety parameter. This parameter encodes whether a particle is considered close to a volume boundary and determines whether the single-scattering regime, and thus small step sizes, should be activated to ensure an accurate description of the boundary crossing. What is puzzling, however, is that the Presafety parameter effectively flags the particle as being close to a boundary at the very beginning of its track. As a consequence, the first tracking step is always limited by MSC, which lies at the heart of the behavior observed in Figure 3.1.

When optical processes are disabled, the electron track proceeds without interruptions : MSC limits the first step, after which ionization becomes the dominant step-limiting process for the remaining tracking steps. In contrast, when optical processes are enabled, the primary electron track is frequently interrupted to generate and transport secondary particles, namely optical photons. Once the tracking of these secondaries is completed and the primary electron tracking resumes, the Presafety parameter effectively treats this continuation as the start of a new track and re-enables the single-scattering algorithm. This mechanism is repeatedly triggered along the electron trajectory, leading to a systematic increase in the number of MSC-limited steps and providing a coherent explanation for the behavior observed in Figure 3.1.

One possible solution would be to postpone the tracking of all secondary particles until the primary electron tracking has been completed. This approach effectively mitigates the

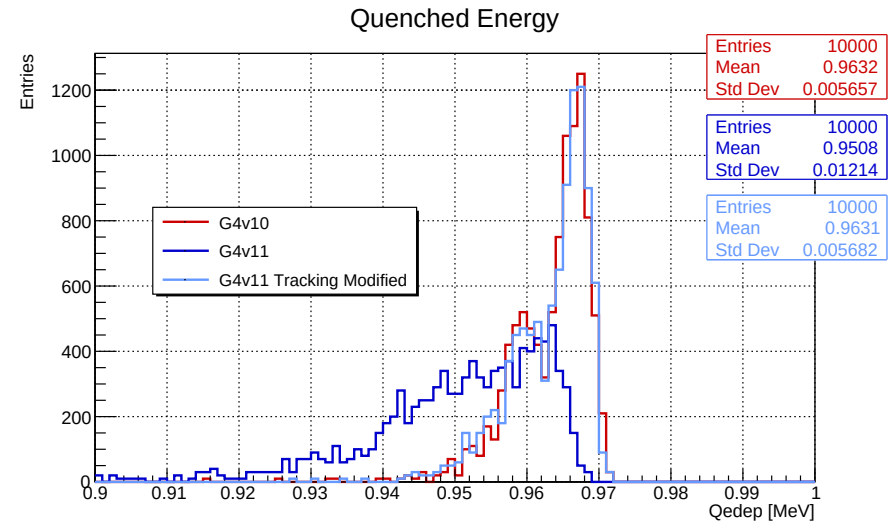

FIGURE 3.4 – Electron quenched energy distribution for different version of Geant4. The light blue distribution represents Geant4 v11.2 with optical photons tracking processed last.

issue by preventing the Goudsmit Saunderson Model from repeatedly triggering the single-scattering regime at each step. The resulting quenched energy distribution is shown by the light blue curve in Figure 3.4, where the Geant4 v11.2 results are in good agreement with those obtained using Geant4 v10.4. However, this solution is only viable for low-energy particles. As the energy of the primary particle increases, the number of secondary particles produced at each step grows significantly. Postponing the tracking of all secondaries until the end of the primary particle simulation places a substantial load on computational resources. This effect is illustrated in Figure 3.5, which shows the memory consumption for a 1 GeV muon simulation within JUNOSW. The light blue points correspond to simulations performed using Geant4 v11.2 with secondary tracking postponed, and they clearly demonstrate a sharp increase in memory usage, by approximately a factor of two for virtual memory and a factor of three for real memory.

As an additional observation, Figure 3.5 also highlights an overall reduction in memory usage when comparing Geant4 v10.4 to Geant4 v11.2. This improvement is consistent with the Geant4 release notes between these versions, which report multiple optimizations, leading to reduced overall computational resource consumption.

3.3.5 Electron simulation correction in new Geant4 release

The behaviour described throughout this section was communicated to the Geant4 developers in order to better understand what solutions could be implemented within JUNOSW. Ideally, the correction should effectively correct the increase in tracking steps while retaining the Goudsmit–Saunderson model in the EmLivermore physics constructor. Although the developers did not classify this behavior as a bug, and therefore did not propose an immediate

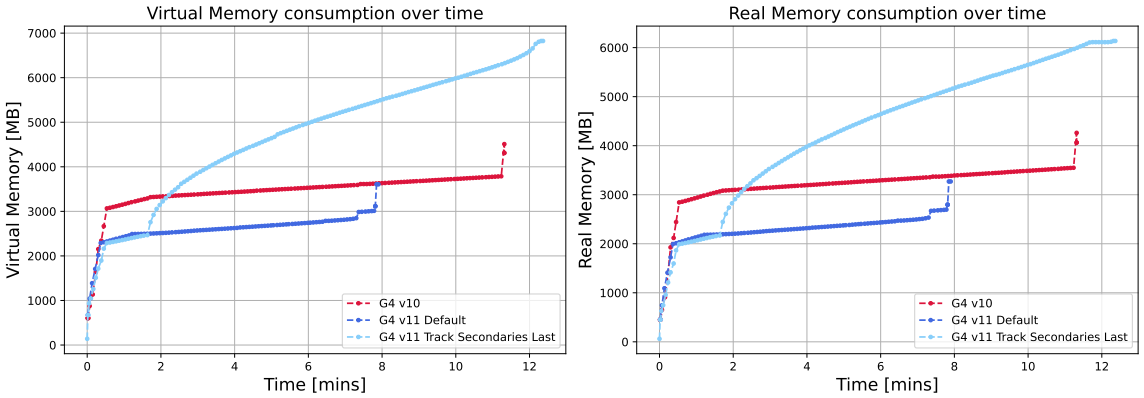

FIGURE 3.5 – Memory consumption of a 1 GeV muon simulation in JUNOSW using different version of Geant4. The light blue points represent Geant4 v11.2 with secondaries tracking processed at the end of the primary track.

corrective patch, the detailed investigations and feedback provided from our side contributed to further examination of the GS implementation. As a result of these exchanges, corrections to the treatment of the Presafety parameter in the Goudsmit–Saunderson model were scheduled in the December 2025 Geant4 release, with the objective of resolving the observed increase in tracking steps.

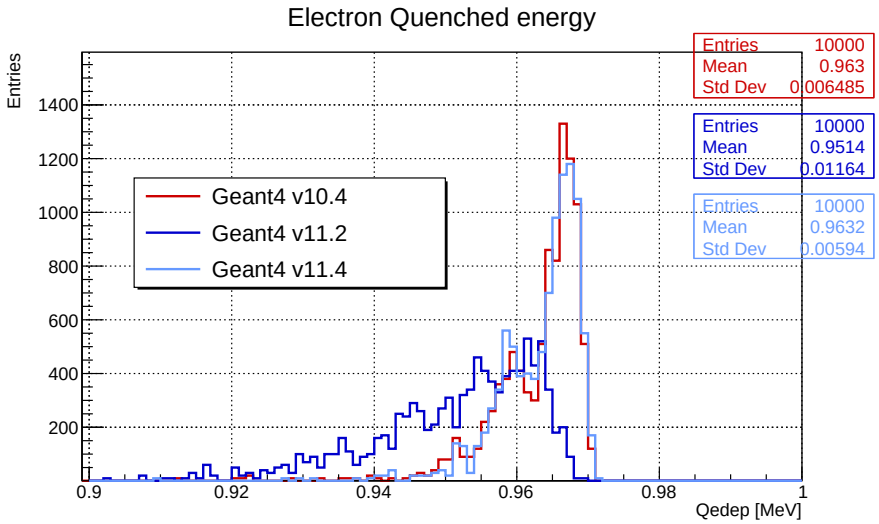

FIGURE 3.6 – Quenched energy distribution of a 1 MeV electron simulated in JUNOSW. The red curve corresponds to Geant4 v10.4, the dark blue curve corresponds to Geant4 v11.2, and the light blue curve corresponds to Geant4 v11.4.

On December 5th, 2025, Geant4 version 11.4 was released and integrated into JUNOSW for further validation. The comparison results are presented in Figure 3.6, where a very good agreement is observed between the quenched energy distributions obtained with Geant4 v10.4 and v11.4. In addition, a further reduction in memory consumption is observed in the more

recent Geant4 versions, as illustrated in Figure 3.7. Overall, Geant4 v11 produces simulations that are, on average, faster and more memory efficient than those obtained with Geant4 v10.4.

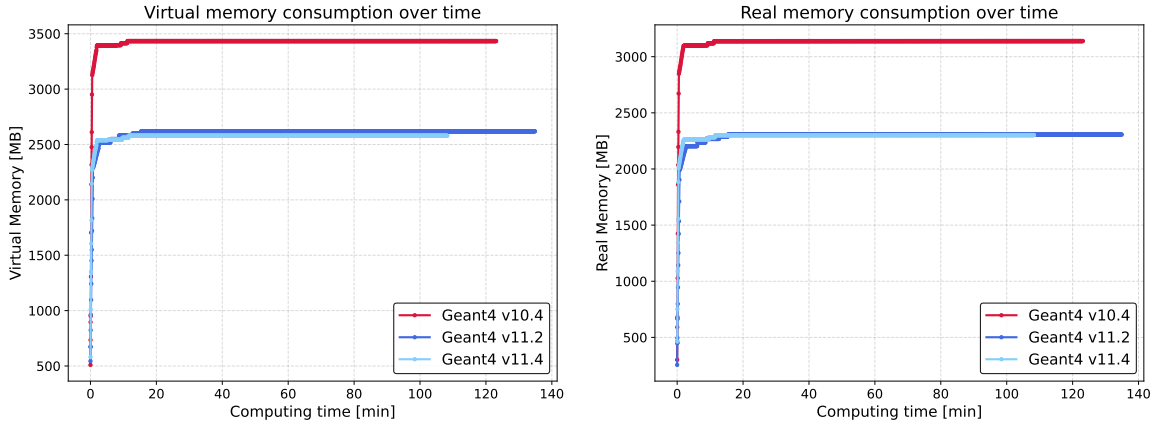

FIGURE 3.7 – Memory consumption of a thousand 10 MeV electrons simulated in JUNOSW.

3.4 Hadronic physics update in Geant4

An accurate description of hadronic processes is of key importance for JUNO. A major source of background in the selection of inverse beta decay (IBD) events arises from intrinsic radioactivity within the detector materials. The estimation of radioactive contamination is performed using Bi–Po transitions in the ^{238}U and ^{232}Th decay chains, which are characterized by a prompt β decay followed by a delayed α emission. This signature closely resembles that of an IBD interaction and can therefore constitute a significant background. It is thus essential to accurately model the energy deposition pattern and range of alpha particles in the JUNO liquid scintillator.

The IBD event selection relies on the time and spatial correlation betweeen the positron ionization signal and the characteristic 2.2 MeV γ ray emitted following the neutron capture on hydrogen happening $\sim$ 200 μs after the IBD interaction. Consequently, the simulation must also provide an accurate description of neutron transport in the liquid scintillator, including elastic scattering, thermalization, and eventual capture, as well as the correct modeling of the emitted gamma-ray energies.

This section presents comparisons made between Geant4 v10.4 and Geant4 v11.4 on α particles and neutron simulation within JUNOSW. No discrepancies were observed between Geant4 v11.2 and Geant4 v11.4 in the description of α particles and neutrons

3.4.1 Alpha Simulation

To assess possible discrepancies in the description of α particles between Geant4 versions, 10 000 events of 5.3 MeV α particles in the center of the detector have been simulated. The results are shown in Figure 3.8, where a clear difference in the treatment of α particles is observed between Geant4 v10.4 and Geant4 v11.4.

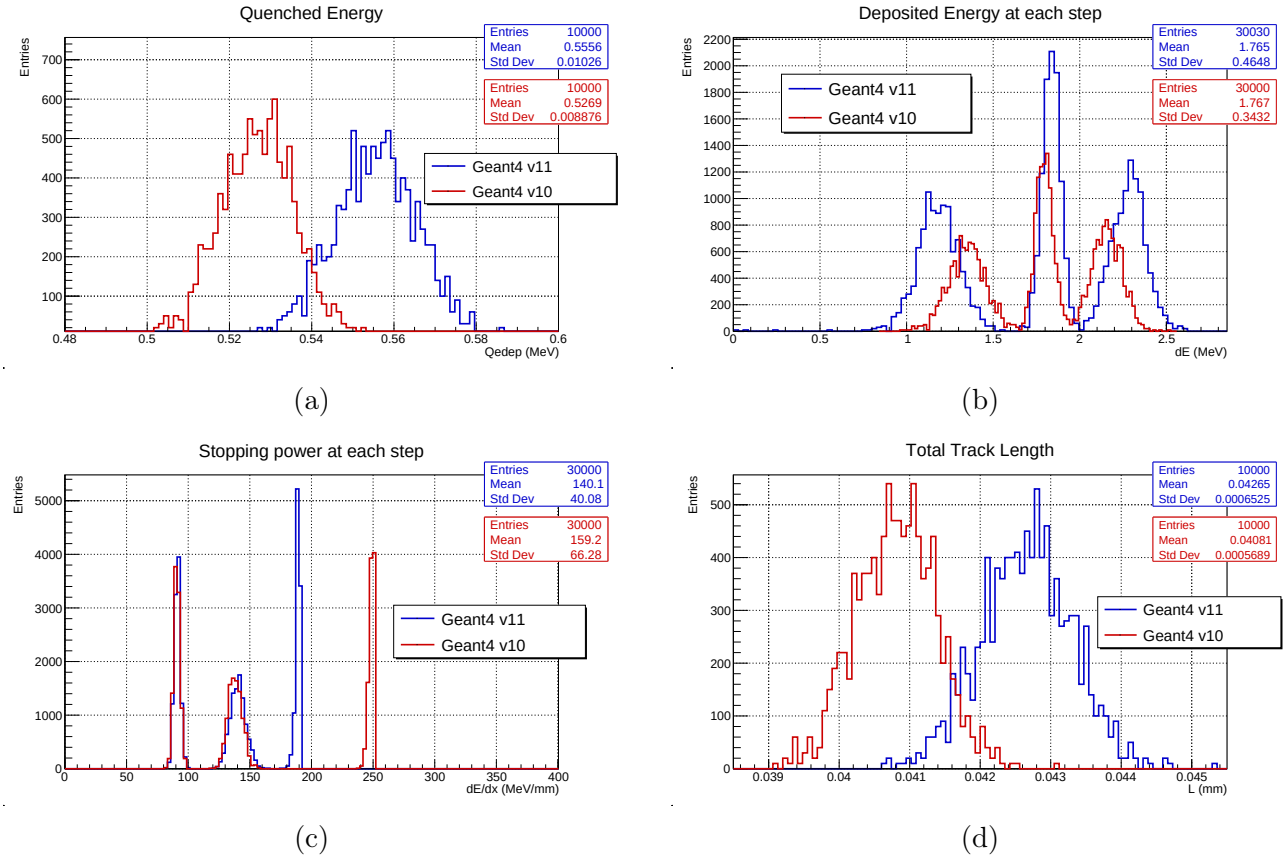

FIGURE 3.8 – Few distributions form the simulation of a 5.3 MeV alpha in JUNOSW : **(a)** Total quenched energy computed using Birks formula at each step then summed over the number of steps. **(b)** Alpha deposited energy at each step. **(c)** Stopping power of the alpha computed at each step of the track by diving the deposited energy (dE) by the step length (dx). **(d)** Total Alpha track length.

As illustrated in Figure 3.8b, the α track is typically divided into three tracking steps, with the deposited energy at each step being, on average, similar in both versions of Geant4. However, Figure 3.8c reveals discrepancies in the stopping power that appear only in the final step of the track, leading on average to reduced stopping power using Geant4 v11.4. As a consequence, the quenched energy computed using Eq. 3.1 is, on average, slightly increased in Geant4 v11.4 as illustrated in Figure 3.8a.

Another notable difference in the treatment of α particles is shown in Figure 3.8d, where a slight increase in the total track length is observed when comparing Geant4 v10.4 and Geant4

v11.4. The observed difference in stopping power can be traced back to the Geant4 v11.0 release notes, which mention the removal of additional corrections previously applied to ion stopping powers in the final tracking step. However, no explicit reference is made to the corresponding increase in total track length.

To determine which Geant4 version provided the more accurate value of α range, we can performed an independent simulation using SRIM (the Stopping and Range of Ions in Matter) [159]. SRIM is a group of programs that calculate the stopping and range of ions into matter using quantum mechanical treatment of ion-atom collisions. Within SRIM, the TRIM (the Transport of Ions in Matter) algorithm allows for detailed particle simulations in more complex user-defined targets that can go up to eight layers of material. Using TRIM, 5.3 MeV α particles were simulated in linear alkylbenzene (LAB), the solvent of JUNO liquid scintillator, in order to estimate their range in the material. The result, shown in Figure 3.9, gives an average α range of R = 42.3 μm, which is in very good agreement with the value R = 42.6 μm predicted by Geant4 v11.4.

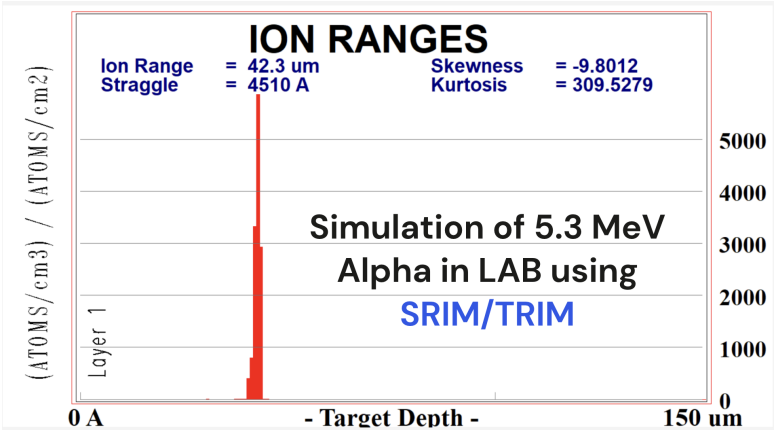

FIGURE 3.9 – 5.3 MeV alpha simulated range in LAB using SRIM/TRIM.

Based on this agreement, it is clear that the updated α description in Geant4 v11.4 provides a more accurate modeling of ion transport. Consequently, the default treatment of α particles in Geant4 v11.4 will be kept without modifications for JUNOSW. However, due to higher quenched energy in Geant4 v11.4, Birk's constant for α particles will require additional tuning in JUNOSW using data.

3.4.2 Neutron Simulation

Neutron simulations checks are a bit difficult to perform within JUNOSW because of all the modifications that were applied to the G4HadronPhysicsQGSP_BERT_HP physics constructor for low energy neutron (< 20 MeV). Inside the customized Geant4 v10.4, the neutron

capture builder has a dedicated configuration for important isotopes (^{12}C, ^{13}C, ^{16}O, ^{17}O, ^{155}Gd ...) where the correct gamma rays are produced according to tabulated data from the National Nuclear Data Center (NNDC). Only the hydrogen is left free to be handled by Geant4 default final state builder. However, recent versions of Geant4 have introduced significant improvements in the treatment of neutron thermalization and following capture on various isotopes. Therefore, a test on the default parametrization of the G4HadronPhysicsQGSP_BERT_HP physics constructor is conducted in Geant4 v11.4, and compare with our customized version implemented inside Geant4 v10.4. Table 3.2 details the configuration of each Geant4 versions in the description of neutron capture processes.

Geant4 Version	10.4.2 (JUNOSW)	11.4.2 (Official)
Hadronic Model	QGSP_BERT_HP	QGSP_BERT_HP
Neutron Builder	G4ParticleHPCapture	G4NeutronRadCaptureHP
Neutron Cross Section Builder	G4ParticleHPCaptureData	G4NeutronCaptureXS

TABLE 3.2 – Hadronic inelastic configuration in Geant4 versions.

3.4.3 Neutron Capture on Hydrogen

Figure 3.10 illustrates the results obtained for 2 MeV neutrons simulated in JUNOSW and captured on hydrogen (^{1}H). The energy of the emitted γ ray in the default Geant4 v11.4 setup (dark blue curve) is consistent with the expected value of ∼2.223 MeV. The slight discrepancy we have between the gamma energy produced by Geant4 v10.4 (red curve) and the experimental value, is a known inaccuracy of v10.4 which uses outdated nuclear data. The fix in v11 brings it within ∼1 keV of the true measured value. Therefore, Geant4 v11.4.2 provides a more accurate description of the gamma emitted following neutron capture on ^{1}H. However, the capture time $\tau \sim 400$ μs, obtained using default v11.4, is approximately two times bigger than the expected value $\tau \sim 200$ μs obtained with v10.4.

This difference can be explained by the introduction of new data base within QGSP_BERT_HP : G4NeutronHPCaptureXS, a compact cross-section database derived from the HP database and mainly optimized for speed, stability and to provide reasonable cross section for transport but not enough precision for neutron lifetime studies. In contrast, the G4NeutronHPCaptureData uses evaluated nuclear data from a wide range of isotopes and provide more accurate results ; this is also the data base used in our custom G4HadronPhysicsQGSP_BERT_HP implementation in Geant4 v10.4, where the name has changed from v11.4 onward. Once we replace the neutron capture data base in Geant4 v11.4 we obtain results in good agreement with experimental results and Geant4 v10.4, as illustrated by the light blue curve on Figure 3.10b.

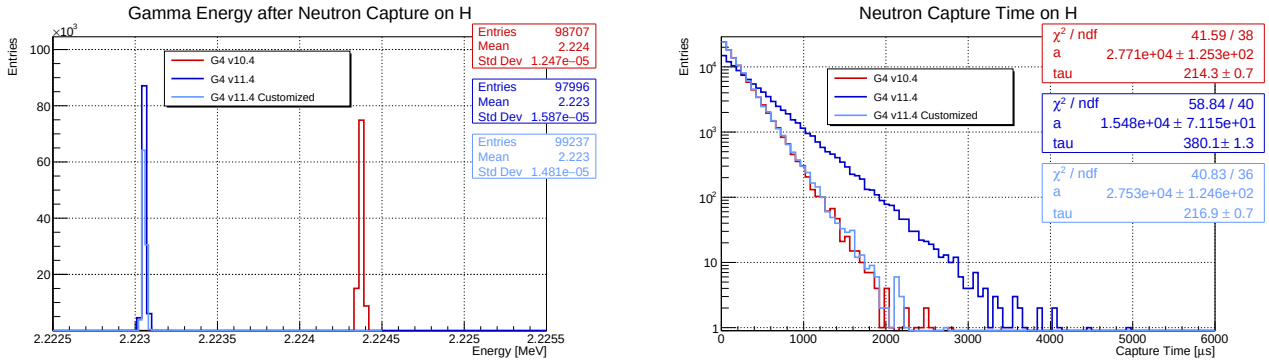

(a) (b)

FIGURE 3.10 – Neutron capture on hydrogen : **(a)** Emitted γ ray. **(b)** Neutron capture time.

3.4.4 Neutron Capture on Carbon

Similarly to the neutron capture on hydrogen, tests were performed for neutron capture on carbon-12 (^{12}C). As opposed to the capture on hydrogen, multiple gammas can be emitted following neutron capture on carbon. The energies of the emitted gamma rays are listed in Table 3.3 along with their respective intensity. The capture is expected to produce a 4.945 MeV γ ray in ∼68 % of the decays, while in ∼32 % of the cases, the two γ rays of 1.261 MeV and 3.683 MeV are emitted. Other energy transitions are much rarer. Moreover, the capture on carbon is less frequent in JUNO than capture on hydrogen, which makes observation of less probable ^{13}C energy transition even more challenging.

Type	**Energy [MeV]**	**I(γ)/I$_{max}$(γ) [%]**
Primary	4.945	100
Secondary	3.683	47.6
Secondary	3.088	0.64
Primary	1.856	0.237
Primary	1.261	48.0
Secondary	0.595	0.356

TABLE 3.3 – Energies and intensities of neutron capture gammas on ^{12}C. Taken from the National Nuclear Data Center.

The simulation results of neutron capture on carbon are presented in Figure 3.11. Similarly to the results on hydrogen, the red curve corresponds to simulations performed in JUNOSW using our customized QGSP_BERT_HP constructor and Geant4 v10.4, while the dark blue curve represents the default QGSP_BERT_HP parametrization in Geant4 v11.4. It is clear, when comparing these two setups, that the default configuration of v11.4 is not able to accurately describe neutron inelastic behaviour in JUNO.
As in the hydrogen case, the neutron capture time on carbon is two times bigger in Geant4

v11.4, but can be easily corrected by replacing the NeutronHPCaptureXS database by the NeutronHPCaptureData, as illustrated by the light blue curve in Figure 3.11b. More importantly, the γ-ray spectrum obtained with the default Geant4 v11.4 configuration presents unfavored ^{13}C energy transition, where 1.856 MeV and 3.088 MeV γ rays are emitted with higher intensities than expected.

The emitted gamma rays from neutron capture on a given isotopes are handled by Geant4 neutron high precision (HP) capture builders and more specifically by how builders handle the nucleus final state. In the customed version of QGSP_BERT_HP used in JUNOSW for Geant4 v10.4, the final state of selected isotopes (Gadolinium, Carbon, Oxygen, Nitrogen...) have been carefully altered to produce correct gamma-ray spectra. Over the years, several improvements have been made on Geant4 Neutron-HP package [160, 161] to enhance builders accuracy such as the NeutronRadCaptureHP : one of the default builders of the QGSP_BERT_HP in Geant4 v11.4. However, this builder only does a specific handling of isotopes with atomic number A $\leq$ 4, for heavier isotopes the builder uses a general model, the Photon Evaporation model, to build nuclei final states including the emitted gamma rays, and seems to not be very accurate in describing ^{13}C.

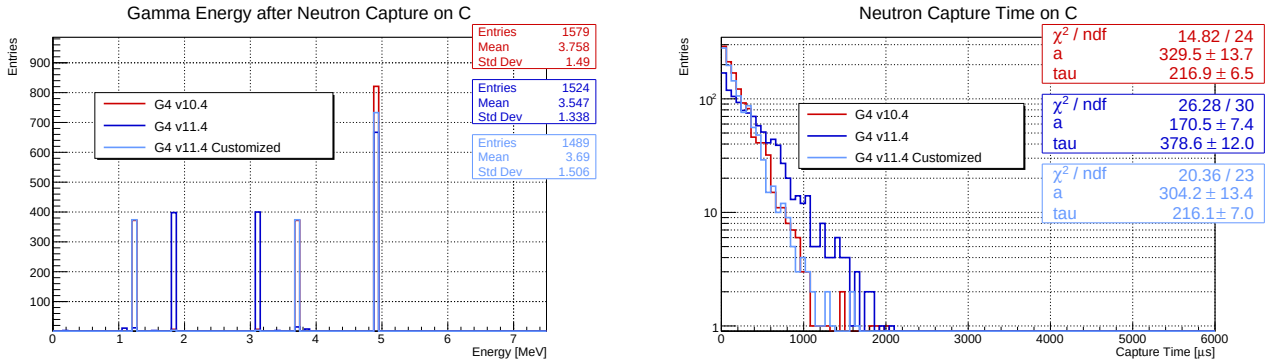

(a) (b)

FIGURE 3.11 – Neutron capture on ^{12}C : **(a)** Emitted γ rays. For E=1.261 MeV and E=3.683 MeV, the red and light blue curve are overlapping each other. **(b)** Neutron capture time.

The wrong gamma ray intensities can be corrected by changing the default builder in QGSP_BERT_HP with G4NeutronHPCapture, which is also used in our custom Geant4 v10.4. The result of this modification on the γ-ray spectrum is highlighted by the light blue curve on Figure 3.11a, where Geant4 v11.4 produces the γ rays with correct intensities and is in good agreement with Geant4 v10.4. However, the use of this builder lead to an unexpected behaviour on the γ-ray spectrum of neutron capture on H : instead of a single 2.223 MeV γ emitted following the capture on ^{1}H, several low energy gammas are produced with energies that summed to 2.223 MeV, as illustrated in Figure 3.12. This is a known bug that was already reported in v11.3 and was allegedly fixed at the release of v11.4. However, the bug is still present and

solutions to fix it are not documented.

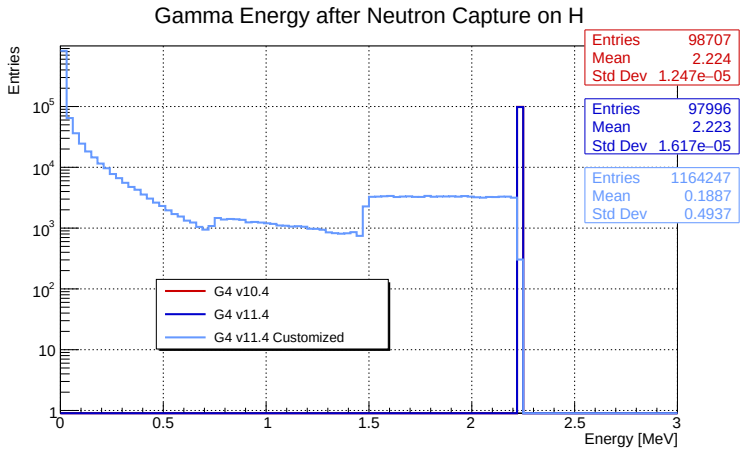

FIGURE 3.12 – Gamma-ray spectrum of neutron capture on ^{1}H using G4NeutronHPCapture builder in Geant4 v11.4 compared to the spectrum obtained with Geant4 v10.4 with the same builder and Geant4 v11.4 with the default builder (G4NeutronRadCaptureHP).

The issues in Geant4 v11.4 description of neutron capture on ^{12}C were reported to Geant4 developers, but no straightforward solution was found. This behaviour seems to be caused by improper reading of the Evaluated Nuclear Structure Data File (ENSDF) used by the Photon Evaporation model within G4NeutronRadCaptureHP. A fix is on-going by the Geant4 developers at the time this thesis is being written, but an immediate correction of the neutron simulation is required in order to proceed with the Geant4 upgrade in JUNOSW.

3.4.5 Correction to Neutron Simulation

The correction of neutron simulation in JUNOSW can be done in two ways :

— Customize the G4NeutronRadCaptureHP builder, so it uses JUNO's tabulated γ energies for carbon and other isotopes while keeping its good description of the γ emitted from neutron capture on ^{1}H.

— Use the already existing customized QGSP_BERT_HP inside JUNOSW, tune it so it's compatible with v11.4 of Geant4, and correct the n-H γ-ray spectrum.

The former solution requires a lot of effort in understanding the structure of the G4NeutronRadCaptureHP, and building additionnal programs to handle the different isotopes, while, the later is easier to implement since all the code is already written, and only compatibility checks needs to done.

The latter option was chosen, leading to use the G4NeutronHPCapture builder, customed for JUNOSW, where the correct gamma rays energies for ^{12}C and other isotopes are specified. An additional file is added to correct the behaviour in Figure 3.12 on the emitted γ-ray from neutron capture on ^{1}H. The corrected γ-ray spectrum form neutron capture on ^{1}H is given in

Figure 3.13. The slight discrepancy we see between our custom version of Geant4 v11.4 and its default configuration can be explained by the data-base used to read the gamma energy. JUNO gamma energy files are based on NNDC tabulated data while the Photon Evaporation model, used in the default configuration of G4NeutronRadCaptureHP, uses ENSDF, which may have slightly different values of the n-H emitted γ ray.

Following the modifications listed throughout this chapter, Geant4 v11.4 has been implemented in JUNOSW.

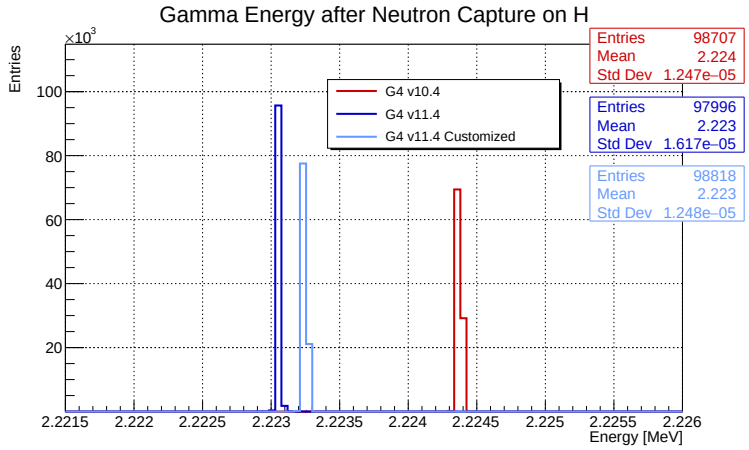

FIGURE 3.13 – Neutron capture on ^{1}H : corrected γ-ray spectrum using JUNOSW custom G4ParticleHPCapture builder.

3.5 Cosmogenic Yield Simulation

Cosmogenic isotopes created by muon spallation on ^{12}C, especially ^{9}Li and ^{8}He, constitute one of the most important source of background for JUNO neutrino mass hierarchy determination. These unstable isotopes often decay by (β-n) process, perfectly mimicking the inverse beta decay signature. This section assesses the ability of Geant4 v11.4 to reproduce the cosmogenic isotope production yields measured by past experiments, and compares the simulated yields against experimental data from KamLAND [162] and Daya Bay [163] rescaled to the JUNO detector conditions.

3.5.1 Geant4 v11.4 Simulation

The cosmogenic yield simulation uses a dedicated muon generator implemented in JUNOSW, based on the MUSIC [164] muon transport code, which simulates a realistic muon flux at the JUNO site and generates an ASCII event file providing the muon kinematics at the detector boundary. This file is used as input to Geant4, which then handles the muon propagation through the detector and the full simulation of secondary particle production, including

hadronic interactions responsible for isotope production via spallation.
The simulation is performed by disabling all optical processes, PMT geometry, and only looking at secondary generation through inelastic hadronic processes. Each isotope yield is estimated by counting the total number of generated isotope i divided by the number of simulated muons (here 10 millions).

3.5.2 Expected Yield at JUNO site

The production yield Y_i of a cosmogenic isotope i by muon spallation is known to follow a power-law dependence on the mean muon energy $\langle E_\mu \rangle$:

$$Y_i = Y_0 \langle E_\mu \rangle^\alpha \tag{3.2}$$

where Y_0 and α are isotope-dependent parameters determined from different experiments measurements. The energy dependence arises from each production processes dependence to the muon mean energy, where at low energy real photon nuclear reaction is the dominant process, while neutron inelastic scattering contribution increases at higher energies [165].

Direct measurement of the cosmogenic isotope yields in LAB-based liquid scintillator has been performed by the KamLAND [162], Daya Bay [163], and Double Chooz [166] experiments. Since these experiments operate at different mean muon energies, detector geometries and liquid scintillator recipe, the measured yields are rescaled to JUNO conditions using Eq. 3.2, accounting for the difference in mean muon energy $\langle E_\mu \rangle$, mean muon track length $\langle L_\mu \rangle$ in the active volume, and liquid scintillator density ρ_{LS} :

$$Y_i = Y_0 \left(\frac{\langle E_\mu \rangle^{\text{JUNO}}}{\langle E_\mu \rangle^{\text{Exp}}} \right)^\alpha \cdot \langle L_\mu \rangle^{\text{JUNO}} \cdot \rho_{LS}^{\text{JUNO}} \tag{3.3}$$

where Y_0, α, and $\langle E_\mu \rangle$ are taken from measurement of KamLAND and Daya Bay, with the muon at JUNO site established to have $\langle E_\mu \rangle^{\text{JUNO}} = 207$ GeV, $\langle L_\mu \rangle^{\text{JUNO}} = 2313$ cm, and the LS density $\rho_{LS}^{\text{JUNO}} = 0.86$ g/cm^3 [167]. Consequently, the quantity resulting from Eq. 3.3 is a number of produced isotope i per muon, which is directly comparable with the quantity extracted from the Geant4 simulation describe above.

3.5.3 Results

The simulated cosmogenic isotope yields obtain with Geant4 v11.4 is compared to experimental measurement rescaled to JUNO in Figure 3.14. The top panel shows the yield per muon for each isotope, comparing the Geant4 v11.4 simulation with the KamLAND, and Daya Bay rescaled values. In addition to the directly measured isotope yields, a FLUKA-based simulation [168] performed by the KamLAND collaboration provides the expected yield of ^{6}He, ^{7}Be,

^{10}Be, and ^{13}B, shown as open red diamonds. The bottom panel shows the ratio of simulated to expected yield, providing a direct measure of the accuracy of Geant4 physics model.

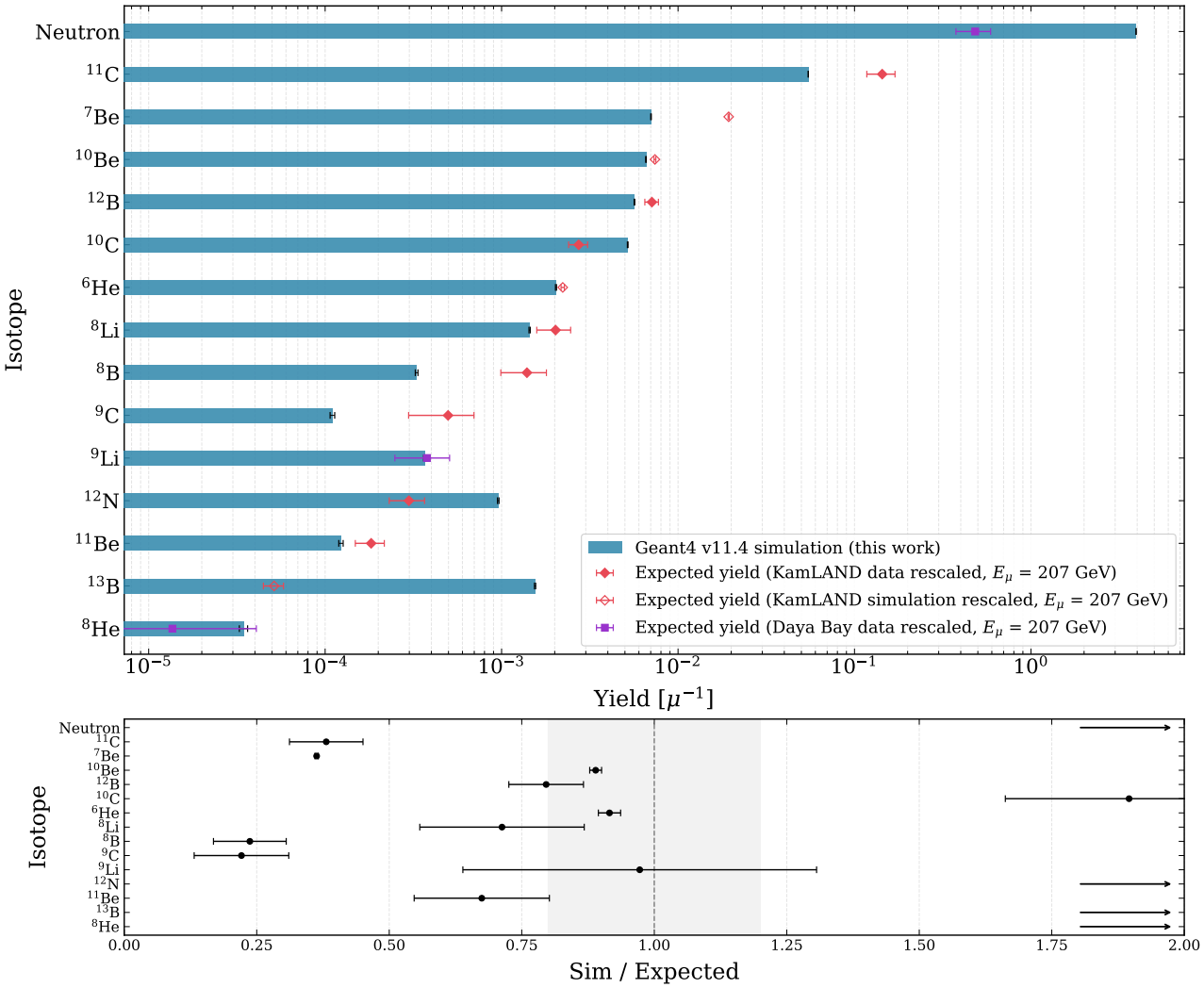

FIGURE 3.14 – Cosmogenic isotope yields per muon from spallation on ^{12}C. **(Top)** Simulated yield per muon using Geant4 v11.4 (the value is read from the right extremity of the blue band, with its associated uncertainty represented by the black lines), compared to the expected yield at JUNO, estimated from experimental (red full diamonds) and simulated (red open diamonds) measurements from KamLAND [162] and Daya Bay (purple squares) [163] rescaled to JUNO's mean muon energy and track length. **(Bottom)** Ratio of simulated to expected yield ; a value of unity indicates perfect agreement.

Geant4 description shows reasonable agreement on most isotopes, most notably ^{9}Li, whose simulated-to-expected ratio of ~ 0.95 is consistent with unity within its (relatively large) uncertainty. This is particularly significant given that ^{9}Li, alongside ^{8}He, are the dominant cosmogenic background of liquid scintillator based reactor neutrino experiments, whose extensive measurement of both isotopes have directly helped constrain Geant4 models.

The remaining isotopes show relatively worse agreement. Most fall within the simulated-to-expected ratio of roughly 0.2–0.9, indicating a systematic under-prediction by Geant4, while

neutrons, ^{12}N, ^{13}B, and ^{8}He are over-predicted by a factor $\gtrsim 1.8$. Notably, ^{8}He, despite being extensively studied together with ^{9}Li, shows the biggest uncertainty on its measured value, which is explained by the relatively low production rate measured by past reactor neutrino experiments [163, 162, 166, 169], compatible with 0.

Cosmogenic ^{9}Li/^{8}He are the only isotopes to have been extensively studied by past experiments, with KamLAND being the sole experiment to have provided an extensive study of the remaining cosmogenic isotope yields. The results shown in Figure 3.14 highlight the need for dedicated studies of the remaining isotopes in order to better constrain Geant4's hadronic models, where JUNO is ideally suited, providing additional constrains beyond the existing KamLAND measurements.

3.6 Conclusion

This chapter has described the JUNO simulation software and the work carried out to validate the upgrade of its Geant4 toolkit from version 10.4.2, to the most recent Geant4 version 11 release. This upgrade was motivated by the numerous physics and performance improvements implemented in recent Geant4 releases, and was conducted to make sure that JUNO's Monte Carlo simulation benefits from the most accurate and up-to-date modeling of particle interactions.

The validation study revealed several discrepancies between Geant4 versions. In electromagnetic physics, the quenched energy of electrons was found to be degraded due to the Goudsmit–Saunderson multiple-scattering model, used in the EmLivermore physics list, which mistook resuming the primary electron tracking after each optical secondary as the start of a new track in Geant4 v11.2. This behaviour was reported to the Geant4 developers and was corrected in the December 2025 release, where the resulting v11.4 reproduces the v10.4 quenched-energy distribution while also being faster and more memory-efficient. In hadronic physics, a comparison against SRIM/TRIM confirmed that the updated α-particle stopping-power treatment in v11.4 is more accurate than in v10.4, at the cost of requiring a retuning of the α Birks constant in JUNOSW. The neutron-capture description, however, shows discrepancies for capture on ^{12}C, and was corrected using a JUNOSW-specific customisation of the capture cross-section and emitted gamma-ray database to correctly reproduce both the capture time and the ^{12}C and ^{1}H de-excitation gamma spectra. A definitive fix for this behaviour has not yet been provided by the Geant4 developers, and the comparison should be performed again once it becomes available. With these corrections in place, Geant4 v11.4 was integrated into JUNOSW.

Finally, the ability of the updated Geant4 version to reproduce cosmogenic isotopes produc-

tion by muon spallation on ^{12}C was assessed against yields measured by KamLAND and Daya Bay and rescaled to JUNO's site conditions. The simulation accuratly reproduces the yield of ^{9}Li, but shows more significant discrepancies for most other isotopes, including ^{8}He. ^{9}Li and ^{8}He are the only isotopes to have been extensively measured by multiple past experiments, with KamLAND being the sole experiment to provide yields for the remaining isotopes studied here. The discrepancies observed from this study motivate further dedicated measurements of these remaining isotope yields with JUNO, which would help constrain Geant4's hadronic models. Moreover, an extensive comparison using different Geant4 hadronic physics lists should be performed in order to provide a more precise MC/data comparison using this latest Geant4 release.

Overall, this validation effort shows that Geant4 v11.4 provides, after the corrections described in this chapter, a simulation of JUNO's electromagnetic and hadronic response consistent with the previous, well-validated v10.4.2, while offering improved computational performance. The next chapter presents a parallel validation effort targeting JUNO's energy response, in which this updated Geant4 version is one of several simulation components compared against calibration data collected during the initial phase of detector operation.

Chapitre 4

Simulation Validation of JUNO's Energy Response

Summary

4.1 Introduction . . . 122
4.2 Early liquid scintillator performance . . . 122
4.2.1 AmBe Source . . . 123
4.2.2 Selection Method . . . 125
4.2.3 Light Yield . . . 128
4.3 Performance of the JUNO simulation . . . 130
4.3.1 Optical parameters . . . 130
4.3.2 Data/MC comparison of the Light Yield . . . 133
4.3.3 Additional implementation to JUNOSW . . . 135
4.4 SPMT energy response . . . 136
4.4.1 Ge68 source . . . 136
4.4.2 First look at SPMT response . . . 139
4.4.3 Layer Response . . . 141
4.4.4 SPMT Photo Detection Efficiency . . . 144
4.5 Energy non-linearity . . . 146
4.5.1 Energy Computation Method . . . 147
4.5.2 Fitting methods . . . 150
4.5.3 Simulation validation . . . 151
4.6 Conclusion . . . 154

4.1 Introduction

Building on the Geant4 simulation upgrade presented in the previous chapter, this chapter focuses on the validation of JUNO's simulated energy response against calibration data, essential to assess the detector performance. As described in Chapter 2, the JUNO detector targets a precise measurement of the reactor antineutrino energy spectrum, a goal that places stringent demands not only on the detector hardware, but also on the understanding of the detector response itself. The Monte Carlo (MC) simulation is the primary tool through which this understanding is built and validated : it is used to verify that the observed detector behaviour is consistent with the underlying physical and optical model, to validate event reconstruction algorithms, and to estimate signal selection efficiencies and background contributions that cannot be easily isolated in data. The validation and tuning of the MC against calibration data is therefore a critical prerequisite to the JUNO physics program.

This chapter presents a series of data/MC comparisons aimed at validating JUNO's simulated energy response using calibration source data collected at different stages of the detector commissioning. These studies cover several key aspects of the detector response, from the modeling of light propagation and collection in the scintillator volume, to the characterization of the energy non-linearity and spatial non-uniformity of the detector. Section 4.2 presents an investigation of the detector light yield during the dual-phase filling period, providing an early probe of the optical model under commissioning conditions. The discrepancies observed during the commissioning period led to tuning of the simulation software described in Section 4.3, in order to better reproduce the light yield curves. The spatial non-uniformity of the detector energy response is investigated in Section 4.4 were a comparison between LPMT and SPMT is performed. Finally, Section 4.5 presents an extensive validation of the energy non-linearity using the full suite of JUNO calibration sources. In each case, discrepancies between data and simulation are used to identify and constrain the underlying detector effects, progressively building confidence in the optical and energy response model implemented in the JUNO simulation.

4.2 Early liquid scintillator performance

The detector response was monitored throughout the different filling phases using calibration sources deployed with the Automated Calibration Unit (ACU). In particular, the optical performance of the liquid scintillator was assessed from the early stages of the second filling phase, during which the Central Detector (CD) contained both liquid scintillator and ultra-pure water simultaneously — a configuration referred to as the *dual phase*.
During this period, the Americium-Beryllium (AmBe) source was deployed along the z-axis using the ACU, allowing the light production and collection properties of the detector to be

evaluated at different positions, and providing the charge maps used to correct the reconstruction algorithms. A schematic representation of JUNO CD's dual phase and AmBe deployment is given in Figure 4.1.

This section presents the early characterization of the liquid scintillator optical response and the initial tuning of the JUNO MC simulation performed to bring it into agreement with data under these commissioning conditions. Most of the results presented are obtained using data taken with 3260 ton of LS, corresponding to a water/liquid scintillator interface located at $z \sim 9$ m.

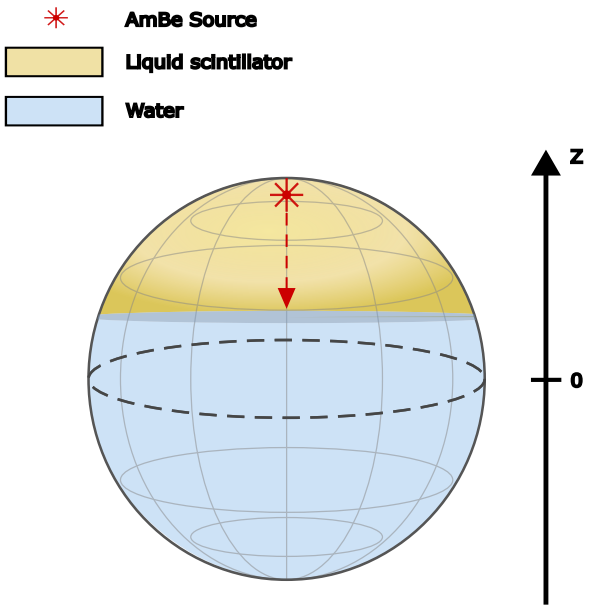

FIGURE 4.1 – Schematic representation of the JUNO Central Detector (CD) during the dual phase period. The deployment of the AmBe source was done along the z axis using the ACU, from the CD chimney to the LS/Water interface.

4.2.1 AmBe Source

Description

The AmBe source is composed of ^{241}Am and ^{9}Be and emits neutrons according to the reaction given by Eq. 4.1. The ^{241}Am first decay to ^{237}Np emitting an α particle. The α particles are emitted with energies primarily around 5.486 MeV (the dominant line, $\sim$85%) and are absorbed by the ^{9}Be within the source enclosure producing an excited ^{12}C* (or ^{12}C) and a fast neutron.

$$\begin{aligned} ^{241}\mathrm{Am} &\rightarrow {}^{237}\mathrm{Np} + \alpha, \\ ^{9}\mathrm{Be} + \alpha &\rightarrow {}^{12}\mathrm{C}^{*} \text{ (or } {}^{12}\mathrm{C}) + n \end{aligned} \tag{4.1}$$

In this process, the carbon can adopt multiple excited states, although only the first excited state emits γ–rays with an energy of 4.4 MeV [170] :

$$^{12}\mathrm{C}^{*} \rightarrow {}^{12}\mathrm{C} + \gamma \ (4.438 \text{ MeV}) \tag{4.2}$$

About 60% of reactions leave ^{12}C in the 4.44 MeV excited state (producing the gamma), while ∼40% leave ^{12}C in the ground state (no gamma emitted). Additionally, the emitted fast neutron will diffuse and eventually thermalize before being captured on a ^{1}H nucleus and produce a delayed γ with a characteristic 2.223 MeV energy. Similarly to the IBD, the selection of AmBe events is done through timing and spatial correlation between prompt and delay events.

Monte Carlo simulation

The JUNO software (JUNOSW) includes a dedicated generator for each of the calibration sources listed in Table 2.3, using any of the calibration systems described in Section 2.4.2 — in this case the ACU — allowing the simulated charge response to be directly compared with data. Figure 4.2 shows the prompt and delayed charge spectra of the AmBe source obtained from the JUNOSW simulation.

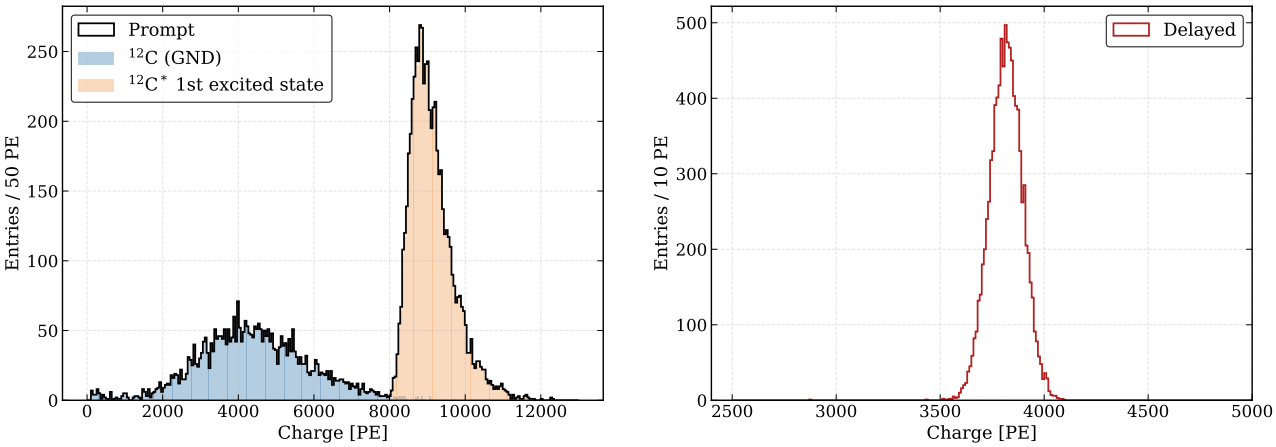

FIGURE 4.2 – AmBe prompt (left) and delayed (right) charge spectrum in photoelectron (PE), simulated using JUNOSW AmBe source generator. Both distributions are obtained from Geant4's true information and does not include additional effects such as dark noise or other electronics-related effects.

The prompt spectrum receives contributions from two distinct processes, depending on the final state of the ^{12}C nucleus produced in the ^{9}Be(α,n)^{12}C reaction :

— When ^{12}C is produced in its ground state, no gamma is emitted and the deposited energy is dominated by proton recoils induced by the neutron. This contribution corresponds to the low-charge region ([0 ; 8000] PE), highlighted in blue in the left plot of Figure 4.2.

— When ^{12}C is produced in its first excited state, it promptly de-excites by emitting a 4.4 MeV γ-ray. The deposited energy in this case is a combination of the neutron-induced proton recoils and the energy deposited by this γ, resulting in the higher charge contribution highlighted in orange in the left plot of Figure 4.2.

The delayed signal arises exclusively from the capture of the neutron on hydrogen, producing a 2.223 MeV γ-ray. Following thermalisation in the liquid scintillator, the neutron is captured on a free proton with a mean capture time of ∼200 μs, well separated in time from the prompt signal. The resulting delayed charge spectrum, shown in the right panel of Figure 4.2, appears as a relatively narrow peak with a mean value of ∼3800 PE.

Event Definition

In JUNO, a physics event is defined as any interaction producing sufficient light to trigger a minimum number of LPMTs within a 1 μs time window. The number of LPMT recording light within this window is referred to as the PMT multiplicity. For standard physics run, the trigger multiplicity threshold is set to a value of $\sim$ 350, corresponding to a visible energy threshold of $\sim$ 200 keV. For calibration runs, this threshold is often raised to suppress low-energy by-products from the source decay chain that would increase the trigger rate and contaminate the calibration sample of interest.

4.2.2 Selection Method

As mentioned previously, AmBe event selection in data relies on the time and spatial correlations between the prompt and delayed signals. Figure 4.3a presents the reconstructed z vs $\rho = \sqrt{x^2 + y^2}$ spatial distribution of events from an AmBe calibration run in which the source was deployed at $z = 15$ m, with the detector filled with 3260 ton of liquid scintillator. A clear localized concentration of events is visible at $z = 15$ m, spreading radially up to $\rho \sim 1.5$ m, consistent with the given range of the thermalization and diffusion of the neutron prior to capture. Under the same configuration, Figure 4.3b shows the LPMT charge distribution as a function of the reconstructed z position. A well-defined cluster of events is visible at $z = 15$ m, where the collected LPMT charge reaches up to ∼15000 PE, corresponding to the high-charge prompt contribution from the 4.4 MeV γ and neutron proton recoils discussed previously. A second distinct population is also visible at ∼4500 PE, consistent with the 2.223 MeV γ-ray from neutron capture on hydrogen, in good agreement with the prompt and delayed charge spectra expected from simulation and shown in Figure 4.2.

To further purify the AmBe candidate sample, complementary selection cuts are applied exploiting the prompt–delayed coincidence topology. The prompt (p) and delayed (d) signals are required to be spatially close, with $\Delta R_{p-d} < 2.0$ m, and temporally consistent with the neutron thermalization and capture timescale, with 10 μs $< \Delta t_{p-d} < 1.0$ ms. A multiplicity cut

is applied to reject events in which additional candidates fall within the prompt charge range in close temporal proximity to the prompt–delayed pair, suppressing accidental coincidences and pile-up. A muon veto is also applied to exclude events temporally associated with the passage of cosmic muons through the detector, preventing the selection of muon-induced backgrounds. A summary of all selection cuts applied to the AmBe sample is given in Table 4.1.

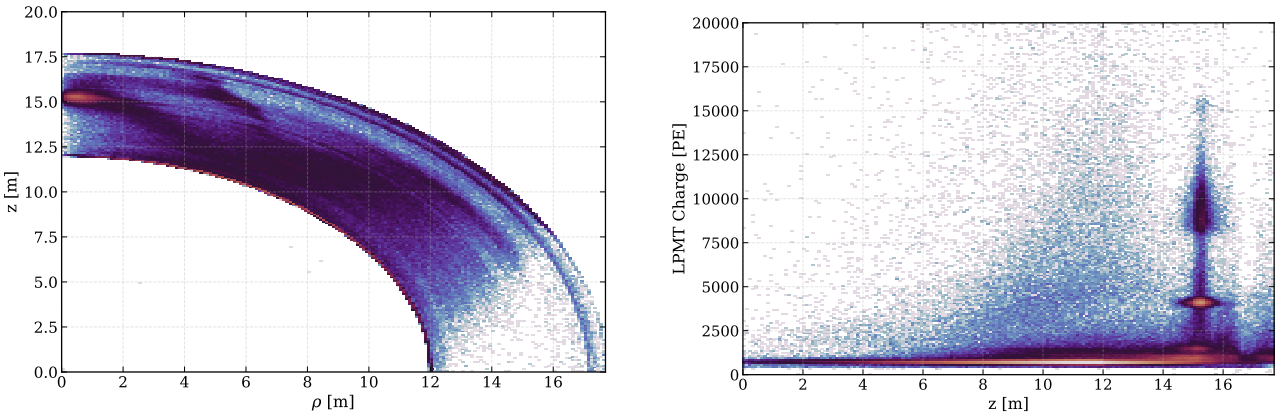

(a) (b)

FIGURE 4.3 – AmBe calibration run for a detector filled with 3260 ton of liquid scintillator and the source deployed with the ACU at z = 15 m. **(a)** z vs ρ distribution of the events. The hot spot at z = 15 m and $\rho < 2.0$ m corresponds to AmBe events. **(b)** LPMT charge as a function of the reconstructed z position of the events. The charge distribution at z = 15 m matches the expected prompt charge spectrum. The hot spot around 4000 PE corresponds to the delay γ–ray of 2.223 MeV.

Selection	**Value / description**
Prompt position	$\lvert z - z_{source} \rvert < 1.5$ m and $\rho < 2.0$ m
Prompt energy	1000 PE $< Q_p <$ 15000 PE
Delayed energy	2500 PE $< Q_d <$ 5000 PE
Prompt–delayed time diff. (Δt)	10 μs $< \Delta t <$ 1.0 ms
Prompt–delayed distance (ΔR)	$\Delta R < 2.0$ m
Multiplicity cut	No events in prompt charge range within 1 ms before the prompt, 1 ms after the delayed, or between p-d.
Muon veto	2 ms veto after CD PE > 30000

TABLE 4.1 – A summary of the selection criteria for AmBe events selection.

The effect of the selection cuts applied to the AmBe sample is illustrated in Figure 4.4. The prompt and delayed energy spectra, shown in Figures 4.4a and 4.4b, respectively, exhibit shapes that are in good agreement with the corresponding simulated spectra presented in Figure 4.2. Some discrepancies are nevertheless observed in the charge range between data and simulation.

These differences are likely attributable to missing contributions in the simulation, such as dark noise, afterpulsing, or other electronic effects, which are not included in the spectra of Figure 4.2.

Furthermore, the distribution of the prompt–delayed time difference, shown in Figure 4.4c, is well described by a simple exponential decay model :

$$f(t) = a \exp\left(-t/\tau\right) + c \tag{4.3}$$

The fit gives a value of c compatible with 0 and a fitted lifetime constant $\tau = 221.04 \pm 4.52$ μs, which is in agreement with the characteristic neutron capture lifetime of approximately 200 μs. This consistency provides additional validation of the AmBe event selection method.

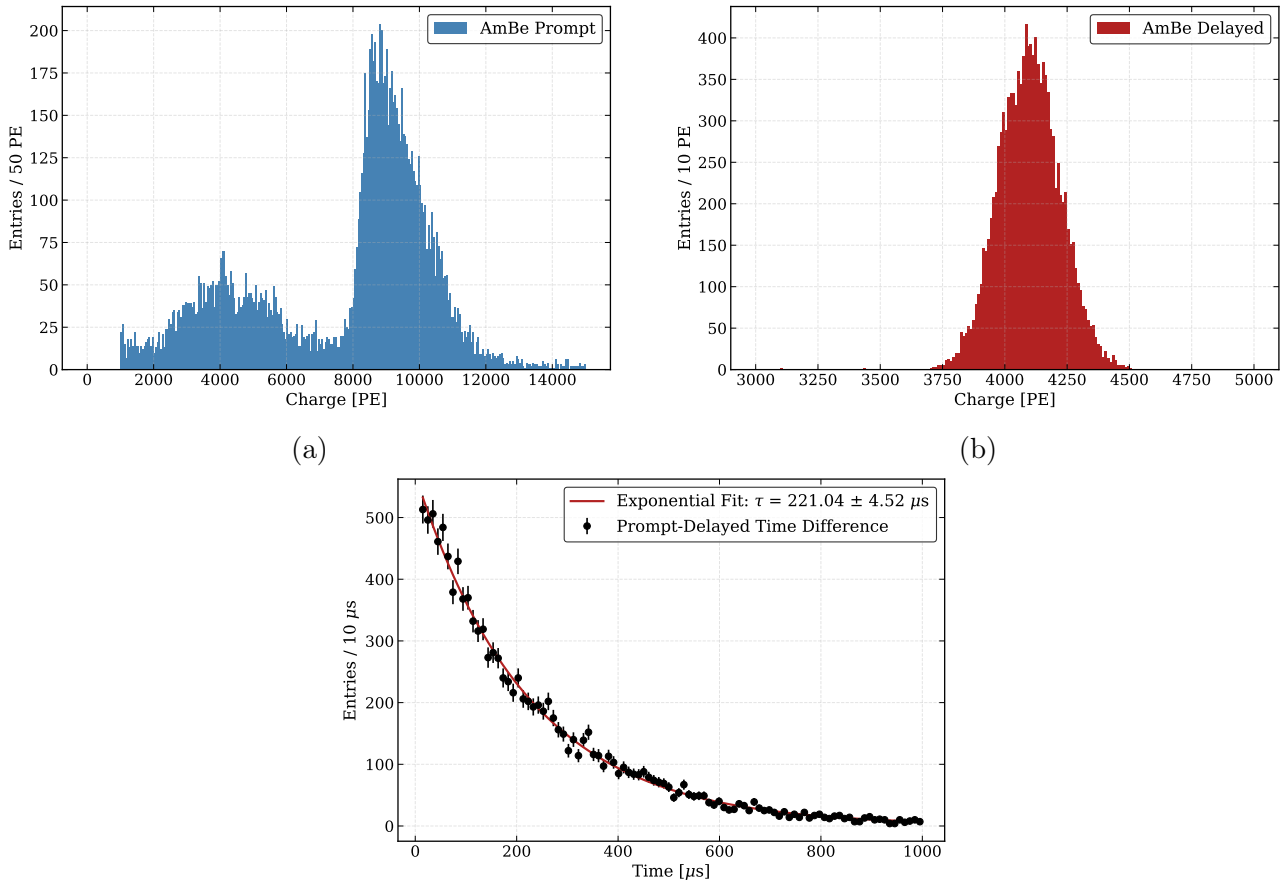

FIGURE 4.4 – Selected AmBe prompt **(a)** and delayed **(b)** events for a calibration run with the source placed at z = 15 m and the detector filled with 3260 ton of LS. **(c)** Time difference between the prompt and delayed events. The fitted lifetime $\tau \sim 221$ μs is in agreement with the expected value.

4.2.3 Light Yield

The monoenergetic signature of the AmBe delayed signal provides a clean probe of the liquid scintillator optical properties. One particularly important characteristic of the scintillator is the amount of photoelectrons collected per unit of deposited energy, referred to as the light yield (LY), which plays a significant role in achieving JUNO's target energy resolution.

Method

The light yield is defined as the amount of charge collected per unit of deposited energy :

$$\mathrm{LY} = \frac{Q_{PE}}{E_{dep}} \tag{4.4}$$

For the AmBe source, the light yield can be estimated directly from the delayed charge spectrum by extracting the mean charge associated with the 2.223 MeV neutron capture γ-ray. This is achieved by fitting the delayed charge spectrum with a Gaussian function and dividing the fitted mean value by 2.223 MeV.

However, the charge collected in the delayed time window is not exclusively from the AmBe signal, and contains additional contributions, the dominant one being dark noise from the LPMTs. To estimate this contribution, we make use of the detector's *periodic trigger*, which was specifically designed to sample the dark noise conditions in each run by triggering the detector periodically between physical events. The muon veto described in Table 4.1 is also applied to periodic trigger events to avoid contamination from muon-induced backgrounds in the dark noise charge estimation. Accounting for the dark noise contribution, Eq. 4.4 becomes :

$$\mathrm{LY} = \frac{Q_{PE} - Q_{DCR}}{E_{dep}} \tag{4.5}$$

where Q_{DCR} is the mean charge induced by dark noise and computed for each run.

Results

An example of light yield computation and dark noise estimation for the AmBe source placed at z = 15 m and 3260 ton of LS is given in Figure 4.5. The mean collected charge associated to the 2.223 MeV of deposited energy is obtained by fitting Figure 4.4b with a gaussian function. The result is given in Figure 4.5a, yielding $Q_{PE} = 4096.54 \pm 0.80$ PE.

The dark noise contribution is obtained by computing the charge distribution of periodic trigger events, as shown in Figure 4.5b. As can be seen, the distribution is not purely gaussian, as contribution from multi-PE dark noise events produce a tail at high charge values (> 600 PE). Applying a Gaussian fit in this case would bias the dark noise estimation, so the mean

value of the histogram is used instead as an estimator of the mean dark noise charge. This gives $Q_{DCR} = 497.49 \pm 0.76$ PE.
The resulting light yield for the AmBe source placed at $z = 15$ m is LY= 1619.01±0.50 PE/MeV, in close agreement JUNO's target value of 1665 PE/MeV [118].

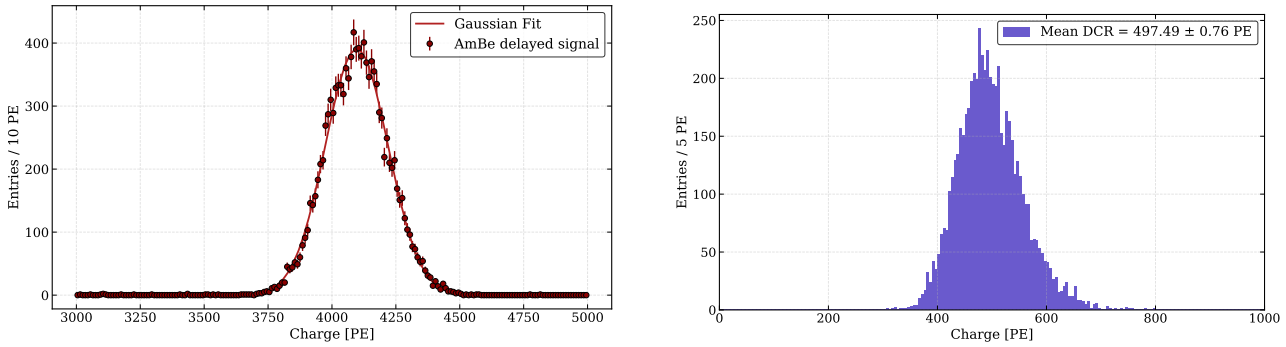

(a) (b)

FIGURE 4.5 – Example of light yield computation for the AmBe source deployed at z = 15 m with 3260 ton of LS. **(a)** AmBe delayed 2.223 MeV γ-ray charge spectrum fitted by a Gaussian function. **(b)** Measured dark noise-induced charge using the periodic trigger

The same procedure is applied across the full calibration campaign, in which the AmBe source was deployed at multiple z positions. The results are presented in Figure 4.6, where the red circles correspond to the 3260 ton filling configuration. In this configuration, the light yield is approximately stable at LY $\sim$ 1600 PE/MeV for $z < 16$ m, before decreasing at higher positions. Also shown on the same figure are results from an earlier period when only 1570 ton of liquid scintillator had been filled. The discrepancy in light yield between the two periods is attributed to the introduction of approximately 500 ton of off-specification liquid scintillator during the filling, where liquid scintillator batches with yellowish PPO were introduced inside the detector. As the filling progressed, the scintillator gradually homogenized, and the light yield recovered, closely reaching JUNO's requirements for the 3260 ton configuration.

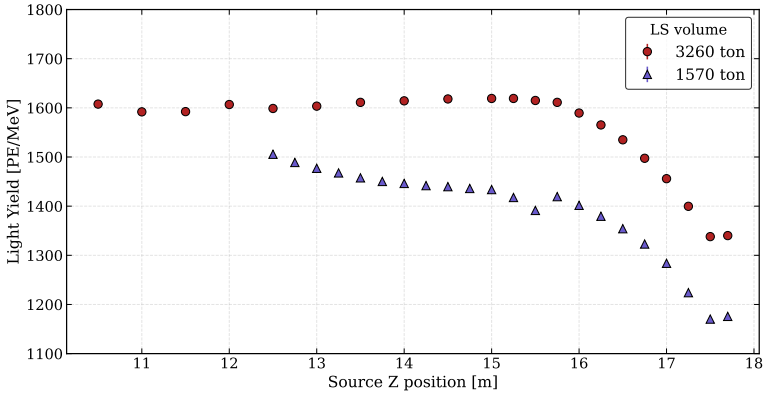

FIGURE 4.6 – Measured light yield using the AmBe calibration source at different z positions during JUNO's liquid scintillator filling. Results from two filling configurations are shown : 3260 ton (circle markers) and 1570 ton (triangle markers) of LS.

4.3 Performance of the JUNO simulation

The detector commissioning is also a good opportunity to assess the reliability of the JUNO detector simulation. JUNOSW's design allows to reproduce the exact configuration of the detector during the different filling phases, by allowing to build a detector in a dual or single phase of liquid scintillator and water, as illustrated by Figure 4.1, while allowing to move the LS/water interface freely. This is especially convenient as it allows to quickly tune the simulation and increase our knowledge of the detector as it is being filled.

4.3.1 Optical parameters

Prior to the end of civil construction and the beginning of the detector filling, several improvements were already made to the LPMTs optical response model inside JUNOSW, detailed in [171, 172], where 20% to 30% light yield increase was observed in the simulation when compared to the old optical response model. Additionally, measurements of the different materials optical properties were conducted during the commissioning of the detector, resulting in modifications of the liquid scintillator and water absorption length inside JUNOSW.

Water Attenuation Length

The water residing in the gap between the Acrylic sphere and the PMTs sphere requires accurate knowledge of the water optical parameters in order to correctly reproduce the photons light path and to estimate the number and the energy of the ones reaching the PMTs inside the simulation. This statement is especially true during the commissioning phase, due to the dual phase configuration of the detector : the light reaching the PMTs located below the LS/water interface must be accurately described.

The water attenuation length (WAL) is estimated through a dedicated system placed at the bottom of the water pool. It is composed of a high blue LED flasher (400nm) which emits light with a 1 kHz trigger frequency, and is collected on five PMTs, facing the LED at distances of 4.9 m, 9.9 m, 13.2 m, 20.5 m, and 24.2 m A visualization of the WAL system and its installation is given in Figure 4.7.

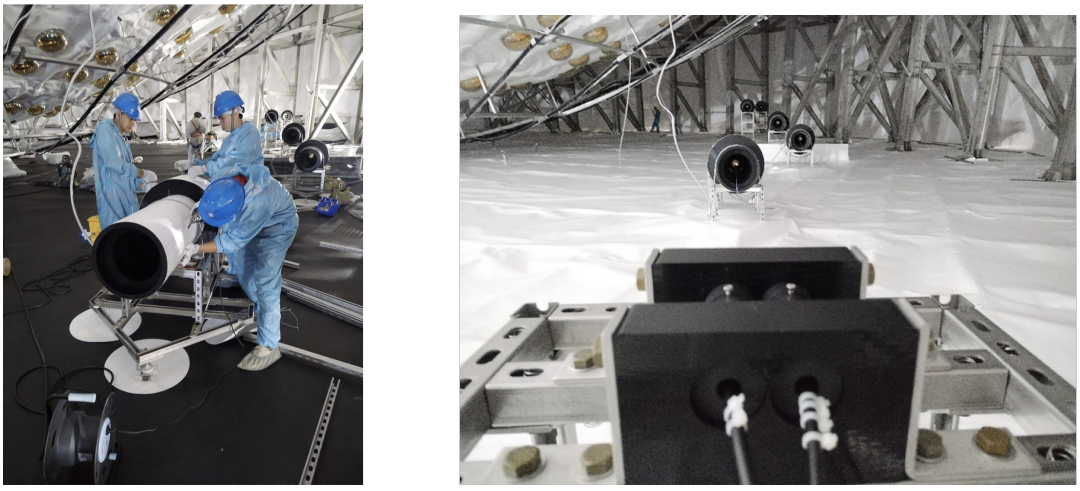

(a) (b)

FIGURE 4.7 – **(a)** Installation of JUNO WAL system. **(b)** Illustration of the PMTs positions along the LED optical path.

The WAL measurement is based on Beer-Lambert law [173] :

$$\mathrm{I} = \mathrm{I}_0 e^{-\frac{x}{\lambda_{att}}} \tag{4.6}$$

where I_0 is the incident intensity, x is the path the light travels and λ_{att} is the attenuation length. The light intensity collected on the PMTs gives five values for different distances from the LED which can be fitted with an exponential model to retrieve the attenuation length. The water absorption length can be obtained from the attenuation length using :

$$\frac{1}{\lambda_{att}} = \frac{1}{\lambda_{scat}} + \frac{1}{\lambda_{abs}} \tag{4.7}$$

where λ_{abs} is the absorption length, and λ_{scat} is the scattering length, which, in the case of ultra-pure water, is dominated by Rayleigh scattering with a value assumed to be 200 m at 400 nm.

The first measurement of the water absorption length at the end of the water filling phase gave $\lambda_{abs} = 26$ m at 400 nm. Following the start of the water circulation, the absorption length increased before stabilizing to $\lambda_{abs} = 59.88$ m at 400nm, which is referred to as the first sample.

The introduction of nitrogen to the water, in order to re–gas the SPMT connectors, made the absorption length further increase, reaching $\lambda_{abs} = 100$ m at 400nm, referred to as the second sample.
In JUNOSW, the water absorption length is defined for $\lambda_{abs} \in [100; 800]$ nm where the value of 40 m at 430 nm is taken as reference, which corresponds to ∼30 m at 400 nm. Using the latest measurements, the water absorption length used in JUNOSW was scaled using the measurements at 400 nm. The resulting distributions and absorption length value at 400 nm and 430nm for the first and second samples are given in Figure 4.8.

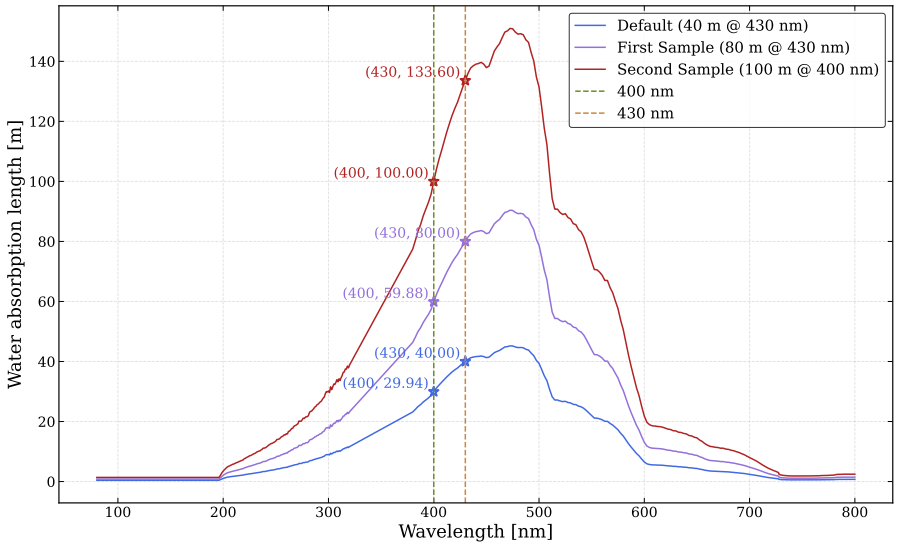

FIGURE 4.8 – Input water absorption length in JUNOSW for different photon wavelength. The default input is represented by the blue distribution. The purple and red distribution are scaled from the default one using the water absorption length of the first and second sample measurement respectively.

LS Attenuation Length

The liquid scintillator is the most important component of JUNO, where the optimization of its optical properties are crucial in order to reach the 3% target energy resolution.
Similarly to water measurement, the liquid scintillator absorption length was evaluated based on Beer Lambert law. However, because of the dual phase configuration of the detector, the light collected on each PMT must also account for possible refraction or total internal reflection on the liquid scintillator/water interface when computing the distance of the light source from the PMT. The measurement was made using a 420 nm laser placed at different z positions inside the detector, ranging from $z = 0$ m to $z = 15$ m, and deployed using the ACU. The reference value set for the liquid scintillator absorption length in JUNOSW was set to 77 m at 430 nm. The first measurement performed using both LPMT types during the early commissioning of the detector, yielded an average value of ∼25.0 m when scaled at 430 nm, significantly lower than the nominal expectation. This discrepancy is attributed to the poor optical quality

of the liquid scintillator batches introduced in the early stages of the filling, as discussed in Section 4.2. A second measurement was performed once the detector was fully filled, where the liquid scintillator absorption length had stabilized at ~ 86.50 m at 430 nm, exceeding the nominal value. The early identification of off-specification batches allowed to promptly correct the purification process, leading to a homogeneous liquid scintillator volume with optical properties surpassing the original requirements.
The resulting liquid scintillator absorption length, defined in the simulation for $\lambda \in [100; 900]$ nm is given in Figure 4.9 for both sample measurements.

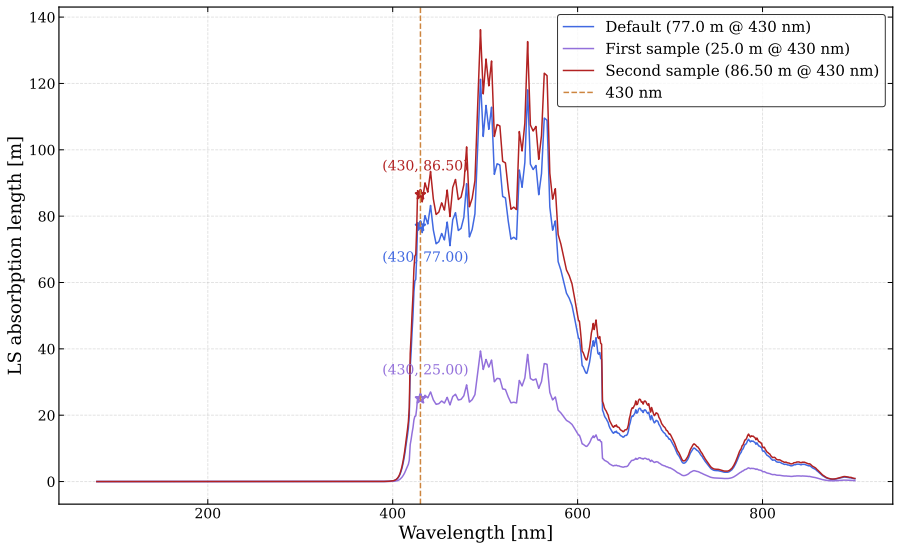

FIGURE 4.9 – Input liquid scintillator absorption length in JUNOSW for different photon wavelength. The default input is represented by the blue distribution. The purple and red distribution are scaled from the default one using the liquid scintillator absorption length of the first and second sample measurement respectively.

The result presented in the next section are obtained with a simulation tuned to the first liquid scintillator sample measurement of 25.0 m at 430 nm, as the second sample value was obtained and integrated into the simulation at a later stage.

4.3.2 Data/MC comparison of the Light Yield

Simulation Setup

To assess the accuracy of the simulation, the light yield results obtained in Figure 4.6 are compared with the results of a dedicated MC simulation of the AmBe source, produced for the same detector configuration (3260 ton of liquid scintillator). The source is simulated inside its enclosure and deployed at the same z positions with the simulated ACU geometry.

The simulation used for this comparison corresponds to the JUNO detector simulation level, referred to as JUNO DetSim. At this level, the simulation solely includes the Geant4 description

information of the detector geometry and components characteristics, in particular the liquid scintillator optical performance and PMTs photo detection efficiency. Simulation of the electronics was not performed, which was still under active tuning. The main contribution from the electronic simulation to the charge spectrum comes from the dark noise, which was effectively removed from the AmBe data as illustrated previously, making the DetSim level simulation a meaningful reference to compare to the data.

In order to make the simulation as realistic as possible to the data, one must account for the detector hardware configuration on a run by run basis, which is essentially the number of PMTs available and presenting good performance during a given run. A list of "bad PMTs" is provided for each run, where the PMTs that exhibit oscillating high voltage, flasher patterns, or were simply off during the run are listed and must be removed from the analysis and the simulation. Due to the early stage of the experiment, the PMT quality monitoring was not fully functioning for this analysis but this method is respected for the other results presented in this chapter.

AmBe Event Selection in Simulation

Event selection in JUNO DetSim is a lot simpler than in data, as cosmogenic or radiogenic backgrounds do not need to be supressed, allowing the time and spatial cuts from Table 4.1 to be bypassed entirely. Moreover, working with the Geant4 output allows to directly select the particles involved in the interactions of interest : the 2.223 MeV γ-ray from neutron capture on hydrogen. The associated charge, in photoelectrons, is collected and used to build the charge spectrum, which is then fitted by a gaussian whose mean value is divided by the 2.223 MeV γ energy to obtain the simulated light yield, according to Eq. 4.4. This is done for all z positions. The results for the default and updated JUNO simulation are compared to the data and the result is shown in Figure 4.10.

Results

The default JUNO simulation, represented by the diamond markers in Figure 4.10, exhibits a gradually increasing light yield from $z = 10.5$ m to $z = 16$ m, before decreasing as the source gets closer to the acrylic boundary. The decreasing light yield pattern for high z positions of the source, can be explained by the increasing probability of total reflection as the source gets closer to the acrylic boundary.

This effect is accurately reproduced by the simulation in general, as the trend of the light yield is similar between the default JUNO simulation and the data for the source placed at high z value (> 16 m). However, the overall trend and values of the light yield are systematically higher in the default simulation when compared to the data across all z positions. This effect is partially corrected after introducing the new liquid scintillator and water absorption length in

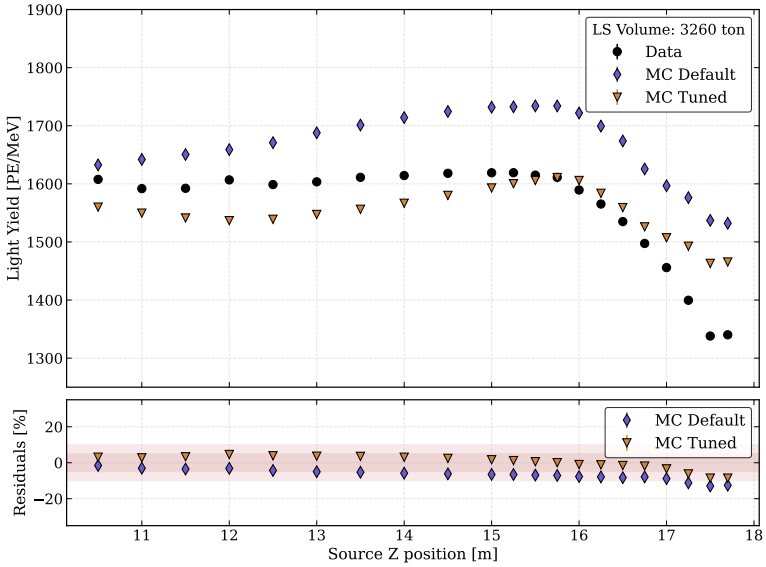

FIGURE 4.10 – **Top** : Light yield comparison between data and MC, for the detector filled with 3260 ton of liquid scintillator. The impact of the liquid scintillator and water absorption length new values on the simulated light yield is illustrated. **Bottom** : Residuals ((data - MC) / MC) between data and MC simulation. The red bands correspond to the ±10% and ±5% regions.

the simulation, represented by the triangle markers in Figure 4.10. The new simulated light yield shows a better agreement with the data, as the residuals, defined as (data - MC) / MC, stays below 5% for $z \leq 16$ m, while still exhibiting higher light yield for the source placed at $z > 16$ m.

Although the liquid scintillator optical performance measured during the early commissioning of the detector was already close to the requirements set for the neutrino mass ordering measurement, the current performance of the fully filled detector exceeds the nominal values specified in Ref. [85]. For instance, the light yield measured using the 2.223 MeV neutron capture γ-ray is found to be 1785 PE/MeV at the detector center, reaching values above 1800 PE/MeV for source positions within $|z| < 15$ m [119]. Consistent with this, the light yield measured using the ^{68}Ge source, with 1.022 MeV γ, exceeds 1600 PE/MeV for source positions within $|z| < 15$ m, with the lower value with respect to the nH measurement being expected from the scintillator energy non-linearity effects further detailed in Section 4.5. The improvement in liquid scintillator optical performance with respect to the early commissioning period is a direct consequence of the prompt identification of off-specification batches and the subsequent corrections applied to the purification process.

4.3.3 Additional implementation to JUNOSW

The assessment of the JUNO simulation's reliability during the liquid scintillator filling phase motivated a series of improvements to various aspects of the simulation. Following the updates to the water and liquid scintillator absorption length values, extensive revisions to

the detector geometry were carried out. The placement of the supporting bars, as well as the height and thickness of the different material composing the water pool, were updated to better reflect the actual detector configuration. Most significantly, the geometry of the CD chimneys (top and bottom) was refined, with detailed descriptions of the internal tubes, pipes, and pillars now included. These geometry improvements help mitigate the discrepancies observed between data and simulation in Figure 4.10 for source positions at $z > 17$ m, where the proximity to the chimney structures induced shadowing effects.

In parallel, several updates were made to the photosensor description in the simulation. The 8-inch PMTs installed at the top of the water pool were added to the geometry, while uninstalled PMTs were removed from the Central Detector description to better match the actual detector layout. Additionally, dedicated laser calibration runs were used to measure the relative photo-detection efficiency (PDE) of each LPMT type, and the resulting PDE corrections were applied in the simulation, effectively correcting the PDE of the Hamamatsu and NNVT PMTs. However, these modifications were integrated much later inside the JUNO simulation software.

4.4 SPMT energy response

Although only slightly more than half of the SPMTs are currently operational, the system remains a valuable tool for gaining additional insight into the detector response and cross-checking results obtained with the LPMT system. The SPMTs were inactive for the majority of the detector commissioning period, and have been reintegrated into the data acquisition system only around August 2025, allowing to join the last calibration campaign before JUNO's first physics data taking period. By this time, the detector filling was completed and several calibrations sources had been deployed to assess the initial performance of the fully filled detector.

This section presents a parallel analysis conducted on the SPMT response, evaluated using the ^{68}Ge source deployed along the z axis for $z \in [-17.7,\ 17.7]$ m, with the primary goal of comparing the LPMT and SPMT responses, especially for the source placed at high z values. Additionally, the system response is compared to the simulation, effectively assessing its good description within the simulation, or refine it as it is done for the LPMTs.

4.4.1 Ge68 source

Description

Germanium-68 (^{68}Ge) is a man-made radionuclide that serves as a well-established and widely used calibration source for detectors, particularly those designed to detect 511 keV

annihilation photons. ^{68}Ge decays with a half-life of 270.95 days via electron capture to Gallium-68 (^{68}Ga), which further decays to stable Zinc-68 (^{68}Zn). As visible in the decay scheme of Figure 4.11, ^{68}Ge emits no significant radiation, it is rather the decay of ^{68}Ga that produces a detectable signal for JUNO. ^{68}Ga decays with a half-life of 67.83 minutes via a combination of electron capture and positron emission, primarily to the ground state of ^{68}Zn, but also with a branch to an excited state that emits a $\sim$ 1.08 MeV γ-ray with a probability of $\sim$3%. The branch to the ground state produces two back-to-back 511 keV annihilation photons upon positron annihilation with an electron of the surrounding medium. In JUNO, the ^{68}Ge source is placed in a dedicated enclosure designed such that the produced positron quickly annihilates within it, with only the two 511 keV γ-rays escaping and depositing energy inside the detector. However, the probability of a positron escaping the source enclosure is non-negligible, leading to events with reconstructed energies greater than 1.022 MeV in the detector. Such events may also be accompanied by the 1.08 MeV γ-ray from the excited state branch.

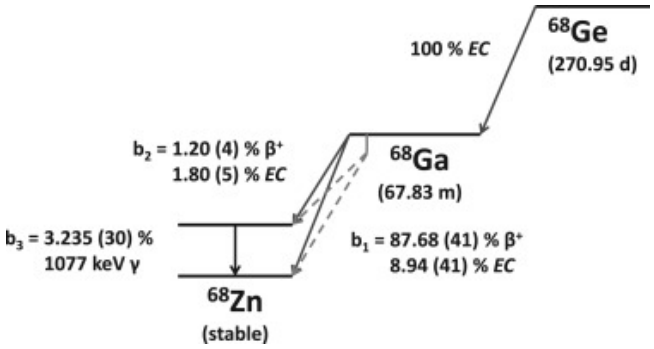

FIGURE 4.11 – ^{68}Ge decay scheme [174].

Event Selection

The amount of light collected by the SPMT system is insufficient for it to be used as a standalone system for physical event selection. Instead, events are first selected using the LPMT system, after which the SPMTs information recorded within the same trigger window is examined.

Unlike the AmBe source, the ^{68}Ge selection does not require a prompt–delayed coincidence, since the two 511 keV annihilation γ-rays produced by the positron emitted in the ^{68}Ga decay are effectively simultaneous. The selection therefore relies solely on spatial cuts around the known source position. An example of the ^{68}Ge event selection with the source deployed at the detector center ($z = 0$ m) is shown in Figure 4.12.

As can be seen in Figure 4.12a, the ^{68}Ge events are more spatially concentrated than AmBe events, with the majority contained within $|z| < 1.0$ m and $\rho < 0.75$ m, reflecting the shorter range of the annihilation γ-rays in the scintillator. A large population of events with LPMT

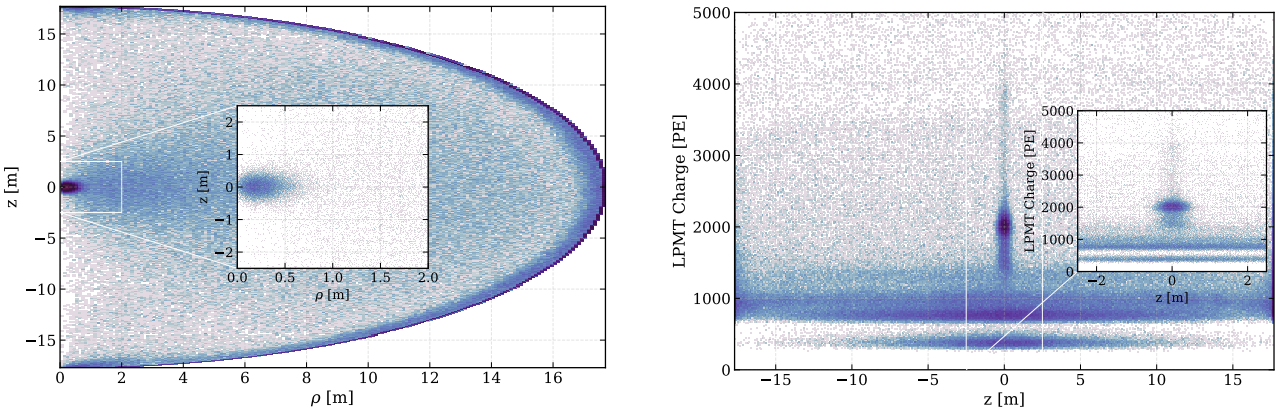

(a) (b)

FIGURE 4.12 – ^{68}Ge calibration run with the detector fully filled with liquid scintillator and the source deployed at $z = 0$ m. **(a)** z vs ρ spatial distribution of events. The ^{68}Ge events are concentrated within $|z| < 1.0$ m and $\rho < 0.75$ m. **(b)** LPMT charge, in photoelectrons (PE), as a function of the reconstructed z position.

charge ∼1000 PE is also visible, which is attributed to natural radioactivity originating from the detector edges and is effectively suppressed by the spatial cuts. Although the cosmogenic contamination is less problematic than for the AmBe selection, a muon veto is nonetheless applied to remove muon-induced backgrounds from the ^{68}Ge sample.

The performance of the selection cuts on the resulting LPMT charge spectrum is highlighted in Figure 4.13, where muon-related and radioactivity background events are effectively reduced, leaving mostly ^{68}Ge events. The 1.022 MeV peak is much more visible and centered around $Q_{LPMT} = 2000$ PE, with an additional peak visible at $Q_{LPMT} \approx 3800$ PE corresponding to the $1.022 + 1.08$ MeV γ-rays following the de-excitation of the ^{68}Zn daughter nucleus.

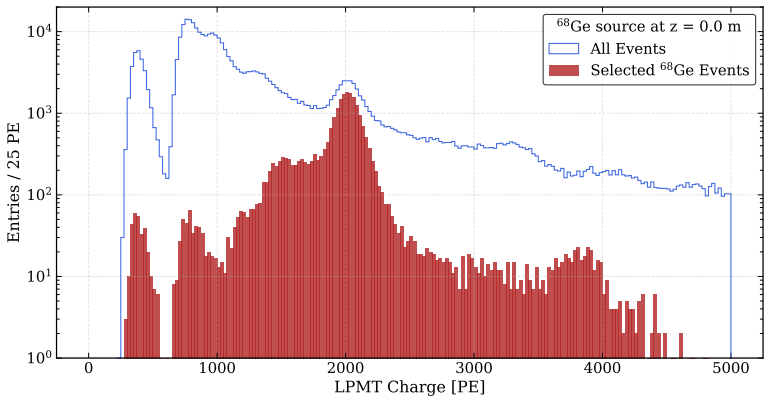

FIGURE 4.13 – LPMT charge spectrum of a ^{68}Ge calibration run with the source positioned at $z = 0$ m, shown before and after the application of selection cuts.

SPMT nHit Spectrum

Given that the SPMTs operate in photon-counting mode and that the mean number of photons reaching a single SPMT per event is rarely greater than one, the hit multiplicity nHit provides a more robust and linear estimator of the total collected light than a charge integral. In this low-occupancy regime, each fired SPMT channel corresponds with high probability to a single detected photon, making nHit a clean Poisson counting observable, unaffected by gain fluctuations that would broaden the charge distribution.

The SPMT nHit spectrum is built by first isolating the 1.022 MeV peak in the LPMT charge spectrum using a Gaussian fit centered around ∼2000 PE, and then selecting all events falling within $\mu_{\text{fit}} \pm 3\sigma_{\text{fit}}$. The result of the fit is given in Figure 4.14a and the resulting SPMT nHit spectrum is given in Figure 4.14b. It should be noted that a simple Gaussian function may be too simplistic for an accurate characterization of the peak shape, and a more rigorous fitting approach — such as the one described in Ref. [119] — would be needed for a precise estimation of the mean and width of the distribution. For the purposes of the present study, a Gaussian fit is applied consistently to both data and simulation as a first approximation.

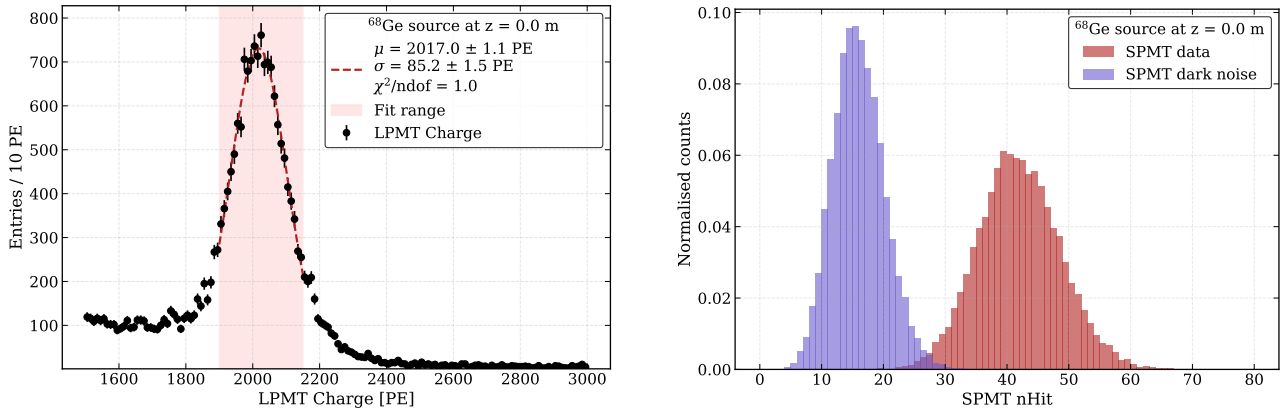

(a) (b)

FIGURE 4.14 – SPMT nHit spectrum building method. **(a)** LPMT charge spectrum. The 1.022 MeV peak corresponding to the two annihilating γ is fitted by a gaussian function whose fitted parameters are used to build the SPMT nHit spectrum. **(b)** (Red) SPMT nHit distribution, obtained by selecting events that fall within the LPMT 1.022 MeV peak. (Purple) Dark noise nHit distribution computed from periodic trigger.

4.4.2 First look at SPMT response

Unlike the LPMT system, the SPMT response was not regularly evaluated nor confronted to simulation during the early stages of commissioning. The August 2025 calibration campaign marked the first period during which the system was sufficiently operational to support systematic studies, providing the first opportunity to assess the status of the SPMT system. The

^{68}Ge source is therefore used to perform a first quantitative comparison of the SPMT response between data and simulation.

SPMT Performance in Data

Following the light yield method introduced in Section 4.2.3, the SPMT light yield is estimated by replacing the charge in PE with the nHit observable and the Gaussian fit with a Poisson fit, more appropriate for low-occupancy count data. Similarly to the LPMT case, the dark noise contribution to the SPMT nHit spectrum is estimated using the periodic trigger, yielding an average dark noise contribution of nHit $= 15.54 \pm 0.02$ hits. Although the channel quality monitoring was fully operational and providing lists of working LPMTs on a run-by-run basis, the SPMTs were not yet included in this monitoring framework due to the still unstable state of the system. However, a list of stable SPMTs was available for the period from August to November 2025, allowing to remove non-stable SPMTs and produce simulations as realistic as possible to the data.

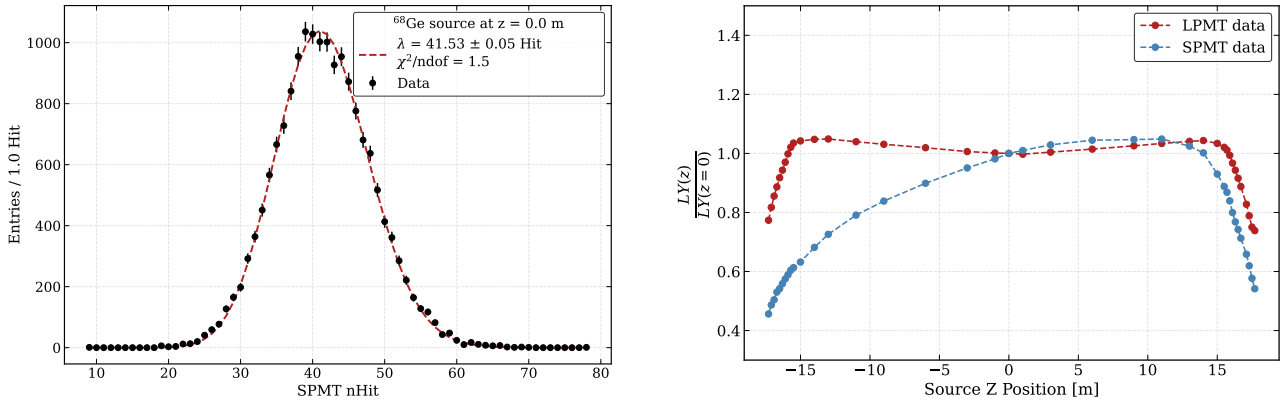

(a) (b)

FIGURE 4.15 – **(a)** SPMT nHit distribution for the ^{68}Ge source placed at $z = 0$ m and fitted with a Poisson function. The dark noise is subtracted from fitted mean value and divided by 1.022 MeV to compute the light yield. **(b)** Computed light yield for all z positions and both SPMT and LPMT system, normalized to the value at $z = 0$ m.

The result of the Poisson fit for the ^{68}Ge source positioned at $z = 0$ m is shown in Figure 4.15a, yielding a mean value of $\lambda = 41.53 \pm 0.05$ hits. After subtracting the dark noise component, the SPMT light yield is LY$= 25.38 \pm 0.05$ hits/MeV. The procedure is repeated for all z positions at which the ^{68}Ge source was deployed and the results are presented in Figure 4.15, where the light yield values are normalized to the value at $z = 0$ m and compared with the LPMT response. With the exception of positions in the lower hemisphere of the detector, where less SPMTs are currently operational, the z-dependence of the SPMT light yield is in good agreement with that of the LPMT system, providing a consistent picture of the spatial response of both photosensor systems.

Data/Simulation Comparison

Using a not fully tuned version of the JUNO software, the ^{68}Ge source is simulated for the same z positions using the ACU, with non-functioning PMTs identified from the data and removed in the simulation. As opposed to the study made on the AmBe source, the electronic response and LPMT waveform reconstruction are included in the simulation chain, which implies that the simulated dark noise must be removed before comparison with data. The results for the LPMT and SPMT system are presented in Figures 4.16a and 4.16b respectively.

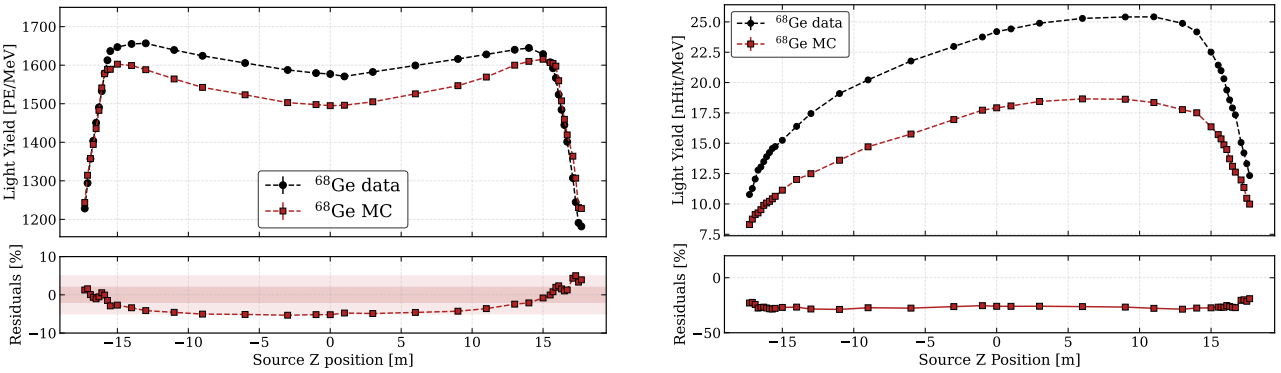

(a) LPMT (b) SPMT

FIGURE 4.16 – **(Top)** PMT light yield for the ^{68}Ge source at different z positions, compared between data and simulations. **(Bottom)** Relative difference between data and simulation ; red band on the LPMT plot indicates the $\pm 5\%$ and $\pm 2\%$ levels.

For the LPMT system, data and simulation are in relatively good agreement, with relative differences contained within $\pm 5\%$ across most z positions, with the largest discrepancies observed for the source positioned at $z \leq 15$ m.
For the SPMT system, a significant disagreement is observed between data and simulation, which is not resolved by the use of a different Geant4 version. The origin of these discrepancies are likely coming from many sources, reflecting the fact that the SPMT system description in the simulation has not yet been tuned to accurately reflect the current hardware configuration of the detector.

4.4.3 Layer Response

To further investigate the SPMT response and the observed discrepancies between data and simulation, the PMT response is studied as a function of detector circle (or layer). A circle-by-circle analysis provides a more granular comprehension of the detector geometry, and can help identify regions where the simulation does not accurately describe the data. The detector is divided into 123 circles, numbered from -62 to 62, with circle 0 containing no PMTs. The distribution of LPMTs and SPMTs across circles is represented on Figure 4.17, where the SPMTs

distribution is notably asymmetric since the majority of currently working SPMTs are located in the upper hemisphere of the detector.

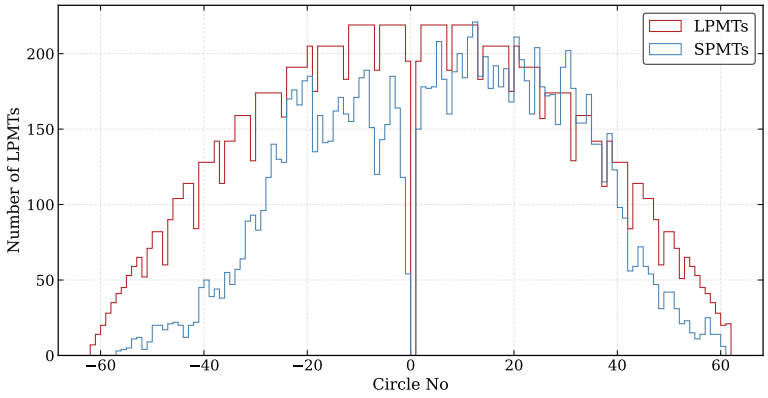

FIGURE 4.17 – Number of working LPMTs (red) and SPMTs (blue) per detector circle. The asymmetric SPMT distribution reflects the partial functioning state of the system, with the majority of operational SPMTs located in the upper hemisphere.

LPMT and SPMT response

For a given calibration run — corresponding to the source placed at a given z position — the number of fired PMTs per circle is defined as the number of PMTs that recorded one or more photons during an event. Given the relatively low energy of ^{68}Ge events and the low photon occupancy per SPMT, the hit multiplicity per channel is not used here and only the binary fired/not-fired information is kept. This quantity is computed for each event and each ring, then averaged over all events in the run. The result for the source placed at $z = 0$ m and $z = 15$ m are shown in Figures 4.18a and 4.18b respectively. However, the discrepancies remain relatively uniform across all circles and for both source z positions, with no regions of the detector leaving hints of possible geometry effects.

A similar investigation is performed on the LPMT system, with the results shown in Figure 4.19a and 4.19b for the source placed at $z = 0$ m and $z = 15$ m respectively. The average number of LPMT fired per circle shows good agreement between simulation and data for both source position, with relative differences mostly contained within $\pm 10\%$ across all circles. This indicates that the discrepancies observed on the SPMT system are not related to the overall optical simulation of the JUNO detector, but rather incomplete or inaccurate description of the SPMT system itself within the simulation. The rest of this section describes the attempts to correct the simulated SPMT response to bring it into agreement with data.

As a first attempt to correct the simulation, the 1/3 PE trigger threshold applied within the simulation was removed. This modification was intended as rapid assessment of the effect of a gain increase, motivated by the fact that the SPMT gain values currently implemented in JUNO are two times bigger than the nominal values, without requiring individual gain

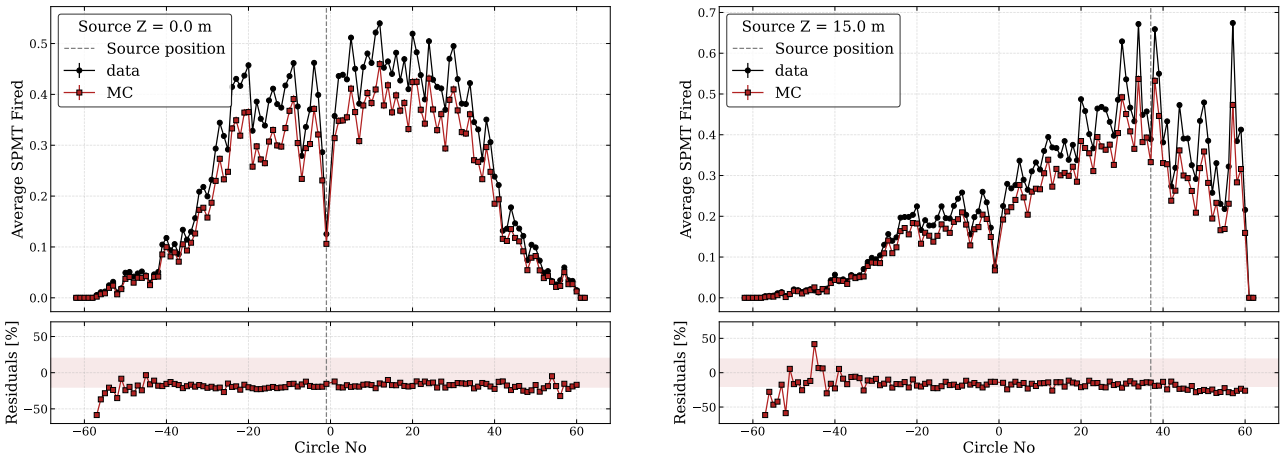

(a) (b)

FIGURE 4.18 – **(Top)** Average number of fired SPMTs per circle for the ^{68}Ge source at $z = 0$ m **(a)** or $z = 15$ m **(b)**, compared between data and simulation. **(Bottom)** Relative difference between data and simulation ; red bands indicate the $\pm 20\%$ level

correction for each SPMT channel in the simulation. The result is shown by the yellow triangle markers in Figures 4.22a and 4.22b for the source at $z = 0$ m and $z = 15$ m respectively. The modification has little to no impact on the average number of fired SPMTs per circle, indicating that the trigger threshold, and therefore the gain increase, might not be the primary source of the observed discrepancies.

Updated simulation

More recently, the updated version of the JUNO simulation software was released, introducing all the improvements listed in Section 4.3.3, including additional correction to the LPMT photo-detection efficiency, accounting for the shadowing effect induced by the detector supporting rods on the LPMT photo-detection efficiency measurement. The resulting light yield curves for the LPMT and SPMT system are shown in Figure 4.20. For the LPMT system, the updated simulation shows an improved agreement with data with respect to Figure 4.16a, with a relative difference fully contained within $\pm 2\%$ for the source placed at $|z| < 15$ m. In contrast, the impact on the SPMT simulated light yield shows only a slight increase, insufficient to resolve the discrepancies observed against data, confirming that the disagreement originates from missing description of the SPMT response within the simulation.

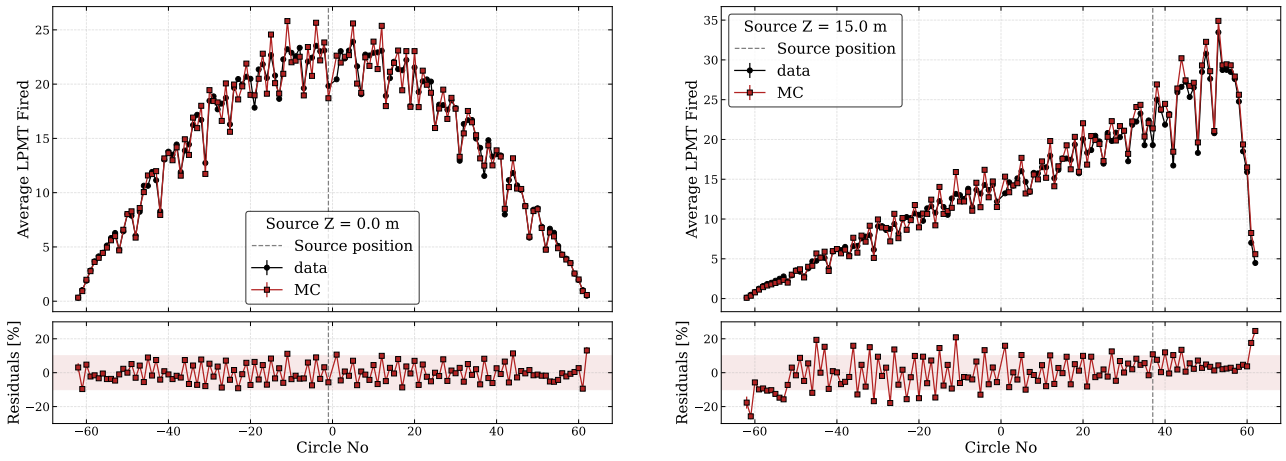

(a) (b)

FIGURE 4.19 – **(Top)** Average number of fired LPMTs per circle for the ^{68}Ge source at $z = 0$ m **(a)** or $z = 15$ m **(b)**, compared between data and simulation. **(Bottom)** Relative difference between data and simulation ; red bands indicate the $\pm 10\%$ level

4.4.4 SPMT Photo Detection Efficiency

Another approach to correcting the data-simulation discrepancy consists of rescaling the SPMT photo-detection efficiency (PDE) in the simulation until agreement with data is achieved. A set of simulations of the ^{68}Ge source at $z = 0$ m is produced, each with the SPMTs PDE uniformly scaled by a factor $\alpha \in [1.1,\ 2.0]$. Since the simulated samples contain only the true Geant4-level information and no electronics noise, the dark noise contribution is subtracted from the data nHit distribution before the comparison. The simulated nHit distributions for each value of α, together with the dark noise-subtracted data distribution, are shown in Figure 4.21a.

The agreement between data and simulation is quantified using the following log-likelihood formula :

$$\chi^2 = 2\sum_{i=1}^{N}\left[\mu_i - n_i + n_i \ln\frac{n_i}{\mu_i}\right] \tag{4.8}$$

where μ_i and n_i are the simulated and observed bin contents of the SPMT nHit spectrum for the i-th bin, and N is the total number of bins. This definition is preferred over a standard χ^2 for binned as it remains well-defined in bins with low event counts. The resulting χ^2 as a function of the scaling factor α is shown in Figure 4.21b, and is minimised at $\alpha = 1.3$, corresponding to a 30% increase in the SPMT PDE. The comparison between data and the rescaled simulation is shown in Figure 4.21c.

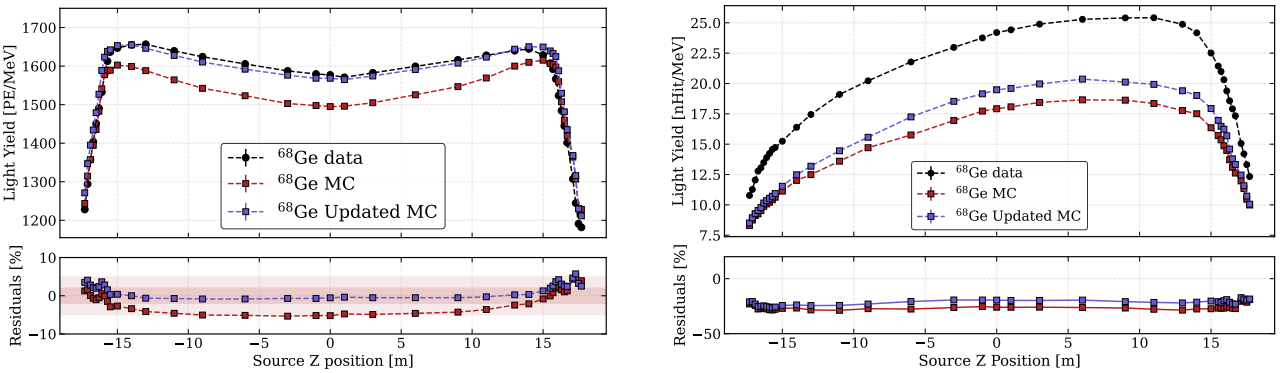

(a) LPMT (b) SPMT

FIGURE 4.20 – Light Yield comparison between the updated simulation and data. **(Top)** PMT light yield for the ^{68}Ge source at different z positions, compared between data and simulations. **(Bottom)** Relative difference between data and simulation ; red band on the LPMT plot indicates the $\pm 5\%$ and $\pm 2\%$ level.

The layer-by-layer response is also significantly improved by the PDE rescaling. As shown in Figure 4.22a, the average number of fired SPMTs per ring is in good agreement between data and the corrected simulation for the source at $z = 0$ m. A similar level of agreement is observed for the source at $z = 15$ m, as shown in Figure 4.22b, confirming that the PDE correction effectively accounts for the observed discrepancies across different source positions and detector regions, without introducing additional position-dependent effects.

Outlook

Rescaling the SPMT photo-detection efficiency by 30% effectively reduces the discrepancies between data and simulation, bringing the relative difference in light yield below 10% across all source positions, as shown in Figure 4.23. However, a 30% increase in PDE is difficult to justify on purely physical grounds, as such a large deviation in the amount of collected light is unlikely to arise from the PMT characteristics alone. While an increase in the effective SPMT PDE cannot be entirely excluded, the excess light collected by the SPMTs relative to simulation is more likely to originate from other effects.

Although a definitive explanation was not found in this study, some approaches are worth exploring to address this issue. For instance, the updated LPMT optical model could be extended to the SPMT system inside the simulation. The impact on the collected light shouldn't be able to account for the observed 30% increase but might contribute partially. Another possibility would be to investigate the positions of the PMTs, where the LPMT system could introduce more important shadowing to the SPMT system than expect. The later study would require to disable the LPMT geometry inside the JUNO simulation, which may not be straightforward. Unfortunately, due to the limited time left before the completion of this thesis, these studies

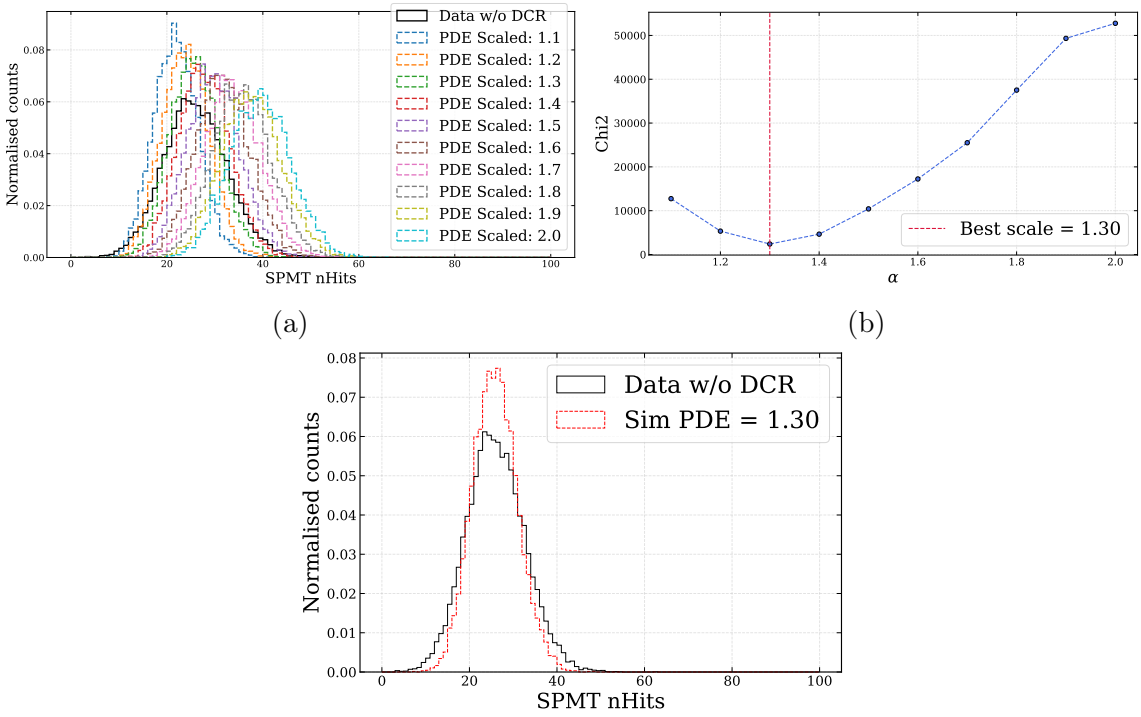

FIGURE 4.21 – **(a)** SPMT nHit spectra for data and simulations with different PDE scaling factors, for the ^{68}Ge source at $z = 0$ m. The dark noise contribution has been subtracted from the data. **(b)** χ^2 between data and simulation as a function of the PDE scaling factor α. The minimum is found at $\alpha = 1.3$, corresponding to a 30% increase in PDE. **(c)** Comparison between data and the simulation level with PDE scaled by 1.3.

were not performed and are left for potential volunteers.

4.5 Energy non-linearity

The detector non linearity is assessed by the use of different calibration sources with energy ranging from 0.511 MeV to 6.13 MeV, effectively covering a good portion of the IBD energy range. This section aims at presenting the energy non-linearity of the JUNO detector, and compare the response to simulated data for the LPMT system only. The corresponding analysis on the SPMT system was conducted in parallel to the following analysis, for the data only, and showed good agreement with the LPMT system, yielding less than ±0.5% instrumental non-linearity [119].

The energy non-linearity is defined as the ratio of the visible energy to the deposited energy (E_{vis}/E_{dep}), and is computed for all calibration sources placed at the center of the detector. The visible energy E_{vis} is calculated using the total collected charge divided by a conversion factor, which is simply the Light Yield computed using the 2.223 MeV γ from neutron capture on

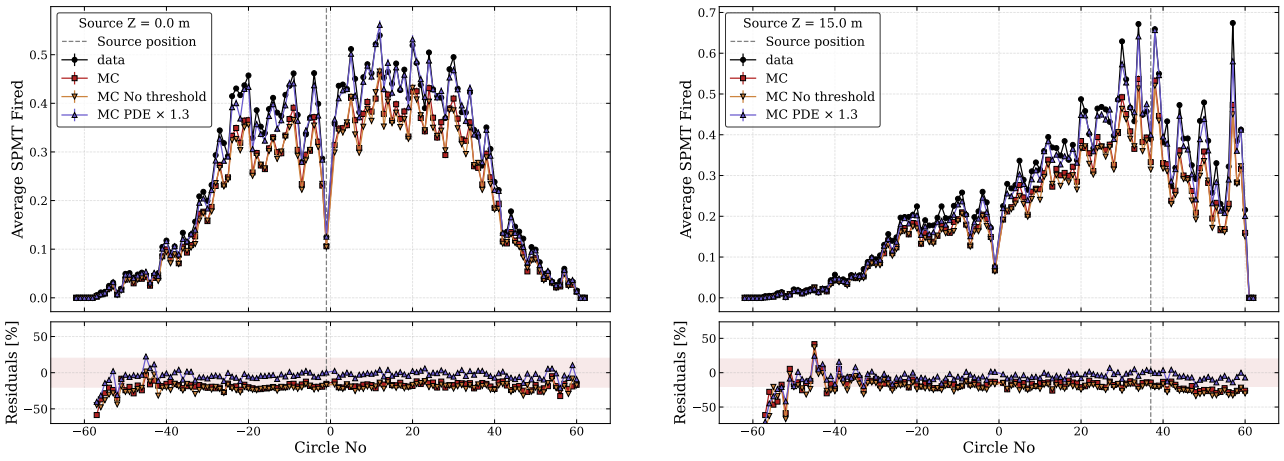

(a) (b)

FIGURE 4.22 – **(Top)** Average number of fired SPMTs per ring for the ^{68}Ge source at $z = 0$ m **(a)** and $z = 15$ m **(b)** , comparing data with the baseline simulation and the PDE-corrected simulation. **(Bottom)** Relative difference between data and simulation ; red bands indicate the $\pm 20\%$ level.

hydrogen, and act as the anchor whose energy non-linearity is normalized to 1. E_{dep} is defined as the total energy deposited by the γ and the ratio (E_{vis}/E_{dep}) is plotted as a function of the effective gamma energy E, which corresponds to the gamma energy if a single gamma is emitted from the source or the average of the gamma energies for sources emitting multiple gammas.

4.5.1 Energy Computation Method

Of the seven γ calibration sources listed in Table 2.3, six are used for the non-linearity study. The AmC source is included as a dedicated high energy source, as its delayed signal provides a neutron capture on hydrogen signature identical to that of the AmBe source, while its prompt signal additionally includes the 6.13 MeV γ-ray from the de-excitation of ^{16}O*, effectively extending the energy range of the calibration dataset. This range could be further extended up to ∼10 MeV using the γ-ray signatures from neutron capture on ^{56}Fe (7.63 MeV), ^{53}Cr (8.88 MeV), and ^{58}Ni (9.00 MeV) but will not be included in this study.

Anchor Point and Conversion Factor

The energy non-linearity computation is anchored to the well-known 2.223 MeV γ-ray from neutron capture on hydrogen, which serves as the reference point for converting the measured charge into deposited energy. This choice is motivated by the clean and mono-energetic signal of the n-H capture, and its relatively high rate in JUNO, making it a reliable reference. The light yield, is used as the conversion factor between collected charge and deposited energy, and is obtained using the AmC source, following a prompt–delayed event selection similar to the one described in Section 4.2.2.

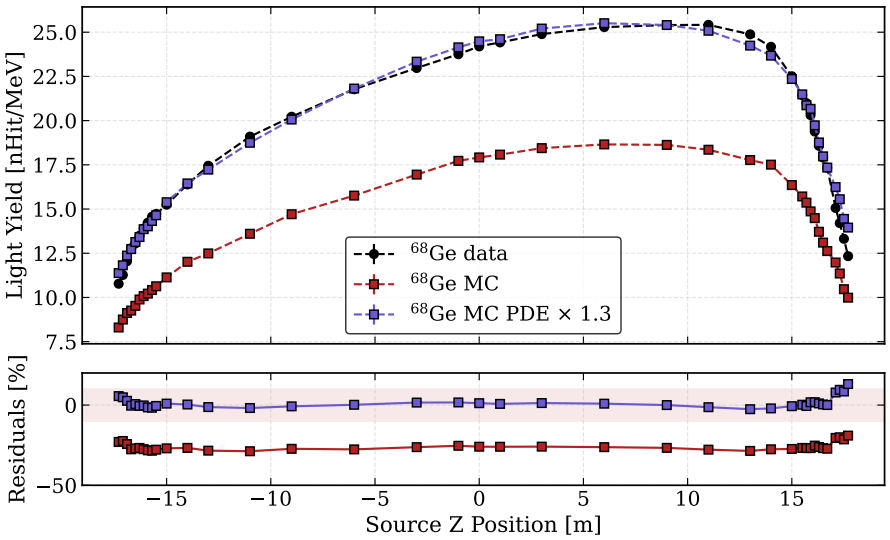

FIGURE 4.23 – **(Top)** SPMT light yield as a function of source position, comparing data with the PDE-corrected simulation ($\alpha = 1.3$). **(Bottom)** Relative difference between data and simulation ; red bands indicate the $\pm 10\%$ level.

The resulting AmC prompt and delayed charge spectra, after subtraction of the dark noise contribution, are shown in Figure 4.24a, where the n-H capture γ peak is clearly identifiable in the delayed spectrum. The charge associated with the 2.223 MeV γ-ray is extracted by fitting the delayed charge spectrum with a Gaussian function, as shown in Figure 4.24b, yielding a fitted mean value of $\mu = 3971.44 \pm 0.96$ PE. The light yield is then computed according to Eq. 4.5, giving LY $= 1786.52 \pm 0.43$ PE/MeV.

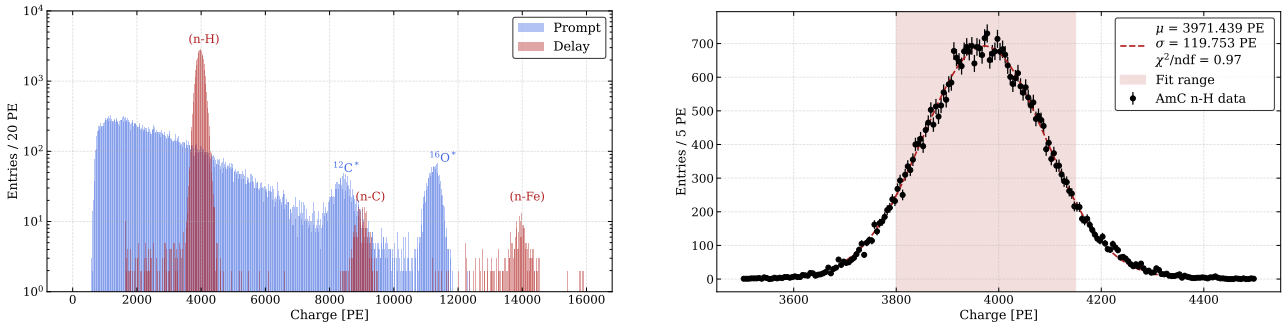

(a) (b)

FIGURE 4.24 – **(a)** AmC charge spectrum after dark noise subtraction, with the prompt and delayed contributions separated following the application of the respective selection cuts. **(b)** Neutron capture on hydrogen γ-ray peak extracted from the AmC delayed charge spectrum, fitted with a Gaussian function to retrieve the mean charge and hence the light yield.

Charge Spectra of Calibration Sources

For the remaining calibration sources, spatial cuts are applied around the known source positions following the same approach described for ^{68}Ge in Section 4.4.1. The resulting charge spectrum for each source is fitted with a Gaussian function, providing a mean charge value associated with the γ-ray energy emitted by that source. While a simple Gaussian fit is used here as a first approximation, it should be noted that the charge spectra of γ sources also contain contributions from Compton scattering, and partial energy deposition in the source enclosure, both of which introduce asymmetries in the peak shape that are clearly visible in the ^{68}Ge spectrum. These effects are mitigated by restricting the fit to a narrow range around the peak. The charge spectra for all six calibration sources, together with their respective Gaussian fits, are shown in Figure 4.25.

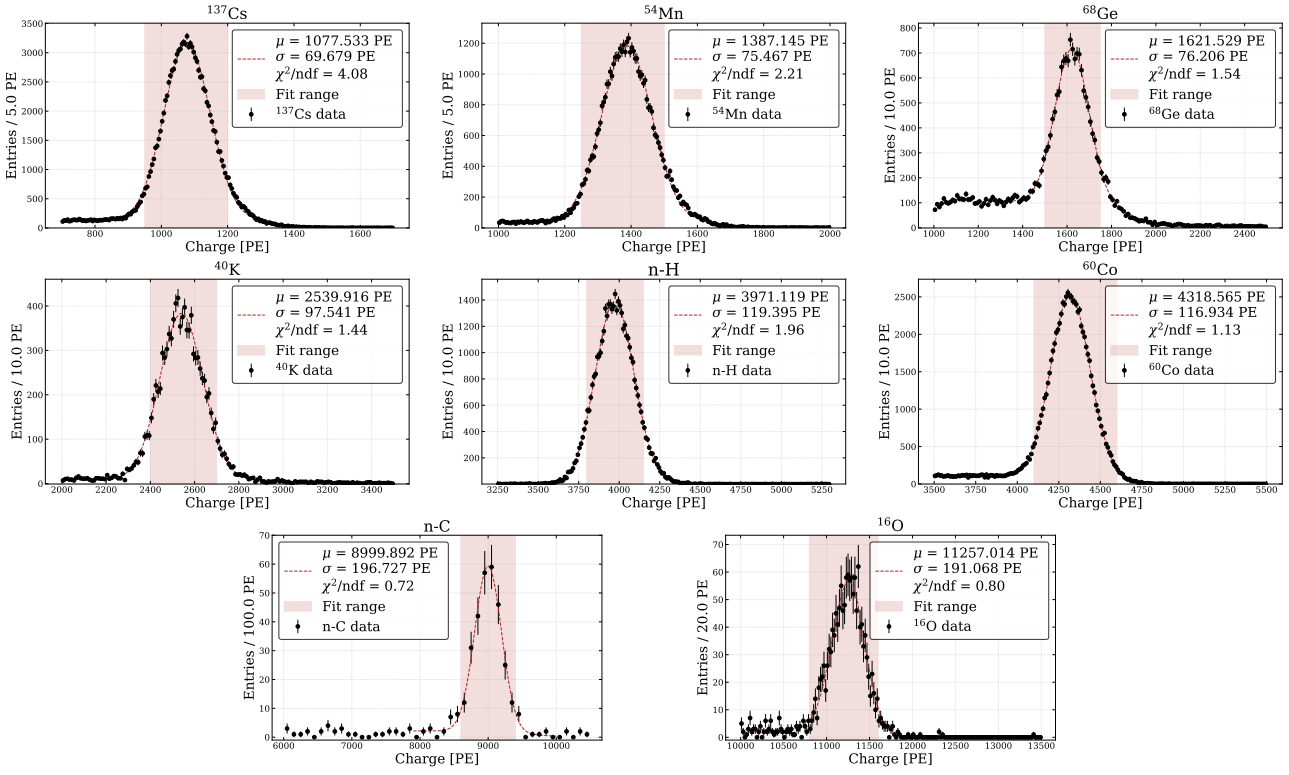

FIGURE 4.25 – Charge spectra for all six calibration sources used in the non-linearity study, each fitted with a simple Gaussian function on a restricted range around the peak. The fitted mean charge values are converted to energy using the computed Light Yield on n-H and used to construct the detector non-linearity curve.

Non linearity curve

The mean charge values extracted from the Gaussian fits are divided by the light yield to obtain a reconstructed energy in MeV for each calibration source, which is then compared to the true γ deposited energy. Among the calibration sources, ^{68}Ge (two 511 keV γ), ^{60}Co (1.173 + 1.333 MeV γ), and the γ-ray(s) from neutron capture on carbon are multi-γ sources, for which the effective deposited energy is averaged on the number of γ emitted. For the n-C capture in particular, multiple γs can be emitted depending on the state of ^{13}C, with two decay branches of highest intensities producing either one 4.94 MeV (68%) γ or two $3.68 + 1.26$ MeV (32%) γ. The effective γ energy is computed as the intensity-weighted average of these two branches. The non-linearity curve obtained from the first calibration period of JUNO is shown in Figure 4.27.

4.5.2 Fitting methods

As described previously, the non-linearity curve is constructed using Gaussian fits to the calibration source charge spectra as a first approximation. This section investigates the impact of more sophisticated fitting functions on the exctracted non-linearity curve.

The main challenge in fitting the charge spectrum of a γ source lies in accurately describing the Compton contribution, which populates the low-charge side of the full-energy peak and partially overlaps with it, directly impacting the estimated Gaussian mean and width. On the high-charge side of the peak, additional contributions may arise from γ-rays emitted by intermediate excited states or from intermediate products escaping the source enclosure and depositing additional energy in the liquid scintillator. Two alternative fitting approaches are considered here to simultaneously describe both the left- and right-hand tails of the peak. The first combines a Gaussian with a polynomial function and the second, motivated by the work of Ref. [175], uses a complementary error function (erfc) to model the Compton edge contribution :

$$f(x) = A_g \cdot \exp\left(-\frac{1}{2}\frac{(x-\mu)^2}{\sigma^2}\right) + A_e \cdot \mathrm{erfc}\left(\frac{(x-x_0)}{\sqrt{2}w}\right) \tag{4.9}$$

where A_g, μ, and σ are the Gaussian amplitude, mean, and standard deviation respectively, and A_e, x_0, and w are the erfc parameters. The parameter x_0 corresponds to the centre of the Compton edge, and w controls the smearing width of the edge transition.

The results of all three fitting approaches applied to the ^{68}Ge charge spectrum are shown in Figure 4.26. Despite the visible differences in how each function describes the tails of the distribution, the impact on the fitted mean value is negligibly small : the relative difference in the extracted mean value with respect to the simple Gaussian fit is no more than 0.1% for both methods.

The effect of the different fitting methods on the non-linearity curve is shown on Figure 4.27, where the relative difference between fitting method is fully contained within 0.5%, confirming

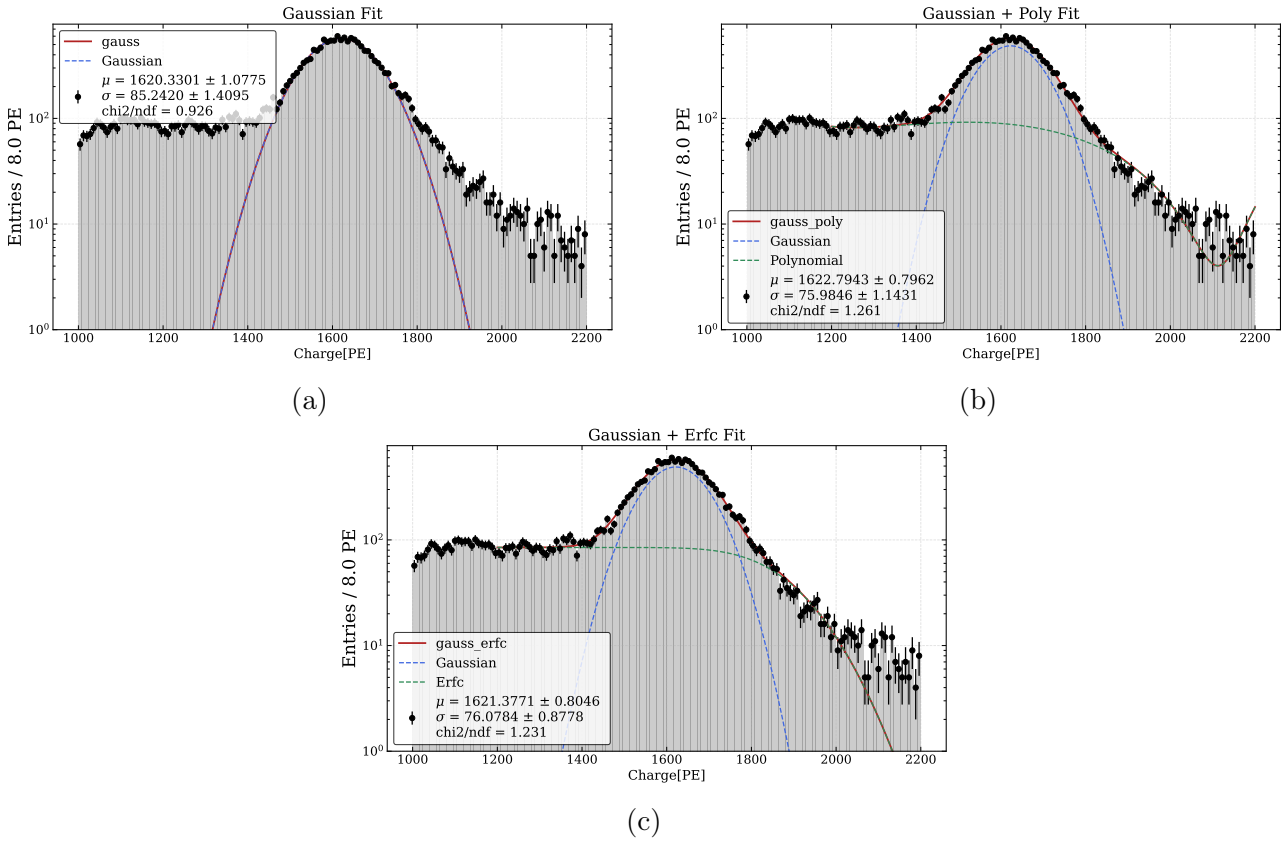

FIGURE 4.26 – Comparison of the three fitting methods applied to the ^{68}Ge charge spectrum : **(a)** simple Gaussian, **(b)** Gaussian combined with a polynomial background, and **(c)** Gaussian combined with an erfc function.

that the non-linearity measurement is robust against the choice of fitting function. Interestingly, while the impact on the Gaussian fitted mean value is minor, the standard deviation is reduced by $\sim 10\%$ when using more sophisticated fitting functions. This leads to a more meaningful estimation of the energy resolution compared to a simple Gaussian fit.

It should be noted that the fitting functions used here are mathematically motivated : their shape are chosen to reproduce the features of the calibration sources spectra, but do not constitute a rigorous physical model. An accurate description would require a dedicated fit function for each source, incorporating an analytical or MC-based model of the Compton contribution, secondary energy depositions, and source enclosure effects, as it is done for the ^{68}Ge source in Ref. [119]. Such an approach is left for future work, and the results presented here should be understood as a first characterization of the JUNO energy non-linearity using the first calibration period data.

4.5.3 Simulation validation

The same analysis is performed using the same calibration sources simulated at the detector center, including the electronics response as well as the LPMT waveform reconstruction in the

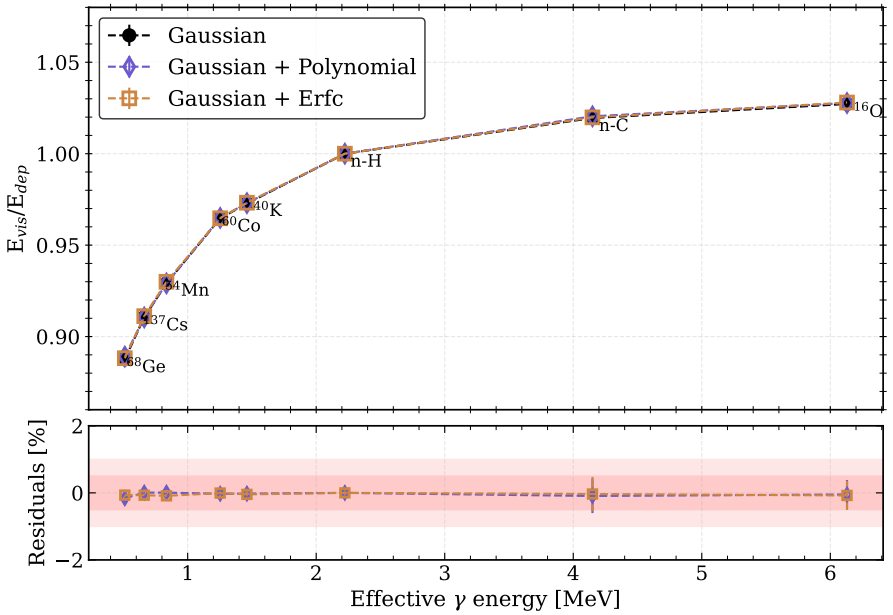

FIGURE 4.27 – Impact of the fitting function choice on the extracted non-linearity curve. The relative difference between the three methods (simple Gaussian, Gaussian + polynomial, and Gaussian + erfc) is fully contained within 0.5%.

simulation chain. As in data, a simple Gaussian fit function is used to extract the mean charge value from each simulated spectrum. The light yield is computed on the simulated n-H γ capture peak of the AmC source, and used to convert the extracted mean charge value of all calibration sources to MeV, following the same procedure. The resulting simulated non-linearity curve is compared to data, and the result in Figure 4.28 shows discrepancies contained within $\pm 1\%$ for nearly all calibration sources.

The most likely explanations of these discrepancies come from the incomplete state of the electronic simulation. Due to the early stage of the experiment, several parts of the simulation were still under active development, in particular the electronics response and waveform reconstruction algorithms. As a result, the full simulation chain required the use of two separate software versions : a more recent version to simulate the physics processes, the detector geometry, and components optical characteristics, and an older version to simulate the electronic response and waveform reconstruction. The discrepancies observed between simulation and data in Figure 4.28 may be introduced by the difference in the simulation accuracy of the versions used to run the full simulation chain.

The updated version of the JUNO simulation enables the use of a full chain simulation, including physics event generation, electronics response, and waveform and event reconstruction within a single framework. This updated version also supports the use of the latest Geant4 release (v11.4). The non-linearity curves obtained using the updated simulation software for both Geant4 versions are compared to data in Figure 4.29.

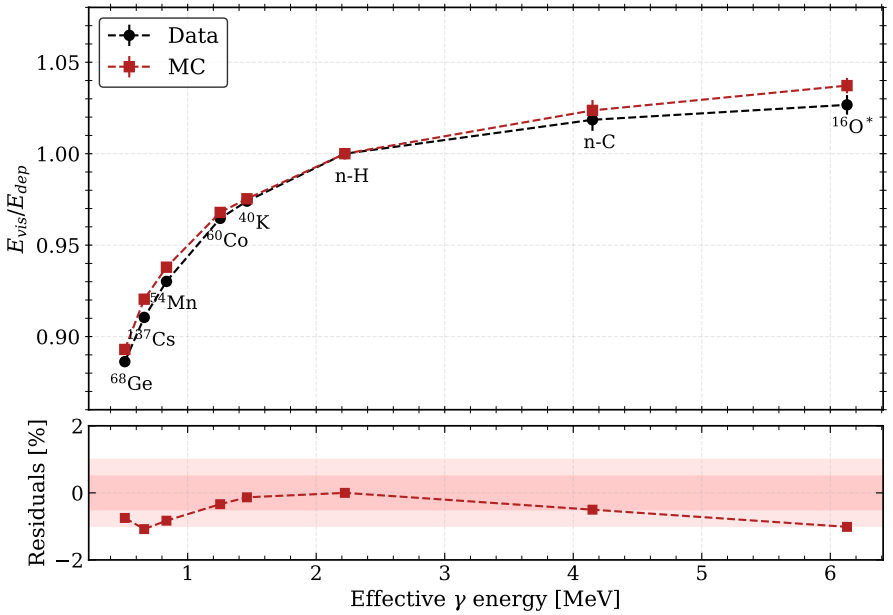

FIGURE 4.28 – Non-linearity curve comparison between data and the default JUNO simulation for calibration sources simulated at the detector center. The red bands in the bottom panel correspond to ±1% and ±0.5% levels.

The updated simulation exhibits a significantly improved agreement with data, with relative difference mostly contained within ±1% across all calibration sources. Discrepancies exceeding 1% remain for ^{68}Ge, ^{137}Cs, and ^{54}Mn. The transition to Geant4 v11.4 further reduces the discrepancies, effectively containing the relative difference between simulation and data within ±0.5%. However, the improvement from the latest Geant4 version appears as a near uniform downward shift of the non-linearity curve below 2.223 MeV. This suggests an overall reduction of the light production in the latest Geant4 version rather than a more accurate description of each calibration sources, and further studies will be needed to understand the underlying effect(s).

Overall, the updated JUNO simulation describes the measured non-linearity with good fidelity, and active work is maintained to further improve the agreement. In particular, the tuning of the Birks quenching constants [132], which describe the liquid scintillator response to different types of particles and directly influence the energy non-linearity, is currently under development.

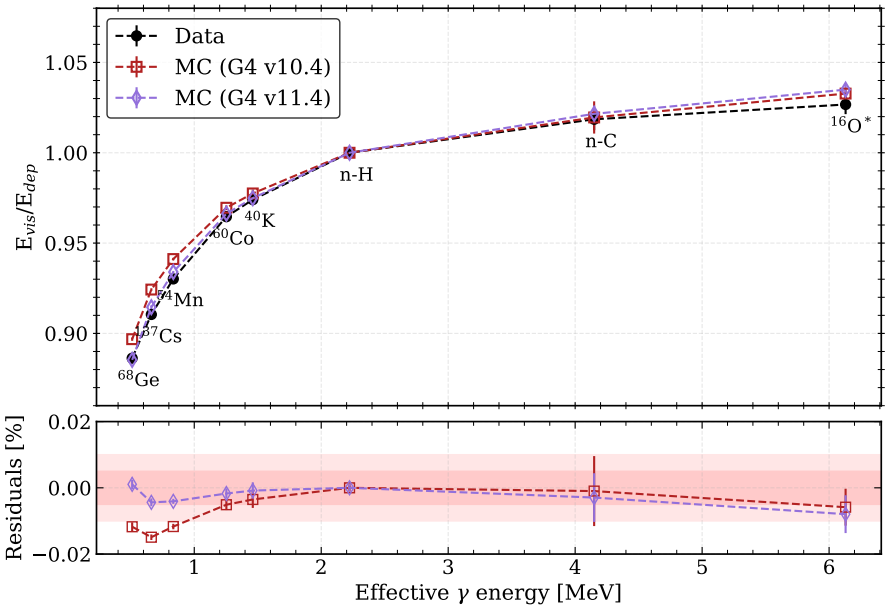

FIGURE 4.29 – Non-linearity curve comparison between data and the updated full-chain JUNO simulation, for both Geant4 v10.4 and v11.4. The red bands in the bottom panel correspond to ±1% and ±0.5% levels.

4.6 Conclusion

This chapter has presented a series of data/MC comparisons aimed at validating JUNO's simulated energy response, using calibration source data collected throughout the different stages of detector commissioning, from the early dual-phase filling period to the fully filled detector.

The early characterisation of the liquid scintillator optical response, performed during the dual-phase filling with the AmBe source, revealed a systematic overestimation of the light yield by the default JUNO simulation, which was reduced once the measured liquid scintillator and water absorption lengths were introduced. This analysis was conducted throughout the entire filling period, effectively providing a systematic MC/Data comparison of the detector energy response evolution. Throughout the commissioning period, extensive efforts were conducted to upgrade the detector geometry following this study, including a more detailed treatment of the CD chimneys, and dedicated PDE corrections for the LPMTs, which together mitigated the shadowing-related discrepancies observed at high z.

In parallel, a comparison between the LPMT and SPMT energy responses using the ^{68}Ge source show good data/MC agreement for the LPMT system, with relative differences contained within ±2% for $|z| < 15$ m after the simulation update. The SPMT system, however, exhibited a significant and large disagreement with simulation across z- and circle-dependent measurement, indicating an incomplete description of the SPMT response itself. Rescaling the

simulated SPMT PDE by 30% brings the data/MC light yield agreement below 10%, but such a large correction is difficult to justify from the PMT characteristics alone, and the physical origin of the discrepancy remains unidentified at the time of writing. Applying the updated LPMT optical model to the SPMT system, and investigating possible additional shadowing from the LPMT geometry on the SPMTs, constitute some possible areas of investigation that could explain the discrepancies observed between data and simulation.

Finally, the energy non-linearity of the detector was characterised over the 0.511–6.13 MeV range using the full set of calibration sources, and shown to be robust against the choice of fitting function, with the mean extracted non-linearity varying by less than 0.5% between a simple Gaussian fit and more sophisticated Gaussian+polynomial or Gaussian+erfc models, the latter also reducing the fitted width by $\sim 10\%$ and thus providing a more reliable estimate of the energy resolution, which is not investigated further in this analysis. The comparison to the full updated simulation chain shows a rather good agreement with data, bringing the data/MC non-linearity agreement to within $\pm 1\%$ for the full set of calibration sources.

Taken together, these studies show that the JUNO simulation, following the updates presented in this chapter, provides a good description of the detector's LPMT-only energy response, with the SPMT response remaining the main area requiring further work. This validation of the energy response confirms that JUNO's energy scale, and the systematic effects that shape it, are now sufficiently well understood and controlled to safely begin the experiment's physics data-taking. The following chapter presents the first physics analysis performed with this data, focusing on the IBD selection and the cosmogenic ^{9}Li/^{8}He background estimation during JUNO's first 60 days of data-taking.

Chapitre 5

Cosmogenic Background Rate Estimation in JUNO

Summary

5.1 Introduction . . . 157
5.2 Inverse Beta Decay Selection . . . 157
5.2.1 Nominal Selection Strategy . . . 158
5.2.2 Early Data-Taking Period Adjustments . . . 159
5.2.3 Results . . . 161
5.3 Cosmogenic ^{9}Li/^{8}He . . . 164
5.3.1 Production . . . 164
5.3.2 Impact on IBD Measurement . . . 165
5.4 Li/He Rate Estimation . . . 166
5.4.1 General Strategy . . . 166
5.4.2 Rate Before the Neutron Veto . . . 166
5.4.3 Accompanying Neutron Efficiency . . . 168
5.4.4 Rate Inside the Neutron Veto . . . 170
5.4.5 Residual Rate After the Neutron Veto . . . 172
5.5 Conclusion . . . 173

5.1 Introduction

As described in Section 2.2.3, JUNO detects reactor antineutrinos via the Inverse Beta Decay (IBD) reaction, exploiting the prompt-delayed coincidence signature to discriminate signal from background. From the validated energy response established in the previous chapter, achieving the precise spectral measurements at the heart of the JUNO physics program requires not only a well-understood detector, but also a robust control of the backgrounds capable of mimicking the IBD signature. This chapter investigate this second requirement, presenting the IBD selection and the estimation of the ^{9}Li/^{8}He backgrounds rate, in the first 60 days of data. This early dataset comes with a particularly challenging environment as reconstruction performance, and data quality are still being established and refined at this stage, requiring careful attention to both the event selection procedure and the treatment of backgrounds, whose characterisation is especially demanding under these conditions. This challenge is further accentuated by the way the JUNO collaboration was organised for this analysis, where three independent, and competing groups — A, B, and C — where born, with Bordeaux taking part in the activities of Group C, referred to as the European/American group. The results presented in this chapter are therefore part of a wider cross-check network, to which this work contributed through the validation of the IBD selection cuts and the estimation of the ^{9}Li/^{8}He background rate.

Following this context, Section 5.2 presents the IBD selection strategy used in this analysis, starting from JUNO's nominal selection and detailing the adjustments made to account for the detector's early-stage performance, before presenting the resulting IBD candidate sample. Section 5.3 then introduces the cosmogenic ^{9}Li/^{8}He background, its characteristic decay signature, and its impact on the IBD measurement, motivating the use of a neutron veto in the absence of a validated muon-track reconstruction method. Finally, Section 5.4 presents the method developed to estimate the residual ^{9}Li/^{8}He rate remaining in the selected IBD sample, by computing its rate before and after the neutron veto is applied, and combining the two to obtain the final residual background rate.

5.2 Inverse Beta Decay Selection

The identification of IBD candidates relies on a series of selection cuts designed to isolate the prompt-delayed coincidence signature while rejecting background events. This section briefly presents the evolution of the selection criteria used for the identification of IBD candidates in JUNO's first dataset, starting from JUNO's nominal selection strategy [85], before detailing the adjustments made by the analysis group, to which this work contributed, to account for the detector's early-stage performance [119]. Based on this revised selection, a dedicated pipeline was developed for the Bordeaux group to select IBD events. The resulting spectrum is presented

at the end of this section.

5.2.1 Nominal Selection Strategy

The nominal IBD selection strategy, established prior to the start of data taking is summarised in Table 5.1. It combines energy and spatial requirements on the prompt and delayed signals with a series of muon-related vetoes, both designed to remove the correlated cosmogenic backgrounds induced by muon spallation and by radioactivity within the liquid scintillator.

The prompt and delayed energy windows are chosen to include the full expected reactor antineutrino spectrum and the characteristic 2.223 MeV n-H capture peak, as well as the 4.945 MeV n-C capture peak, used to tag the delayed signal (see Section 2.2.3). The fiducial volume cut suppresses radioactivity events originating near the boundary of the detector — mainly from the PMT glass — which, combined with the prompt-delayed spatial and temporal coincidence, reject most of the uncorrelated accidental backgrounds. Finally, the muon-related vetoes address the muon spallation-induced backgrounds in the liquid scintillator, and are divided into two categories depending on track reconstruction status, where further details can be found in [85].

Selection	**Value / description**	**Efficiency [%]**
Prompt energy	$E \in [0.8, 12]$ MeV	100
Delayed energy	$E \in [1.9, 2.5]$ MeV or $[4.4, 5.5]$ MeV	99.8
Fiducial Volume (FV)	$R < 17.2$ m	91.5
Prompt-delayed time diff. (Δt)	$\Delta t < 1.0$ ms	99.0
Prompt-delayed distance (ΔR)	$\Delta R < 1.5$ m	99.2
Muon		
Muon veto (WP and/or CD only)	1 ms veto of the full LS after muon tagged in the WP and/or the CD	91.6
Muon veto (CD + track)	For reconstructed muon tracks, a progressive veto time window is applied for different radius cuts depending on the track topology and event distance from the track	
Total		82.2

TABLE 5.1 – A summary of the nominal selection criteria for IBD candidates, defined in [85], and their respective efficiency.

Overall, the nominal selection strategy gives a total efficiency of 82.2%, effectively reducing the expected $\sim$ 57 IBD events per day to $\sim$ 47 tagged IBD events per day. The largest source of loss comes from the fiducial volume requirement, followed by the combined muon veto. Notably,

this strategy was designed assuming final-state event reconstruction performance, including a 99% muon-track reconstruction efficiency.

5.2.2 Early Data-Taking Period Adjustments

The event reconstruction performance established with the early-stage JUNO detector [119] led to a revision of the selection cuts defined in Table 5.1. The resulting, updated selection criteria are summarised in Table 5.2, and justification for each additional or modified cut is given below.

Selection	**Value / description**	**Efficiency [%]**
Prompt energy	$0.7\,\text{MeV} < E_p < 12\,\text{MeV}$	100
Delayed energy	$2.0\,\text{MeV} < E_d < 2.5\,\text{MeV}$	98.6
Fiducial Volume (FV)	$R < 16.5\,\text{m}$; Remove ($\lvert z\rvert > 15.5\,\text{m}$ and $\rho < 2.0\,\text{m}$)	81.3
Prompt-delayed time diff. (Δt)	$5\,\mu\text{s} < \Delta t < 1\,\text{ms}$	96.8
Prompt-delayed distance (ΔR)	$\Delta R < 1.5\,\text{m}$	97.5
Multiplicity cut	No events in full volume (not vetoed by muons) in [2, 12] MeV energy range within 1 ms before the prompt, 1 ms after the delayed, or between prompt - delay	98.3
Muon		
Muon veto (CD+WP)	5 ms veto after WP PE > 400 (and CD PE > 30 000) with ±500 ns coincidence with CD event	95.5
Muon veto (WP-only)	5 ms veto after WP PE > 700, no CD pe > 30k with ±500 ns	
Muon veto (CD-only)	5 ms veto after CD PE > 30k, no WP trigger > 400 PE in ±500 ns and after > 2 ms from last muon	
Neutron veto	4 m radius spherical veto for 1.2 s around spallation neutron candidate (20 μs $<\Delta t_\mu <$ 2 ms, with energy in [1.5, 20] MeV, and hit time standard deviation < 275 ns)	99.2
Total		70.3

TABLE 5.2 – A summary of the updated selection criteria for IBD candidates, and their respective efficiency, for the early data-taking period of JUNO.

Fiducial Volume and Chimney Events

The most significant modification to the nominal cuts is the revised fiducial volume, lowered to $R < 16.5$ m to account for the degraded energy uniformity observed above this value [119].

In addition, two clusters of events were identified near the top and bottom chimneys of the detector, whose origin is not yet fully understood. This is visible in Figure 5.1, which shows a 2D z vs x spatial distribution of events reconstructed from a ^{68}Ge calibration run with the source deployed at the center, where two hot spots appear near $z = \pm 16$ m. These two clusters increase the rate of accidental background events in the selection, motivating the addition of an explicit cut removing events with $|z| > 15.5$ m and $\rho = \sqrt{x^2 + y^2} < 2.0$ m. Combined, these two spatial cuts give a selection efficiency of 81.3%, constituting the principal source of statistical loss in this first dataset.

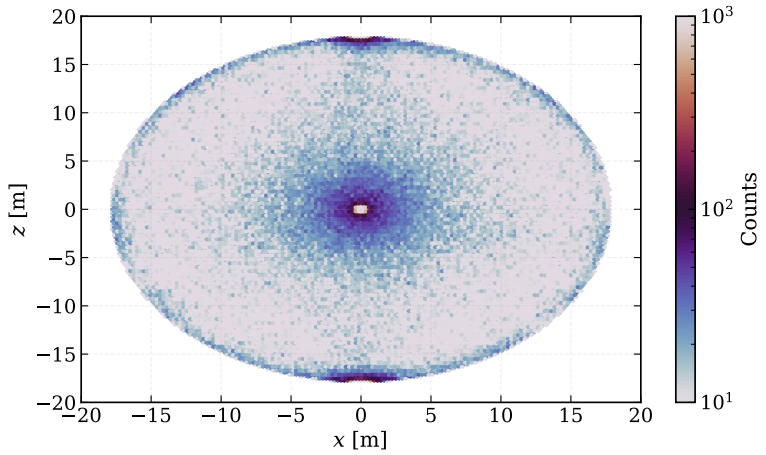

FIGURE 5.1 – 2D z vs x spatial distribution of reconstructed events from a ^{68}Ge calibration run with the source deployed at the CD center. Two additional clusters of events are located near the top and bottom chimneys.

Prompt-Delayed Time Coincidence

The prompt-delayed time coincidence window was tightened to include an explicit lower bound, $5\,\mu\text{s} < \Delta t < 1\,\text{ms}$. This removes very short time differences dominated by after-pulses and correlated PMT noise following the prompt signal, rather than by the genuine ~ 200 μs neutron capture time characteristic of a real IBD pair. This cut reduces the associated selection efficiency to 96.8%.

Multiplicity Cut

A multiplicity cut was introduced, rejecting IBD candidates for which any additional event above 2 MeV, and not already removed by the muon veto, is reconstructed anywhere in the detector volume within a fixed time window around the prompt-delayed pair. This criterion suppresses accidental coincidences arising from natural radioactivity and other uncorrelated activity in the detector, complementing the spatial and temporal coincidence requirements already imposed on the prompt-delayed pair itself. This cut has a selection efficiency of 98.3%,

which further reduces the available statistics, but, when combined with the revised time coincidence and fiducial volume cuts, the resulting accidental rate was found to be reduced by several orders of magnitude relative to the nominal expectation [139].

Muon Veto

Most importantly, the cylindrical muon-track veto included in the nominal strategy could not be applied to the full dataset, as a reliable muon-track reconstruction had not yet been validated for this analysis. The muon-related vetoes are therefore currently limited to three PE-threshold-based muon topologies : the nominal CD-only and WP-only categories, complemented by an additional CD+WP category, defined from the time correlation between relatively high-charge WP and CD events, further detailed in Table 5.2. This revised muon veto strategy, without an additional track-based veto, gives a selection efficiency of 95.5%.

Neutron Veto

The missing muon-track veto is replaced by a spallation neutron veto, whose motivation is further discussed in Section 5.3. This veto consists of a 4 m radius spherical veto, applied for 1.2 s around each tagged spallation neutron candidate, defined as an event with energy in $[1.5, 20]$ MeV, reconstructed within a $[20\,\mu\text{s}, 2\,\text{ms}]$ time window following a muon. Spallation neutron events have to be further distinguished from PMT after-pulses induced by high-intensity cosmic muons [176]. The latter populate the event window with a flat hit time profile, and a correspondingly larger standard deviation than the peaked signature of genuine physics events, allowing the two populations to be discriminated. The two populations can be clearly distinguished in Figure 5.2, where a population with near-constant standard deviation is visible above 275 ns, motivating the use of this threshold as an additional constraint in the spallation neutron tagging criterion.

Summary

The revised set of selection cuts gives a total efficiency of 70.3%, significantly lower than the nominal value. This reduction is caused primarily by the reduced fiducial volume, and extensive efforts are ongoing to recover the nominal $R < 17.2$ m boundary in future iterations of this analysis.

5.2.3 Results

The validation of the selection strategy defined in Table 5.2 was performed collaboratively among analysers of the European/American analysis group. A dedicated selection pipeline was developed for the Bordeaux group and applied to new runs on a daily basis, contributing directly to this validation effort. Once the selection strategy was validated, it was applied to the entire

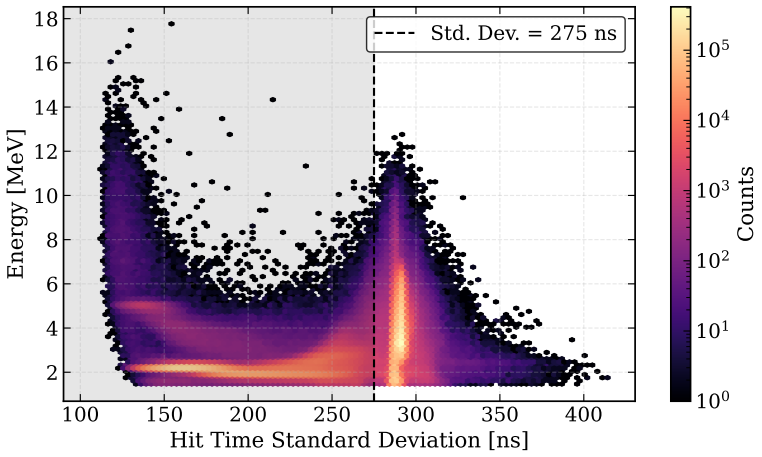

FIGURE 5.2 – Spallation neutron candidate energy as a function of the event's hit time distribution standard deviation. The grey band corresponds to events retained after the 275 ns standard deviation cut.

available dataset, yielding a total of 5082 raw IBD candidates, reduced to 2498 candidates after applying the neutron veto — a reduction of more than half the initial sample, illustrating the cosmogenic contamination discussed further in the remainder of this chapter. The daily rate of these candidates is shown in Figure 5.3 as a function of the date, averaging 46.1 IBD counts per day (cpd) and fully compatible with the expected 47.1 cpd [85].

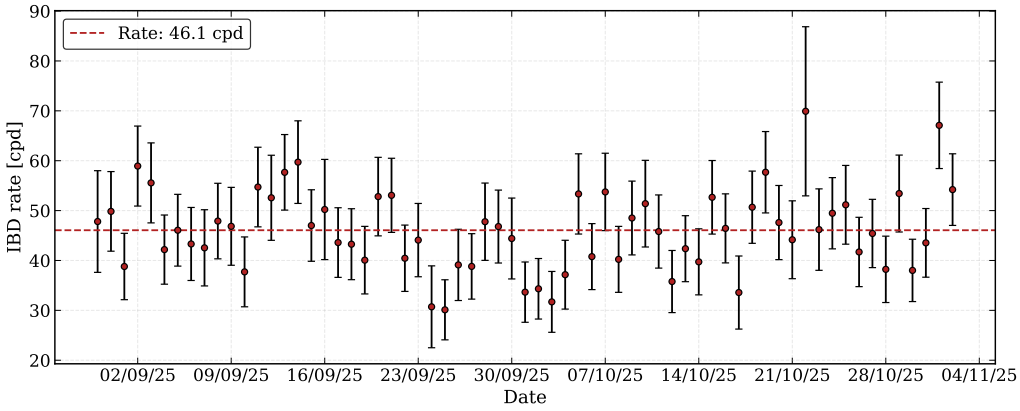

FIGURE 5.3 – Rate of IBD candidates, in counts per day (cpd), without efficiency correction, as a function of the date. The selection retrieves an average rate of 46.1 cpd.

The performance of the selection can be assessed further from Figure 5.4, which shows the prompt and delayed energy spectra, together with the prompt-delayed time and distance correlations.

The prompt energy spectrum reproduces the expected shape of the reactor antineutrino spectrum, while the delayed energy spectrum peaks at a mean energy of 2.226 ± 0.001 MeV, in good agreement with the expected n-H γ-ray energy of 2.223 MeV. The selection is further validated by extracting the decay time of the prompt-delayed time coincidence distribution, shown in the bottom right panel of Figure 5.4 : an exponential fit yields a decay time $\tau = 226.3 \pm 9.4$ μs,

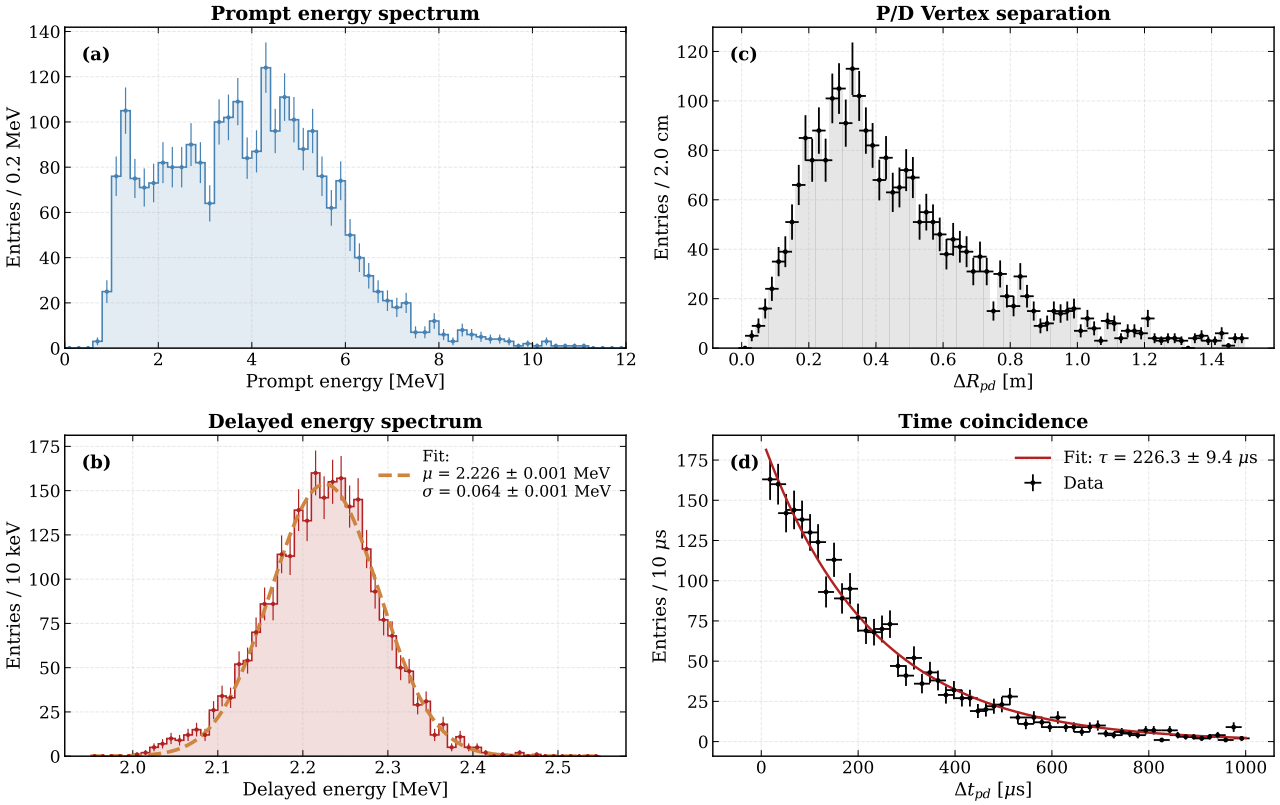

FIGURE 5.4 – Selected IBD candidate distributions. **(a)** Prompt energy spectrum. **(b)** Delayed energy spectrum, with a Gaussian fit yielding a mean energy of 2.226 ± 0.001 MeV. **(c)** Distribution of the prompt-delayed distance, ΔR. **(d)** Distribution of the prompt-delayed time coincidence, Δt, with an exponential fit yielding a decay time of $\tau = 226.3 \pm 9.4$ μs.

compatible with the expected ~ 200 μs neutron capture time in the JUNO liquid scintillator. The prompt-delayed distance distribution, shown in the top right panel, is peaked around 0.3 m, with less than 10% of IBD correlated pairs separated by more than a meter.

The revised selection strategy shows good overall performance in retrieving IBD candidates, yielding an IBD rate compatible with expectations. The resulting IBD spectrum, however, contains an unavoidable residual level of background contamination, whose rate and shape needs to be correctly estimated prior to the oscillation fit, in order to reduce biases as much as possible.

5.3 Cosmogenic ^{9}Li/^{8}He

Among the backgrounds of concern, the cosmogenic isotopes ^{9}Li and ^{8}He need to be carefully constrained as they are able to closely mimic the IBD signal. This section presents the physical origin of this background and its characteristic decay signature, before detailing its impact on the measured IBD sample.

5.3.1 Production

Highly energetic muons crossing the JUNO liquid scintillator can undergo spallation interactions with ^{12}C nuclei, the dominant carbon isotope in the scintillator, producing a range of unstable secondary nuclei alongside free neutrons. Among the resulting cosmogenic isotopes, ^{9}Li and ^{8}He constitute the most significant background to the IBD selection, owing to their characteristic decay signature detailed below. Their respective decay chains are shown in Figure 5.5.

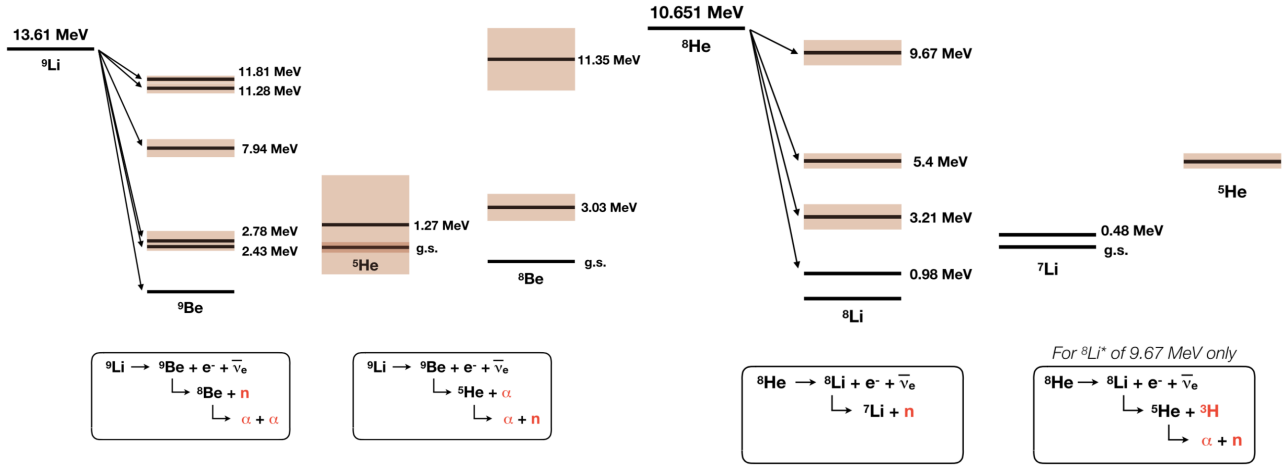

FIGURE 5.5 – Decay schemes of ^{9}Li (left) and ^{8}He (right). The available decay route of each isotopes is given in the boxes located underneath each decay tree, also giving the subsequent particle emission from each step. Taken from [177].

^{9}Li

In 49.2% of decays, ^{9}Li does not constitute a background for reactor antineutrino events, as the β^{-} decay proceeds directly to the ground state of ^{9}Be, with no correlated neutron emission. In the remaining 50.8% of decays, however, ^{9}Li populates an excited state of ^{9}Be, which decays via two routes, both producing $2\alpha + n$: neutron emission to an excited or ground state of ^{8}Be, itself decaying into two α particles ; or α decay to an excited or ground state of ^{5}He, which further decays into $\alpha + n$. It is this second population of decays that gives rise to the β-n

signature responsible for mimicking the IBD signal, and is illustrated in the left decay tree of Figure 5.5.

^{8}He

Only 16% of ^{8}He decays happen via β^{-} emission, populating one of several excited states of ^{8}Li. The highest-energy level, at 9.67 MeV, decays via triton and ^{5}He emission, with the latter subsequently decaying into $\alpha + n$. For the remaining excited states, the decay happens via direct neutron emission. In both cases, the ^{8}Li excited states release a free neutron, again producing the characteristic β-n signature. The corresponding decay scheme is illustrated in the right decay tree of Figure 5.5.

5.3.2 Impact on IBD Measurement

Both ^{9}Li and ^{8}He are predominantly β^{-}-neutron emitters, whose prompt-delayed signature closely mimics the genuine IBD coincidence. Both isotopes are, moreover, long-lived, with mean lifetimes of $\tau = 257.2$ ms and $\tau = 171.7$ ms for ^{9}Li and ^{8}He respectively, requiring the detector to be vetoed over a relatively long period following each muon in order to suppress the subsequent misidentification of these cosmogenic decays as genuine IBD events. Since the prompt-delayed signature of both event types is identical, this background cannot be removed through spatial and temporal correlation with the prompt-delayed pair alone, motivating the development of dedicated, muon-related veto strategies capable of exploiting the correlation between the parent muon and the induced isotope over these longer timescales.

The nominal strategy for this purpose relies on a veto constructed around the reconstructed muon track itself. In the absence of a validated muon-track reconstruction at this early stage of JUNO operation, an alternative approach is instead adopted, exploiting the fact that the same spallation process producing ^{9}Li and ^{8}He also produces free neutrons along the muon track. Tagging these accompanying neutrons therefore provides an indirect handle on the probability that the parent-muon produced a cosmogenic isotope along the track.

This alternative approach also comes with its limitations : in addition to occasionally removing genuine IBD events, its cosmogenic ^{9}Li/^{8}He background reduction capabilities are less powerful than the nominal muon-track veto, and might lead to a greater residual cosmogenic background rate than expected. Quantifying this residual rate is therefore essential to properly constrain the oscillation fit, and is the subject of the remainder of this chapter.

5.4 Li/He Rate Estimation

5.4.1 General Strategy

The neutron veto efficiency given in Table 5.2 provides no direct information on the amount of cosmogenic background surviving the cut, leaving an unknown residual ^{9}Li/^{8}He contamination in the final IBD sample. This section presents a method developed to estimate this residual rate, exploiting the correlation between each IBD candidate and any preceding muon capable of producing a cosmogenic isotope.

For every IBD candidate, the time difference $dt = t_{\mathrm{IBD}} - t_{\mu}$ is computed with respect to every muon crossing the CD within a 1.2 s window preceding the IBD, and requiring the muon to have produced at least one spallation neutron. Since genuine IBD events and other muon-uncorrelated backgrounds occur independently of any muon, they populate this dt distribution uniformly, producing a flat component across the 1.2 s window. Cosmogenic ^{9}Li/^{8}He events, however, are produced by one specific muon within that window, and populate the distribution as an exponential decay with a rate corresponding to the isotope's lifetime. This shape allows the total cosmogenic rate to be extracted directly from data, through an exponential decay fit of each component. It should be noted that this method does not associate a single (IBD, muon) pair to each IBD event, but connects the event to all the muons within the window, leading to the flat component being a mixture of genuine muon-uncorrelated events and ^{9}Li/^{8}He events paired with the wrong muons.

The method is applied twice, to two distinct populations : first to the full IBD sample, before the neutron veto is applied (Section 5.4.2), and then to the population of events removed by the neutron veto, i.e. the *in-veto* sample (Section 5.4.4). The residual ^{9}Li/^{8}He rate, remaining in the final IBD sample, is obtained by comparing the rate extracted from the full IBD sample — before the neutron veto — and the in-veto sample using :

$$R^{\mathrm{final}}_{\mathrm{Li/He}} = R^{\mathrm{full}}_{\mathrm{Li/He}} - R^{\mathrm{inveto}}_{\mathrm{Li/He}} \tag{5.1}$$

5.4.2 Rate Before the Neutron Veto

The dt distribution of all (IBD, muon) pairs satisfying $N_{\mathrm{n}} \geq 1$, where N_{n} is the number of spallation neutrons tagged for that muon, is described by a three-components model :

$$f(t) = \frac{N_{\mathrm{Li}}}{\tau_{\mathrm{Li}}}\, e^{-t/\tau_{\mathrm{Li}}} + \frac{N_{\mathrm{He}}}{\tau_{\mathrm{He}}}\, e^{-t/\tau_{\mathrm{He}}} + N_{\mathrm{bkg}} \tag{5.2}$$

where τ_{Li} and τ_{He} are fixed to the ^{9}Li and ^{8}He mean lifetimes, N_{Li}, N_{He}, are their fitted

yields, and N_{bkg} is the flat background amplitude, giving the rate of muon-uncorrelated (IBD, muon) pairs. The fit is performed as an unbinned maximum-likelihood fit using `MINUIT` [178], with the negative log-likelihood defined as :

$$-\log \mathcal{L} = \nu - \sum_i \log \lambda(t_i) \tag{5.3}$$

where $\lambda(t_i)$ is the un-normalised event density, defined by Eq. 5.2, and ν is its integral over the $[0, 1.2]$ s fit window. This unbinned approach is motivated by the limited early-stage statistics, and avoids any information loss from using binned distributions. The resulting fit is shown in Figure 5.6.

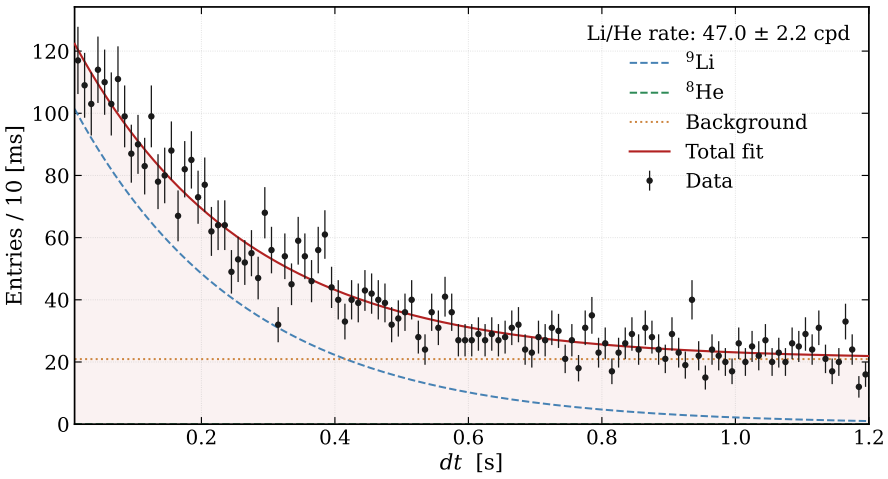

FIGURE 5.6 – IBD–muon time difference dt for all pairs with at least one accompanying spallation neutron ($N_{\text{n}} \geq 1$). The distribution is fitted using the model given by Eq. 5.2. The fitted ^{9}Li and ^{8}He components (dashed line) and the flat accidental background (dotted line) are shown alongside the total model (solid line) and the binned data (points). The best fit is obtained for a combined Li/He rate of 47.0 ± 2.2 cpd.

Li/He Rate

The fit yields a total ^{9}Li/^{8}He rate of

$$R^{\text{full}}_{\text{Li/He}} = \frac{N_{\text{Li}} + N_{\text{He}}}{T_{\text{eff}}} = 47.0 \pm 2.2 \text{ cpd} \tag{5.4}$$

where $T_{\text{eff}} = 57.7$ days is the effective livetime of the dataset. Naively, the fit seems to favour a dominant ^{9}Li contribution in the dt distribution. However, due to the relatively close values of $\tau_{\text{Li}} = 257$ ms and $\tau_{\text{He}} = 172$ ms compared to the fit window, the individual yields N_{Li} and N_{He} are strongly correlated and not well constrained individually by the dt shape alone. An additional constraint is therefore required to disentangle the two (see Section 5.4.4). Consequently, only their sum, $N_{\text{Li}} + N_{\text{He}}$, is presented at this stage.

5.4.3 Accompanying Neutron Efficiency

The rate given above must be corrected for the fact that not every ^{9}Li/^{8}He decay is accompanied by a detected spallation neutron. This rate cannot therefore be directly compared to a rate computed from in-veto events unless it is first corrected by the accompanying-neutron efficiency ε_n, defined as the fraction of ^{9}Li/^{8}He decays satisfying $N_{\mathrm{n}} \geq 1$. Measuring ε_n requires a pure cosmogenic control sample. While the fully validated muon track reconstruction discussed earlier in this chapter is not yet available for this analysis, a preliminary track reconstruction, relying solely on WP information, could be used to build this control sample. The latter is therefore constructed using the subset of muons with a single, well-reconstructed track ($\sim 64\%$ of the total CD+WP tagged muon sample). For each of these muons, the distance dR between the IBD vertex and the reconstructed muon track is computed for every (IBD, muon) pair correlated within the 1.2 s window. For a sufficiently small radius cut R_{cut}, the resulting subsample should correspond to a high-purity cosmogenic Li/He selection, from which ε_n can be extracted.

Radius Cut Optimisation

The optimal radius cut R_{cut} is determined by fitting the dt distribution for different values of R_{cut}, and evaluating three figures of merit :

1. **Purity.** Defined as $N_{\mathrm{Li/He}}/(N_{\mathrm{Li/He}} + N_{\mathrm{bkg}})$, it gives the fraction of the sample corresponding to genuine cosmogenic Li/He decays, with each component extracted from the dt fit.
2. **Relative Precision.** Defined as $\sigma_{N_{\mathrm{LiHe}}}/N_{\mathrm{LiHe}}$, it quantifies how well the statistics obtained for a given radius cut, properly constrain the extracted ^{9}Li/^{8}He yield.
3. **Significance.** Defined as $S/\sqrt{S+B}$, with $S = N_{\mathrm{Li/He}}$ and $B = N_{\mathrm{bkg}}$, it provides a direct handle on the statistical confidence with which the surviving sample can be distinguished from a background-only hypothesis.

The dt distributions obtained for $R_{\mathrm{cut}} \in [10\ \mathrm{cm}; 10\ \mathrm{m}]$ are fitted using Eq. 5.2, and the evolution of each figure of merit is shown in Figure 5.7. The purity degrades gradually as R_{cut} increases, as more accidental events are introduced into the pure, low-radius Li/He sample. The significance rises sharply at small R_{cut}, since the majority of cosmogenic isotopes are concentrated near the parent muon track, before stabilising once the cut is wide enough to contain the full cosmogenic population, and decreasing slowly as background continues to accumulate. The chosen working point, $R_{\mathrm{cut}} = 2$ m, lies just before the significance plateau, and retains a purity of $\sim 95\%$.

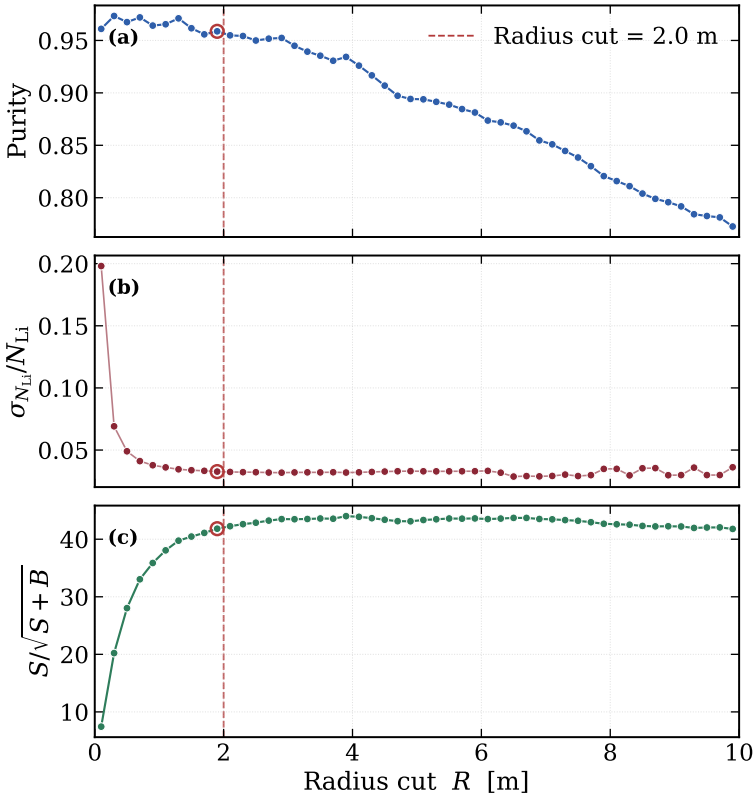

FIGURE 5.7 – Purity, relative statistical uncertainty on the fitted ^{9}Li yield, and significance $S/\sqrt{S+B}$ as a function of the IBD–track distance cut dR. The chosen working point, $dR <$ 2.0 m (dashed line), lies at the onset of the significance plateau, beyond which further loosening the cut adds little statistical power while steadily degrading purity.

Corrected Li/He Rate Before Veto

Having extracted an optimal value for R_{cut}, the accompanying-neutron efficiency is estimated from the sample of IBD events located within 2 m of their time-correlated muon track, split into two subsamples depending on whether an accompanying neutron is found : unaccompanied ($N_{\text{n}} = 0$) and accompanied ($N_{\text{n}} \geq 1$), as shown in Figure 5.8. A dt distribution is constructed for each subsample and fitted using Eq. 5.2, as shown in Figure 5.9. The fit yields a Li/He rate of $N_{\text{Li/He}}^{\text{unacc}} = 3.1 \pm 0.4$ cpd for the unaccompanied sample and $N_{\text{Li/He}}^{\text{acc}} = 32.3 \pm 0.9$ cpd for the accompanied one. Figure 5.9. The accompanying-neutron efficiency is directly obtained from these values :

$$\varepsilon_n = \frac{N_{\text{LiHe}}^{\text{acc}}}{N_{\text{LiHe}}^{\text{acc}} + N_{\text{LiHe}}^{\text{unacc}}} = 91.3 \pm 1.4\% \tag{5.5}$$

and the corrected before-veto rate is obtained by dividing the rate computed in Eq. 5.4 by ε_n :

$$R_{\text{Li/He}}^{\text{full,corr}} = \frac{R_{\text{Li/He}}^{\text{full}}}{\varepsilon_n} = 51.5 \pm 2.5 \text{ cpd} \tag{5.6}$$

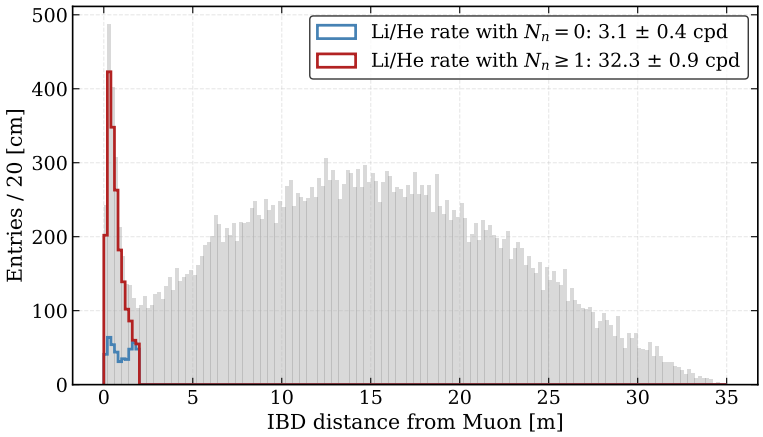

FIGURE 5.8 – dR distribution of all IBD–muon pairs (grey), split into the accompanied ($N_\mathrm{n} \geq 1$, blue) and unaccompanied ($N_\mathrm{n} = 0$, red) subsamples, and yielding a combined ^{9}Li+^{8}He rate of 32.3 ± 0.9 and 3.1 ± 0.4 respectively.

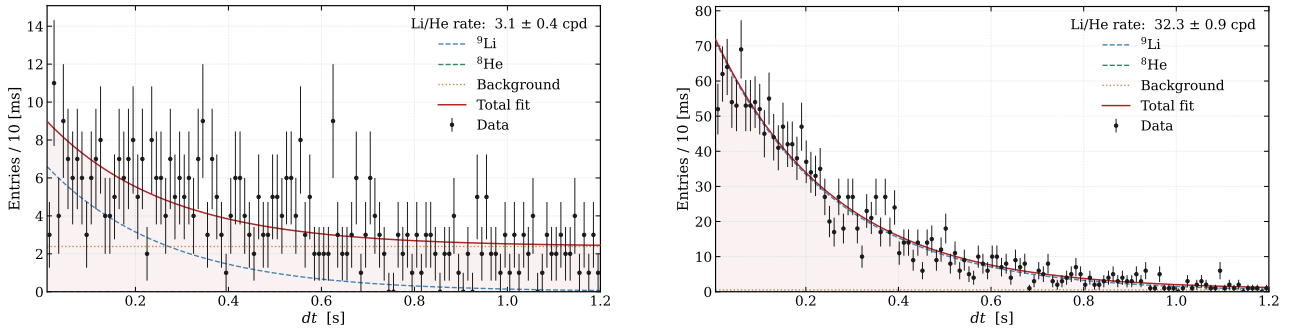

(a) (b)

FIGURE 5.9 – dt distribution and corresponding fit for the **(a)** neutron-unaccompanied and **(b)** neutron-accompanied Li/He subsamples.

5.4.4 Rate Inside the Neutron Veto

As mentioned in Section 5.4.2, the similarity between τ_Li and τ_He relative to the dt fit window makes the individual yields N_Li and N_He strongly degenerate when extracted from timing information alone. The additional handle required to break this degeneracy lies in the energy spectrum of the in-veto IBD events, whose distinct ^{9}Li and ^{8}He spectral shapes provide the additional constraint needed to disentangle the two contributions. This is achieved through a combined fit of the in-veto IBD–muon dt distribution and prompt energy spectrum.

Time Correlation

The in-veto dt distribution is constructed from the correlation between each vetoed IBD candidate and the muon that produced the vetoing spallation neutron, following the spallation neutron definition given in Table 5.2. Unlike the before-veto sample, this sample contains a

single (IBD-like, muon) pair per in-veto IBD-like event. Following the same procedure as in Section 5.4.2, this distribution is fitted using the model defined in Eq. 5.2.

Energy Spectrum

The prompt energy spectrum of the in-veto sample is constructed directly from data, and fitted using a mixture of Monte Carlo-based and data-driven templates. Since the ^{9}Li and ^{8}He energy spectra are not directly accessible from data, they are instead simulated using the full JUNOSW simulation chain, up to the reconstructed energy. These simulations precede the upgrades described in Section 4.3.3, and were not reproduced with the updated software, as its production is computationally expensive and could not be performed within the time available for this thesis. As a result, the simulated energy response does not yet fully reproduce JUNO's current detector response, so that the resulting ^{9}Li and ^{8}He template shapes may be slightly different than their true spectra. The accidental background template, by contrast, is constructed directly from data, using an off-window method to select events accidentally falling within the neutron veto.

The total energy probability density is then given by :

$$f(E) = \alpha_{\mathrm{Li}}\, f_{\mathrm{Li}}(E) + \alpha_{\mathrm{He}}\, f_{\mathrm{He}}(E) + \alpha_{\mathrm{bkg}}\, f_{\mathrm{bkg}}(E) \tag{5.7}$$

where f_{Li}, f_{He}, and f_{bkg} are the corresponding ^{9}Li, ^{8}He, and accidental templates described above and normalised to unity, and

$$\alpha_k = \frac{N_k}{N_{\mathrm{tot}}}, \qquad N_{\mathrm{tot}} = N_{\mathrm{Li}} + N_{\mathrm{He}} + N_{\mathrm{bkg}}, \qquad k \in \{\mathrm{Li}, \mathrm{He}, \mathrm{bkg}\} \tag{5.8}$$

are the fractions associated to each template, so that $f(E)$ integrates to unity. The combined negative log-likelihood is therefore the sum of an extended unbinned term for the dt distribution and a binned term for the energy spectrum, both evaluated simultaneously for a common set of yields $(N_{\mathrm{Li}}, N_{\mathrm{He}}, N_{\mathrm{bkg}})$:

$$-\log \mathcal{L}_{\mathrm{comb}} = \underbrace{\left[\nu_{dt} - \sum_i \log \lambda_i(t_i)\right]}_{\text{extended, unbinned } dt} \underbrace{- \sum_j n_j \log p_j(E)}_{\text{shape-only, binned energy}} \tag{5.9}$$

where $\lambda_i(t)$ is given by Eq. 5.2, ν_{dt} is its integral over the dt fit window, n_j is the measured count in energy bin j, and

$$p_j(E) = \int_{E_j}^{E_{j+1}} f(E')\, dE' \tag{5.10}$$

is obtained by integrating Eq. 5.7 over bin j, giving the bin's predicted probability, so that

$\sum_j p_j(E) = 1$.

This construction constrains the total yield $N_{\text{tot}} = N_{\text{Li}} + N_{\text{He}} + N_{\text{bkg}}$ exactly once, through the extended dt term. The energy term instead constrains only the relative ^{9}Li/^{8}He/accidental composition, through the fractions α_k, rather than acting as an independent extended binned Poisson likelihood, which would separately re-constrain the same total yield and artificially increase the statistical precision of the combined fit. The fit is performed with `MINUIT`, and the result is shown in Figure 5.10, with the best fit obtained for the following rates :

$$\begin{aligned} R_{\text{Li}}^{\text{final}} &= 42.7 \pm 1.4 \text{ cpd} \\ R_{\text{He}}^{\text{final}} &= 2.2 \pm 1.0 \text{ cpd} \\ R_{\text{bkg}}^{\text{final}} &= 1.2 \pm 0.5 \text{ cpd} \end{aligned} \tag{5.11}$$

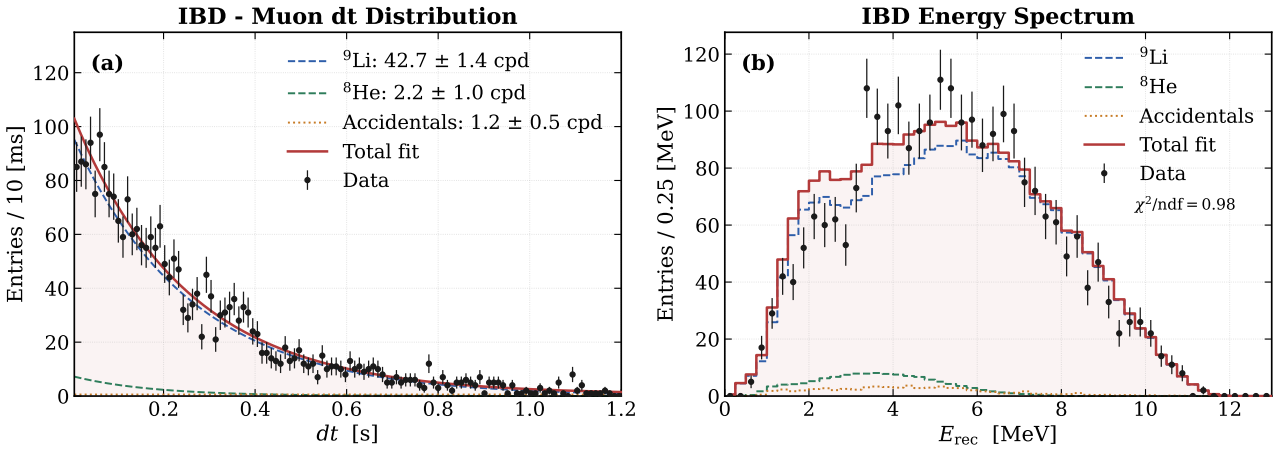

FIGURE 5.10 – Simultaneous fit of the in-veto dt distribution **(a)** and prompt energy spectrum **(b)**, sharing the ^{9}Li, ^{8}He, and accidental yields between the two observables. The extracted rate from the combined fit is given in the legend of **(a)**.

5.4.5 Residual Rate After the Neutron Veto

Li/He Fraction

The relative contribution of each isotope to the in-veto sample is quantified by the Li/He fraction :

$$f_{\text{Li}} = \frac{N_{\text{Li}}}{N_{\text{Li}} + N_{\text{He}}} \tag{5.12}$$

evaluated directly from the yields of the combined fit, giving $f_{\text{Li}} = 95.1\% \pm 2.3\%$. This preliminary result is consistent with the higher ^{9}Li production rate and branching ratio discussed in Section 5.4, and shows good agreement with a small but non-zero contribution from ^{8}He when compared to the measurements reported by previous reactor neutrino experiments [163, 166, 169, 162].

Residual Rate

Summing the fitted ^{9}Li and ^{8}He yields, and accounting for the correlation term in the covariance matrix, gives a total in-veto Li/He rate of $R^{\text{inveto}}_{\text{Li/He}} = 44.9 \pm 1.0$ cpd. Combined with the corrected before-veto rate of Eq. 5.6 and following the relation of Eq. 5.1, the residual ^{9}Li/^{8}He rate remaining in the final, selected IBD sample is estimated to be :

$$R^{\text{final}}_{\text{Li/He}} = 51.5 - 44.9 = 6.6 \pm 2.7 \text{ cpd} \tag{5.13}$$

in good agreement with the residual rate independently obtained by other analysers within the collaboration, providing a cross-check of the method presented in this section. This value is, however, considerably higher than the nominal rate of 0.8 cpd expected for this background, a discrepancy most likely coming from the absence of a muon-track veto in this analysis.

5.5 Conclusion

This chapter presented the revision of JUNO's nominal IBD selection strategy to account for the reconstruction and calibration performance available during the early stage of data-taking, and the development of a dedicated pipeline able to consistently retrieve IBD events as JUNO's data were taken. Applying this selection to the first 60 days of JUNO data yielded the first IBD candidate sample of the experiment, with a rate of 46.1 cpd, compatible with the 47.1 cpd nominal expectation. The selection was further validated by investigating the delayed energy spectrum and the prompt–delayed time correlation, which yield, respectively, a mean energy $E_d = 2.226 \pm 0.001$ MeV and a decay time $\tau = 226 \pm 9.4$ μs, both compatible with their expected values.

The remainder of the chapter was dedicated to developing a method to estimate the residual ^{9}Li/^{8}He rate in the final IBD sample. This method yields a total residual rate of $R^{\text{final}}_{\text{Li/He}} = 6.6 \pm 2.7$ cpd, higher than the nominal expectation for this background. This excess is most likely explained by the absence of a muon-track veto in the current analysis, and its reduction should be a priority for future iterations of this work.

The selection methodology developed throughout this chapter, and its daily application to data, lead to the continuous accumulation of IBD statistics since the beginning of JUNO's data-taking. This growing dataset opens the possibility of developing a complementary background-discrimination method, exploiting the formation of ortho-positronium following a genuine IBD interaction. Its delayed signature can be used through pulse shape discrimination techniques to distinguish signal from background and is presented in the following chapter.

Chapitre 6

Ortho-Positronium formation in JUNO

Summary

6.1 Introduction . . . 175
6.2 Ortho-Positronium . . . 175
6.2.1 Formation and Signature . . . 175
6.2.2 Experimental Measurements . . . 176
6.2.3 Limitations . . . 177
6.3 Fitting Framework . . . 178
6.3.1 Building the Model . . . 178
6.3.2 Fit Architecture . . . 179
6.3.3 Parameter Initialisation and Constraints . . . 181
6.3.4 Minimisation Strategy . . . 182
6.4 Characterisation on Simulated Data . . . 183
6.4.1 Single-Point Analysis at 3 MeV . . . 183
6.4.2 Constraining non o-Ps Population . . . 185
6.4.3 Formation Fraction and Lifetime Estimation . . . 186
6.4.4 Spatial Dependence . . . 189
6.4.5 Energy Dependence . . . 192
6.5 Results on JUNO Data . . . 195
6.5.1 IBD Candidate Sample . . . 195
6.5.2 Fitted o-Ps Parameters . . . 196
6.5.3 Outlook . . . 200
6.6 Prospects with Improved PMT Timing (Hamamatsu Subset) . . . 200
6.6.1 Fit Performance on Simulated Data . . . 201
6.6.2 Investigating the Origin of Bias . . . 202
6.6.3 Prospects . . . 203
6.7 Conclusion . . . 204

6.1 Introduction

A technique commonly used in liquid scintillator-based detectors to discriminate signal from background is Pulse Shape Discrimination (PSD) [179]. Based on differences in energy loss per unit path length in scintillating media, PSD allows heavy particles such as α particles and protons, which deposit energy more densely, to be distinguished from lighter particles such as electrons and positrons. However, this method is ineffective at discriminating between particles with similar energy loss profiles, such as positrons and electrons. As an alternative approach to e^+/e^- discrimination, a PSD technique can be developed based on the formation of ortho-positronium (o-Ps), which introduces a characteristic distortion in the time profile of the scintillation signal.

This chapter presents a first investigation of ortho-positronium formation in JUNO, using both simulation and the first JUNO data. The o-Ps formation fraction and lifetime in the JUNO liquid scintillator are estimated using a dedicated fitting method applied to the time profile of the scintillation signal. The chapter is organised as follows. Section 6.2 introduces the physics of ortho-positronium formation in liquid scintillator, reviews previous o-Ps-based measurements, it's detection in scintillator-based detectors, and discusses the limitations expected in JUNO. Section 6.3 describes the fitting framework developed to identify the o-Ps signature on an event-by-event basis, including the construction of the time profile PDF and the minimisation strategy. This framework is characterised on simulated data in Section 6.4, where its spatial and energy dependence are investigated and used to define the selection criteria applied on data. Section 6.5 applies this framework to the first 193.2 days of JUNO data, presenting the first measurement of the o-Ps formation fraction and lifetime in the JUNO liquid scintillator. Finally, Section 6.6 investigates the prospects offered by the improved timing resolution of the Hamamatsu PMT subset.

6.2 Ortho-Positronium

6.2.1 Formation and Signature

The positron emitted following an IBD interaction may either annihilate directly with an electron of the medium, or form a bound state known as positronium (Ps) [180]. Positronium forms in two possible spin configurations : the singlet state, with antiparallel spins, known as para-positronium (p-Ps), and the triplet state, with parallel spins, known as ortho-positronium (o-Ps). The p-Ps state accounts for 25% of all positronium formed and has a vacuum lifetime of 125 ps [181], while o-Ps accounts for the remaining 75% and has a vacuum lifetime of 142 ns [182]. In vacuum, p-Ps decays by emitting two back-to-back 511 keV γ-rays, while o-Ps predo-

minantly decays via the emission of three γ-rays.

In matter, however, the o-Ps lifetime is dramatically shortened by several quenching mechanisms. The most relevant in organic liquid scintillators are : *pick-off* annihilation, in which the o-Ps positron annihilates with a surrounding electron of opposite spin from the medium, emitting two 511 keV γ-rays [183, 184] ; *spin conversion*, in which o-Ps converts to p-Ps via spin-exchange interactions with paramagnetic molecules such as O_2 [185, 186] ; and chemical reactions such as oxidation [184]. Through these processes, the effective o-Ps lifetime in organic liquid scintillators is reduced to only a few nanoseconds, several orders of magnitude shorter than its vacuum value. Since the three-γ decay channel only becomes accessible on the full vacuum lifetime, it is strongly suppressed once o-Ps is quenched, and therefore decays predominantly via the two-γ channel through one of the quenching mechanisms listed above.

The p-Ps lifetime, being comparable to that of directly annihilating positrons (∼few hundreds of picoseconds), cannot be observed in most experimental setups. The o-Ps formation, on the other hand, introduces a measurable delay of a few nanoseconds between the initial positron energy deposition and the emission of the annihilation γ-rays, which manifests as a characteristic distortion in the time profile of the scintillation signal.

6.2.2 Experimental Measurements

o-Ps formation in liquid scintillator has been studied extensively in the context of liquid scintillator-based neutrino experiments, including the LAB-based scintillator recipe used in JUNO. Measurements performed using Positron Annihilation Lifetime Spectroscopy (PALS), yield an average o-Ps lifetime compatible with ~ 3 ns [153, 187, 188] with a formation probability ranging from $43.7 \pm 1.2\%$ [187] to $54.2 \pm 0.5\%$ [153].

The time profile distortion induced by o-Ps formation provides a powerful tool for discriminating between positron and electron events in liquid scintillator detectors. Since ^{9}Li and ^{8}He decay via β^{-}-neutron emission, their prompt signal is produced by an electron, which does not form positronium and therefore produces no o-Ps delayed annihilation component in the scintillation time profile. In contrast, the IBD prompt signal is produced by a positron, which can form o-Ps and therefore exhibits the characteristic delayed annihilation signature. This fundamental difference in the time profile of the two event types constitutes the basis of an o-Ps-based PSD technique, allowing IBD events to be statistically distinguished from ^{9}Li/^{8}He background events.

Such an approach is complementary to the veto-based methods described in the previous chapter assuming that the detector timing resolution is sufficient to resolve the nanosecond-

scale o-Ps lifetime, and has the advantage of not introducing any additional signal inefficiency. The o-Ps PSD technique was successfully demonstrated in the Double Chooz [189] experiment, where the o-Ps formation fraction and lifetime were measured to $44\% \pm 12\%$ (sys.) $\pm 5\%$ (stat.) and 3.68 ns$\pm$0.17 ns (syst.)$\pm$0.15 ns (stat.) respectively. Additionally, the Borexino experiment proved the possibility to use o-Ps observation in a statistical way to discriminate e^+/e^- events, effectively reducing the contamination of cosmogenic ^{11}C backgrounds in the solar *pep* neutrino observation [190].

6.2.3 Limitations

Despite its potential, the implementation of an o-Ps-based PSD technique in JUNO faces several challenges. The first is the energy dependence of the o-Ps identification, which relies on the ability to identify the delayed annihilation component in the scintillation time profile. At higher positron energies, the number of photons produced by the prompt ionisation signal increases roughly linearly with energy, while the amplitude of the delayed annihilation component remains fixed at 1.022 MeV energy. The annihilation component therefore becomes an increasingly small fraction of the total signal as the positron energy increases, making it progressively harder for the fit to identify the annihilation, burried below a much larger prompt ionisation signal, ddegrading the sensitivity of the o-Ps identification. This is consistent with the approach adopted by Double Chooz, where the o-Ps analysis was restricted to positron energies below 3 MeV to ensure a reliable identification of the delayed component [189].

The second challenge is the timing resolution of the detector, as o-Ps identification heavily relies on the ability to resolve the nanosecond-scale lifetime of the o-Ps. JUNO is equipped with two types of LPMTs with different time resolution, as illustrated by Figure 2.13b : the NNVT and Hamamatsu PMTs have a transit time spread (TTS) of 7.53 ns (σ) and 1.93 ns (σ) respectively. Although the Hamamatsu PMTs offer a timing resolution competitive with that of the Dooble Chooz photomultiplier system, which had a TTS of 2.8 ns [191], the coverage of Hamamatsu PMTs in the JUNO detector is considerably sparser than that of NNVT's, introducing statistical limitations in the reconstruction of the photon time distribution if used alone.

6.3 Fitting Framework

Although challenging for the reasons outlined above, the identification of ortho-positronium can be performed in JUNO, with the central difficulty being the separation of the prompt ionisation signal from the delayed annihilation component in the time profile. The methods presented in this section are largely inspired by the analysis developed in Ref. [189] and adapted to the specific characteristics of the JUNO detector.

6.3.1 Building the Model

Motivations

The o-Ps identification relies on the decomposition of the IBD prompt event time profile into two components : a prompt ionisation contribution from the positron loosing energy in the scintillator, and a delayed annihilation contribution from the o-Ps decay into two 511 keV γ-rays. Although these two contributions arise from distinct processes, the shape of their time profiles is produced by the same detector response, dominated by the PMT timing resolution and the scintillator's photon emission and propagation properties. A single time profile PDF can therefore describe both components distinguished solely by their relative amplitude.

The time profile PDF is constructed from ^{68}Ge calibration source events, which produce two simultaneous back-to-back 0.511 MeV γ-rays, effectively providing an accurate template for the annihilation signal. The PDF is constructed by accumulating the time profiles of ^{68}Ge events on an event-by-event basis, following the selection procedure described in Section 4.4.1, and correcting two effects that introduce a broadening in the accumulated distribution.

Corrections and PDF building

First, a deformation of the time profile can be introduced by the position of the event : a photon emitted at a given position in the detector will reach PMTs at different distances around the sphere at different times, introducing a spread in the raw hit time distribution. Each photon hit time should be corrected for the time-of-flight (ToF) from the reconstructed vertex to the PMT. For events produced at the center of the detector, the light path to the PMTs on the sphere is identical, so the ToF correction is negligible. To remove any additional contribution that could arise from vertex reconstruction, the PDF is therefore constructed using the ^{68}Ge source deployed at the center of the detector via the ACU.

Secondly, the event-by-event variations in the signal rise time can introduce additional smearing in the accumulate time profile PDF. Therefore, each event time profile is aligned by shifting it so that its inflection point — the mid-point of rise on the time profile — is set to a

common reference time of $t = 200$ ns prior to accumulation. The inflection point of each time profile is extracted by fitting a logistic (sigmoid) function on a short window around the signal rise :

$$f(x) = \frac{A}{1 + e^{-k(x-x_0)}} \tag{6.1}$$

where A is the amplitude, k is the steepness of the rising edge, and x_0 is the inflection point. Simpler alignment strategies, such has aligning the maximum of each event's time profile were considered but found to introduce artifacts at the alignment point, making the sigmoid-based inflection point method the preferred choice. An illustration of the sigmoid fit and the resulting alignment is shown in Figure 6.1.

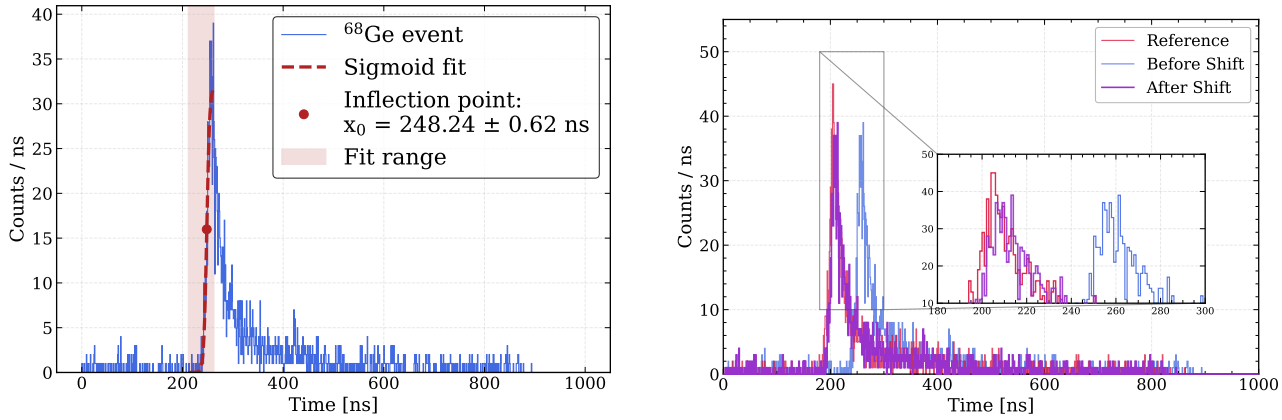

(a) (b)

FIGURE 6.1 – Illustration of the time profile alignment procedure. **(a)** Example sigmoid fit applied to a single ^{68}Ge event time profile, used to extract the inflection point x_0. **(b)** Resulting time profiles before and after the alignment shift to the common reference time $t = 200$ ns and compared to an already shifted reference event.

The resulting shifted and accumulated distribution is shown in Figure 6.2, where the alignment procedure produces a noticeably narrower distribution compared to the unaligned case, directly improving the sensitivity of the following fit routine to the delayed o-Ps component identification. The final PDF takes the shifted and accumulated ^{68}Ge distribution after subtracting the flat background component estimated through a fit of the first 150 ns.

6.3.2 Fit Architecture

Fit Function

The o-Ps identification is performed through an event-by-event fit of the time profile of IBD candidate events, using the PDF constructed above to describe both the prompt and delayed components simultaneously. The fit function depends on five free parameters :

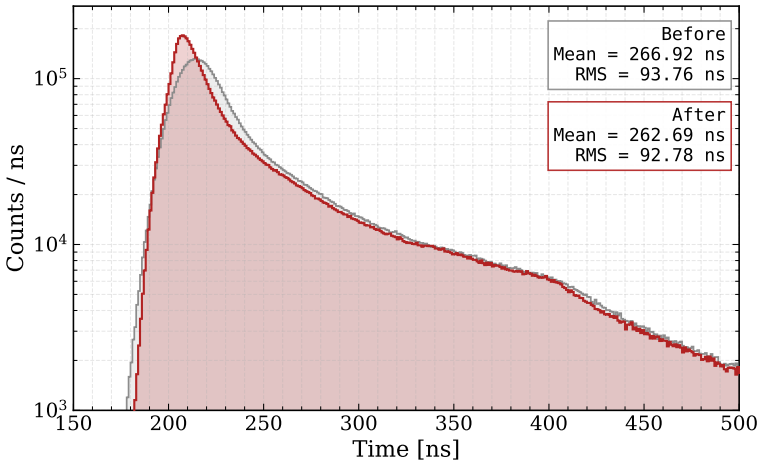

FIGURE 6.2 – Time profile probability density function created by accumulating ^{68}Ge events at the center of the detector. The PDF before and after the alignment procedure are represented in blue and red respectively.

— **Ionisation and annihilation normalisations** A_1 and A_2 : the amplitudes of the ionisation and annihilation components respectively.
— **An initial alignment shift** t_0, which accounts for the spread in rise time on an event-by-event basis.
— **A delayed annihilation time offset** dt relative to the prompt component. A non-zero value of dt directly signals the presence of o-Ps formation.
— **A flat background component** c, simply accounting for the flat background contribution in the time profile.

These five parameters are combined into the following fit function :

$$f(t) = A_1 \cdot f_{PDF}(t - t_0) + A_2 \cdot f_{PDF}(t - t_0 - dt) + c \tag{6.2}$$

where $f_{PDF}(t)$ is the time profile PDF constructed above. The first term describes the prompt positron ionisation signal, while the second describes the delayed o-Ps annihilation component, offset in time by dt relative to the prompt component. In the absence of o-Ps formation, the two components overlap completely ($dt = 0$) and Eq.6.2 reduces to a single rescaled PDF.

Minimization framework

The event-by-event identification of o-Ps formation is performed by comparing the IBD candidate time profile distribution with the time profile PDF constructed above. A physics event in JUNO is recorded on a 1 μs time window, where the number of pulses per bin (1000 bins of 1 ns) follows Poisson and does not contain enough statistics to use a classical Pearson χ^2 estimator of the goodness of fit, which assumes Gaussian uncertainties on each bin. For low statistics Poisson distributed data, it is common to perform the minimisation using an extend

binned Poisson likelihood whose definition is given by [192] :

$$-2\ln\mathcal{L} = 2\sum_{i=1}^{N}\left[\mu_i - n_i + n_i \ln\frac{n_i}{\mu_i}\right] \tag{6.3}$$

where the sum runs over all N time bins, n_i is the observed number of hits in bin i, and $\mu_i = f(t_i)$ is the predicted number of hits from Eq. 6.2 evaluated at the bin center t_i. This estimator reduces to the standard χ^2 for sufficiently large μ_i, and remains well-defined for bins with very few counts. The minimisation of Eq. 6.3 over the five free parameters of Eq. 6.2 is performed using `MINUIT`.

6.3.3 Parameter Initialisation and Constraints

The performance of the fit architecture described above relies heavily on the initial values and bounds of the five free parameters defined in Eq. 6.2. These parameters can be well constrained by the underlying physics of o-Ps formation, as described below.

Normalisation Constants

The annihilation normalisation constant A_2 is the most straightforward parameter to initialise and constrain. Since the positron annihilation signal always deposits 1.022 MeV regardless of its kinetic energy, ^{68}Ge events provide a direct estimate of the annihilation component amplitude. A Gaussian function is therefore fitted to the distribution of ^{68}Ge event time profile integrals, and the fitted mean value μ is used to initialise A_2.

The ionisation normalisation A_1 is initialised from the integral of the time profile being fitted, after subtracting the expected annihilation contribution defined above and any residual flat background contribution.

The two parameters are constrained differently. To prevent A_2 from drifting to unphysical values during minimisation, a Gaussian penalty term is added to the χ^2 estimator of Eq. 6.3 :

$$\epsilon_{oPs} = \left(\frac{A_2 - \mu}{\sigma}\right)^2 \tag{6.4}$$

where μ and σ are the Gaussian parameters obtained from the initialisation of A_2. The ionisation and annihilation normalisations are both bounded to a $\pm 3\sigma$ range from their initial value.

Background

The flat background constant c is evaluated from the first 150 ns of the time profile, which contains only dark noise. A flat fit is applied to this region to extract an initial value for c, subsequently refined by `MINUIT`.

Time Shifts

The time shift parameters, t_0 and dt, are more challenging to initialise and constrain, as no direct instrumental or physical constraint is available for either. The alignment shift t_0 is initialised so that the maximum of the ionisation PDF coincides with the maximum of the event's time profile, and is allowed to vary within ± 10 ns of this initial value.

Owing to the relatively short o-Ps lifetime, dt rarely exceeds 30 ns and can therefore be constrained to a $[0, 50]$ ns range. Unlike t_0, it cannot easily be initialised from the event's hit time distribution alone, since no equivalent constraint on its starting value is available. The annihilation shift is therefore initialised to 0 and refined alongside t_0 prior to the `MINUIT` minimisation.

6.3.4 Minimisation Strategy

(t_0, dt) Pre-Scan

The fit function of Eq. 6.2 contains two copies of the same PDF, offset by dt. When dt is small compared to the width of the PDF, the two component overlap and a shift in t_0 can be partially compensated by a shift in dt while leaving the predicted time profile nearly unchanged. This behaviour introduces a strong parameter degeneracy that translates into an elliptical χ^2 landscape in the (t_0, dt) plane at low dt. This effect spans in dt depending on the intrinsic timing resolution of the detector, and is further discussed and characterised in Section 6.4.2. Given the number of free parameters in the fit and the limited constraints available for them, convergence to a reliable estimate of dt is not always achieved from the seeds defined above. A pre-minimisation of Eq. 6.3 is therefore performed on a 50×50 grid in the (t_0, dt) space, with the normalisations and background parameters held fixed. The (t_0, dt) pair that minimises the χ^2 is taken as the new starting value for those two parameters.

Minuit

The minimisation of Eq. 6.3 is performed in two stages, following the initialisation described above. The first stage uses the `SIMPLEX` algorithm, a derivative-free method that converges slowly and does not provide reliable parameter uncertainties. It is used only to bring the parameters close to the global minimum, starting from a point identified by the (t_0, dt) pre-scan

described above.

The result of the SIMPLEX minimisation seeds the second stage, performed with the MIGRAD algorithm, which offers faster convergence and access to the covariance matrix of the fitted parameters. To improve the reliability of convergence, MIGRAD is run for up to three successive attempts, using progressively looser tolerances (2.5×10^{-3}, 10^{-2}, and 0.1) and correspondingly smaller function-call budgets. If a given attempt returns a valid minimum (Minuit status ≤ 1), subsequent attempts are skipped. Otherwise, the loosest converged result is retained. This approach was found to reduce the fraction of events for which the fit failed to converge, relative to a single MIGRAD call at fixed tolerance.

Parameter uncertainties are estimated using the HESSE algorithm, which computes the covariance matrix from the second derivatives of the χ^2 estimator of Eq. 6.3 at the minimum, and returns symmetric errors.

6.4 Characterisation on Simulated Data

A characterisation of the fit routine is done on simulated o-Ps samples, primarily to assess its performance with respect to the limitations described in Section 6.2.3. A description of o-Ps formation is integrated in the simulation software of JUNO [150], with a 3.08 ns lifetime and 54.5% formation probability [193]. A primary study is therefore conducted on a full-chain simulated sample of o-Ps events, including the event reconstruction, and for various configurations, in order to better constraint the o-Ps selection and fit routine.

6.4.1 Single-Point Analysis at 3 MeV

Simulation Sample

The first configuration considered is a sample of $N = 100\,000$ positrons simulated at 3 MeV at the center of the detector. For each event, the photon hit time distribution is retrieved after correcting for the time-of-flight, using the event's reconstructed vertex, before being passed as input of the fit. Since only 54.5% of simulated events form an o-Ps state, the remaining events have no delayed annihilation component and are assigned a true annihilation shift $dt_{\text{true}} = 0$: this population is kept in the sample to verify that the fit routine correctly gives small values of dt in the absence of o-Ps formation.

Fit Performance

An example of fit results is shown in Figure 6.3 for different true dt values, where the fit successfully decomposes the time profile into its ionisation and annihilation components.

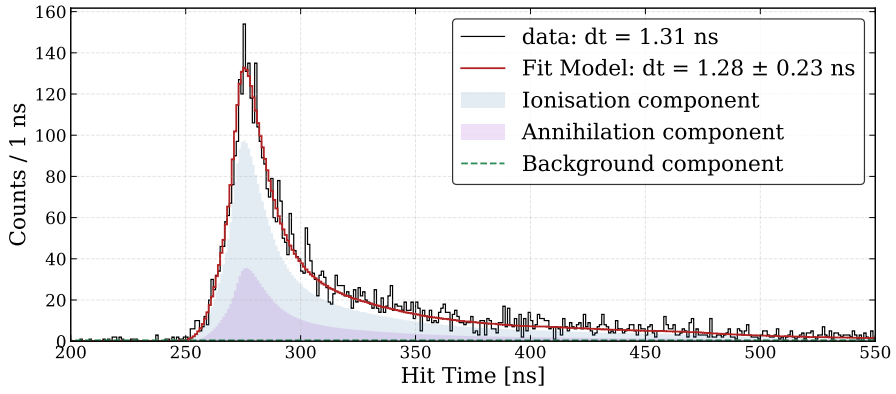

(a)

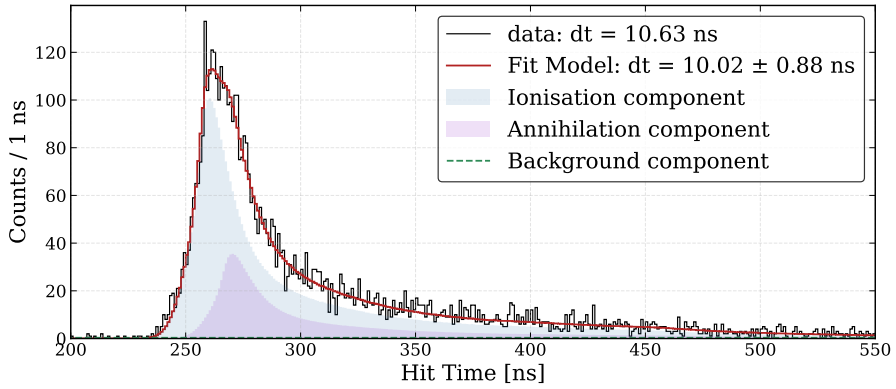

(b)

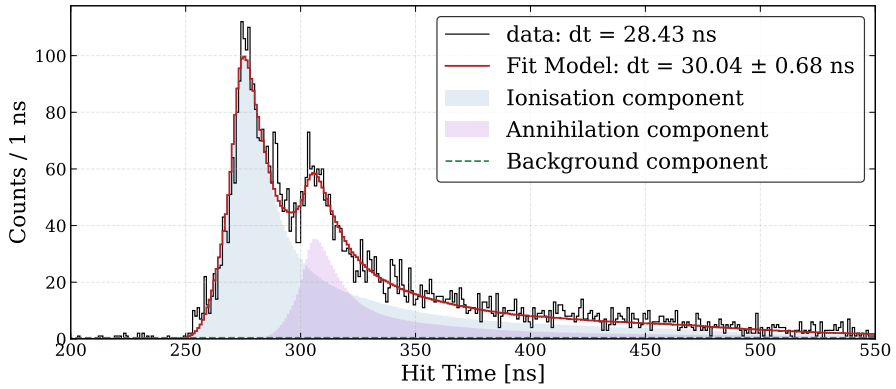

(c)

FIGURE 6.3 – Result of the fit routine on a simulated 3 MeV positron sample at the detector center. **(a)** o-Ps formation with a true $dt = 1.31$ ns and a fitted $dt = 1.28 \pm 0.23$ ns. **(b)** True $dt = 10.63$ ns, fitted $dt = 10.02 \pm 0.84$ ns. **(c)** True $dt = 28.43$ ns, fitted $dt = 30.04 \pm 0.68$ ns.

Beyond individual event examples, the accuracy of the fit routine can be assessed on the entire sample level using the true dt information available in the simulation. Figure 6.4 compares the distribution of fitted dt values to the corresponding distribution of true dt values across the full simulated sample.

The shape and overall trend of the fitted dt distribution closely follows the true distribution, indicating a good ability of the fit to identify the formation of o-Ps across the sample. Computing

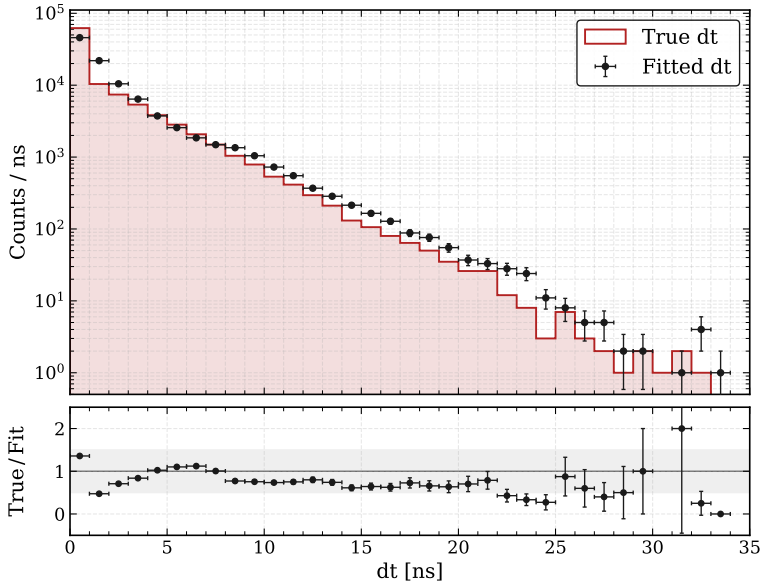

FIGURE 6.4 – Result of the fit routine on centered 3 MeV positron sample. **(Top)** Comparison between the true o-Ps annihilation shift distribution (red) and the fitted annihilation shift (black). **(Bottom)** Ratio of the true and fitted distribution. The bands represent the ±50% region.

the ratio between the true and fitted distribution, however, reveals a bias at low dt, consistent with the (t_0, dt) degeneracy identified in Section 6.3.2 : events with a true annihilation decay close to zero are not always correctly fitted with $dt \approx 0$ and the fit can instead return a non-zero value. This effect seems to stabilise around $dt = 8$ ns, beyond which the ratio remains roughly constant, suggesting that the bias is confined to a low-dt region rather than propagating across the full range of the distribution.

6.4.2 Constraining non o-Ps Population

The bias at low dt observed in Figure 6.4 is expected to depend primarily on the detector's timing resolution and must be characterise thoroughly in order to evaluate how it spreads into the o-Ps sample and would bias the lifetime estimation.

This is achieved using an o-Ps free control sample such as ^{60}Co : since ^{60}Co decays via the prompt emission of two γ-rays, it does not form an o-Ps and has by construction a true annihilation decay $dt_{\text{true}} = 0$, providing a clean estimation of the fit bias in attributing non-zero fitted dt to a non o-Ps event. A sample of $N = 100\,000$ simulated ^{60}Co events was generated at the center of the detector and passed through the same fit routine used for the positron samples.

The results are shown by the black points in Figure 6.5, which shows that even in the complete absence of o-Ps formation, the fit can return values as large as $dt \sim 13$ ns.

This confirms that the raw fitted dt distribution cannot be interpreted as a pure o-Ps signal

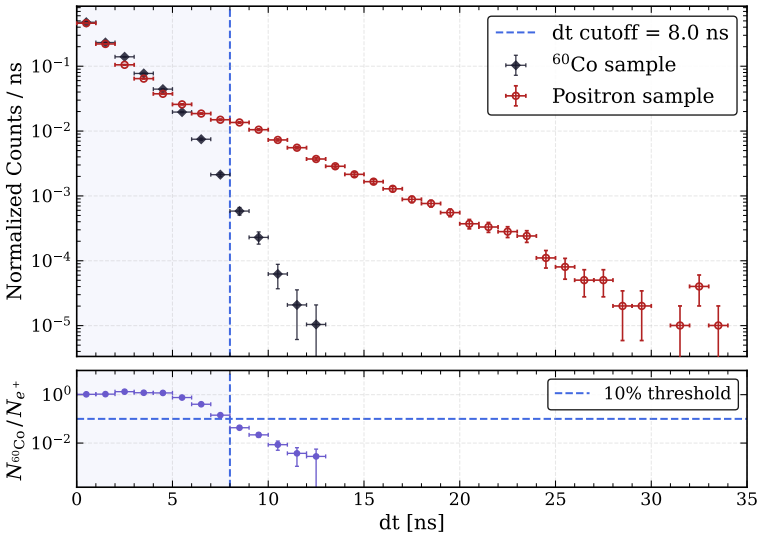

FIGURE 6.5 – **(Top)** Normalised dt distributions from fit results on positron (red points) and ^{60}Co samples (black points). **(Bottom)** Bin-by-bin ratio between ^{60}Co and the positron distributions. A dt threshold of 8 ns is estimated for a bin ratio of ^{60}Co events to e^+ events lower than 10%. The bands on both panels indicate the dt region removed by the threshold.

below 13 ns, and motivates the introduction of a cutoff, below which, fitted events are excluded from the o-Ps lifetime and formation fraction estimation. This cutoff is computed by scanning the bin ratio of the ^{60}Co and e^+ fitted dt requiring that the ^{60}Co contamination in a given e^+ bin remain below 10% for the lifetime and formation fraction to be safely estimated. This procedure is presented in the bottom panel of Figure 6.5, which gives a cutoff at $dt = 8$ ns. The events removed from the lifetime and formation fraction estimation are contained within the blue band, representing nearly 95% of the sample.

At this point of the analysis, it is already clear that the main limitation in correctly estimating the o-Ps lifetime and formation fraction is the available statistics, since in this idealised, centered configuration, only 5% of the sample remains above threshold, and will require this cutoff to be lowered as much as possible to increase the available statistics for the o-Ps lifetime and formation probability extraction.

6.4.3 Formation Fraction and Lifetime Estimation

Once the cutoff established in Section 6.4.2 removes the low-dt region affected by the (t_0, dt) degeneracy, the remaining distribution of fitted dt values can be used to extract the o-Ps lifetime and formation fraction. This section describes the estimation procedure, applied here to the centred 3 MeV positron sample as a first validation against the simulation input (54.5% formation probability, 3.08 ns lifetime).

Lifetime Extraction

The true o-Ps annihilation delay is expected to follow an exponential distribution with decay constant τ. However, the fitted value dt obtained from Eq. 6.2, for a given event, is not equal to the true delay, but is smeared by the precision of the fit performed with `MINUIT`, with an event-by-event uncertainty σ_{dt} available from the `HESSE` error estimation. The distribution of fitted dt values above the cutoff is therefore modeled as an Exponentially Modified Gaussian (EMG), the probability density function obtained by convolving an exponential decay of rate $1/\tau$ with a Gaussian of width σ_{dt} :

$$g(dt;\tau,\sigma_{dt}) = \frac{1}{2\tau}\,\exp\left(\frac{\sigma_{dt}^2}{2\tau^2} - \frac{dt}{\tau}\right)\,\mathrm{erfc}\left(\frac{1}{\sqrt{2}}\frac{\sigma_{dt}/\tau - dt/\sigma_{dt}}{\sqrt{2}}\right) \tag{6.5}$$

Here, σ_{dt} is taken event-by-event, reflecting the individual fitted event uncertainty rather than an averaged resolution over the whole sample. This procedure assumes that the χ^2 landscape around the fitted minimum is well-approximated by a parabola in dt. This assumption is expected to remain true above the $dt_{\mathrm{cut}} = 8$ ns threshold but not below it, where the (t_0, dt) degeneracy produces an elliptical χ^2 surface. The EMG-based fit is therefore only applied above cutoff.

The lifetime τ is extracted through an unbinned maximum-likelihood fit, using the individual $(dt_i, \sigma_{dt,i})$ pair of every event surviving the $dt_{\mathrm{cut}} = 8$ ns cutoff. Since only the range $[dt_{\mathrm{cut}}, dt_{\mathrm{max}}]$ is populated — dt_{max} being the largest fitted dt value in the sample — the EMG is truncated to this interval, with each event's probability density renormalised individually :

$$\mathcal{L}(\tau) = \prod_{i=1}^{N_{\mathrm{window}}} \frac{g(dt_i;\tau,\sigma_{dt,i})}{\displaystyle\int_{dt_{\mathrm{cut}}}^{dt_{\mathrm{max}}} g(dt;\tau,\sigma_{dt,i})\,dt} \tag{6.6}$$

where N_{window} is the number of events with a fitted dt in $[dt_{\mathrm{cut}}, dt_{\mathrm{max}}]$. The best-fit lifetime τ is obtained by minimising $-\ln\mathcal{L}(\tau)$ using `MINUIT`.

Formation Fraction Extraction

The truncated fit defined by Eq. 6.6 only constrains the shape of the dt distribution through the estimation of the o-Ps decay time τ. The fit does not give access to the total number of o-Ps events in the sample, since a fraction of the true exponential distribution necessarily lies below the 8 ns cutoff and is therefore excluded from N_{window}. This missing fraction is recovered using the fitted lifetime τ, where the probability for an exponential with decay time τ to fall within $[dt_{\mathrm{cut}}, dt_{\mathrm{max}}]$ is given by :

$$F(\hat{\tau}) = \exp\left(-\frac{dt_{\mathrm{cut}}}{\hat{\tau}}\right) - \exp\left(-\frac{dt_{\mathrm{max}}}{\hat{\tau}}\right) \tag{6.7}$$

where the total number of o-Ps events expected in the sample can be extrapolated by :

$$N_{oPs} = \frac{N_{\text{window}}}{F(\hat{\tau})} \tag{6.8}$$

The o-Ps formation fraction is then obtained by normalising N_{oPs} to the total number of events in the fitted sample, N_{tot} :

$$f_{oPs} = \frac{N_{oPs}}{N_{\text{tot}}} = \frac{N_{\text{window}}}{F(\hat{\tau})\, N_{\text{tot}}} \tag{6.9}$$

Validation on the 3 MeV Centered Sample

Applying this procedure to the centered 3 MeV positron sample yields the results presented in Table 6.1. The performance of the EMG truncated fit are shown, for the fitted *dt* distribution, in Figure 6.6. Two intermediate results are shown in addition to the true simulated input : the row labeled *True MC* applies a simple exponential decay fit to the true, unsmeared, simulated *dt* distribution restricted to the fit window, isolating the bias introduced by the truncation and extrapolation method itself. The row labeled *Fitted MC* applies the EMG fit procedure to the fitted *dt* distribution, introducing the detector timing resolution and `MINUIT` fit-level bias.

	Lifetime [ns]	**Formation Fraction [%]**
True MC (input)	3.08	54.5
True MC (Fit in window)	3.16 ± 0.05	50.8 ± 2.2
Fitted MC (Fit in window)	3.36 ± 0.05	58.7 ± 2.1

TABLE 6.1 – Resulting o-Ps lifetime and formation fraction, extracted from the truncated EMG fit on the centered 3 MeV positron sample's fitted *dt* distribution, compared to the simulation input and the true *dt* distribution fitted with a simple exponential decay function.

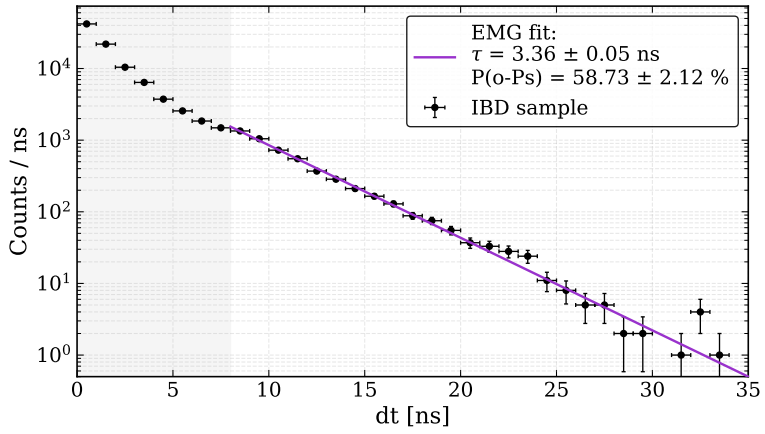

FIGURE 6.6 – EMG fit applied to the centered 3 MeV sample's fitted *dt* distribution. The fit yields a lifetime of 3.36 ± 0.05 ns, which is subsequently used to estimate the formation fraction.

The fitted lifetime and formation fraction are found to be in reasonable agreement with the simulated input, with deviations of +9.1% and +7.9% respectively for the *Fitted MC* row. Part of this deviation is already present at the level of the *True MC* row (+2.6% on the lifetime, −6.9% on the formation fraction), originating purely from reduced statistics due to the truncation and extrapolation procedure rather than from the detector response or the fit itself. Overall, the method is found to recover both the o-Ps lifetime and formation fraction to within about 10% of their true simulated values, providing a satisfactory validation of the extraction procedure before applying it to more realistic configurations in the remainder of this chapter.

6.4.4 Spatial Dependence

On a real data sample, restricting the selection to only events reconstructed at the center of the detector would considerably reduce the available statistics for determining the o-Ps lifetime and formation probability. The performance of the fit is therefore assessed on a 3 MeV positron sample simulated uniformly around the detector, in order to determine if the fit performance remain stable away from the center and, if not, to what radius the selection must be restricted.

Fit Performance

The performance of the fit routine on this uniformly distributed sample is show in Figure 6.7a, where a clear excess of events appears in the fitted distribution for high dt values, hinting at an additional geometry-induced bias.

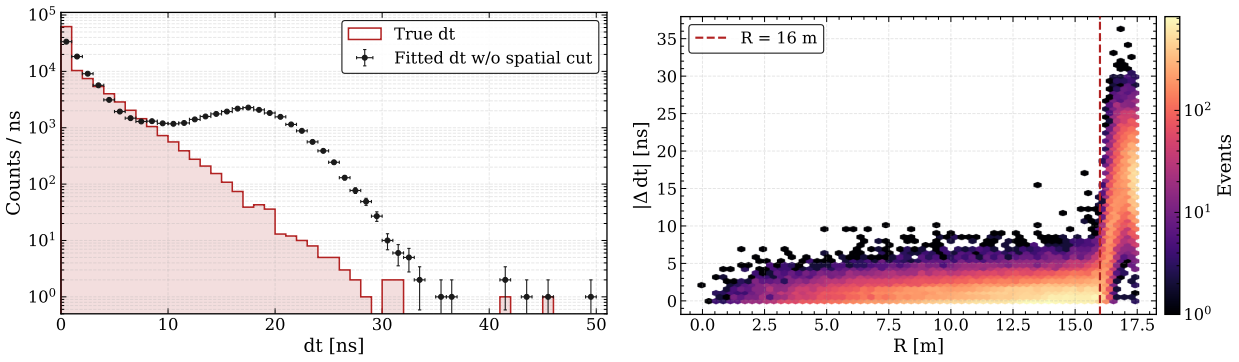

(a) (b)

FIGURE 6.7 – **(a)** Distribution of fitted dt values compared to the true simulated dt values, for events simulated uniformly across the detector with no constraints on the reconstructed position. **(b)** Absolute bias between true and fitted dt as a function of the event's reconstructed position from the center, R. A sharp increase in bias appears at $R = 16$ m, represented by the red dashed vertical line.

This is investigated further in Figure 6.7b, which shows the absolute bias between the true and fitted dt values as a function of the event's reconstructed distance from the center, R. The

bias increases slowly as a function of the radius, remaining on average below 10 ns up to $R = 16$ m, beyond which a sharp increase in bias is visible, corresponding to events reconstructed at the boundary of the detector.

Constraints from Time Profile Statistics

This behaviour is expected : the implemented ToF correction assumes that photon propagate along a straight line from the reconstructed vertex to each PMT, neglecting any optical effects, such as photon absorption/re-emission, reflection, or refraction on the acrylic vessel, that becomes increasingly significant as events are produced close to the detector boundary. Moreover, the ToF correction strongly depends of the quality of the reconstructed vertex, which is also subject to stronger biases near the boundary of the detector. As a consequence, the ToF correction becomes inaccurate near the boundary, and can be characterised independently of the dt fit itself by examining the statistics of the event raw hit time distribution as a function of radius. An accurate ToF correction should produce a hit time distribution whose statistics are essentially flat as a function of radius R. Any deviation from this flat behaviour signals an inaccuracy in the ToF correction's modelling of the photon path.

This is investigated in Figure 6.8, where the Mean, RMS, Skewness and Kurtosis of the events' hit time distribution are represented as a function of the events' distance from the center, R. Except for the mean, whose value is strongly correlated to the corrected peak position, all parameters remains close to constant up to $R \sim 12.5$ m, beyond which they begin to drift from their flat, low R behaviour, well before the sharp bias increase indentified in Figure 6.7b at $R = 16$.

Since the hit time statistics provide a more direct handle of the ToF correction's accuracy than the dt bias itself, the more conservative radius identified here, $R = 12.5$ m, is adopted in place of the $R = 16$ m threshold suggested by Figure 6.7b. In order to minimise geometrical effects, events with a reconstructed $R > 12.5$ m are discarded.

Resulting Lifetime and Formation Fraction

Applying the extraction procedure defined in Section 6.4.3 to the uniformly distributed 3 MeV positron sample restricted to $R \leq 12.5$ m, and to the $dt_{\text{cut}} = 8$ ns threshold, yields the results shown in Table 6.2 and a visualtion of the fit on the sample is given in Figure 6.9. Comparing those results to the centered sample values in Table 6.1 reveals several effects.

Applying the extraction on the *True MC* yields a lifetime and formation fraction compatible with both the simulation input and the result extracted from the centered sample, within their statistical uncertainties. This agreement could be attributed to statistical fluctuations since $\sim 35\%$ of the sample remains after the radius cut.

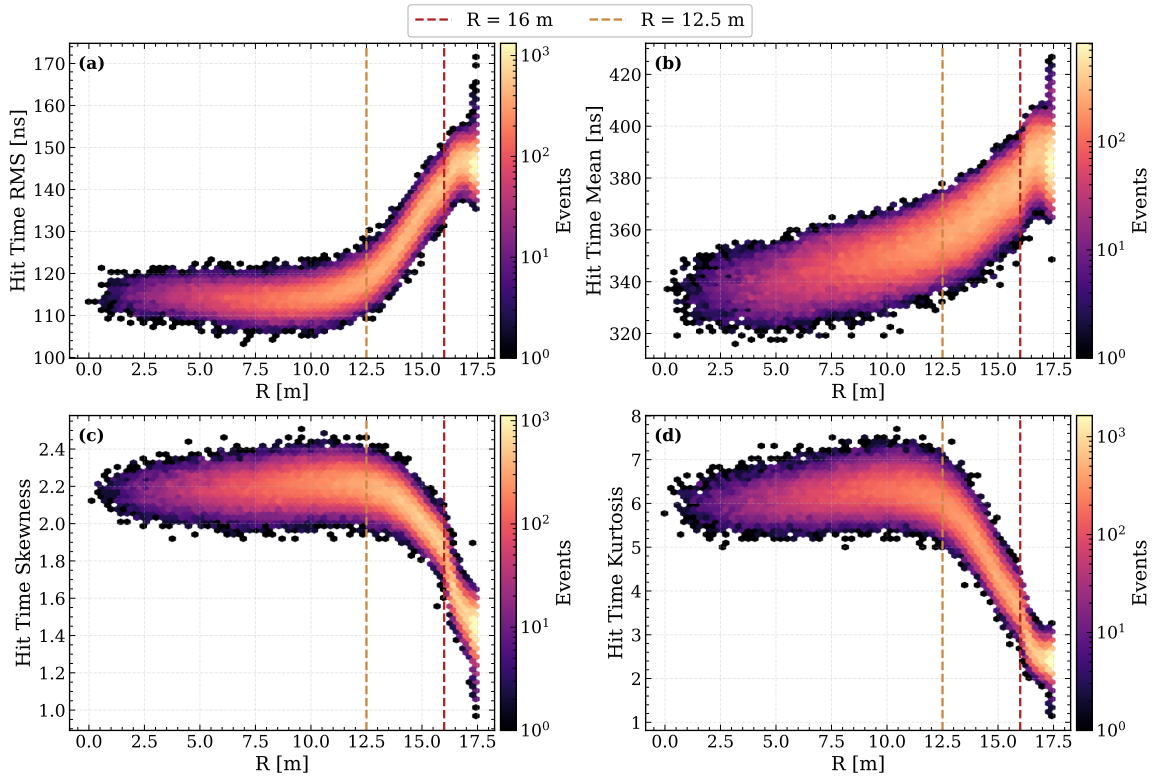

FIGURE 6.8 – **(a)** RMS, **(b)** Mean, **(c)** Skewness, and **(d)** Kurtosis of the hit time distribution as a function of the event's reconstructed distance from the center, R, for the uniformly distributed 3 MeV positron sample. The vertical dashed lines indicate the radius at which the time profile statistics begin to deviate from their flat, low-R behaviour ($R = 12.5$ m, orange) and the radius identified from the dt-bias study of Figure 6.7b ($R = 16$ m, red).

The lifetime extracted from the fitted dt distributions shows a similar bias ($+9,1\%$ centered, $+8.1\%$ uniform) to the simulation input, indicating that the applied radius cut effectively reduces the geometry bias introduced in Figure 6.7a.

For the formation fraction, the -9% decrease bias to the simulated input is also compatible with a statistical fluctuation and stays in rather good agreement with the simulation input.

	Lifetime [ns]	**Formation Fraction [%]**
True MC (input)	3.08	54.5
True MC (Fit in window)	3.07 ± 0.09	52.50 ± 4.05
Fitted MC (Fit in window)	3.34 ± 0.09	50.88 ± 3.39

TABLE 6.2 – Resulting o-Ps lifetime and formation fraction, extracted from the truncated EMG fit on the uniformly distributed 3 MeV positron sample's fitted dt distribution, compared to the simulation input and the true dt distribution.

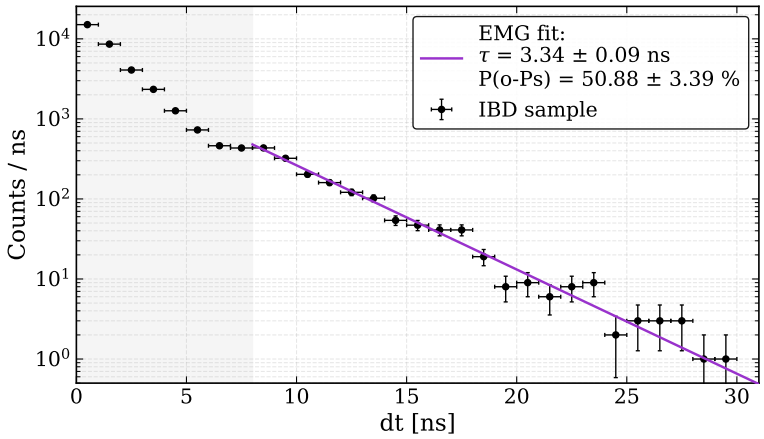

FIGURE 6.9 – EMG fit applied to the uniformly distributed 3 MeV sample's fitted dt distribution. The fit yields a lifetime of 3.34 ± 0.09 ns, with a $50.88 \pm 3.39\%$ formation probability.

6.4.5 Energy Dependence

As discussed in Section 6.2.3, one of the decisive limitation of this PSD technique lies in its energy dependence : the identification of the annihilation component becomes more challenging as the positron energy increases. Consequently, the performance of the fit routine is assessed on $N = 100\,000$ positron events simulated at the center of the detector with energies generated uniformly in a $[1.5, 8.0]$ MeV range.

Fit Performance

The fitted dt distribution is compared to the true dt distribution in Figure 6.10 without applying any energy cut. Although less pronounced than for the uniformly distributed events, an excess of events at high dt value is again visible.

This excess is attributed to the inability of the fit to correctly assess the annihilation shift for events combining a small true dt values with a high positron energy. This effect is more explicit in Figure 6.11a, which shows that the bias in dt increases with positron energy. This effect is concentrated among events with a small true annihilation delay : Figure 6.11b shows that it is mostly events with $dt_{\text{true}} < 10$ ns that exhibit the largest bias, which reduces considerably for larger true dt values. This behaviour is explained by the relative weight of the two fit components at high energy : as the positron energy increases, the ionisation normalisation A_1 grows proportionally with the deposited energy, while the annihilation normalisation A_2 remains fixed by the constant 1.022 MeV annihilation signal. The annihilation component therefore becomes an increasingly small fraction of the total signal at high energy, leaving `MINUIT` comparatively little constraint on where to place it within the time profile ; in this regime, the minimiser can more easily attribute a large dt to events that, in reality, have little or no delayed component.

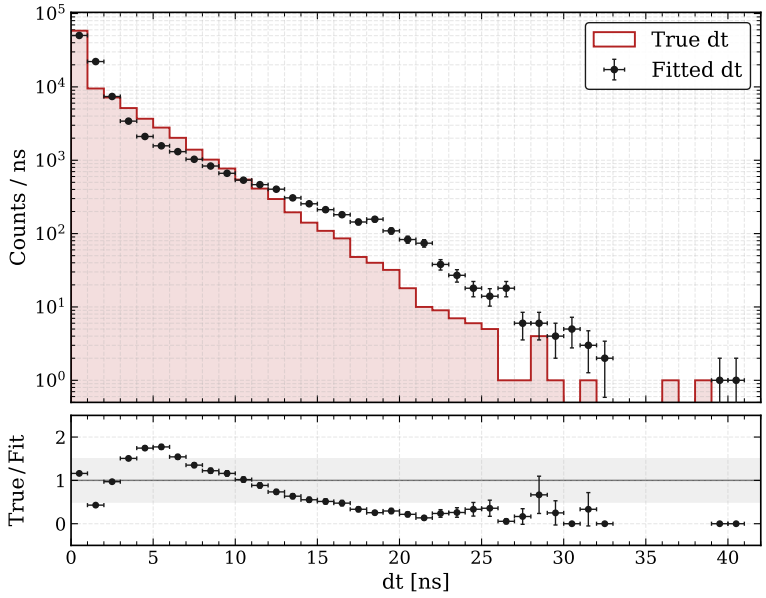

FIGURE 6.10 – Distribution of fitted dt values compared to the true simulated dt values, for positron events simulated at the detector centre with energies uniformly distributed over $[1.5, 8.0]$ MeV, with no cut applied on energy.

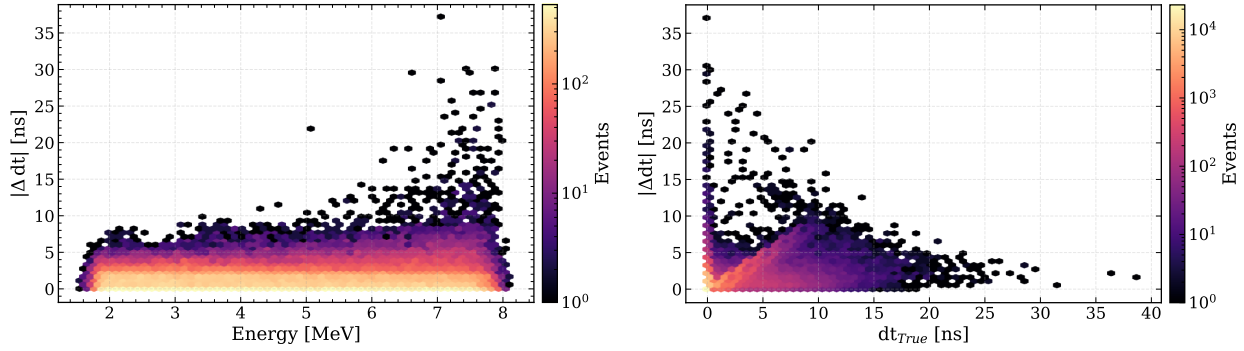

(a) (b)

FIGURE 6.11 – **(a)** $|\Delta dt|$ as a function of positron energy E : the bulk of events remain close to $|\Delta dt| \leq 10$ ns across the full energy range, with a growing population appearing above $\sim$ 5–6 MeV. **(b)** $|\Delta dt|$ as a function of the true annihilation delay dt_{true} : the largest biases are located at small true dt, forming a triangular shape and narrows rapidly as dt_{true} increases. The high bias region is mostly due to events combining a small true delay and a high positron energy.

Energy Constrain

There is not a straight forward solution to correct this effect except reducing the energy range of the selected events, while retaining enough statistics to correctly evaluate the o-Ps lifetime and formation probability. To determine an appropriate energy cut, the extraction procedure of Section 6.4.3 is applied to the sample under a series of energy cuts, $E \leq E_{\text{cut}}$, with E_{cut} ranging from 3 to 7 MeV. The resulting fitted and true-MC lifetime and formation fraction, together with the number of events N_{window} retained above the $dt_{\text{cut}} = 8$ ns threshold at each

cut, are summarised in Table 6.3.

The *True MC* columns show no clear trend depending on E_{cut}, where the lifetime and formation fraction biases fluctuate around a few per cent across the full range of cuts.
The *Fitted MC* lifetime bias decreases as the energy cut tightens, from +35.7% at $E \leq 7$ MeV to -0.3% at $E \leq 3$ MeV, while the formation fraction bias improves from -38.3% at $E \leq 7$ MeV to a minimum deviation of -8.7% at $E \leq 5$ MeV, before increasing in the opposite direction at tighter cuts, reaching +28.1% at $E \leq 3$ MeV. Since no single value of E_{cut} simultaneously minimises the bias on both observables, an energy threshold of $E \leq 5$ MeV is adopted for the remainder of this chapter, as it corresponds to the point of closest agreement for the formation fraction while retaining a comparatively large sample and a moderate bias on the lifetime.

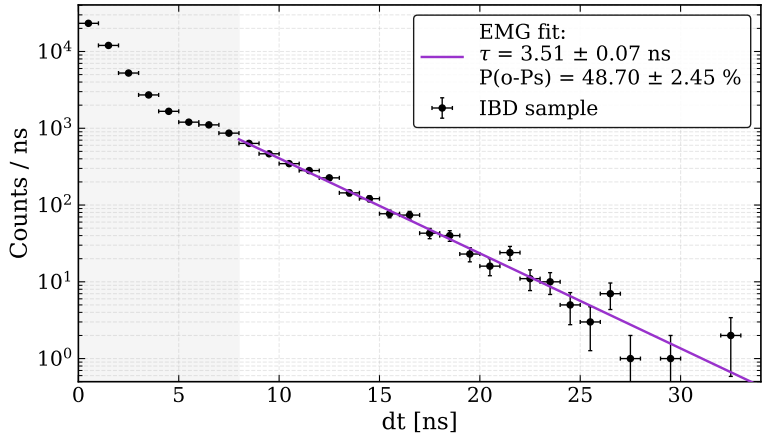

FIGURE 6.12 – Fitted *dt* distribution of the centered positron sample with E≤ 5 MeV. The fit yields a lifetime of 3.51 ± 0.07 ns, and a resulting $49.70 \pm 2.45\%$ formation probability.

E_{cut} [MeV]	N_{window}	True MC		Fitted MC	
		τ [ns]	f_{oPs} [%]	τ [ns]	f_{oPs} [%]
≤ 7	80418	3.04 ± 0.05 (−1.3%)	55.83 ± 2.77 (+2.4%)	4.18 ± 0.07 (+35.7%)	33.61 ± 1.16 (−38.3%)
≤ 6	65579	3.04 ± 0.06 (−1.3%)	54.94 ± 3.03 (+0.8%)	3.79 ± 0.07 (+23.1%)	40.80 ± 1.68 (−25.1%)
≤ 5	50615	3.03 ± 0.07 (−1.6%)	55.00 ± 3.51 (+0.9%)	3.50 ± 0.07 (+13.6%)	49.78 ± 2.50 (−8.7%)
≤ 4	35355	2.93 ± 0.08 (−4.9%)	60.23 ± 4.72 (+10.5%)	3.17 ± 0.08 (+2.9%)	65.64 ± 4.17 (+20.4%)
≤ 3	19434	2.97 ± 0.11 (−3.6%)	55.71 ± 5.95 (+2.2%)	3.07 ± 0.10 (−0.3%)	69.83 ± 6.22 (+28.1%)

TABLE 6.3 – Fitted o-Ps lifetime and formation fraction, extracted from the true and fitted *dt* distributions of the simulated positron sample, as a function of the maximum positron energy E_{cut} included in the fit. N_{window} is the number of events with a fitted *dt* above the $dt_{\text{cut}} = 8$ ns threshold, out of the 100 000 simulated events at each energy cut. Relative deviations from the simulated input ($\tau = 3.08$ ns, $f_{oPs} = 54.5\%$) are given in parentheses.

6.5 Results on JUNO Data

Having validated the fit routine on simulation and established both the $R \leq 12.5$ m, and $E \leq 5$ MeV selection criteria required to control the spatial and energy-dependent biases discussed above, the fit routine is now applied to IBD candidate events selected from a larger JUNO data set, following the revised selection strategy defined in Section 5.2.

6.5.1 IBD Candidate Sample

Selection

The IBD candidate sample used in this analysis is selected following the criteria summarised in Table 5.2. This selection yields an accumulated exposure of 193.2 days of data, corresponding to a total of 16857 IBD candidate pairs, including cosmogenics or other correlated backgrounds. The resulting prompt and delayed energy spectra are shown in Figure 6.13.

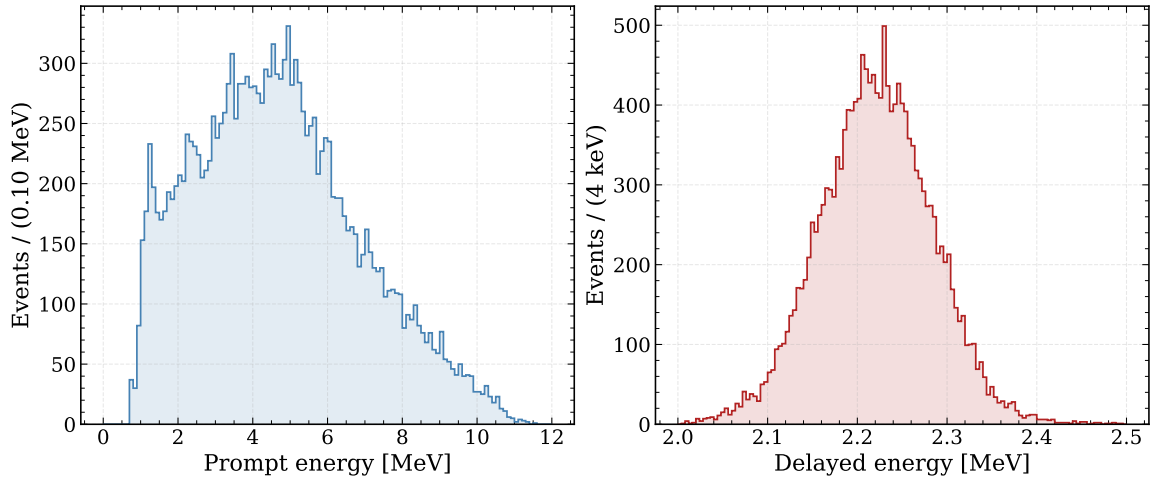

FIGURE 6.13 – Prompt (left) and delayed (right) energy spectra of the selected IBD candidate sample, accumulated over 193.2 days of JUNO data.

The accuracy of the IBD selection is further validated by fitting the distribution of the prompt–delay time difference, shown in Figure 6.14, with an exponential decay. The fit yields a decay constant $\tau = 218.0 \pm 3.2$ μs, in good agreement with the expected neutron capture time in the JUNO liquid scintillator

In addition to the IBD selection criteria, the spatial and energy restrictions established in Sections 6.4 are applied to the prompt positron candidate : events reconstructed with $R > 12.5$ m or with a prompt energy above 5 MeV are excluded from the o-Ps fit, in order to remain within the regime where the fit routine has shown reliable performances. These additional constraints reduce the sample to 3930 IBD candidate events suitable for the o-Ps time profile fit.

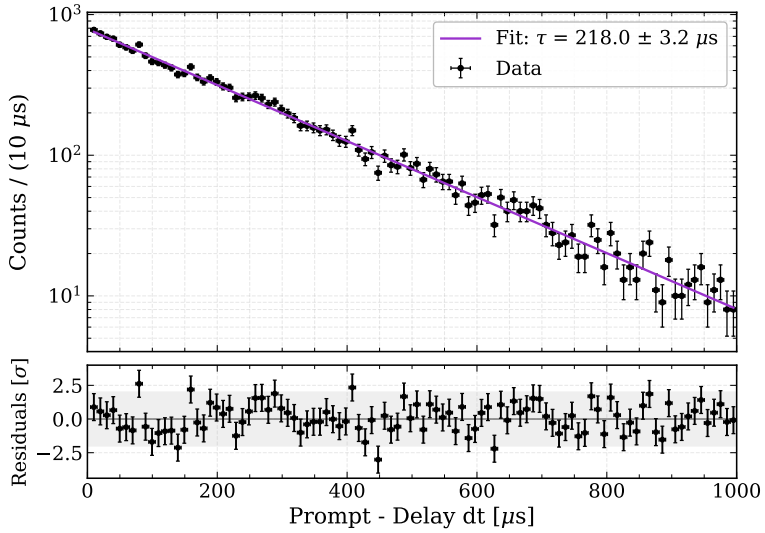

FIGURE 6.14 – Distribution of the time difference between the prompt and delayed signals of the selected IBD candidate sample, fitted with an exponential decay of constant $\tau = 218.0 \pm 3.2$ μs. The bottom panel shows the fit residuals, normalised to the bins statistical uncertainty ((data - model)/σ).

Releasing Constraints

The statistics remaining for the extraction of the o-Ps lifetime and formation fraction are very limited — 23% of the full IBD sample — motivating an effort to relax some of the constraints established in Section 6.4. The energy constraint is difficult to loosen, since the true *dt* information isn't available to quantify the energy-dependent fit bias. The radius constraint, however, can be re-evaluated using the same method introduced in the simulation study : the correlation between reconstructed radius and the event's hit time distribution statistics, investigated on data in Figure 6.15.

The time profile statistics show that the $R \leq 12.5$ m cut established from the simulation is overly conservative in data : the event time profile statistics only begin to deviate from a flat behaviour around $R \simeq 15$ m. This value is therefore adopted as the new radius cut for the analysis on data instead of the simulated-derived value, effectively increasing the available statistics to $N = 6928$, corresponding to 41% of the total sample, and nearly doubling the sample size obtained with the simulation based cut.

6.5.2 Fitted o-Ps Parameters

Data / Simulation Comparison

Following the revised spatial cut established on data, the full extraction method characterised on simulated positronium data is applied to the IBD sample. The PDF is constructed

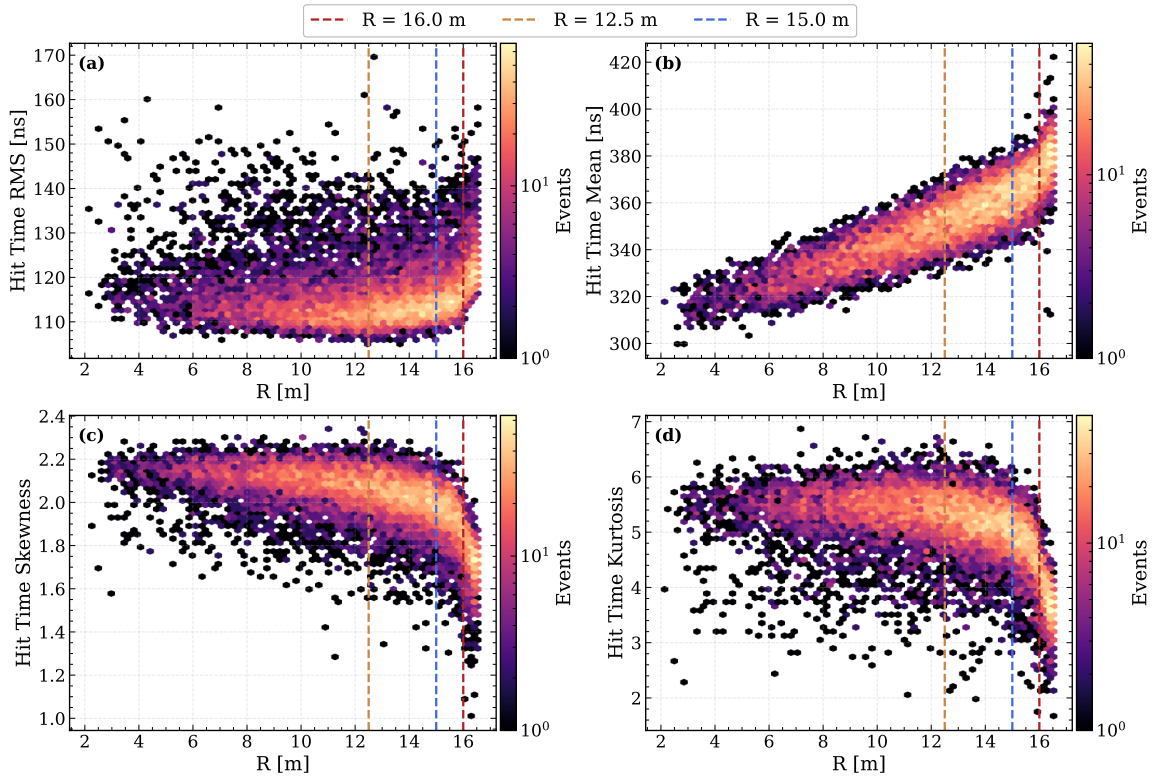

FIGURE 6.15 – **(a)** RMS, **(b)** Mean, **(c)** Skewness, and **(d)** Kurtosis of the hit time distribution of the IBD candidate sample, as a function of the event's reconstructed distance from the center R. The red and orange vertical dashed lines indicate the radius cuts established from the analysis on simulated data ($R = 16$ m and $R = 12.5$ m, respectively ; see Section 6.4.4), while the blue dashed line indicates the radius at which the time profile statistics begin to deviate from a flat behaviour in data.

by accumulating ^{68}Ge events from the JUNO calibration data introduced in Section 4.4.1. The resulting PDF is compared to the one constructed from simulation in Figure 6.16, where the accumulated data time profile shows a larger mean and spread (Mean = 277.84 ns, Std. Dev. = 105.23 ns) than the simulated profile (Mean = 262.69 ns, Std. Dev. = 92.78 ns), with the Data/MC ratio deviating from unity through most of the 1 μs range.

Background contamination

The selected IBD sample contains various sources of background below 5 MeV, which would bias the extraction of the o-Ps lifetime and formation probability if left uncorrected. Consequently, a 4 m sphere veto is applied around tagged spallation neutron events, for 1.2 s, to remove contamination from ^{9}Li/^{8}He cosmogenic background events, following the revised selection criteria of Section 5.2. The use of a muon-track space and time correlation was not possible, as the muon tracks were not available for the full sample, which motivated the consistent use of the neutron veto method across the sample instead. The remaining IBD sample, following the neutron veto method amount for 4585 $\overline{\nu}_e$ events. Using the background rate established in

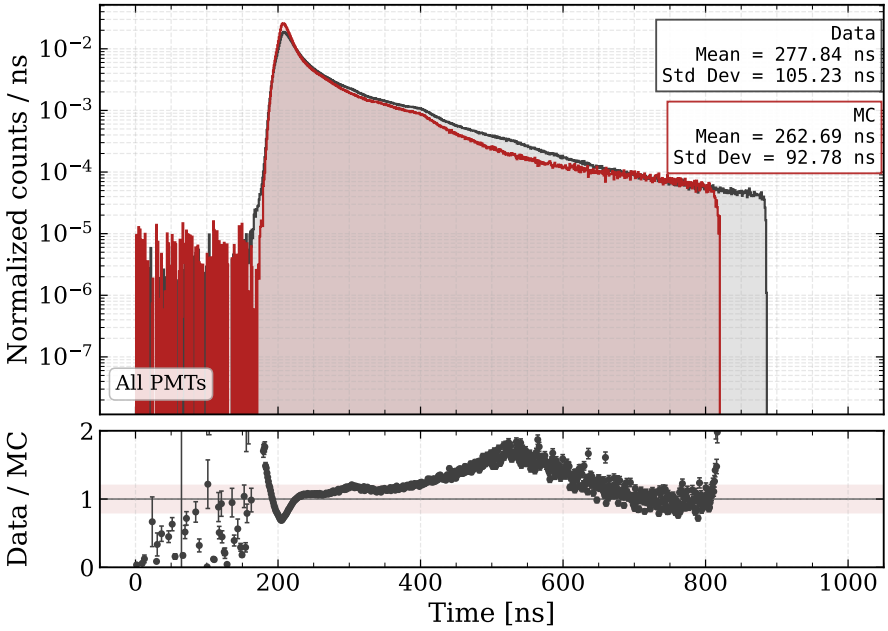

FIGURE 6.16 – Normalised, accumulated PMT hit time profile from ^{68}Ge calibration events, compared between data and simulation. The bottom panel shows the Data/MC ratio. The simulated profile underestimates both the mean and the spread of the measured time profile, indicating an incomplete description of the detector's timing response in the current simulation.

the first analysis of JUNO data [139], the total rate of backgrounds events contaminating the ≤ 5 MeV region is estimated at 389 ± 69 events over the 193.2 days of data, and will be taken into account when extracting the o-Ps formation probability.

Non o-Ps Population Constraint

Similarly to the procedure performed in Section 6.4.2, the sample's contamination by non o-Ps events can be estimated by applying the fit to a ^{60}Co calibration sample. This is shown in Figure 6.17, where the dt distribution obtained from the fit on the $\bar{\nu}_e$ sample is compared with the one extracted from the fit on the ^{60}Co sample. The bin-by-bin ratio between the two distributions falls below 10% for $dt_{\text{cut}} = 7$ ns, which is adopted as the dt cutoff for this data sample.

o-Ps Lifetime and Formation Fraction in JUNO Data

Events with a fitted dt below a 7 ns cutoff are excluded from the o-Ps lifetime and formation fraction estimation. The resulting dt distribution above threshold is fitted with a truncated EMG function using `MINUIT`, following the procedure defined in Section 6.4.3. The results are presented in Figure 6.18, from which the o-Ps formation fraction and lifetime are extracted, giving :

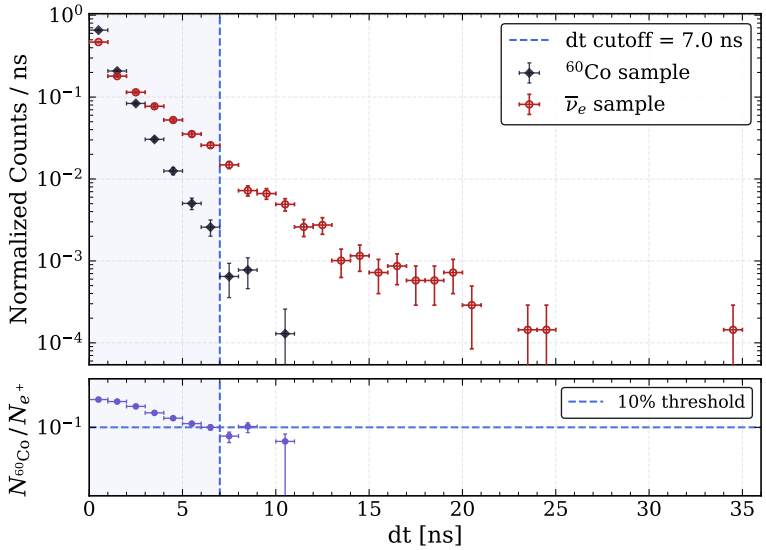

FIGURE 6.17 – **(Top)** Normalised dt distributions from fit results on the IBD candidate sample (red) and a ^{60}Co calibration sample (black). **(Bottom)** Bin-by-bin ratio between the ^{60}Co and $\bar{\nu}_e$ distributions. A dt threshold of 7 ns is estimated for a bin ratio of ^{60}Co to $\bar{\nu}_e$ events below 10%. The shaded band in both panels indicates the dt region removed by the threshold.

$$\tau_{oPs} = 3.26 \text{ ns} \pm 0.21 \text{ ns} \tag{6.10}$$

$$f_{oPs} = 54.2\% \pm 8.2\% \tag{6.11}$$

The extracted lifetime is compared to previous PALS measurements on LAB-based liquid scintillator in Table 6.4. Although the central value is noticeably higher than any of the published results — by 5–10% depending on the reference — the large statistical uncertainty of this early measurement keeps it compatible with all three, with the closest agreement found with the measurements of Perasso et al. [153] and Cheng et al. [187]. The formation fraction, however, shows excellent agreement with the $54.2 \pm 0.5\%$ measurement of [153].

Source	τ_{oPs} **[ns]**	f_{oPs} **[%]**
This work	3.26 ± 0.21	54.2 ± 8.2
[153]	3.08 ± 0.03	54.2 ± 0.5
[187]	3.10 ± 0.07	43.7 ± 1.2
[188]	2.97 ± 0.04	-

TABLE 6.4 – Comparison of the o-Ps lifetime and formation fraction measured in this work with previous PALS measurements on LAB-based liquid scintillator.

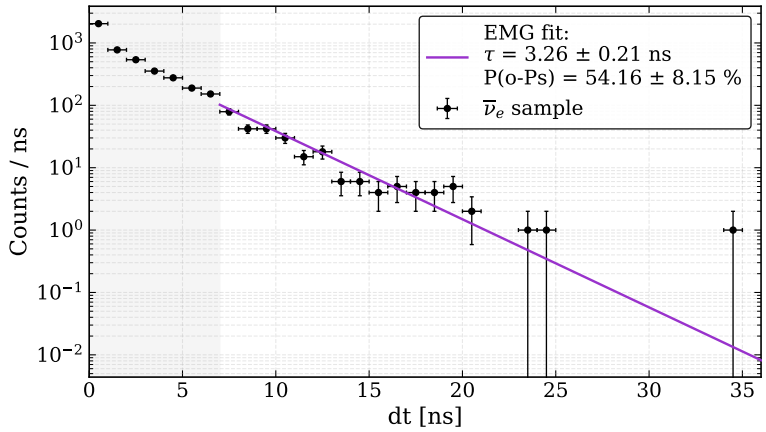

FIGURE 6.18 – Distribution of fitted dt values for the selected IBD candidate sample (black points), with the truncated EMG fit (purple line) performed above the $dt = 7$ ns threshold (shaded region). The fit yields $\tau_{oPs} = 3.26 \pm 0.21$ ns and $f_{oPs} = 54.16\% \pm 8.15\%$.

6.5.3 Outlook

This first measurement of the o-Ps lifetime and formation fraction on JUNO's early dataset is limited in several aspects. The most immediate limitation is statistics : less than 30% of the initial IBD sample remains after applying the spatial and energy selections, in addition to the neutron veto discussed in Section 5.2. This directly limits the precision of the extracted lifetime and formation fraction, and will improve naturally as JUNO accumulates more data.

A second limitation comes from the early-stage performance of the event reconstruction algorithms, which directly affects the accuracy of the ToF correction applied to the hit time distribution, and therefore the shape of the time profile PDF, central to the entire fit. The ToF correction currently relies on a simplified straight-line propagation model, which does not take into account the different optical processes taking place inside the detector. Work is currently ongoing to introduce a more refined description of photon absorption and re-emission, total internal reflection, and refraction at the detector boundary. This improved photon propagation model is expected to be integrated into the JUNO software in the near future, improving both the reconstruction algorithms and future iterations of this analysis.

6.6 Prospects with Improved PMT Timing (Hamamatsu Subset)

As mentioned in Section 6.2.3, the timing resolution of the JUNO detector is one of the important limitations of the o-Ps PSD identification technique developed throughout this chapter. The detector is mostly instrumented with NNVT PMTs, which have a poor transit time spread (TTS) of 7.53 ns (σ), while the Hamamatsu PMTs, with a TTS of 1.93 ns (σ), provide a more

competitive timing resolution but are less populated in the detector.

This section explores the performance of the fit routine when restricted to the Hamamatsu PMT subset alone, in order to assess the potential benefit of improved single-photon timing resolution on the o-Ps identification, while having reduced photon statistics.

6.6.1 Fit Performance on Simulated Data

The fit routine described in Section 6.3.2 is applied, without modification, to the centered 3 MeV positron sample of Section 6.4, restricting the hit time distribution to hits recorded on Hamamatsu PMTs only. The resulting fitted dt distribution, compared to the true simulated dt distribution, is shown in Figure 6.19a.

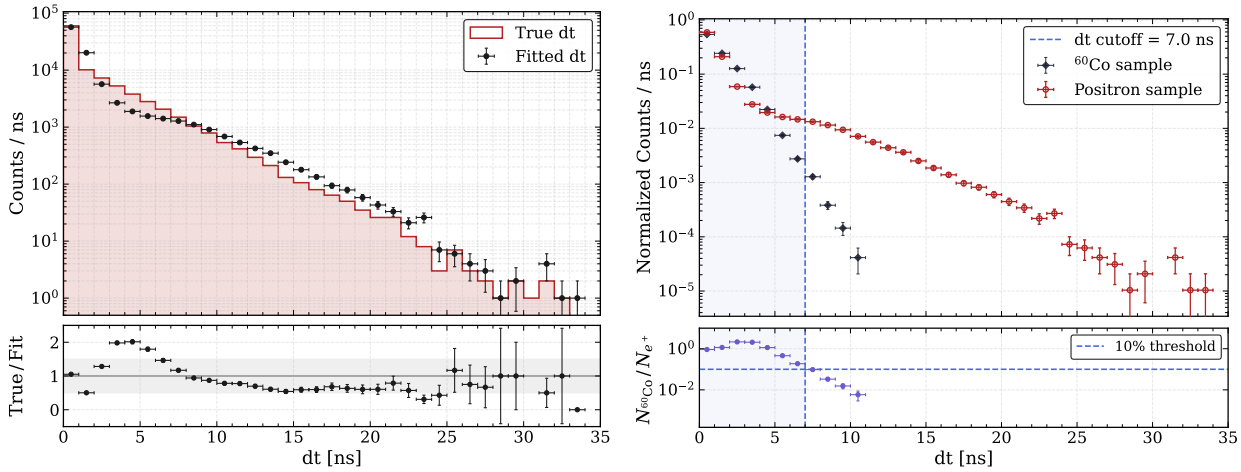

(a) (b)

FIGURE 6.19 – **(a)** Distribution of fitted dt values compared to the true simulated dt values, for the 3 MeV positron sample simulated at detector center, restricting the time profile fit to Hamamatsu PMTs only. The bottom panel shows the ratio of the true to the fitted distribution, with the bands representing the ±50% region. **(b)** Comparison of the fit results on the positron and ^{60}Co samples, where the time profiles are computed from hits on Hamamatsu PMTs only. The bottom panel shows the bin-by-bin ratio between the two samples, yielding a $dt = 7$ ns cutoff for a 10% threshold value.

Unlike the full-LPMT case discussed in Section 6.4.3, the fitted dt distribution obtained with only Hamamatsu PMTs shows a more irregular shape in the low-dt region : the true dt over fitted dt ratio deviation from unity is more pronounced, exceeding a factor of 2 around $dt \sim 3$–7 ns and dropping to roughly 0.5–0.6, similarly to the all-LPMT case, in the $dt \sim 13$–20 ns range.

The cutoff procedure is applied following the method described in Section 6.4.2, using the simulated ^{60}Co sample. The result is shown in Figure 6.19b, which shows a reduced bias for the non-oPs sample, with a maximum value found at $dt = 10.4$ ns instead of 13 ns in the all-LPMT

case, and yields a $dt_{\text{cut}} = 7$ ns for a bin-by-bin threshold of 10% — a reduction of 1 ns relative to the full-LPMT case. This cutoff value, however, falls directly into the irregular region identified in Figure 6.19a, where the trend of the distribution favours high values of τ. The extraction procedure of Section 6.4.3, applied above this threshold, yields a lifetime $\tau = 3.77 \pm 0.05$ ns, substantially higher than both the simulated input and the extracted value using all LPMTs. Increasing the cutoff value allows to recover a better lifetime estimation but defeats the purpose of using the Hamamatsu system alone in order to reduce the cutoff value.

6.6.2 Investigating the Origin of Bias

The observed behaviour contradicts the naive expectation that improved timing resolution would reduce the fit bias, motivating a closer investigation of any underlying effects.

Overall Bias at Sample Level

As a first step, the direction towards which events with $dt_{\text{true}} \in [3, 7]$ ns are biased is further studied. This is done in Figure 6.20, where the bias $\Delta dt = dt_{\text{fit}} - dt_{\text{true}}$ is determined as a function of dt_{true} for the analysis conducted with either Hamamatsu PMTs only (Figure 6.20a) or with all LPMTs (Figure 6.20b).

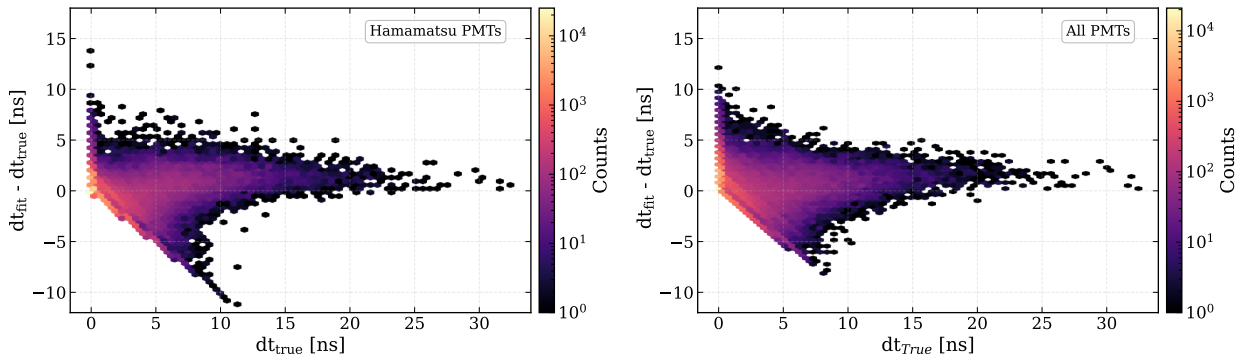

(a) (b)

FIGURE 6.20 – Bias between the true annihilation shift dt_{true} and the fitted shift dt_{fit} as a function of dt_{true} when the analysis is performed with **(a)** Hamamatsu PMT or with **(b)** all LPMTs.

The all-LPMT subset shows a moderately more compact Δdt bias as a function of dt_{true}, compared to the Hamamatsu-only subset, whose spread is slightly larger, particularly at low dt_{true}. This is compatible with a difference in the photon statistics available on an event-by-event basis between the two subsets, which could amplify the bias in the estimation of the annihilation shift when using Hamamatsu PMTs alone. Moreover, the Hamamatsu-only subset leans more strongly towards negative Δdt values at low dt_{true} than the all-LPMT subset, indicating that the missing events in Figure 6.19a most likely populate the $dt = 0$ bin.

Event Level Example

The lack of photon statistics is directly illustrated by the example event shown in Figure 6.21, with $dt_{\text{true}} = 5.8$ ns : in contrast to the smooth, high-statistics time profiles obtained with the full PMT system (Figure 6.1), the per-event distribution is more irregular, with larger bin-to-bin fluctuations. These fluctuations are large enough to be occasionally mistaken by the fit for a genuine delayed annihilation component, as shown by the corresponding (t_0, dt) pre-scan in Figure 6.22 : alongside a broad region of low χ^2 near the true value ($dt < 10$ ns), a deeper, spurious minimum appears around $dt \sim 15$ ns, driven by a statistical fluctuation in the sparse hit time distribution rather than by a genuine annihilation component. Since the pre-scan procedure seeds the subsequent minimisation with the global minimum of this grid, the fit converges on the spurious solution, returning a fitted $dt \simeq 14.46$ ns for this event.

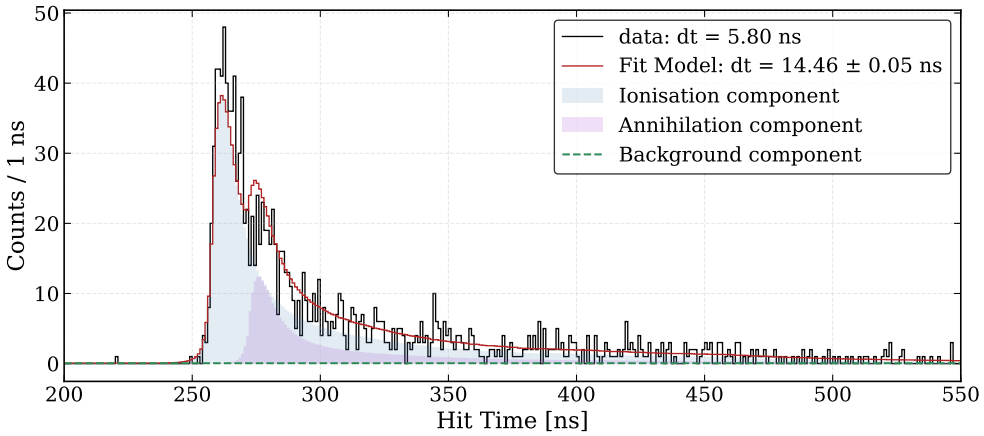

FIGURE 6.21 – Raw hit time distribution of a single simulated event, using Hamamatsu PMTs only. The reduced photon statistics, compared to the full PMT system, result in large bin-to-bin fluctuations.

6.6.3 Prospects

The results above indicate that, despite its better timing resolution, the Hamamatsu PMT subset alone does not currently provide a more reliable o-Ps identification than the full PMT system, owing to the substantially reduced photon statistics available per event. The next straightforward step is to combine the Hamamatsu PMT subset with the SPMT system, which offers a transit time spread of 1.3 ns, that could help recover sufficient photon statistics per event while retaining a good timing resolution. Unfortunately, the SPMT system was not fully operational during the data taking period from which the sample used in Section 6.5 was produced. Moreover, a separate analysis on simulated data exhibited a timing misalignment between the SPMT and LPMT systems, which needs further correction before combining them for the analysis.

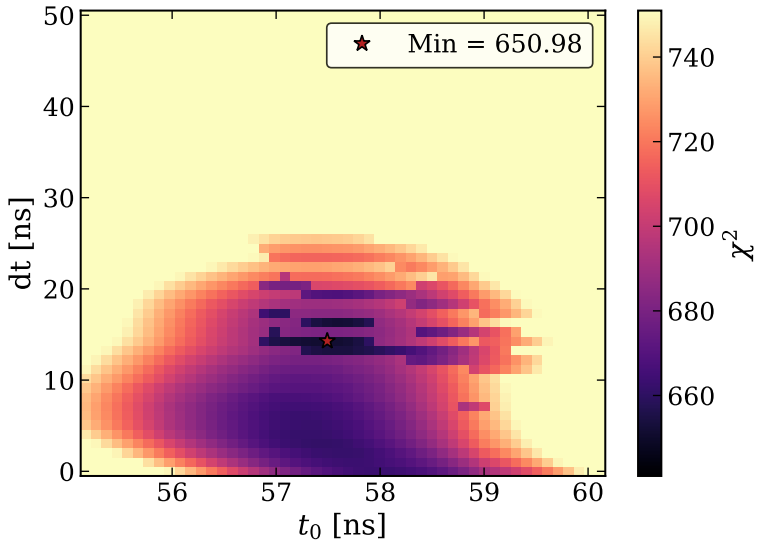

FIGURE 6.22 – Example (t_0, dt) pre-scan χ^2 map, evaluated on a single simulated event with a true annihilation delay of $dt_{\text{true}} = 5.8$ ns, using Hamamatsu PMTs only. In addition to a broad region of low χ^2 ($dt < 10$ ns), degenerate minima appear around $dt \sim 15$ ns, driven by a statistical fluctuation event hit time distribution. The star indicates the global minimum of the grid, which seeds the following `MINUIT` minimisation and leads to a fitted $dt \simeq 14.46$ ns.

6.7 Conclusion

This chapter presented a first attempt to identify ortho-positronium formation and extract its lifetime and formation fraction in JUNO. A dedicated fitting framework was developed to identify this signature on an event-by-event basis, decomposing the IBD time profile into a prompt ionisation and a delayed annihilation component, described by a common, ^{68}Ge-derived time profile PDF. The resulting five-parameter fit, minimised using `MINUIT`, was first characterised on simulated samples in order to assess its spatial and energy dependence, and was shown to recover the o-Ps lifetime and formation fraction to within about 10% of their simulated input values.

Applying this framework to the first 193.2 days of JUNO data yielded the first measurement of the o-Ps formation fraction and lifetime in JUNO's liquid scintillator :

$$\tau_{oPs} = 3.26 \text{ ns} \pm 0.21 \text{ ns} \tag{6.12}$$

$$f_{oPs} = 54.2\% \pm 8.2\% \tag{6.13}$$

Although the central lifetime value remains somewhat higher than previous PALS measurements, both results are compatible within the large statistical uncertainty of this early dataset, with the formation fraction found in excellent agreement with the measurement of [153]. This measurement is currently limited by the available statistics — less than 30% of the initial IBD sample surviving the combined spatial, energy, and neutron veto selections — and by

the early-stage performance of the event reconstruction algorithms, which directly affects the time-of-flight correction use to produce the time profile PDF and applied on each events' hit time distribution prior to the fit. Improving the description of photon propagation inside the detector, currently under development, is expected to improve future iterations of this work, alongside the increased statistics as JUNO accumulates further data. The fitting framework developed in this chapter is projected to be integrated into JUNOSW, allowing the o-Ps lifetime and formation fraction to be monitored and refined continuously as more data becomes available.

Finally, the prospect of exploiting the better timing resolution of the Hamamatsu PMT subset was investigated. Contrary to the expectation that this should uniformly improve the o-Ps identification, the reduced photon statistics available per event were found to reinforce the existing bias in the $[3, 7]$ ns region instead. Future work should therefore focus on combining the Hamamatsu and SPMT PMT systems, once the latter is fully operational during data taking.

Conclusion

Neutrino physics has entered an era of precision measurement, where several decades of breakthroughs have shaped the current experimental landscape and narrowed its remaining open questions. Among them, the neutrino mass ordering is crucial to unveiling the complete neutrino oscillation framework. The JUNO experiment has been designed with the determination of the neutrino mass ordering as its primary goal, while also targeting sub-percent precision on the remaining oscillation parameters. This thesis has followed the JUNO experiment through a crucial period of its lifetime, and contributed to several of key aspects, from the validation of its simulation software to the analysis of its first physics data.

The first part of this thesis was dedicated to the optimisation of JUNO's simulation software and its validation against detector commissioning and calibration data. This began with the validation and upgrade of JUNO's Geant4 simulation toolkit, first tested from version 10.4 to v11.2. A discrepancy identified between the two versions was traced to over-tracking in the updated Goudsmit–Saunderson multiple scattering model, now used by default in the EmLivermore physics list of recent Geant4 releases. This bug was reported to the Geant4 developers and corrected in the subsequent v11.4 release. Moreover, recent Geant4 versions show improved description of alpha particle, while presenting inaccuracy in the neutron capture description. The neutron capture in the latest v11.4 version was corrected internally before integration into JUNO's simulation software. This new Geant4 version was further shown to accurately reproduce the cosmogenic ^{9}Li yield, though larger discrepancies remain for most other isotopes, including ^{8}He. The simulation was further validated through a series of data/Monte Carlo studies performed using commissioning and calibration data to characterise the detector's light yield, spatial non-uniformity, and energy non-linearity for both PMT subsystems and led to further optimisation of the simulation. The LPMT-based energy response showed good agreement with data following these simulation upgrades, with the simulated non-linearity found within 1% of the measured value ; the SPMT response, by contrast, was found to require further investigation to identify the origin of its missing collected energy. Together, these studies established the level of understanding of JUNO's energy leading to the first physics data-taking campaign.

The final part of this thesis was dedicated to analyses conducted on the first sets of JUNO data. This began with contributions to the experiment's first oscillation analysis, where extensive work was devoted to develop an IBD selection framework for the Bordeaux group,

providing cross-checks that contributed to establish the IBD selection strategy of one of the three JUNO's analysis group. Once stabilised, this selection was applied to the first 60 days of JUNO data, yielding an IBD rate of 46.1 cpd, consistent with expectations. A method was further developed to estimate the residual ^{9}Li/^{8}He background contamination in the final IBD sample, yielding a residual rate of $R^{\text{final}}_{\text{Li/He}} = 6.6 \pm 2.7$ cpd, higher than the nominal expectation and attributed to the temporary absence of a muon-track veto in this early-stage analysis. A complementary background rejection method, based on the identification of ortho-positronium formation in JUNO's liquid scintillator, was then explored : a dedicated fitting framework was developed and applied on an event-by-event basis, yielding the first measurement of the ortho-positronium formation fraction and lifetime in JUNO's liquid scintillator, $\tau_{oPs} = 3.26 \pm 0.21$ ns and $f_{oPs} = 54.2\% \pm 8.2\%$, compatible with previous PALS measurements within the statistical uncertainty of this early dataset.

Several results presented throughout this thesis remain preliminary, reflecting the early stage of JUNO's detector performance and of its underlying simulation, and point towards concrete directions for future work. The remaining discrepancies in Geant4's description of cosmogenic isotope yields can be further constrained by future measurements from JUNO. The origin of the SPMT energy response discrepancy was traced to an unexplained $\sim 30\%$ deficit in PMT quantum efficiency, with no clear physical origin identified to date, requiring further investigation of its optical response model and of possible shadowing effects from the LPMTs. Both analyses conducted on JUNO's first data are directly limited by the detector's early-stage performance : the extracted residual ^{9}Li/^{8}He background contamination is limited by the current absence of a muon-track veto, while the o-Ps analysis is currently limited primarily by statistics, and is expected to become increasingly competitive as reconstruction algorithms are refined and time-of-flight corrections incorporating detailed optical processes are integrated into JUNOSW.

Taken together, the work presented in this thesis has contributed to establishing JUNO's early-stage detector and simulation performance, and to conducting analyses on the experiment's first IBD sample. Beyond these specific results, this thesis has produced a set of procedures, methods, and tools — from the Geant4 validation framework and the IBD selection pipeline developed for the Bordeaux group, to the ^{9}Li/^{8}He rate estimation method and the o-Ps fitting framework — that extend beyond their immediate results and are directly available to support future iterations of this work. As JUNO continues to accumulate data in the coming years, these tools are expected to serve as benchmarks against which future detector and simulation upgrades can be assessed, directly supporting the collaboration's progress towards its central goal : the determination of the neutrino mass ordering.

Bibliographie

[1] Henri Becquerel. « Sur les radiations émises par phosphorescence ». In : *Comptes Rendus Hebdomadaires des Séances de l'Académie des Sciences* 122 (1896), p. 420-421.

[2] Henri Becquerel. « Sur les radiations invisibles émises par les corps phosphorescents ». In : *Comptes Rendus Hebdomadaires des Séances de l'Académie des Sciences* 122 (1896), p. 501-503.

[3] Marie Curie. « Rayons émis par les composés de l'uranium et du thorium ». In : *Comptes Rendus Hebdomadaires des Séances de l'Académie des Sciences* 126 (1898), p. 1101-1103.

[4] J. Chadwick. « The intensity distribution in the magnetic spectrum of β particles from radium (B + C) ». In : *Verh. Phys. Gesell.* 16 (1914), p. 383-391.

[5] Charles Drummond Ellis et W. A. Wooster. « The average energy of disintegration of radium E ». In : *Proceedings of the Royal Society of London. Series A, Containing Papers of a Mathematical and Physical Character* 117.776 (jan. 1997). Publisher : Royal Society, p. 109-123. DOI : 10.1098/rspa.1927.0168. URL : https://royalsocietypublishing.org/doi/10.1098/rspa.1927.0168 (visité le 18/08/2025).

[6] W. Pauli. « Dear radioactive ladies and gentlemen ». In : *Phys. Today* 31N9 (1978), p. 27.

[7] J. Chadwick. « Possible Existence of a Neutron ». In : *Nature* 129 (1932), p. 312. DOI : 10.1038/129312a0.

[8] E. Fermi. « Tentativo di una teoria dei raggi β ». In : *Il Nuovo Cimento (1924-1942)* 11.1 (1934), p. 1-19. DOI : 10.1007/BF02959820.

[9] E. Fermi. « An attempt of a theory of beta radiation. 1. » In : *Z. Phys.* 88 (1934), p. 161-177. DOI : 10.1007/BF01351864.

[10] Hans Bethe et Rudolf Peierls. « The "Neutrino" ». In : *Nature* 133.3362 (1934), p. 532. DOI : 10.1038/133532a0.

[11] C. L. Cowan et al. « Detection of the free neutrino : A Confirmation ». In : *Science* 124 (1956), p. 103-104. DOI : 10.1126/science.124.3212.103.

[12] J. C. Street et E. C. Stevenson. « New Evidence for the Existence of a Particle of Mass Intermediate Between the Proton and Electron ». In : *Phys. Rev.* 52 (9 sept. 1937), p. 1003-1004. DOI : 10.1103/PhysRev.52.1003. URL : https://link.aps.org/doi/10.1103/PhysRev.52.1003.

[13] G. Danby et al. « Observation of High-Energy Neutrino Reactions and the Existence of Two Kinds of Neutrinos ». In : *Phys. Rev. Lett.* 9 (1 juill. 1962), p. 36-44. DOI : 10.1103/PhysRevLett.9.36. URL : https://link.aps.org/doi/10.1103/PhysRevLett.9.36.

[14] M. L. Perl et al. « Evidence for Anomalous Lepton Production in $e^+ - e^-$ Annihilation ». In : *Phys. Rev. Lett.* 35 (22 déc. 1975), p. 1489-1492. DOI : 10.1103/PhysRevLett.35.1489. URL : https://link.aps.org/doi/10.1103/PhysRevLett.35.1489.

[15] K. Kodama et the DONUT Collaboration. « Observation of Tau Neutrino Interactions ». In : *Physics Letters B* 504.3 (2001), p. 218-224. DOI : 10.1016/S0370-2693(01)00307-0. eprint : hep-ex/0012035.

[16] S. Schael et al. « Precision electroweak measurements on the Z resonance ». In : *Phys. Rept.* 427 (2006), p. 257-454. DOI : 10.1016/j.physrep.2005.12.006. arXiv : hep-ex/0509008.

[17] Georges Aad et al. « Observation of a new particle in the search for the Standard Model Higgs boson with the ATLAS detector at the LHC ». In : *Phys. Lett. B* 716 (2012), p. 1-29. DOI : 10.1016/j.physletb.2012.08.020. arXiv : 1207.7214 [hep-ex].

[18] Serguei Chatrchyan et al. « Observation of a New Boson at a Mass of 125 GeV with the CMS Experiment at the LHC ». In : *Phys. Lett. B* 716 (2012), p. 30-61. DOI : 10.1016/j.physletb.2012.08.021. arXiv : 1207.7235 [hep-ex].

[19] Sabarnya Mitra. « Exponential Resummation of QCD at finite chemical potential ». In : (juill. 2023). DOI : 10.48550/arXiv.2307.05751.

[20] F. Englert et R. Brout. « Broken Symmetry and the Mass of Gauge Vector Mesons ». In : *Phys. Rev. Lett.* 13 (9 août 1964), p. 321-323. DOI : 10.1103/PhysRevLett.13.321. URL : https://link.aps.org/doi/10.1103/PhysRevLett.13.321.

[21] Peter W. Higgs. « Broken Symmetries and the Masses of Gauge Bosons ». In : *Phys. Rev. Lett.* 13 (16 oct. 1964), p. 508-509. DOI : 10.1103/PhysRevLett.13.508. URL : https://link.aps.org/doi/10.1103/PhysRevLett.13.508.

[22] G. S. Guralnik, C. R. Hagen et T. W. B. Kibble. « Global Conservation Laws and Massless Particles ». In : *Phys. Rev. Lett.* 13 (20 nov. 1964), p. 585-587. DOI : 10.1103/PhysRevLett.13.585. URL : https://link.aps.org/doi/10.1103/PhysRevLett.13.585.

[23] T. W. B. Kibble. « Symmetry Breaking in Non-Abelian Gauge Theories ». In : *Phys. Rev.* 155 (5 mars 1967), p. 1554-1561. DOI : 10.1103/PhysRev.155.1554. URL : https://link.aps.org/doi/10.1103/PhysRev.155.1554.

[24] M. Goldhaber, L. Grodzins et A. W. Sunyar. « Helicity of Neutrinos ». In : *Phys. Rev.* 109 (1958), p. 1015-1017. DOI : 10.1103/PhysRev.109.1015.

[25] B. Pontecorvo. « Mesonium and Antimesonium ». In : *Sov. Phys. JETP* 6 (1958), p. 429-431.

[26] Ziro Maki, Masami Nakagawa et Shoichi Sakata. « Remarks on the unified model of elementary particles ». In : *Prog. Theor. Phys.* 28 (1962), p. 870-880. DOI : 10.1143/PTP.28.870.

[27] B. Pontecorvo. « Neutrino Experiments and the Problem of Conservation of Leptonic Charge ». In : *Sov. Phys. JETP* 26 (1968), p. 984-988.

[28] John N. Bahcall, Aldo M. Serenelli et Sarbani Basu. « New solar opacities, abundances, helioseismology, and neutrino fluxes ». In : *Astrophys. J. Lett.* 621 (2005), p. L85-L88. DOI : 10.1086/428929. arXiv : astro-ph/0412440.

[29] Bruno M. Pontecorvo. *Inverse β Process*. Report P.D.-205. Lecture given at a Nuclear Physics Conference, issued as Report P.D.-205. Chalk River, Ontario, Canada : National Research Council of Canada, Division of Atomic Energy, Chalk River Laboratories, nov. 1946.

[30] B. T. Cleveland et al. « Measurement of the solar electron neutrino flux with the Homestake chlorine detector ». In : *Astrophys. J.* 496 (1998), p. 505-526. DOI : 10.1086/305343.

[31] John N. Bahcall et M. H. Pinsonneault. « What Do We (Not) Know Theoretically about Solar Neutrino Fluxes ? » In : *Physical Review Letters* 92.12 (mars 2004). ISSN : 1079-7114. DOI : 10.1103/physrevlett.92.121301. URL : http://dx.doi.org/10.1103/PhysRevLett.92.121301.

[32] W. Hampel et al. « GALLEX solar neutrino observations : Results for GALLEX III. » In : *Phys. Lett. B* 388 (1996), p. 384-396. DOI : 10.1016/S0370-2693(96)01121-5.

[33] Dzh. N. Abdurashitov et al. « The Russian-American gallium experiment (SAGE) Cr neutrino source measurement ». In : *Phys. Rev. Lett.* 77 (1996), p. 4708-4711. DOI : 10.1103/PhysRevLett.77.4708.

[34] Y. Fukuda et al. « Solar neutrino data covering solar cycle 22 ». In : *Phys. Rev. Lett.* 77 (1996), p. 1683-1686. DOI : 10.1103/PhysRevLett.77.1683.

[35] Y. Fukuda et al. « Measurement of the solar neutrino energy spectrum using neutrino electron scattering ». In : *Phys. Rev. Lett.* 82 (1999), p. 2430-2434. DOI : 10.1103/PhysRevLett.82.2430. arXiv : hep-ex/9812011.

[36] Q. R. Ahmad et al. « Direct Evidence for Neutrino Flavor Transformation from Neutral-Current Interactions in the Sudbury Neutrino Observatory ». In : *Phys. Rev. Lett.* 89 (1 juin 2002), p. 011301. DOI : 10.1103/PhysRevLett.89.011301. URL : https://link.aps.org/doi/10.1103/PhysRevLett.89.011301.

[37] R. Becker-Szendy et al. « Neutrino measurements with the IMB detector ». In : *Nucl. Phys. B Proc. Suppl.* 38 (1995), p. 331-336. DOI : 10.1016/0920-5632(94)00765-N.

[38] M Ambrosio et al. « Measurement of the atmospheric neutrino induced upgoing muon flux using MACRO ». In : *Phys. Lett. B* 434 (1998), p. 451-457. DOI : 10.1016/S0370-2693(98)00885-5. arXiv : hep-ex/9807005.

[39] W. W. M. Allison et al. « Measurement of the atmospheric neutrino flavor composition in Soudan-2 ». In : *Phys. Lett. B* 391 (1997), p. 491-500. DOI : 10.1016/S0370-2693(96)01609-7. arXiv : hep-ex/9611007.

[40] Y. Fukuda et al. « Atmospheric muon-neutrino / electron-neutrino ratio in the multi-GeV energy range ». In : *Phys. Lett. B* 335 (1994), p. 237-245. DOI : 10.1016/0370-2693(94)91420-6.

[41] Y. Fukuda et al. « Evidence for oscillation of atmospheric neutrinos ». In : *Phys. Rev. Lett.* 81 (1998), p. 1562-1567. DOI : 10.1103/PhysRevLett.81.1562. arXiv : hep-ex/9807003.

[42] Nicola Cabibbo. « Unitary Symmetry and Leptonic Decays ». In : *Phys. Rev. Lett.* 10 (1963), p. 531-533. DOI : 10.1103/PhysRevLett.10.531.

[43] Makoto Kobayashi et Toshihide Maskawa. « CP Violation in the Renormalizable Theory of Weak Interaction ». In : *Prog. Theor. Phys.* 49 (1973), p. 652-657. DOI : 10.1143/PTP.49.652.

[44] Ivan Esteban et al. « NuFit-6.0 : updated global analysis of three-flavor neutrino oscillations ». In : *JHEP* 12 (2024), p. 216. DOI : 10.1007/JHEP12(2024)216. arXiv : 2410.05380 [hep-ph].

[45] L. Wolfenstein. « Neutrino Oscillations in Matter ». In : *Phys. Rev. D* 17 (1978), p. 2369-2374. DOI : 10.1103/PhysRevD.17.2369.

[46] S. P. Mikheyev et A. Yu. Smirnov. « Resonance Amplification of Oscillations in Matter and Spectroscopy of Solar Neutrinos ». In : *Sov. J. Nucl. Phys.* 42 (1985), p. 913-917.

[47] Ettore Majorana. « Teoria simmetrica dell'elettrone e del positrone ». In : *Nuovo Cim.* 14 (1937), p. 171-184. DOI : 10.1007/BF02961314.

[48] S. R. Elliott et M. Franz. « Colloquium : Majorana Fermions in nuclear, particle and solid-state physics ». In : *Rev. Mod. Phys.* 87 (2015), p. 137. DOI : 10.1103/RevModPhys.87.137. arXiv : 1403.4976 [cond-mat.supr-con].

[49] Peter Minkowski. « $\mu \to e\gamma$ at a Rate of One Out of 10^9 Muon Decays ? » In : *Phys. Lett. B* 67 (1977), p. 421-428. DOI : 10.1016/0370-2693(77)90435-X.

[50] Rabindra N. Mohapatra et Goran Senjanovic. « Neutrino Mass and Spontaneous Parity Nonconservation ». In : *Phys. Rev. Lett.* 44 (1980), p. 912. DOI : 10.1103/PhysRevLett.44.912.

[51] V. I. Tretyak et Yuri G. Zdesenko. « Tables of double beta decay data : An update ». In : *Atom. Data Nucl. Data Tabl.* 80 (2002), p. 83-116. DOI : 10.1006/adnd.2001.0873.

[52] W. H. Furry. « On transition probabilities in double beta-disintegration ». In : *Phys. Rev.* 56 (1939), p. 1184-1193. DOI : 10.1103/PhysRev.56.1184.

[53] S. Abe et al. « Search for Majorana Neutrinos with the Complete KamLAND-Zen Dataset ». In : *Phys. Rev. Lett.* 135.26 (2025), p. 262501. DOI : 10.1103/jkf6-48j8. arXiv : 2406.11438 [hep-ex].

[54] Eleonora Di Valentino, Stefano Gariazzo et Olga Mena. *Neutrinos in Cosmology*. 2024. arXiv : 2404.19322 [astro-ph.CO]. URL : https://arxiv.org/abs/2404.19322.

[55] A. G. Adame et al. « DESI 2024 VI : cosmological constraints from the measurements of baryon acoustic oscillations ». In : *JCAP* 02 (2025), p. 021. DOI : 10.1088/1475-7516/2025/02/021. arXiv : 2404.03002 [astro-ph.CO].

[56] David N. Schramm. « Neutrinos from Supernova 1987A ». In : *Comments Nucl. Part. Phys.* 17.5 (1987), p. 239-278.

[57] Thomas J. Loredo et Don Q. Lamb. « Bayesian analysis of neutrinos observed from supernova SN-1987A ». In : *Phys. Rev. D* 65 (2002), p. 063002. DOI : 10.1103/PhysRevD.65.063002. arXiv : astro-ph/0107260.

[58] Max Aker et al. « Direct neutrino-mass measurement based on 259 days of KATRIN data ». In : *Science* 388.6743 (2025), adq9592. DOI : 10.1126/science.adq9592. arXiv : 2406.13516 [nucl-ex].

[59] KATRIN collaboration. *KATRIN : A next generation tritium beta decay experiment with sub-eV sensitivity for the electron neutrino mass*. 2001. arXiv : hep-ex/0109033 [hep-ex]. URL : https://arxiv.org/abs/hep-ex/0109033.

[60] Patrick Huber, Michele Maltoni et Thomas Schwetz. « Resolving parameter degeneracies in long-baseline experiments by atmospheric neutrino data ». In : *Phys. Rev. D* 71 (2005), p. 053006. DOI : 10.1103/PhysRevD.71.053006. arXiv : hep-ph/0501037.

[61] S. Abubakar et al. « Joint neutrino oscillation analysis from the T2K and NOvA experiments ». In : *Nature* 646.8086 (2025), p. 818-824. DOI : 10.1038/s41586-025-09599-3. arXiv : 2510.19888 [hep-ex].

[62] Babak Abi et al. « Deep Underground Neutrino Experiment (DUNE), Far Detector Technical Design Report, Volume II : DUNE Physics ». In : (fév. 2020). DOI : 10.2172/1599307. arXiv : 2002.03005 [hep-ex].

[63] K. Abe et al. « Hyper-Kamiokande Design Report ». In : (mai 2018). arXiv : 1805.04163 [physics.ins-det].

[64] Claire Dalmazzone. « Measurement of the CP violation in neutrino flavour oscillations with Hyper-Kamiokande ». In : *PoS* EPS-HEP2025 (2026), p. 156. DOI : 10.22323/1.485.0156.

[65] W. Hampel et al. « Final results of the Cr-51 neutrino source experiments in GALLEX ». In : *Phys. Lett. B* 420 (1998), p. 114-126. DOI : 10.1016/S0370-2693(97)01562-1.

[66] V. M. Vermul. « Results from SAGE ». In : *Nucl. Phys. B Proc. Suppl.* 110 (2002). Sous la dir. d'A. Bettini, A. Bottino et A. Di Credico, p. 315-319. DOI : 10.1016/S0920-5632(02)01496-2.

[67] V. V. Barinov et al. « Results from the Baksan Experiment on Sterile Transitions (BEST) ». In : *Phys. Rev. Lett.* 128.23 (2022), p. 232501. DOI : 10.1103/PhysRevLett.128.232501. arXiv : 2109.11482 [nucl-ex].

[68] G. Mention et al. « Reactor antineutrino anomaly ». In : *Physical Review D* 83.7 (avr. 2011). ISSN : 1550-2368. DOI : 10.1103/physrevd.83.073006. URL : http://dx.doi.org/10.1103/PhysRevD.83.073006.

[69] A. Aguilar et al. « Evidence for neutrino oscillations from the observation of $\bar{\nu}_e$ appearance in a $\bar{\nu}_\mu$ beam ». In : *Phys. Rev. D* 64 (2001), p. 112007. DOI : 10.1103/PhysRevD.64.112007. arXiv : hep-ex/0104049.

[70] Himal Acharya et al. « Sterile-neutrino search based on 259 days of KATRIN data ». In : *Nature* 648.8092 (2025), p. 70-75. DOI : 10.1038/s41586-025-09739-9. arXiv : 2503.18667 [hep-ex].

[71] M. Andriamirado et al. « Final Search for Short-Baseline Neutrino Oscillations with the PROSPECT-I Detector at HFIR ». In : *Phys. Rev. Lett.* 134.15 (2025), p. 151802. DOI : 10.1103/PhysRevLett.134.151802. arXiv : 2406.10408 [hep-ex].

[72] H. Almazán et al. « STEREO neutrino spectrum of ^{235}U fission rejects sterile neutrino hypothesis ». In : *Nature* 613.7943 (2023), p. 257-261. DOI : 10.1038/s41586-022-05568-2. arXiv : 2210.07664 [hep-ex].

[73] P. Adamson et al. « Search for sterile neutrinos in MINOS and MINOS+ using a two-detector fit ». In : *Phys. Rev. Lett.* 122.9 (2019), p. 091803. DOI : 10.1103/PhysRevLett.122.091803. arXiv : 1710.06488 [hep-ex].

[74] Hiroshi Nunokawa, Stephen J. Parke et Jose W. F. Valle. « CP Violation and Neutrino Oscillations ». In : *Prog. Part. Nucl. Phys.* 60 (2008), p. 338-402. DOI : 10.1016/j.ppnp.2007.10.001. arXiv : 0710.0554 [hep-ph].

[75] M. Bass et al. « Baseline Optimization for the Measurement of CP Violation, Mass Hierarchy, and θ_{23} Octant in a Long-Baseline Neutrino Oscillation Experiment ». In : *Phys. Rev. D* 91.5 (2015), p. 052015. DOI : 10.1103/PhysRevD.91.052015. arXiv : 1311.0212 [hep-ex].

[76] X. Qian et P. Vogel. « Neutrino Mass Hierarchy ». In : *Prog. Part. Nucl. Phys.* 83 (2015), p. 1-30. DOI : 10.1016/j.ppnp.2015.05.002. arXiv : 1505.01891 [hep-ex].

[77] Babak Abi et al. « Deep Underground Neutrino Experiment (DUNE), Far Detector Technical Design Report, Volume I Introduction to DUNE ». In : *JINST* 15.08 (2020), T08008. DOI : 10.1088/1748-0221/15/08/T08008. arXiv : 2002.02967 [physics.ins-det].

[78] S. Aiello et al. « Determining the neutrino mass ordering and oscillation parameters with KM3NeT/ORCA ». In : *Eur. Phys. J. C* 82.1 (2022), p. 26. DOI : 10.1140/epjc/s10052-021-09893-0. arXiv : 2103.09885 [hep-ex].

[79] Mattias Blennow et al. « Quantifying the sensitivity of oscillation experiments to the neutrino mass ordering ». In : *JHEP* 03 (2014), p. 028. DOI : 10.1007/JHEP03(2014)028. arXiv : 1311.1822 [hep-ph].

[80] M. G. Aartsen et al. « PINGU Sensitivity to the Neutrino Mass Hierarchy ». In : *Snowmass 2013 : Snowmass on the Mississippi*. Juin 2013. arXiv : 1306.5846 [astro-ph.IM].

[81] S.T. Petcov et M. Piai. « The LMA MSW solution of the solar neutrino problem, inverted neutrino mass hierarchy and reactor neutrino experiments ». In : *Physics Letters B* 533.1-2 (mai 2002), p. 94-106. ISSN : 0370-2693. DOI : 10.1016/s0370-2693(02)01591-5. URL : http://dx.doi.org/10.1016/S0370-2693(02)01591-5.

[82] Sandhya Choubey, S. T. Petcov et M. Piai. « Precision neutrino oscillation physics with an intermediate baseline reactor neutrino experiment ». In : *Physical Review D* 68.11 (déc. 2003). ISSN : 1089-4918. DOI : 10.1103/physrevd.68.113006. URL : http://dx.doi.org/10.1103/PhysRevD.68.113006.

[83] Shao-Feng Ge et al. « Determination of mass hierarchy with medium baseline reactor neutrino experiments ». In : *JHEP* 05 (2013), p. 131. DOI : 10.1007/JHEP05(2013)131. arXiv : 1210.8141 [hep-ph].

[84] K. K. Joo. « New results from RENO & prospects with RENO-50 ». In : *J. Phys. Conf. Ser.* 888.1 (2017), p. 012012. DOI : 10.1088/1742-6596/888/1/012012.

[85] Angel Abusleme et al. « Potential to identify neutrino mass ordering with reactor antineutrinos at JUNO ». In : *Chin. Phys. C* 49.3 (2025), p. 033104. DOI : 10.1088/1674-1137/ad7f3e. arXiv : 2405.18008 [hep-ex].

[86] Hiroshi NUNOKAWA, Stephen J. PARKE et Renata ZUKANOVICH FUNCHAL. « Another possible way to determine the neutrino mass hierarchy ». In : *Phys. Rev. D* 72 (2005), p. 013009. DOI : 10.1103/PhysRevD.72.013009. arXiv : hep-ph/0503283.

[87] Amir N. KHAN, Hiroshi NUNOKAWA et Stephen J PARKE. « Why matter effects matter for JUNO ». In : *Phys. Lett. B* 803 (2020), p. 135354. DOI : 10.1016/j.physletb.2020.135354. arXiv : 1910.12900 [hep-ph].

[88] Peter B. DENTON et Stephen J. PARKE. « Smallness of matter effects in long-baseline muon neutrino disappearance ». In : *Physical Review D* 109.5 (mars 2024). ISSN : 2470-0029. DOI : 10.1103/physrevd.109.053002. URL : http://dx.doi.org/10.1103/PhysRevD.109.053002.

[89] Stephen J. PARKE et Renata ZUKANOVICH-FUNCHAL. « Mass ordering sum rule for the neutrino disappearance channels in T2K, NOvA, and JUNO ». In : *Phys. Rev. D* 111.1 (2025), p. 013008. DOI : 10.1103/PhysRevD.111.013008. arXiv : 2404.08733 [hep-ph].

[90] Liang ZHAN et al. « Experimental requirements to determine the neutrino mass hierarchy using reactor neutrinos ». In : *Phys. Rev. D* 79 (7 avr. 2009), p. 073007. DOI : 10.1103/PhysRevD.79.073007. URL : https://link.aps.org/doi/10.1103/PhysRevD.79.073007.

[91] Liang ZHAN et al. « Determination of the neutrino mass hierarchy at an intermediate baseline ». In : *Phys. Rev. D* 78 (11 déc. 2008), p. 111103. DOI : 10.1103/PhysRevD.78.111103. URL : https://link.aps.org/doi/10.1103/PhysRevD.78.111103.

[92] Yu-Feng LI et al. « Unambiguous determination of the neutrino mass hierarchy using reactor neutrinos ». In : *Phys. Rev. D* 88 (1 juill. 2013), p. 013008. DOI : 10.1103/PhysRevD.88.013008. URL : https://link.aps.org/doi/10.1103/PhysRevD.88.013008.

[93] Angel ABUSLEME et al. « Sub-percent precision measurement of neutrino oscillation parameters with JUNO ». In : *Chin. Phys. C* 46.12 (2022), p. 123001. DOI : 10.1088/1674-1137/ac8bc9. arXiv : 2204.13249 [hep-ex].

[94] Thomas ADAM et al. « Prospects for geoneutrino detection with JUNO ». In : (nov. 2025). arXiv : 2511.07227 [hep-ex].

[95] Angel ABUSLEME et al. « JUNO sensitivity to ^{7}Be, pep, and CNO solar neutrinos ». In : *JCAP* 10 (2023), p. 022. DOI : 10.1088/1475-7516/2023/10/022. arXiv : 2303.03910 [hep-ex].

[96] Jie ZHAO et al. « Model-independent Approach of the JUNO ^{8}B Solar Neutrino Program ». In : *Astrophys. J.* 965.2 (2024), p. 122. DOI : 10.3847/1538-4357/ad2bfd. arXiv : 2210.08437 [hep-ex].

[97] Angel Abusleme et al. « Feasibility and physics potential of detecting ^{8}B solar neutrinos at JUNO ». In : *Chin. Phys. C* 45.2 (2021), p. 023004. DOI : 10.1088/1674-1137/abd92a. arXiv : 2006.11760 [hep-ex].

[98] Angel Abusleme et al. « JUNO sensitivity to low energy atmospheric neutrino spectra ». In : *Eur. Phys. J. C* 81 (2021), p. 10. DOI : 10.1140/epjc/s10052-021-09565-z. arXiv : 2103.09908 [hep-ex].

[99] Angel Abusleme et al. « Prospects for detecting the diffuse supernova neutrino background with JUNO ». In : *JCAP* 10 (2022), p. 033. DOI : 10.1088/1475-7516/2022/10/033. arXiv : 2205.08830 [hep-ex].

[100] Angel Abusleme et al. « JUNO Sensitivity on Proton Decay $p \to \bar{\nu}K^+$ Searches ». In : *Chin. Phys. C* 47.11 (2023), p. 113002. DOI : 10.1088/1674-1137/ace9c6. arXiv : 2212.08502 [hep-ex].

[101] Angel Abusleme et al. « JUNO sensitivity to the annihilation of MeV dark matter in the galactic halo ». In : *JCAP* 09 (2023), p. 001. DOI : 10.1088/1475-7516/2023/09/001. arXiv : 2306.09567 [hep-ex].

[102] Y. Abe et al. « Improved measurements of the neutrino mixing angle ϑ 13 with the Double Chooz detector ». In : *Journal of High Energy Physics* 2014.10 (oct. 2014). ISSN : 1029-8479. DOI : 10.1007/jhep10(2014)086. URL : http://dx.doi.org/10.1007/JHEP10(2014)086.

[103] F. P. An et al. « Comprehensive Measurement of the Reactor Antineutrino Spectrum and Flux at Daya Bay ». In : *Physical Review Letters* 134.20 (mai 2025). ISSN : 1079-7114. DOI : 10.1103/physrevlett.134.201802. URL : http://dx.doi.org/10.1103/PhysRevLett.134.201802.

[104] K. Eguchi et al. « First results from KamLAND : Evidence for reactor anti-neutrino disappearance ». In : *Phys. Rev. Lett.* 90 (2003), p. 021802. DOI : 10.1103/PhysRevLett.90.021802. arXiv : hep-ex/0212021.

[105] F. P. An et al. « Observation of electron-antineutrino disappearance at Daya Bay ». In : *Phys. Rev. Lett.* 108 (2012), p. 171803. DOI : 10.1103/PhysRevLett.108.171803. arXiv : 1203.1669 [hep-ex].

[106] Y. Abe et al. « Indication of Reactor $\bar{\nu}_e$ Disappearance in the Double Chooz Experiment ». In : *Phys. Rev. Lett.* 108 (2012), p. 131801. DOI : 10.1103/PhysRevLett.108.131801. arXiv : 1112.6353 [hep-ex].

[107] P. Vogel et J. F. Beacom. « Angular distribution of neutron inverse beta decay ». In : *Physical Review D* 60.5 (juill. 1999). ISSN : 1089-4918. DOI : 10.1103/physrevd.60.053003. URL : http://dx.doi.org/10.1103/PhysRevD.60.053003.

[108] P. Vogel, L.J. Wen et C. Zhang. « Neutrino oscillation studies with reactors ». In : *Nature Communications* 6.1 (avr. 2015). ISSN : 2041-1723. DOI : 10.1038/ncomms7935. URL : http://dx.doi.org/10.1038/ncomms7935.

[109] In : *Progress in Particle and Nuclear Physics* 123 (mars 2022), p. 103927. ISSN : 0146-6410. DOI : 10.1016/j.ppnp.2021.103927. URL : http://dx.doi.org/10.1016/j.ppnp.2021.103927.

[110] T. Adam et al. « The OPERA experiment target tracker ». In : *Nucl. Instrum. Meth. A* 577 (2007), p. 523-539. DOI : 10.1016/j.nima.2007.04.147. arXiv : physics/0701153.

[111] Angel Abusleme et al. « The JUNO experiment Top Tracker ». In : *Nucl. Instrum. Meth. A* 1057 (2023), p. 168680. DOI : 10.1016/j.nima.2023.168680. arXiv : 2303.05172 [hep-ex].

[112] A. Abusleme et al. « Optimization of the JUNO liquid scintillator composition using a Daya Bay antineutrino detector ». In : *Nucl. Instrum. Meth. A* 988 (2021), p. 164823. DOI : 10.1016/j.nima.2020.164823. arXiv : 2007.00314 [physics.ins-det].

[113] Zhihang Zhu et al. « Optical purification pilot plant for JUNO liquid scintillator ». In : *Nucl. Instrum. Meth. A* 1048 (2023), p. 167890. DOI : 10.1016/j.nima.2022.167890.

[114] C. Landini et al. « Distillation and gas stripping purification plants for the JUNO liquid scintillator ». In : *Nucl. Instrum. Meth. A* 1069 (2024), p. 169887. DOI : 10.1016/j.nima.2024.169887. arXiv : 2406.01381 [physics.ins-det].

[115] Jiaxuan Ye et al. « Development of water extraction system for liquid scintillator purification of JUNO ». In : *Nucl. Instrum. Meth. A* 1027 (2022), p. 166251. DOI : 10.1016/j.nima.2021.166251. arXiv : 2109.07317 [physics.ins-det].

[116] Xin Ling et al. « JUNO high purity nitrogen plant ». In : *Appl. Radiat. Isot.* 208 (2024), p. 111305. DOI : 10.1016/j.apradiso.2024.111305.

[117] Angel Abusleme et al. « The design and sensitivity of JUNO's scintillator radiopurity pre-detector OSIRIS ». In : *Eur. Phys. J. C* 81.11 (2021), p. 973. DOI : 10.1140/epjc/s10052-021-09544-4. arXiv : 2103.16900 [physics.ins-det].

[118] Angel Abusleme et al. « Prediction of Energy Resolution in the JUNO Experiment ». In : *Chin. Phys. C* 49.1 (2025), p. 013003. DOI : 10.1088/1674-1137/ad83aa. arXiv : 2405.17860 [hep-ex].

[119] Angel Abusleme et al. « Initial performance results of the JUNO detector ». In : (nov. 2025). arXiv : 2511.14590 [hep-ex].

[120] Zelimir Djurcic et al. « JUNO Conceptual Design Report ». In : (août 2015). arXiv : 1508.07166 [physics.ins-det].

[121] T. Y. Guan et al. « Development of low-radon ultra-pure water for the Jiangmen Underground Neutrino Observatory ». In : *Nucl. Instrum. Meth. A* 1063 (2024), p. 169244. DOI : 10.1016/j.nima.2024.169244. arXiv : 2403.12414 [physics.ins-det].

[122] F.P. An et al. « The muon system of the Daya Bay Reactor antineutrino experiment ». In : *Nuclear Instruments and Methods in Physics Research Section A : Accelerators, Spectrometers, Detectors and Associated Equipment* 773 (fév. 2015), p. 8-20. ISSN : 0168-9002. DOI : 10.1016/j.nima.2014.09.070. URL : http://dx.doi.org/10.1016/j.nima.2014.09.070.

[123] F. P. An et al. « The Detector System of The Daya Bay Reactor Neutrino Experiment ». In : *Nucl. Instrum. Meth. A* 811 (2016), p. 133-161. DOI : 10.1016/j.nima.2015.11.144. arXiv : 1508.03943 [physics.ins-det].

[124] L.J. Wen et al. « A quantitative approach to select PMTs for large detectors ». In : *Nuclear Instruments and Methods in Physics Research Section A : Accelerators, Spectrometers, Detectors and Associated Equipment* 947 (déc. 2019), p. 162766. ISSN : 0168-9002. DOI : 10.1016/j.nima.2019.162766. URL : http://dx.doi.org/10.1016/j.nima.2019.162766.

[125] Matsusada Precision Inc. *Photomultiplier Tubes — Power Supply Applications*. URL : https://www.matsusada.com/application/ps/photomultiplier_tubes/.

[126] Ziyu Liu et al. « The Development of a Large-Area Microchannel Plate Photomultiplier Tube with a Gate Function ». In : *Photonics* 12.1 (2025), p. 46. DOI : 10.3390/photonics12010046. URL : https://www.mdpi.com/2304-6732/12/1/46.

[127] Yifang Wang et al. « The R&D of the 20 in. MCP–PMTs for JUNO ». In : *Nuclear Instruments and Methods in Physics Research Section A : Accelerators, Spectrometers, Detectors and Associated Equipment* 824 (2016), p. 143-144. DOI : 10.1016/j.nima.2015.10.106.

[128] Zelimir Djurcic et al. « JUNO Conceptual Design Report ». In : (août 2015). arXiv : 1508.07166 [physics.ins-det].

[129] Angel Abusleme et al. « Mass testing and characterization of 20-inch PMTs for JUNO ». In : *Eur. Phys. J. C* 82.12 (2022), p. 1168. DOI : 10.1140/epjc/s10052-022-11002-8. arXiv : 2205.08629 [physics.ins-det].

[130] Chuanya Cao et al. « Mass production and characterization of 3-inch PMTs for the JUNO experiment ». In : *Nuclear Instruments and Methods in Physics Research Section A : Accelerators, Spectrometers, Detectors and Associated Equipment* 1005 (juill. 2021), p. 165347. ISSN : 0168-9002. DOI : 10.1016/j.nima.2021.165347. URL : http://dx.doi.org/10.1016/j.nima.2021.165347.

[131] Fengpeng An et al. « Neutrino Physics with JUNO ». In : *J. Phys. G* 43.3 (2016), p. 030401. DOI : 10.1088/0954-3899/43/3/030401. arXiv : 1507.05613 [physics.ins-det].

[132] J. B. Birks. « Scintillations from Organic Crystals : Specific Fluorescence and Relative Response to Different Radiations ». In : *Proc. Phys. Soc. A* 64 (1951), p. 874-877. DOI : 10.1088/0370-1298/64/10/303.

[133] I. M. Frank et I. E. Tamm. « Coherent visible radiation of fast electrons passing through matter ». In : *Compt. Rend. Acad. Sci. URSS* 14.3 (1937). Sous la dir. de V. L. Ginzburg, B. M. Bolotovsky et I. M. Dremin, p. 109-114. DOI : 10.3367/UFNr.0093.196710o.0388.

[134] Anatael Cabrera et al. « Multi-calorimetry in light-based neutrino detectors ». In : *JHEP* 12 (2024), p. 002. DOI : 10.1007/JHEP12(2024)002. arXiv : 2312.12991 [hep-ex].

[135] Angel Abusleme et al. « Calibration Strategy of the JUNO Experiment ». In : *JHEP* 03 (2021), p. 004. DOI : 10.1007/JHEP03(2021)004. arXiv : 2011.06405 [physics.ins-det].

[136] J. Liu et al. « Automated calibration system for a high-precision measurement of neutrino mixing angle ϑ13 with the Daya Bay antineutrino detectors ». In : *Nuclear Instruments and Methods in Physics Research Section A : Accelerators, Spectrometers, Detectors and Associated Equipment* 750 (juin 2014), p. 19-37. ISSN : 0168-9002. DOI : 10.1016/j.nima.2014.02.049. URL : http://dx.doi.org/10.1016/j.nima.2014.02.049.

[137] Barbara Caccianiga et Alessandra Carlotta Re. « The calibration system for the Borexino experiment ». In : *Int. J. Mod. Phys. A* 29 (2014), p. 1442010. DOI : 10.1142/S0217751X1442010X.

[138] Yuhang Guo et al. « Design of the Guide Tube Calibration System for the JUNO experiment ». In : *JINST* 14.09 (2019), T09005. DOI : 10.1088/1748-0221/14/09/T09005. arXiv : 1905.02077 [physics.ins-det].

[139] Angel Abusleme et al. « First measurement of reactor neutrino oscillations at JUNO ». In : (nov. 2025). arXiv : 2511.14593 [hep-ex].

[140] Angel Abusleme et al. « TAO Conceptual Design Report : A Precision Measurement of the Reactor Antineutrino Spectrum with Sub-percent Energy Resolution ». In : (mai 2020). arXiv : 2005.08745 [physics.ins-det].

[141] J. H. Choi et al. « Observation of Energy and Baseline Dependent Reactor Antineutrino Disappearance in the RENO Experiment ». In : *Phys. Rev. Lett.* 116.21 (2016), p. 211801. DOI : 10.1103/PhysRevLett.116.211801. arXiv : 1511.05849 [hep-ex].

[142] Feng Peng An et al. « Measurement of the Reactor Antineutrino Flux and Spectrum at Daya Bay ». In : *Phys. Rev. Lett.* 116.6 (2016). [Erratum : Phys.Rev.Lett. 118, 099902 (2017)], p. 061801. DOI : 10.1103/PhysRevLett.116.061801. arXiv : 1508.04233 [hep-ex].

[143] H. de Kerret et al. « Double Chooz θ_{13} measurement via total neutron capture detection ». In : *Nature Phys.* 16.5 (2020), p. 558-564. DOI : 10.1038/s41567-020-0831-y. arXiv : 1901.09445 [hep-ex].

[144] Patrick Huber. « On the determination of anti-neutrino spectra from nuclear reactors ». In : *Phys. Rev. C* 84 (2011). [Erratum : Phys.Rev.C 85, 029901 (2012)], p. 024617. DOI : 10.1103/PhysRevC.85.029901. arXiv : 1106.0687 [hep-ph].

[145] Th. A. Mueller et al. « Improved Predictions of Reactor Antineutrino Spectra ». In : *Phys. Rev. C* 83 (2011), p. 054615. DOI : 10.1103/PhysRevC.83.054615. arXiv : 1101.2663 [hep-ex].

[146] Feng Peng An et al. « Improved Search for a Light Sterile Neutrino with the Full Configuration of the Daya Bay Experiment ». In : *Phys. Rev. Lett.* 117.15 (2016), p. 151802. DOI : 10.1103/PhysRevLett.117.151802. arXiv : 1607.01174 [hep-ex].

[147] H. Almazán et al. « Improved sterile neutrino constraints from the STEREO experiment with 179 days of reactor-on data ». In : *Phys. Rev. D* 102.5 (2020), p. 052002. DOI : 10.1103/PhysRevD.102.052002. arXiv : 1912.06582 [hep-ex].

[148] Y. J. Ko et al. « Sterile Neutrino Search at the NEOS Experiment ». In : *Phys. Rev. Lett.* 118.12 (2017), p. 121802. DOI : 10.1103/PhysRevLett.118.121802. arXiv : 1610.05134 [hep-ex].

[149] Hangkun Xu et al. « Calibration strategy of the JUNO-TAO experiment ». In : *Eur. Phys. J. C* 82.12 (2022), p. 1112. DOI : 10.1140/epjc/s10052-022-11069-3. arXiv : 2204.03256 [physics.ins-det].

[150] Tao Lin et al. « Simulation software of the JUNO experiment ». In : *The European Physical Journal C* 83.5 (mai 2023). ISSN : 1434-6052. DOI : 10.1140/epjc/s10052-023-11514-x. URL : http://dx.doi.org/10.1140/epjc/s10052-023-11514-x.

[151] J. H. Zou et al. « SNiPER : an offline software framework for non-collider physics experiments ». In : *J. Phys. Conf. Ser.* 664.7 (2015), p. 072053. DOI : 10.1088/1742-6596/664/7/072053.

[152] S. Agostinelli et al. « GEANT4 - A Simulation Toolkit ». In : *Nucl. Instrum. Meth. A* 506 (2003), p. 250-303. DOI : 10.1016/S0168-9002(03)01368-8.

[153] S. Perasso et al. « Measurement of ortho-Positronium Properties in Liquid Scintillators ». In : *JINST* 9 (2014). Sous la dir. de Pietro Govoni et al., p. C03028. DOI : 10.1088/1748-0221/9/03/C03028. arXiv : 1306.6001 [physics.ins-det].

[154] C. Jollet et A. Meregaglia. « ^{9}Li and ^{8}He decays in GEANT4 ». In : *Nucl. Instrum. Meth. A* 949 (2020), p. 162904. DOI : 10.1016/j.nima.2019.162904. arXiv : 1910.01060 [nucl-ex].

[155] Laszlo Urban. « A model for multiple scattering in Geant4 ». In : (déc. 2006).

[156] V. N. Ivanchenko et al. « Geant4 models for simulation of multiple scattering ». In : *Journal of Physics : Conference Series*. T. 219. 3. IOP Publishing, 2010. DOI : 10.1088/1742-6596/219/3/032045.

[157] S. Goudsmit et J. L. Saunderson. « Multiple Scattering of Electrons ». In : *Phys. Rev.* 57 (1 jan. 1940), p. 24-29. DOI : 10.1103/PhysRev.57.24. URL : https://link.aps.org/doi/10.1103/PhysRev.57.24.

[158] Mihaly Novak. *On the new and accurate (Goudsmit-Saunderson) model for describing e-/e+ multiple Coulomb scattering (Geant4 Technical Note)*. 2025. arXiv : 2410.13361 [physics.comp-ph]. URL : https://arxiv.org/abs/2410.13361.

[159] J. F. Ziegler, M. D. Ziegler et J. P. Biersack. « SRIM - The stopping and range of ions in matter (2010) ». In : *Nuclear Instruments and Methods in Physics Research B* 268 (juin 2010), p. 1818-1823. DOI : 10.1016/j.nimb.2010.02.091.

[160] M. Zmeškal, L. Thulliez et E. Dumonteil. *Improvement of Geant4 Neutron-HP package : Doppler broadening of the neutron elastic scattering kernel and cross sections*. 2023. arXiv : 2303.07300 [physics.comp-ph]. URL : https://arxiv.org/abs/2303.07300.

[161] M. Zmeškal et al. *Improvement of Geant4 Neutron-HP package : Unresolved Resonance Region description with Probability Tables*. 2024. arXiv : 2404.16389 [physics.comp-ph]. URL : https://arxiv.org/abs/2404.16389.

[162] S. Abe et al. « Production of Radioactive Isotopes through Cosmic Muon Spallation in KamLAND ». In : *Phys. Rev. C* 81 (2010), p. 025807. DOI : 10.1103/PhysRevC.81.025807. arXiv : 0907.0066 [hep-ex].

[163] F. P. An et al. « First measurement of the yield of He8 isotopes produced in liquid scintillator by cosmic-ray muons at Daya Bay ». In : *Phys. Rev. D* 110.1 (2024), p. L011101. DOI : 10.1103/PhysRevD.110.L011101. arXiv : 2402.05383 [nucl-ex].

[164] V. A. Kudryavtsev. « Muon simulation codes MUSIC and MUSUN for underground physics ». In : *Comput. Phys. Commun.* 180 (2009), p. 339-346. DOI : 10.1016/j.cpc.2008.10.013. arXiv : 0810.4635 [physics.comp-ph].

[165] Karim Zbiri. « Remark on the studies of the muon-induced neutron background in the liquid scintillator detectors ». In : *Nuclear Instruments and Methods in Physics Research Section A : Accelerators, Spectrometers, Detectors and Associated Equipment* 615.2 (avr. 2010), p. 220-222. ISSN : 0168-9002. DOI : 10.1016/j.nima.2010.01.035. URL : http://dx.doi.org/10.1016/j.nima.2010.01.035.

[166] H. de Kerret et al. « Yields and production rates of cosmogenic ^{9}Li and ^{8}He measured with the Double Chooz near and far detectors ». In : *JHEP* 11 (2018), p. 053. DOI : 10.1007/JHEP11(2018)053. arXiv : 1802.08048 [hep-ex].

[167] Haoqi Lu. « The JUNO water Cherenkov detector system ». In : *Nucl. Instrum. Meth. A* 1056 (2023), p. 168623. DOI : 10.1016/j.nima.2023.168623.

[168] Alfredo Ferrari et al. « FLUKA : A multi-particle transport code (Program version 2005) ». In : (oct. 2005). DOI : 10.2172/877507.

[169] H. G. Lee et al. « Measurement of cosmogenic Li9 and He8 production rates at RENO ». In : *Phys. Rev. D* 106.1 (2022), p. 012005. DOI : 10.1103/PhysRevD.106.012005. arXiv : 2204.09215 [nucl-ex].

[170] Takatomi Yano et al. « Comprehension of AmBe+BGO source to calibrate neutron tagging in electron antineutrino physics ». In : *PoS* ICRC2023 (2023), p. 1067. DOI : 10.22323/1.444.1067.

[171] Yaoguang Wang et al. « A new optical model for photomultiplier tubes ». In : *The European Physical Journal C* 82.4 (avr. 2022). ISSN : 1434-6052. DOI : 10.1140/epjc/s10052-022-10288-y. URL : http://dx.doi.org/10.1140/epjc/s10052-022-10288-y.

[172] Y. Ren et al. *Development of a comprehensive PMT optical model for the JUNO experiment*. 2026. arXiv : 2601.19081 [hep-ex]. URL : https://arxiv.org/abs/2601.19081.

[173] August Beer. « Bestimmung der Absorption des rothen Lichts in farbigen Flüssigkeiten ». In : *Annalen der Physik und Chemie* 162.5 (1852), p. 78-88. DOI : 10.1002/andp.18521620505.

[174] Stuart M. Marshall, Alastair R. G. Murray et Leroy Cronin. « Pathway complexity as a measure of biological complexity ». In : *Current Biology* 27.23 (2017), R1180-R1185. DOI : 10.1016/j.cub.2017.10.032. URL : https://www.sciencedirect.com/science/article/pii/S0969804317305134.

[175] Mohammad Javad Safari. « Differentiation method for Compton edge characterization in organic scintillation detectors ». In : *Radiation Physics and Engineering* 1.4 (oct. 2020). DOI : 10.22034/rpe.2020.104839. URL : https://doi.org/10.22034/rpe.2020.104839.

[176] Xiaojie Luo et al. « Long-Delayed Afterpulse Measurement of JUNO 20-inch Photomultiplier Tubes ». In : (août 2026). arXiv : 2608.01943 [hep-ex].

[177] *Precise measurements of the β-decays of ^{9}Li and ^{8}He for reactor neutrino experiments*. Rapp. tech. INTC-P-549. CERN, 2020. URL : https://cds.cern.ch/record/2717820/files/INTC-P-549.pdf.

[178] F. James et M. Roos. « Minuit : A System for Function Minimization and Analysis of the Parameter Errors and Correlations ». In : *Comput. Phys. Commun.* 10 (1975), p. 343-367. DOI : 10.1016/0010-4655(75)90039-9.

[179] G. Ranucci, A. Goretti et P. Lombardi. « Pulse-shape discrimination of liquid scintillators ». In : *Nucl. Instrum. Meth. A* 412 (1998), p. 374-386. DOI : 10.1016/S0168-9002(98)00456-2.

[180] Martin Deutsch. « Evidence for the Formation of Positronium in Gases ». In : *Phys. Rev.* 82 (1951), p. 455-456. DOI : 10.1103/PhysRev.82.455.

[181] A. H. Al-Ramadhan et D. W. Gidley. « New precision measurement of the decay rate of singlet positronium ». In : *Phys. Rev. Lett.* 72 (11 mars 1994), p. 1632-1635. DOI : 10.1103/PhysRevLett.72.1632. URL : https://link.aps.org/doi/10.1103/PhysRevLett.72.1632.

[182] J. S. Nico et al. « Precision measurement of the orthopositronium decay rate using the vacuum technique ». In : *Phys. Rev. Lett.* 65 (1990), p. 1344. DOI : 10.1103/PhysRevLett.65.1344.

[183] Werner Brandt, S. Berko et W. W. Walker. « Positronium Decay in Molecular Substances ». In : *Phys. Rev.* 120 (4 nov. 1960), p. 1289-1295. DOI : 10.1103/PhysRev.120.1289. URL : https://link.aps.org/doi/10.1103/PhysRev.120.1289.

[184] S. J. Tao. « The Formation of Positronium in Molecular Substances ». In : *Appl. Phys.* 10 (1976), p. 67-79. DOI : 10.1007/BF00929530.

[185] Richard A. Ferrell. « Ortho-Parapositronium Quenching by Paramagnetic Molecules and Ions ». In : *Phys. Rev.* 110 (6 juin 1958), p. 1355-1357. DOI : 10.1103/PhysRev.110.1355. URL : https://link.aps.org/doi/10.1103/PhysRev.110.1355.

[186] David B. Cassidy et Allen P. Mills Jr. « Physics with dense positronium ». In : *physica status solidi c* 4.10 (2007), p. 3419-3428. DOI : https://doi.org/10.1002/pssc.200675760. eprint : https://onlinelibrary.wiley.com/doi/pdf/10.1002/pssc.200675760. URL : https://onlinelibrary.wiley.com/doi/abs/10.1002/pssc.200675760.

[187] Ya-Ping CHENG et al. « e+/e- discrimination in liquid scintillator and its usage to suppress ⁸He/⁹Li backgrounds ». In : *Chinese Physics C* 41.1 (jan. 2017), p. 016101. ISSN : 1674-1137. DOI : 10.1088/1674-1137/41/1/016101. URL : http://dx.doi.org/10.1088/1674-1137/41/1/016101.

[188] Mario SCHWARZ et al. « Measurements of the Lifetime of Orthopositronium in the LAB-Based Liquid Scintillator of JUNO ». In : *Nucl. Instrum. Meth. A* 922 (2019), p. 64-70. DOI : 10.1016/j.nima.2018.12.068. arXiv : 1804.09456 [physics.ins-det].

[189] Y. ABE et al. « Ortho-positronium observation in the Double Chooz Experiment ». In : *JHEP* 10 (2014), p. 032. DOI : 10.1007/JHEP10(2014)032. arXiv : 1407.6913 [physics.ins-det].

[190] G. BELLINI et al. « First evidence of pep solar neutrinos by direct detection in Borexino ». In : *Phys. Rev. Lett.* 108 (2012), p. 051302. DOI : 10.1103/PhysRevLett.108.051302. arXiv : 1110.3230 [hep-ex].

[191] C. BAUER et al. « Qualification Tests of 474 Photomultiplier Tubes for the Inner Detector of the Double Chooz Experiment ». In : *JINST* 6 (2011), P06008. DOI : 10.1088/1748-0221/6/06/P06008. arXiv : 1104.0758 [physics.ins-det].

[192] S. NAVAS et al. « Review of particle physics ». In : *Phys. Rev. D* 110.3 (2024), p. 030001. DOI : 10.1103/PhysRevD.110.030001.

[193] Cécile JOLLET et al. *Modified GEANT4 processes for JUNO Simulation*. Indico contribution 5805327. URL : https://indico.cern.ch/event/1366947/contributions/5805327/attachments/2801700/4887978/JUNOSimulation_GEANT4Forum.pdf.